

# Remote Sensing of Supraglacial Lake Dynamics in Antarctica

Exploiting Methods from Artificial Intelligence for Derivation of Antarctic Supraglacial Lake Extents in Multi-Sensor Remote Sensing Data

Dissertation zur Erlangung der Doktorwürde der Philosophischen Fakultät der Julius-Maximilians-Universität Würzburg

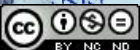
vorgelegt von

**Mariel Christina Dirscherl**

Dezember 2021



Julius-Maximilians-  
**UNIVERSITÄT  
WÜRZBURG**



Titelbild: Supraglaziale Seen auf dem George VI Schelfeis, Antarktische Halbinsel. Sentinel-2 Falschfarben-Komposit überlagert mit einer Sentinel-1 und Sentinel-2 basierten Klassifikation der supraglazialen Seen im Januar 2020. Daten: Copernicus Sentinel Daten.

**Eingereicht am:** 02.12.2021

**Von:** Mariel Christina Dirscherl

**Ort:** Lehrstuhl für Fernerkundung der Julius-Maximilians-Universität Würzburg,  
in Kooperation mit dem Deutschen Fernerkundungsdatenzentrum (DFD) des  
Deutschen Zentrums für Luft- und Raumfahrt (DLR)

**Tag des Kolloquiums:** 08.06.2022

**Erstbetreuerin:** Prof. Dr. Claudia Künzer

**Zweitbetreuer:** Prof. Dr. Christof Kneisel

This dissertation was prepared at the “Land Surface Dynamics” department of the German Remote Sensing Data Center (DFD), Earth Observation Center (EOC), German Aerospace Center (DLR), Oberpfaffenhofen, Germany.





*“Science makes people reach selflessly for truth and objectivity; it teaches people to accept reality, with wonder and admiration, not to mention the deep awe and joy that the natural order of things brings to the true scientist.”*

– Lise Meitner



# Table of Contents

<b>Acknowledgements</b> .....	<b>XI</b>
<b>Summary</b> .....	<b>XIII</b>
<b>Zusammenfassung</b> .....	<b>XV</b>
<b>Resumen en Español</b> .....	<b>XVII</b>
<b>Chinese Summary (中文摘要)</b> .....	<b>XIX</b>
<b>List of Figures</b> .....	<b>XXI</b>
<b>List of Tables</b> .....	<b>XXVII</b>
<b>List of Abbreviations</b> .....	<b>XXIX</b>
<b>1 Introduction</b> .....	<b>1</b>
1.1 Scientific Relevance.....	1
1.2 Research Motivation.....	7
1.3 Research Objectives.....	8
1.4 Thesis Outline.....	11
<b>2 Physical Characteristics of Antarctica</b> .....	<b>13</b>
2.1 Glaciology.....	13
2.1.1 Ice Sheet Structure.....	15
2.1.2 Ice Dynamical Change.....	18
2.2 Climatology.....	21
2.2.1 Wind.....	21
2.2.2 Air Temperature.....	23
2.2.3 Precipitation.....	26
2.3 Oceanography.....	26
<b>3 A Review on Fundamentals of Antarctic Surface Hydrology</b> .....	<b>29</b>
3.1 Controls on Supraglacial Lake Formation and Appearance.....	31
3.1.1 Local Controls.....	31
3.1.2 Regional Controls.....	32
3.1.3 Large-Scale Controls.....	33
3.2 Supraglacial Lake Distribution.....	34
3.2.1 Antarctic Peninsula.....	34
3.2.2 East Antarctica.....	35
3.2.3 West Antarctica.....	35
3.3 Supraglacial Lake Impacts on Ice Dynamics.....	36
3.4 Summary.....	40
<b>4 A Review on Spaceborne Remote Sensing of Antarctic Supraglacial Lake Extents</b> .....	<b>41</b>
4.1 Results of the Literature Review on Spaceborne Remote Sensing of Antarctic Supraglacial Lakes.....	41
4.1.1 Applied Satellite Sensors.....	42
4.1.2 Applied Mapping Techniques.....	45
4.1.3 Geospatial Coverage of Studies.....	47
4.1.4 Temporal Resolution of Studies.....	50

4.2	Potentials and Challenges of Spaceborne Remote Sensing for Antarctic Supraglacial Lake Extent Mapping.....	50
4.2.1	Optical Remote Sensing .....	51
4.2.2	SAR Remote Sensing .....	53
4.2.3	Optical versus SAR.....	56
4.3	Discussion of Requirements of Spaceborne Remote Sensing of Antarctic Supraglacial Lakes .....	58
4.3.1	Requirement of a Higher Temporal and Spatial Coverage of Studies on Antarctic Supraglacial Lakes.....	58
4.3.2	Future Method Requirements for Antarctic Supraglacial Lake Extent Mapping.....	61
4.4	Summary.....	62
<b>5</b>	<b>A Novel Framework for Antarctic Supraglacial Lake Extent Mapping .....</b>	<b>63</b>
5.1	Training and Testing Sites .....	64
5.2	Input Data .....	68
5.2.1	Sentinel-1 Data.....	68
5.2.2	Sentinel-2 Data.....	71
5.2.3	Training Labels .....	72
5.2.4	Topographic Data .....	73
5.2.5	Coastline Data .....	73
5.3	Methodological Framework.....	74
5.3.1	Sentinel-1 .....	74
5.3.1.1	Data Preparation and Pre-Processing.....	75
5.3.1.2	Deep Learning Model Training.....	77
5.3.1.3	Post-Processing.....	81
5.3.2	Sentinel-2 .....	82
5.3.2.1	Data Preparation and Pre-Processing.....	82
5.3.2.2	Random Forest Model Training.....	85
5.3.2.3	Post-Processing.....	88
5.3.3	Fusion of Sentinel-1 and Sentinel-2 Classifications.....	89
5.4	Results.....	90
5.4.1	Sentinel-1 .....	90
5.4.2	Sentinel-2 .....	95
5.4.3	Fused Classification Products.....	100
5.5	Accuracy Assessment.....	104
5.5.1	Sentinel-1 .....	105
5.5.2	Sentinel-2 .....	106
5.6	Implementation of Methods for Circum-Antarctic Processing .....	107
5.7	Discussion .....	109
5.7.1	Mapping Results .....	109
5.7.1.1	Sentinel-1 .....	109
5.7.1.2	Sentinel-2 .....	109
5.7.1.3	Fused Classification Products.....	110

5.7.2	Accuracy Assessment.....	111
5.7.2.1	Sentinel-1.....	111
5.7.2.2	Sentinel-2.....	112
5.7.3	Future Requirements .....	113
5.8	Summary .....	114
<b>6</b>	<b>Environmental Controls on Antarctic Supraglacial Lake Formation in 2015-2021.....</b>	<b>117</b>
6.1	Study Sites.....	118
6.2	Datasets.....	120
6.2.1	Satellite Imagery .....	120
6.2.2	ERA5-Land Climate Reanalysis Data.....	122
6.3	Methods .....	124
6.3.1	Pre-Processing of ERA5-Land Climate Reanalysis Data.....	124
6.3.2	Time Series Generation .....	124
6.3.3	Multi-Temporal Statistical Correlation Analysis.....	125
6.4	Results.....	126
6.4.1	Antarctic Peninsula Ice Shelves .....	127
6.4.1.1	Supraglacial Lake Extent Dynamics in 2015-2021 .....	127
6.4.1.2	Multi-Temporal Correlation Analysis with Spatial Averages.....	129
6.4.1.3	Multi-Temporal Correlation Analysis at Pixel Level.....	131
6.4.2	East Antarctic Ice Shelves.....	132
6.4.2.1	Supraglacial Lake Extent Dynamics in 2016-2021 .....	132
6.4.2.2	Multi-Temporal Correlation Analysis with Spatial Averages.....	133
6.4.2.3	Multi-Temporal Correlation Analysis at Pixel Level.....	134
6.5	Discussion.....	137
6.5.1	Antarctic Peninsula Ice Shelves .....	137
6.5.1.1	Local Controls .....	137
6.5.1.2	Regional Controls .....	138
6.5.1.3	Large-Scale Controls .....	139
6.5.2	East Antarctic Ice Shelves.....	140
6.5.2.1	Local Controls.....	140
6.5.2.2	Regional Controls .....	141
6.5.2.3	Large-Scale Controls .....	142
6.5.3	Implications for the Antarctic Continent .....	143
6.5.4	Potential Implications for Future Ice Shelf Stability .....	144
6.6	Summary .....	145
<b>7</b>	<b>Synthesis and Outlook .....</b>	<b>147</b>
7.1	Summary and Conclusive Findings .....	147
7.2	Future Challenges and Opportunities .....	154
	<b>Bibliography .....</b>	<b>157</b>
	<b>Eidesstattliche Erklärung .....</b>	<b>181</b>
	<b>Curriculum Vitae .....</b>	<b>183</b>





# Acknowledgements

This thesis would not have been possible without the support and guidance of many people to whom I would like to express my sincere gratitude:

To my mentor and supervisor at the German Remote Sensing Data Center (DFD) of the German Aerospace Center (DLR), Prof. Dr. Claudia Kuenzer, for her continuous support and outstanding guidance throughout the learning process of my dissertation. I am deeply grateful for her invaluable feedback on my research and her commitment to support and advance my scientific career beyond my expectations.

To my mentors at the University of Wuerzburg, Prof. Dr. Christof Kneisel and PD Dr. Tobias Ullmann, for agreeing to supervise this thesis and their helpful feedback and advice on my dissertation.

To my team leader at DLR-DFD, Dr. Andreas Dietz, for his continuous support and helpful discussions on polar research. I am very thankful for the opportunity to work in such an open-minded and experienced research group.

To the institute leader of DLR-DFD, Prof. Dr. Stefan Dech, for his keen interest in my dissertation as well as the opportunity to work in such an inspiring and supporting research environment.

To my colleagues at DLR-DFD, especially Dr. Celia Baumhoer, for valuable discussions on Antarctic research as well as the many coffee breaks and conferences we were able to visit together. Special appreciation also goes to my team colleagues and fellow PhD students Dr. Ya-Lun Tsai, Jonas Koehler, Dr. Zhongyang Hu, Dr. Sebastian Roeßler, Marius Philipp, Soner Ureyen, Aiyem Orynbaikyzy, Sophie Reinermann, Daniela Palacios Lopez and Thorsten Hoeser for being an extremely supportive group throughout the entire PhD and during the difficult times a global pandemic comes with. Furthermore, Julian Zeidler is thanked for his continuous and patient IT support and Chaonan Ji and Dr. Emmanuel Da Ponte Canova are thanked for translating the summary of this thesis.

To my whole family, for their endless support, trust and encouragement during the past years. Without the patience and continuous moral and financial support of my parents and brother, I would not have been able to complete this dissertation. This dissertation is dedicated to them as well as to my grandmother whose excitement and joy about my research truly encouraged me during my PhD studies.

To all my friends, for their constant support and motivation as well as the ability to cheer me up even during the most intensive stages of my PhD.



## Summary

With accelerating global climate change, the Antarctic Ice Sheet is exposed to increasing ice dynamic change. During 1992 and 2017, Antarctica contributed ~7.6 mm to global sea-level-rise mainly due to ocean thermal forcing along West Antarctica and atmospheric warming along the Antarctic Peninsula (API). Together, these processes caused the progressive retreat of glaciers and ice shelves and weakened their efficient buttressing force causing widespread ice flow accelerations. Holding ~91% of the global ice mass and 57.3 m of sea-level-equivalent, the Antarctic Ice Sheet is by far the largest potential contributor to future sea-level-rise.

Despite the improved understanding of Antarctic ice dynamics, the future of Antarctica remains difficult to predict with its contribution to global sea-level-rise representing the largest uncertainty in current projections. Given that recent studies point towards atmospheric warming and melt intensification to become a dominant driver for future Antarctic ice mass loss, the monitoring of supraglacial lakes and their impacts on ice dynamics is of utmost importance. In this regard, recent progress in Earth Observation provides an abundance of high-resolution optical and Synthetic Aperture Radar (SAR) satellite data at unprecedented spatial and temporal coverage and greatly supports the monitoring of the Antarctic continent where ground-based mapping efforts are difficult to perform. As an automated mapping technique for supraglacial lake extent delineation in optical and SAR satellite imagery as well as a pan-Antarctic inventory of Antarctic supraglacial lakes at high spatial and temporal resolution is entirely missing, this thesis aims to advance the understanding of Antarctic surface hydrology through exploitation of spaceborne remote sensing.

In particular, a detailed literature review on spaceborne remote sensing of Antarctic supraglacial lakes identified several research gaps including the lack of (1) an automated mapping technique for optical or SAR satellite data that is transferable in space and time, (2) high-resolution supraglacial lake extent mappings at intra-annual and inter-annual temporal resolution and (3) large-scale mapping efforts across the entire Antarctic continent. In addition, past method developments were found to be restricted to purely visual, manual or semi-automated mapping techniques hindering their application to multi-temporal satellite imagery at large-scale. In this context, the development of automated mapping techniques was mainly limited by sensor-specific characteristics including the similar appearance of supraglacial lakes and other ice sheet surface features in optical or SAR data, the varying temporal signature of supraglacial lakes throughout the year as well as effects such as speckle noise and wind roughening in SAR data or cloud coverage in optical data. To overcome these limitations, this thesis exploits methods from artificial intelligence and big data processing for development of

an automated processing chain for supraglacial lake extent delineation in Sentinel-1 SAR and optical Sentinel-2 satellite imagery. The combination of both sensor types enabled to capture both surface and subsurface lakes as well as to acquire data during cloud cover or wind roughening of lakes. For Sentinel-1, a deep convolutional neural network based on residual U-Net was trained on the basis of 21,200 labeled Sentinel-1 SAR image patches covering 13 Antarctic regions. Similarly, optical Sentinel-2 data were collected over 14 Antarctic regions and used for training of a Random Forest classifier. Optical and SAR classification products were combined through decision-level fusion at bi-weekly temporal scale and unprecedented 10 m spatial resolution. Finally, the method was implemented as part of DLR's High-Performance Computing infrastructure allowing for an automated processing of large amounts of data including all required pre- and post-processing steps. The results of an accuracy assessment over independent test scenes highlighted the functionality of the classifiers returning accuracies of 93% and 95% for supraglacial lakes in Sentinel-1 and Sentinel-2 satellite imagery, respectively.

Exploiting the full archive of Sentinel-1 and Sentinel-2, the developed framework for the first time enabled the monitoring of seasonal characteristics of Antarctic supraglacial lakes over six major ice shelves in 2015-2021. In particular, the results for API ice shelves revealed low lake coverage during 2015-2018 and particularly high lake coverage during the 2019-2020 and 2020-2021 melting seasons. On the contrary, East Antarctic ice shelves were characterized by high lake coverage during 2016-2019 and extremely low lake coverage during the 2020-2021 melting season. Over all six investigated ice shelves, the development of drainage systems was revealed highlighting an increased risk for ice shelf instability. Through statistical correlation analysis with climate data at varying time lags as well as annual data on Southern Hemisphere atmospheric modes, environmental drivers for meltwater ponding were revealed. In addition, the influence of the local glaciological setting was investigated through computation of annual recurrence times of lakes. Over both ice sheet regions, the complex interplay between local, regional and large-scale environmental drivers was found to control supraglacial lake formation despite local to regional discrepancies, as revealed through pixel-based correlation analysis. Local control factors included the ice surface topography, the ice shelf geometry, the presence of low-albedo features as well as a reduced firn air content and were found to exert strong control on lake distribution. On the other hand, regional controls on lake evolution were revealed to be the amount of incoming solar radiation, air temperature and wind occurrence. While foehn winds were found to dictate lake evolution over the API, katabatic winds influenced lake ponding in East Antarctica. Furthermore, the regional near-surface climate was shown to be driven by large-scale atmospheric modes and teleconnections with the tropics. Overall, the results highlight that similar driving factors control supraglacial lake formation on the API and EAIS pointing towards their transferability to other Antarctic regions.



## Zusammenfassung

Der antarktische Eisschild erfährt angesichts der globalen Erderwärmung zunehmende eisdynamische Veränderungen. Zwischen 1992 und 2017 trug die Antarktis mit ~7.6 mm zum globalen Meeresspiegelanstieg bei, was vor allem auf die Erwärmung des Ozeans entlang der Westantarktis und die Erwärmung der Atmosphäre entlang der Antarktischen Halbinsel zurückzuführen ist. Zusammen verursachten diese Prozesse den fortschreitenden Rückgang von Gletschern und Schelfeis und schwächten ihren Rückhalteeffekt. Mit einem Anteil von ~91% an der globalen Eismasse und einem Meeresspiegeläquivalent von 57.3 m ist der antarktische Eisschild der größte potentielle Verursacher eines zukünftigen Meeresspiegelanstiegs.

Trotz des verbesserten Verständnisses der antarktischen Eisdynamik kann die Zukunft der Antarktis nur schwer vorhergesagt werden. In Anbetracht der Tatsache, dass die Erwärmung der Atmosphäre und die damit einhergehende Oberflächenschmelze eine der Hauptursachen für künftige Massenverluste der Antarktis sein werden, ist die Kartierung von supraglazialen Seen von größter Bedeutung und Wichtigkeit. In dieser Hinsicht liefert die Erdbeobachtung eine Vielzahl von räumlich und zeitlich hochaufgelösten Satellitendaten für das Monitoring der Antarktis. Da eine automatisierte Methode zur Kartierung von supraglazialen Seen in Satellitendaten sowie ein großräumiges Inventar gänzlich fehlen, ist das Ziel dieser Arbeit zu einem besseren Verständnis der antarktischen Oberflächenhydrologie beizutragen. Zu diesem Zweck wurde ein neuartiges Prozessierungsverfahren für die automatisierte Kartierung von supraglazialen Seen in Sentinel-1 und Sentinel-2 Satellitenbilddaten entwickelt.

Basierend auf einer umfassenden Literaturrecherche in Bezug auf die satellitengestützte Fernerkundung von antarktischen supraglazialen Seen wurden mehrere Forschungslücken identifiziert, darunter das Fehlen von (1) einem automatisierten Klassifikationsalgorithmus für optische und Radar Satellitendaten, der in Raum und Zeit übertragbar ist, (2) hochaufgelösten Kartierungen von supraglazialen Seen mit jährlicher sowie saisonaler zeitlicher Auflösung und (3) großräumigen Kartierungen über der gesamten Antarktis. Darüber hinaus wurde festgestellt, dass sich vergangene Methodenentwicklungen auf eine rein visuelle, manuelle oder halbautomatisierte Kartierungstechnik stützten, was ihre Anwendung auf multitemporale Satellitenbilder über dem gesamten Kontinent verhinderte. Die Entwicklung einer automatisierten Kartierungsmethode wurde hierbei vor allem durch sensorspezifische Merkmale eingeschränkt, darunter das ähnliche Erscheinungsbild von supraglazialen Seen und anderen Landbedeckungsklassen in optischen oder Radar Daten, die variierende zeitliche Signatur von supraglazialen Seen sowie Effekte wie Speckle-Rauschen oder die Windaufrauung von Seen in Radar Daten. Um diese Limitierungen

zu überwinden, basiert der entwickelte Algorithmus zur automatisierten Kartierung von supraglazialen Seen in optischen and Radar Satellitendaten auf Methoden der künstlichen Intelligenz und der Big-Data-Analytik. Die Kombination von beiden Sensortypen ermöglicht es, sowohl supraglaziale als auch mit Schnee bedeckte Seen zu erfassen. Für Sentinel-1 wurde ein neuronales Netzwerk basierend auf „residual U-Net“ mittels 21,200 Radaraufnahmen über 13 antarktischen Regionen trainiert. In ähnlicher Weise wurden optische Sentinel-2 Daten über 14 antarktischen Regionen gesammelt und zum Trainieren eines „Random Forest“ Klassifikators verwendet. Die beiden Methoden wurden durch die Fusion von optischen und Radar Klassifikationsergebnissen kombiniert und als Teil der DLR-internen Prozessierungs-Infrastruktur auf Hochleistungsrechnern implementiert, die eine vollautomatische Verarbeitung großer Datenmengen einschließlich aller erforderlichen Vor- und Nachverarbeitungsschritte ermöglichen. Eine Fehleranalyse über unabhängigen Testszenen zeigte die Funktionalität der Algorithmen, die Genauigkeiten von 93% bzw. 95% für supraglaziale Seen in Sentinel-1 und Sentinel-2 Daten erreichten.

Unter Nutzung des gesamten Archivs an Sentinel-1 und Sentinel-2 Daten im Zeitraum 2015-2021 ermöglichte die entwickelte Prozessierungs-Kette erstmals die Erfassung von saisonalen Merkmalen supraglazialer Seen über sechs großen Schelfeis-Regionen. Die Ergebnisse für die Antarktische Halbinsel zeigten ein geringes Auftreten von supraglazialen Seen im Zeitraum 2015-2018 und ein stark erhöhtes Auftreten von supraglazialen Seen während der Schmelzsaison 2019-2020 und 2020-2021. Im Gegensatz dazu war die Ostantarktis durch ein stark erhöhtes Auftreten von supraglazialen Seen in den Jahren 2016-2019 sowie ein stark reduziertes Auftreten von supraglazialen Seen während der Schmelzsaison 2020-2021 gekennzeichnet. Über beiden Regionen entwickelten sich ausgeprägte Seen-Netzwerke, die ein erhöhtes Risiko für die Stabilität von Schelfeis darstellen. Durch statistische Korrelationsanalysen mit saisonalen Klimadaten sowie jährlichen Daten zu atmosphärischen Modi wurden Umwelteinflüsse auf die Entstehung von Seen analysiert. In beiden antarktischen Regionen wurde festgestellt, dass das komplexe Zusammenspiel von lokalen, regionalen und großräumigen Umweltfaktoren die Entstehung von supraglazialen Seen begünstigt. Zu den lokalen Einflussfaktoren gehören die Topographie, die Schelfeisgeometrie, das Vorhandensein von Oberflächen mit geringer Albedo sowie ein reduzierter Luftgehalt im Firn. Andererseits wurde festgestellt, dass die Sonneneinstrahlung, die Lufttemperatur und Wind die Entstehung von Seen regional beeinflussen. Während Föhnwinde über der Antarktischen Halbinsel auftreten, dominieren katabatische Winde in der Ostantarktis. Darüber hinaus wurde verdeutlicht, dass das regionale Klima von atmosphärischen Modi beeinflusst wird. Insgesamt deuten die Ergebnisse darauf hin, dass ähnliche Umweltfaktoren die Entstehung von supraglazialen Seen über beiden Regionen steuern, was Rückschlüsse auf ihre Übertragbarkeit in andere antarktische Regionen zulässt.

## Resumen en Español

Con el acelerado paso del cambio climático global, la capa de hielo de la Antártida está expuesta a un creciente cambio en la dinámica del hielo. Entre 1992 y 2017, la Antártida contribuyó con ~7.6 mm en el incremento global del nivel del mar, principalmente debido al recalentamiento del océano a lo largo de la Antártida Occidental y al calentamiento atmosférico largo de la Península Antártica. Estos procesos provocaron el retroceso progresivo de los glaciares y las plataformas de hielo. La Antártida almacena 91% del volumen de hielo mundial, equivalente a 58.3 m del nivel del mar, y es el factor más importante de un potencial aumento del nivel del mar.

A pesar de la mejor comprensión de la Antártida, su futuro sigue difícil de pronosticar. Teniendo en cuenta que estudios recientes apuntan al recalentamiento de la atmósfera y al incremento del deshielo como en una de las principales causas de la futura pérdida de masa de hielo antártica, el monitoreo de los lagos supraglaciales es de suma importancia. En este contexto, los avances recientes en la observación de la tierra proporcionan cuantiosos datos satelitales de alta resolución que apoyan en gran medida al monitoreo del continente antártico. Dado a la falta de una metodología automatizada para la clasificación de los lagos supraglaciales aplicada a imágenes satélites ópticas y de radar además de un inventario antártico de los lagos, esta tesis doctoral proporciona un avance en la comprensión de la hidrología de la superficie antártica mediante la teledetección espacial.

Tran un análisis exhaustivo de la teledetección espacial aplicada al monitoreo de los lagos supraglaciales antárticos, se identificaron varios vacíos de investigación, como la falta de (1) una técnica de clasificación automatizada para datos de satelitales ópticos y de radar; (2) cartografías de alta resolución temporal de los lagos supraglaciales; (3) mapeo a gran escala del antártico. Además, se encontraron que los métodos desarrollados anteriormente se limitaban a técnicas de cartografía puramente visuales, manuales o semiautomatizadas, lo que dificultaba su aplicación en imágenes satelitales multitemporales a gran escala. Asimismo, el desarrollo de técnicas de mapeo automatizado se vio limitado por las características específicas de los sensores, como la similitud en apariencia de los lagos supraglaciales y otras características de la superficie de la capa de hielo en los datos satelitales ópticos y de radar, la firma temporal variable de los lagos supraglaciales, como así también efectos de ruido como el moteado y la rugosidad de las superficies de los lagos provocada por el viento en los datos de radar.

Para superar estas limitaciones, esta tesis utilizó métodos de inteligencia artificial y de procesamiento de grandes bases de datos para el desarrollo de una cadena de procesamiento automatizada para la delineación de los lagos supraglaciales en las

imágenes satelitales de radar (Sentinel-1) y ópticas (Sentinel-2). Para Sentinel-1, se entrenó una red neuronal convolucional profunda basada en el “residual U-Net” sobre la base de 21,200 parches de imágenes de Sentinel-1 distribuidas a lo largo de 13 regiones antárticas. Igualmente, datos ópticos de Sentinel-2 se recogieron en 14 regiones antárticas y se utilizaron para el entrenamiento de un clasificador “Random Forest”. Los dos métodos se combinaron a través de la fusión de los productos clasificación y seguidamente se implementaron como parte de la infraestructura interna de computación de alto rendimiento de la DLR, lo cual permitió un procesamiento automatizado de grandes cantidades de datos satelitales. Los resultados referentes al análisis de exactitud en los datos de prueba independientes confirmaron la funcionalidad de los clasificadores, con una precisión del variando entre 93% y 95% para las imágenes de los satélites Sentinel-1 y Sentinel-2, respectivamente.

A través del procesamiento de los archivos completos de Sentinel-1 y Sentinel-2, el método desarrollado permitió por primera vez la computación de las características estacionales de los lagos supraglaciales antárticos en seis grandes plataformas de hielo para el periodo comprendido entre 2015-2021. En particular, los resultados para las plataformas de hielo de la Península Antártica revelaron una cobertura baja con lagos supraglaciales entre 2015-2018 y una cobertura particularmente alta durante los años 2019-2020 y 2020-2021. Por el contrario, las plataformas de hielo de la Antártida Oriental se caracterizaron por una alta cobertura con lagos supraglaciales durante 2016-2019 y una cobertura extremadamente baja durante 2020-2021. A través de un análisis de correlación estadística con datos climáticos de resolución temporal estacional y anual sobre los modos atmosféricos, se revelaron los factores ambientales que influyen en la aparición de los lagos supraglaciales. Además, se investigó la influencia del entorno glaciológico local mediante el cálculo de los tiempos de recurrencia anual de los lagos supraglaciales. En ambas regiones, se descubrió que la compleja interacción entre los factores ambientales locales, regionales y a gran escala controlan la formación y distribución de los lagos supraglaciales. Los factores de control locales incluyeron la topografía y la geometría de las plataformas de hielo, la presencia de superficies de bajo albedo, como así también un contenido reducido de aire de nieve. Por otra parte, los controles regionales resultaron ser la cantidad de radiación solar, la temperatura del aire y la presencia de vientos. Mientras que los “foehn” vientos dictaron la evolución de los lagos supraglaciales en la Península Antártica, los vientos catabáticos influyeron en la formación de lagos supraglaciales en la Antártida Oriental. Además, se demostró que el clima regional está influenciado por los modos atmosféricos a gran escala. En general, los resultados ponen en manifiesto que factores similares controlan la formación de lagos supraglaciales en la Península Antártica y la Antártida Oriental, lo que apunta a su transferibilidad a otras regiones antárticas.

## Chinese Summary (中文摘要)

随着全球气候变化的加速，南极冰盖面临着日益增加的环境压力。南极冰盖拥有约91%的全球冰量和57.3米的海平面当量，是迄今为止对未来海平面上升的最大潜在贡献者。从1992年到2017年，南极洲经历了巨大的变化，为全球海平面上升贡献了约7.6毫米，其中主要是由于南极洲西部的海洋热力作用和南极半岛（API）的大气变暖。这些过程共同导致了冰川和冰架的逐步退缩，削弱了其有效支撑力，造成了大面积的冰流加速和排冰量增加。

尽管对南极洲冰层动态的理解有所提高，但南极洲的未来仍然难以预测，其中对全球海平面上升的贡献具有最大的不确定性。最近的研究表明，大气变暖和融化加剧将成为未来南极洲冰块损失的主要驱动力，因此监测冰上湖泊及其对冰层动态的影响非常重要。在该方面，地球观测的最新进展提供了大量高分辨率的光学和合成孔径雷达（SAR）卫星数据，其空间和时间覆盖范围前所未有的，极大地支持了对南极大陆上难以进行实地测绘工作区域的监测。由于光学和SAR卫星图像中划定超冰川湖范围的自动制图技术、以及南极超冰川湖的泛南极清单的缺失，本论文基于Sentinel-1 卫星的SAR数据和Sentinel-2卫星的光学数据开发了一个全新的超冰川湖自动分类框架，以推进对南极表面水文的理解。

本论文在对南极洲超冰川湖的航空遥感进行详细调查后，发现了一些研究空白，包括（1）缺乏在空间和时间上具有转移性的光学或SAR卫星数据的自动制图技术；（2）缺乏年内和年际时间分辨率的高分辨率超冰川湖范围图；（3）缺乏整个南极洲的大规模制图工作。此外，过去的研究方法局限于纯粹的视觉、手动或半自动的制图技术，阻碍了其在大规模多时空卫星图像上的应用。在该背景下，自动制图技术的发展受到了传感器特定特性的限制，包括超冰川湖和其他冰原表面特征在光学和SAR卫星数据中的相似外观，超冰川湖在一年中不同的时间特征，以及SAR数据中的斑点噪声和风的粗糙化或光学数据中频繁的云层覆盖等影响。为了克服这些限制，本论文利用人工智能和大数据处理的方法，开发了一个自动处理链，用于在Sentinel-1 的SAR数据和Sentinel-2的光学影像中划定超冰川湖范围。两种类型的传感器的结合使其能够捕捉到地表和地下湖泊，以及在云层或湖面被



风吹皱时获取数据。对于Sentinel-1数据，本文在覆盖13个南极地区的21,200个标记的Sentinel-1 的SAR图像斑块的基础上，训练了一个基于残差U-Net的深度卷积神经网络。并且，本文在14个南极地区收集了Sentinel-2的光学数据，并训练了一个随机森林分类器。这两种方法通过光学和合成孔径雷达分类产品的决策级融合方法相结合，并成为了德国航空航天中心内部高性能计算基础设施的一部分，允许自动处理大量的卫星数据，包括所有必要的预处理和后处理步骤。对独立检测场景的精度评估结果显示，该分类器在Sentinel-1和Sentinel-2卫星图像中对超冰川湖的检测准确率分别达到93%和95%。

通过使用 "哨兵一号 "和 "哨兵二号 "的全部历史数据，本论文开发的框架首次实现了对2015至2021年期间六个主要冰架上的南极冰川上湖的季节性特征的监测。API冰架的结果显示，2015至2018年期间湖泊覆盖率低，2019至2020年和2020至2021年融化季节的湖泊覆盖率特别高。相反，南极洲东部冰架在2016至2019年期间湖泊覆盖率高，而在2020至2021年融化季节湖泊覆盖率极低。在六个被调查的冰架上都观察到了水系的发展，这凸显了冰架不稳定的风险增加。对不同时间滞后的气候再分析数据以及南半球大气模式的年度数据进行的统计学相关性分析，揭示了超冰川融水积水的环境驱动因素。

此外，通过对湖泊的年重现时间的计算，研究了当地冰川环境的影响。在这两个冰原区域，尽管有局部和区域的差异，但通过基于像素的相关性分析，发现了局部、区域和大尺度环境驱动因素之间复杂的相互作用控制着超冰川湖的形成和分布。各种本地控制因素对超冰川湖的分布产生了强烈的影响，因素包括冰面地形、冰架几何形状、低含水层特征的存在以及冷空气含量的减少。对超冰川湖演变的区域控制原因是太阳辐射量、空气温度和风的出现。结果显示，foehn风决定了API上的湖泊演变，katabatic风影响了东南极洲的湖泊积水。此外，区域近地表气候由大尺度大气模式和与热带地区的远程联系驱动。总的来说，研究结果指出了API和EAIS的超冰川湖形成的相似驱动因素以及该因素对其他南极地区的适用性。

# List of Figures

Figure 1.1. Cumulative mass changes and sea-level-equivalent over the Greenland (a) and Antarctic (b) ice sheets in 1992-2018 and 1992-2017, respectively .....	2
Figure 1.2. Overview map of Antarctica showing the three main sectors Antarctic Peninsula (API), West Antarctic Ice Sheet (WAIS) and East Antarctic Ice Sheet (EAIS) as well as major glaciers and ice shelves (blue). The background is a gridded bathymetry raster from the General Bathymetric Chart of the Oceans (GEBCO) .....	3
Figure 1.3. Sketch of features and processes (A-P) at an ocean-terminating outlet glacier in Antarctica with focus on hydrology .....	5
Figure 1.4. Antarctic surface meltwater volume from simulations of RACMO2 reanalysis data and QuikSCAT satellite observations under two climate projections. Right: Mean Antarctic surface meltwater volume ( $\pm\sigma$ ) per decade .....	5
Figure 2.1. Idealized sketch of gravitational ice sheet flow from regions of snow accumulation to regions of ablation including the different glacier zones. The setting on the left shows typical ablation conditions at outlet glaciers with ice shelf in Antarctica. The setting on the right represents ablation conditions at outlet glaciers in Greenland.....	14
Figure 2.2. Spatio-temporal ice flow pattern over Antarctica. (a) Landsat 8 Ice Speed of Antarctica (LISA) during 2013-2017. (b) LISA inset for the Amundsen Sea sector. Central grounding line velocity trend over Pine Island (c) and Thwaites (d) glaciers, West Antarctica .....	16
Figure 2.3. Surface (a) and bedrock (b) elevation of the Antarctic continent. (c) Elevation profile over West Antarctica. (d-e) Elevation profiles over East Antarctica. The ice thickness of Ross Ice Shelf in (c) as well as the water level in Lake Vostok in (d) were sketched .....	17
Figure 2.4. Antarctic ice dynamic change. (a) Basal melting (2003-2008) and iceberg calving (2007-2008) of Antarctic ice shelves. (b) Antarctic surface elevation change from satellite altimetry in 1992-2017 .....	20
Figure 2.5. Antarctic ocean fronts and wind systems. The background image is a gridded bathymetry raster from GEBCO. ....	22
Figure 2.6. Antarctic climatic conditions calculated from ERA5-Land reanalysis (a-d) and station data (e-f). (a) Maximum Antarctic wind speed in 2019. (b) Average annual precipitation in 1981-2020. (c) Mean Antarctic air temperature in 1981-2020. (d) Mean Antarctic air temperature change between 2000-2010 and 2010-2020. Monthly mean temperature (red) and precipitation (blue) at O'Higgins (e) and Vostok (f) stations in 1961-1990.....	25
Figure 2.7. Average Antarctic Sea Surface Temperature (SST) for austral summers 1979-2019 and median sea ice extent for March and September 1981-2010 .....	28
Figure 3.1. Appearance of Antarctic supraglacial lakes in Sentinel-2 image extracts of (a) 19 January 2020 on George VI Ice Shelf, (b) 2 February 2017 on Riiser-Larsen Ice Shelf, (c) 21 January 2019 on Nivlisen Ice Shelf, (d) 2 January 2019 on Amery Ice Shelf, (e) 29 January 2019 on Shackleton Ice Shelf and (f) 27 December 2019 on Pine Island Ice Shelf .....	30
Figure 3.2. Supraglacial lake formation near rock outcrop and blue ice on (a) 19 January 2020 upstream of George VI Ice Shelf, (b) 23 January 2021 near Wilkins Ice Shelf, (c) 2 January 2019 upstream of Amery Ice Shelf and (d) 21 January 2019 around Nivlisen Ice Shelf. The black arrows in (b) indicate the direction of ice flow .....	32
Figure 3.3. Geospatial distribution of Antarctic supraglacial lake observations. The point layer (blue) shows supraglacial lakes across East Antarctica during January 2017 (Stokes et al., 2019). Additional sightings of supraglacial lakes are marked in red .....	35

Figure 3.4. Supraglacial lake impacts on ice sheet dynamics. (a) Direct surface runoff leading to ice thinning. (b) Meltwater-induced fracturing leading to ice shelf collapse. (c) Basal injection of meltwater causing glacier acceleration and frontal melting. (d) Modified ice surface albedo initiating melt-albedo feedbacks and accelerated melting and thinning .....	36
Figure 3.5. Temporal trends of central calving front velocity over tributaries of former ice shelves including (a) Sjögren, (b) Crane, (c) Drygalski and (d) Hektor Glacier .....	39
Figure 4.1. Potentials of EO for the monitoring of Antarctic ice sheet dynamics .....	42
Figure 4.2. Temporal evolution of studies on spaceborne remote sensing of Antarctic supraglacial lakes between January 1980 and June 2021 with respect to the (a) used sensor types, (b) spatial coverage and (c) temporal resolution. The launch years of important satellite missions are marked in grey (a) .....	44
Figure 4.3. Distribution of used sensor types and frequency of use of data from specific satellite missions for the mapping of Antarctic supraglacial lakes in 1980-2021 .....	45
Figure 4.4. Spatial extent and focus regions of spaceborne investigations on Antarctic supraglacial lakes.....	48
Figure 4.5. (a) Geospatial distribution of spaceborne studies on Antarctic supraglacial lakes over individual drainage basins and ice shelves (circles). Purple points are lakes identified by Stokes et al. (2019). (b) Magnification over the northern Antarctic Peninsula.....	49
Figure 4.6. (a) Reflectance properties of basaltic rock and different snow and ice types. (b) Spectral albedo of different snow and ice types, open ocean and meltwater ponds.....	52
Figure 4.7. Appearance of Antarctic supraglacial lakes and ice sheet surface features with similar spectral reflectance in Sentinel-2 imagery. Lakes adjacent to (a) rock outcrop and cloud shadow, (b) topographic shadow on ice, (f) slush as well as within a (c) crevasse and (d) blue ice field or (e) atop and around submerged icebergs .....	53
Figure 4.8. Radar backscattering characteristics of different radar glacier zones and sea ice in Antarctica. Overview maps (a,d) showing the locations of the mean SAR intensity images over the East Antarctic Ice Sheet (EAIS) (b-c) and the Antarctic Peninsula (API) (e-f) during austral summer (b,e) and winter (c,f). The grounding line is illustrated in grey .....	54
Figure 4.9. Exemplary backscattering signature of different snow and ice types as well as of liquid water throughout the course of a year, as extracted from single-polarized Sentinel-1 imagery over a selected test site on the Antarctic Peninsula .....	55
Figure 4.10. Appearance of Antarctic supraglacial lakes and resembling ice sheet surface features in Sentinel-1 imagery. Lakes and lake refreezing on George VI (a) and Amery ice shelves (b-c). (d) Lakes with low visual contrast on Amery Ice Shelf. (e-f) Lakes and wet snow on George VI Ice Shelf. (g) Shallow lakes adjacent to slush on George VI Ice Shelf. Shadowing in ice shelf fractures on Shackleton Ice Shelf (h) as well as near rock outcrop (i) and at a fractured ice tongue (j) close to Larsen C Ice Shelf. Bare ice and dry snow near rock on Rennick Ice Shelf (k) and bare ice near Nivlisen Ice Shelf (l).....	57
Figure 4.11. Appearance of supraglacial lakes in SAR (a,c) and optical (b,d) satellite imagery of 19 January 2020 over George VI Ice Shelf. (a-b) and (c-d) show the same locations.....	58
Figure 4.12. (a) Geospatial distribution of spaceborne studies on Antarctic ice motion over individual drainage basins. (b) Magnification over the northern Antarctic Peninsula. The heat maps are assembled from 201 scientific papers published in 1984-2018.....	60
Figure 5.1. Spatial distribution of training and testing regions for Sentinel-1 (a) and Sentinel-2 (b). Stars highlight regions where training and testing data of different dates were overlapping. The dashed red line in (b) shows the test site over Amery Ice Shelf (Figure 5.2) .....	66

Figure 5.2. Geospatial coverage of Sentinel-2 data over Amery Ice Shelf during melting seasons 2016-2017 to 2019-2020. The grey area shows the overlap area of all years and the red area shows the region of interest (ROI) that was analyzed in Figure 5.21 .....	67
Figure 5.3. Temporal availability of Sentinel-1 (a) and Sentinel-2 (b) training and test data during melting seasons 2016-2017 to 2019-2020. The green stars in (a) highlight acquisitions that were used for training and testing despite training data being aggregated monthly data products. The green stars in (b) highlight additional test data over Amery .....	67
Figure 5.4. Sentinel-1 observation scenario over the Antarctic coastline. (a) Revisit and coverage frequency. (b) Acquisition modes and polarization scheme .....	69
Figure 5.5. Sentinel-1A/B (a) and Sentinel-2A/B (b) acquisition segments during exemplary 14-day intervals.....	69
Figure 5.6. Workflow for Antarctic supraglacial lake extent classification in Sentinel-1 SAR imagery using deep learning .....	75
Figure 5.7. Deep learning architecture based on residual U-Net used for semantic segmentation of Sentinel-1 SAR imagery .....	78
Figure 5.8. Sketch of a single downsampling unit with a residual connection and dropout. To simplify, no activation function (act.) is applied .....	79
Figure 5.9. Exemplary functions available for activation of convoluted layers .....	79
Figure 5.10. Performance metrics of the training process. (a) Loss obtained from the training (blue) and validation (red) subset with the best model performance marked at epoch 30 (black cross). (b) Accuracy obtained from the training (blue) and validation (red) subset. ....	80
Figure 5.11. Prediction results for an exemplary 480 x 480-pixel patch. (a) Original Sentinel-1 input patch. (b) Manually drawn label. (c) Prediction outcome for the input patch in (a). The x- and y-axes show the number of pixels in both directions.....	81
Figure 5.12. Workflow for Antarctic supraglacial lake extent classification in optical Sentinel-2 imagery using machine learning.....	83
Figure 5.13. Discrimination analysis for classes “rock”, “shadow”, “snow/ice” and “water”. Sentinel-2 bands 2, 3, 4 and 8 (a-d), normalized indices (e-n) and scaled topographic variables (o-r). The boxplots show the interquartile ranges, the median, the full data range and outliers .....	84
Figure 5.14. Sketch of Random Forest with multiple decision trees and majority voting. ....	86
Figure 5.15. Sketch of 3-fold cross-validation for robust Random Forest model training. ....	86
Figure 5.16. Variable importance plots obtained from training the Random Forest model (a) with all features, (b) without topographic variables, (c) with 10 m bands and indices only and (d) with variables representing the upper median of all importance values only. Importance values represent the mean of all classes and training regions .....	88
Figure 5.17. Classification results for the Sentinel-1 test data. From left to right, each sub-plot in (a-j) shows an overview map of the location of the Sentinel-1 test scene (blue shading), an extract of the Sentinel-1 test scene at the location of the red circle in (a-j) as well as the automated classification result for the image extract. (a) Abbot, (b) Bach, (c) George VI, (d) Larsen C, (e) Riiser-Larsen, (g) Amery, (h) Shackleton and (i) Moscow University ice shelves. (f) Enderby Land. (j) Rennick Glacier. The red line in (c,f) shows the 2018 Sentinel-1 coastline.....	91
Figure 5.18. (a) Overview map of the study region covering northern George VI Ice Shelf (blue shading). (b) Intra-annual supraglacial lake evolution during summer 2019-2020. December 2019 and February 2020 represent maximum lake extent mapping products and January 2020 represents four individual Sentinel-1 acquisitions .....	94

Figure 5.19. Automated classification result (c) for an image extract (b) of a Sentinel-1 acquisition of 28 July 2018 over the south-west Greenland Ice Sheet (a).....	94
Figure 5.20. Automated classification results for the Sentinel-2 test data. From left to right, the sub-plots in (a-n) show the Sentinel-2 test scene, an extract at the location of the red outline in (a-n) as well as the automated classification result for the image extract. (a) Hull Glacier. (b) Abbot, (c) Cosgrove, (e-f) George VI, (g) Larsen C, (h) Nivlisen, (i) Roi Baudouin and (l) Moscow University ice shelves. (d) Pine Island Bay. (j) Enderby Land. (k) Wilhelm II and (m) Adelie Coast. (n) Drygalski Ice Tongue .....	96
Figure 5.21. Maximum lake extent in January 2019 over Amery Ice Shelf (a). Mappings over region of interest (ROI) 1 for January 2017 (b), 2018 (c), 2019 (d) and 2020 (e).....	99
Figure 5.22. Inter-annual evolution of maximum supraglacial lake extents during January 2017-2020 over Amery Ice Shelf. See Figure 5.2 for the outlines of the spatial units .....	99
Figure 5.23. Classification result (c) for an image extract (b) of the additional Sentinel-2 test scene of 10 August 2019 over Greenland (a) .....	100
Figure 5.24. Decision-level fusion of automatically generated Sentinel-1 and Sentinel-2 maximum lake extent classification products covering the first half of January 2020 over George VI Ice Shelf (a). (b) Inset over the region outlined in (a) (red). (c) Sentinel-1 SAR backscattering minimum product for January 2020. (d) Sentinel-2 imagery of 9 January 2020. The fused classification product is shown as an overlay with Sentinel-2 data of 19 January 2020 .....	101
Figure 5.25. Decision-level fusion of automatically generated Sentinel-1 and Sentinel-2 maximum lake extent classification products covering the second half of January 2020 over George VI Ice Shelf (a). (b) Inset over the region outlined in (a) (red). (c) Sentinel-1 SAR backscattering minimum product for January 2020. (d) Sentinel-2 imagery of 19 January 2020. The fused classification product is shown as an overlay with Sentinel-2 data of 19 January 2020 .....	102
Figure 5.26. Decision-level fusion of automatically generated Sentinel-1 and Sentinel-2 maximum lake extent classification products covering the first half of January 2019 over Amery Ice Shelf (a). (b) Inset over the region outlined in (a) (red). (c) Sentinel-1 SAR imagery of 12 January 2019. (d) Sentinel-2 imagery of 2 January 2019. The fused classification product is shown as an overlay with the Landsat Image Mosaic of Antarctica (LIMA). The data basis for the additional Sentinel-1 scenes over Amery Ice Shelf is outlined in Chapter 6.2 .....	103
Figure 5.27. Kappa coefficient for the Sentinel-1 (a) and Sentinel-2 (b) test data. ....	106
Figure 5.28. Sketch of the automated processing pipeline for classification of Sentinel-1 and Sentinel-2 imagery on DLR's High-Performance Computing infrastructure .....	108
Figure 6.1. Overview map of Antarctica showing the locations of the six investigated ice shelves George VI (a), Bach (b), Wilkins (c), Riiser-Larsen (d), Nivlisen (e) and Amery (f). The area of interest for satellite data acquisition and lake extent mapping corresponds to the red outlines and the area of interest used for statistical analyses corresponds to the shaded blue area in (a-f). Over Amery, a permanent lake feature at the western grounding line (Beaver Lake) was excluded from analyses to avoid misclassifications in optical imagery .....	119
Figure 6.2. Sentinel-2 imagery showing supraglacial lakes on (a) George VI (19 January 2020), (b) Bach (29 January 2020), (c) Wilkins (23 January 2021), (d) Riiser-Larsen (2 February 2017), (e) Nivlisen (21 January 2019) and (f) Amery (2 January 2019) ice shelves .....	120
Figure 6.3. Data source of bi-weekly lake extent classifications over George VI (a), Bach (b) and Wilkins (c) ice shelves from Sentinel-1, Sentinel-2 or both.....	121
Figure 6.4. Data source of bi-weekly lake extents over Riiser-Larsen (a), Nivlisen (b) and Amery (c) ice shelves from Sentinel-1, Sentinel-2 or both .....	122



Figure 6.5. Supraglacial lake extent dynamics in 2015-2021 over George VI (a), Bach (b), Wilkins (c), Riiser-Larsen (d), Nivlisen (e) and Amery (f) ice shelves. The periods represent bi-weekly temporal intervals where “A” is the first half of a month and “B” the second half..... 126

Figure 6.6. Anomalies of bi-weekly supraglacial lake extent time series during November to March of a melting season in the reference period 2015-2021 (a-c) and 2016-2021 (d-f) over George VI (a), Bach (b), Wilkins (c), Riiser-Larsen (d), Nivlisen (e) and Amery (f) ice shelves. For Riiser-Larsen and Nivlisen, data gaps are visible due to the interpolation with the bi-weekly long-term mean 2016-2021. Melting seasons are separated with dashed lines..... 127

Figure 6.7. Inter-annual January recurrence of supraglacial lakes over George VI (a), Bach (b), Wilkins (c), Riiser-Larsen (d), Nivlisen (e) and Amery (f) ice shelves. The overview map in the middle shows the approximate location of the AOIs. In some regions, the movement of lakes with ice flow might have biased the calculation of annual lake recurrence times ..... 128

Figure 6.8. Results of the statistical correlation analysis for variables average air temperature (temp), maximum air temperature (temp max), solar radiation (solar rad), precipitation (precip), wind magnitude (wind) and direction (wind dir) as well as snowmelt (melt). Correlations are shown for spatial averages (a) and anomalies of spatial averages (b) of bi-weekly fractional lake extent and climate time series at lags 0-4. The correlation coefficient  $r$  is illustrated for significant correlations with  $p < 0.05$  only ..... 130

Figure 6.9. Spatially averaged fractional lake extents shown with lag 1 wind direction (a) and lag 1 solar radiation (c) as well as anomalies thereof (b,d) for melting seasons 2019-2020 and 2020-2021 over Wilkins Ice Shelf. Wind from north, east, south and west corresponds to  $0^\circ$ ,  $90^\circ$ ,  $180^\circ$  and  $270^\circ$  in degrees (deg) ..... 130

Figure 6.10. Pixel-based Pearson correlation (a,c,e,g,i,k,m,o,q,s,u,w) and corresponding temporal lags (b,d,f,h,j,l,n,p,r,t,v,x) between fractional lake extents and climate variables air temperature (temp), solar radiation (rad), wind direction (dir) and snowmelt (melt) over George VI (a-h), Bach (i-p), and Wilkins (q-x) ice shelves for pixels with  $p < 0.05$ . ..... 131

Figure 6.11. Supraglacial lake evolution during January 2017 (a), 2018 (b), 2019 (c), 2020 (d) and 2021 (e) over Nivlisen Ice Shelf..... 133

Figure 6.12. Spatially averaged fractional lake extents shown with wind direction (a,c,e) and anomalies (b,d,f) during 2016-2021 at lag 0 over Riiser Larsen Ice Shelf (a,b) at lag 1 over Nivlisen Ice Shelf (c,d) and at lag 1 over Amery Ice Shelf (e-f). Wind from north, east, south and west corresponds to  $0^\circ$ ,  $90^\circ$ ,  $180^\circ$  and  $270^\circ$  in degrees (deg) ..... 134

Figure 6.13. Spatially averaged fractional lake extents shown with wind magnitude (a,c,e) and anomalies (b,d,f) during 2016-2021 at lag 0 over Riiser Larsen Ice Shelf (a,b) at lag 1 over Nivlisen Ice Shelf (c,d) and at lag 1 over Amery Ice Shelf (e-f)..... 135

Figure 6.14. Pixel-based Pearson correlation (a,c,e,g,i,k,m,o,q,s,u,w) and corresponding temporal lags (b,d,f,h,j,l,n,p,r,t,v,x) between fractional lake extents and climate variables air temperature (temp), solar radiation (rad), wind magnitude (mag), wind direction (dir), precipitation (prec) and snowmelt (melt) over Riiser-Larsen (a-l), Nivlisen (m-p), and Amery (q-x) ice shelves for pixels with  $p < 0.05$  ..... 136

Figure 6.15. Pixel-based correlation between January fractional lake extents and previous-year precipitation over George VI (a), Bach (b), Wilkins (c), Riiser-Larsen (d), Nivlisen (e) and Amery (f) ice shelves. Due to the low number of observations, also correlations with  $p > 0.05$  are shown ..... 137

Figure 6.16. Annual observations of Southern Annular Mode (SAM) and Dipole Mode Index (DMI) between 1981 and 2020. The study period is highlighted in blue ..... 140



## List of Tables

Table 4.1. Main characteristics of recently launched optical and SAR satellite sensors for supraglacial lake extent mapping in Antarctica. Specific focus is on the Sentinel and Landsat satellite missions.....	51
Table 5.1. Training and testing regions used for method developments with Sentinel-1. Each training region corresponds to an aggregated monthly backscattering minimum raster and each testing region corresponds to one Sentinel-1 IW acquisition except for region 3, where multiple data products were evaluated .....	70
Table 5.2. Sentinel-2 MSI spectral bands .....	71
Table 5.3. Training and testing regions used for method developments with Sentinel-2.....	72
Table 5.4. Selected spectral indices for supraglacial lake classification with a RF classifier. See Table 5.2 for more detailed information on the spectral bands used for index calculation ....	85
Table 5.5. Hyperparameter tuning for supraglacial lake extent classification in Sentinel-2 imagery with the RF classifier.....	87
Table 5.6. Results of the accuracy assessment for the Sentinel-1 test data. From left to right, the columns for each class represent the Precision, Recall, F-score, error of commission and error of omission .....	106
Table 5.7. Results of the accuracy assessment for the Sentinel-2 test data. From left to right, the columns for each class represent the Precision, Recall, F-score, error of commission and error of omission .....	107
Table 6.1. Sentinel-1 and Sentinel-2 data availability over the six investigated ice shelves .....	122
Table 6.2. Results of the statistical correlation analysis between January fractional lake extent and annual SAM as well as previous-year precipitation. Due to the low number of observations used for correlation, the p-value might not be representative and rather the Pearson correlation coefficient (r) should be considered for interpretation.....	136
Table 6.3. Summary of environmental controls on 2015-2021 meltwater ponding on six investigated Antarctic ice shelves. The table summarizes pixel-based and spatially averaged correlations, also considering weak correlations and neglecting spurious results. Positive and negative signs indicate positive and negative relationships, respectively. The signs '+/-' and '/' denote the coexistence of positive and negative links as well as no observed links, respectively. The strength or lag of correlations is not shown .....	144



## List of Abbreviations

ACC	Antarctic Circumpolar Current
AI	Artificial Intelligence
AIS	Antarctic Ice Sheet
ALOS	Advanced Land Observing Satellite
ANN	Artificial Neural Network
AOI	Area of Interest
API	Antarctic Peninsula
ASAR	Advanced Synthetic Aperture Radar
ASL	Amundsen Sea Low
ASPP	Atrous Spatial Pyramid Pooling
CDW	Circumpolar Deep Water
CNN	Convolutional Neural Network
DCNN	Deep Convolutional Neural Network
DEM	Digital Elevation Model
DL	Deep Learning
DMI	Dipole Mode Index
EA	Expected Accuracy
EAIS	East Antarctic Ice Sheet
ELU	Exponential Linear Unit
ENSO	El Niño-Southern Oscillation
ENVISAT	Environmental Satellite
EO	Earth Observation
ERC	Error of Commission
ERO	Error of Omission
ERS	European Remote Sensing Satellites
ESA	European Space Agency
EW	Extra Wide
$F_1$	F-score
FAC	Firn Air Content
FCN	Fully Convolutional Network
FN	False Negatives
FP	False Positives
GARS	German Antarctic Receiving Station
GEBCO	General Bathymetric Chart of the Oceans
GHG	Greenhouse Gas
GL	Grounding Line
GPS	Global Positioning System
GPT	Graph Processing Tool
GPU	Graphics Processing Unit
GRD	Ground Range Detected
GRDH	Ground Range Detected High Resolution
Gt	Gigatons

HPC	High-Performance Computing
IDA	Internal Data Access
IOD	Indian Ocean Dipole
IW	Interferometric Wide
K	Cohen's Kappa
LeakyReLU	Leaky non-linear Rectified Linear Unit
LISA	Landsat 8 Ice Speed of Antarctica
ML	Machine Learning
MODIS	Moderate-resolution Imaging Spectroradiometer
MSI	Multispectral Instrument
NDSI	Normalized Difference Snow Index
NDWI	Normalized Difference Water Index
OA	Overall Accuracy
OLI	Operational Land Imager
P	Precision
PF	Polar Front
R	Recall
RACMO	Regional Atmospheric Climate Model
RCM	RADARSAT Constellation Mission
ReLU	Rectified Linear Unit
REMA	Reference Model of Antarctica
RF	Random Forest
RGB	Red-Green-Blue
SAF	Subantarctic Front
SAM	Southern Annular Mode
SAR	Synthetic Aperture Radar
SCAR	Scientific Committee on Antarctic Research
SCL	Scene Classification Layer
SH	Southern Hemisphere
SLE	Sea-Level-Equivalent
SLR	Sea-Level-Rise
SMB	Surface Mass Balance
SNAP	Sentinel Application Platform
SO	Southern Ocean
SST	Sea Surface Temperature
SSW	Sudden Stratospheric Warming
SWW	Southern Westerly Winds
TN	True Negatives
TP	True Positives
TS	Total Samples
WAIS	West Antarctic Ice Sheet
XML	Extensible Markup Language

# CHAPTER 1

## 1 Introduction

### 1.1 Scientific Relevance

With accelerating global climate change, cryospheric research received an ever-increasing attention emphasizing its fundamental role within the Earth system. In particular, the components of the cryosphere, including snow, glaciers, ice sheets, permafrost as well as lake, river and sea ice, exert strong control on the global water cycle, sea level, surface energy budget, primary productivity and surface gas exchange, thus large parts of the physical, biological and socio-economic environment (Vaughan et al., 2013). As the cryosphere is particularly sensitive to even small-scale meteorological changes, it is one of the Earth system components most vulnerable to a changing climate. In fact, changing boundary conditions such as rising air temperatures may provoke a far-reaching cryospheric response including a further forcing and amplification of climate change through feedback mechanisms, thresholds of abrupt change as well as irreversible long-term changes (IPCC, 2019a, 2019b; Vaughan et al., 2013).

Over the last decades, global warming caused dramatic changes of the cryosphere. Between 1979 and 2018, the monthly Arctic sea ice extent decreased with unprecedented September sea ice reductions up to  $12.8 \pm 2.3\%$  per decade (IPCC, 2019b). At the same time, polar and high-mountain permafrost temperatures increased by  $0.29^\circ\text{C} \pm 0.12^\circ\text{C}$  between 2007 and 2016 causing widespread permafrost thawing as well as a destabilization and failure of slopes (IPCC, 2019b). Furthermore, Arctic June snow cover as well as its depth and duration decreased by  $13.4 \pm 5.4\%$  per decade in 1967-2018 (IPCC, 2019b). Yet, one of the most alarming consequences of global warming are melting glaciers and ice sheets. Together with ocean thermal expansion, their rapid melting represents the main cause for global mean sea-level-rise (SLR) threatening low-lying coastal populations and environments at all spatial scales (IPCC, 2019a, 2019b; Larsen et al., 2014; Vaughan et al., 2013). Between 2006 and 2015, glaciers worldwide lost an average mass of  $220 \pm 30$  Gt per year, thus contributed  $0.61 \pm 0.08$  mm annually to global mean SLR (IPCC, 2019b). Likewise, the global ice sheets

are losing mass at ever-increasing rates. During 1992-2018, the Greenland Ice Sheet lost  $3,902 \pm 341$  billion tons of ice and contributed  $10.8 \pm 0.9$  mm sea-level-equivalent (SLE) (Figure 1.1a) (The IMBIE Team, 2020) to an overall global SLR of  $\sim 87$  mm over the same period (Beckley et al., 2017; IPCC, 2019a). Similarly, the loss of  $2,720 \pm 1,390$  billion tons of ice on the Antarctic Ice Sheet (AIS) caused a total SLR contribution of  $7.6 \pm 3.9$  mm in 1992-2017 (The IMBIE Team, 2018) with accelerating rates since the mid-2000s (Figure 1.1b) (Bamber et al., 2018; Gardner et al., 2018; Martín-Español et al., 2016; Rignot et al., 2019). In this context, the role of the AIS under a changing climate is particularly relevant as its vast size accounts for  $\sim 91\%$  of the global ice mass (Swithinbank, 1988) or  $\sim 57.3$  m of SLE if melted entirely (Rignot et al., 2019).

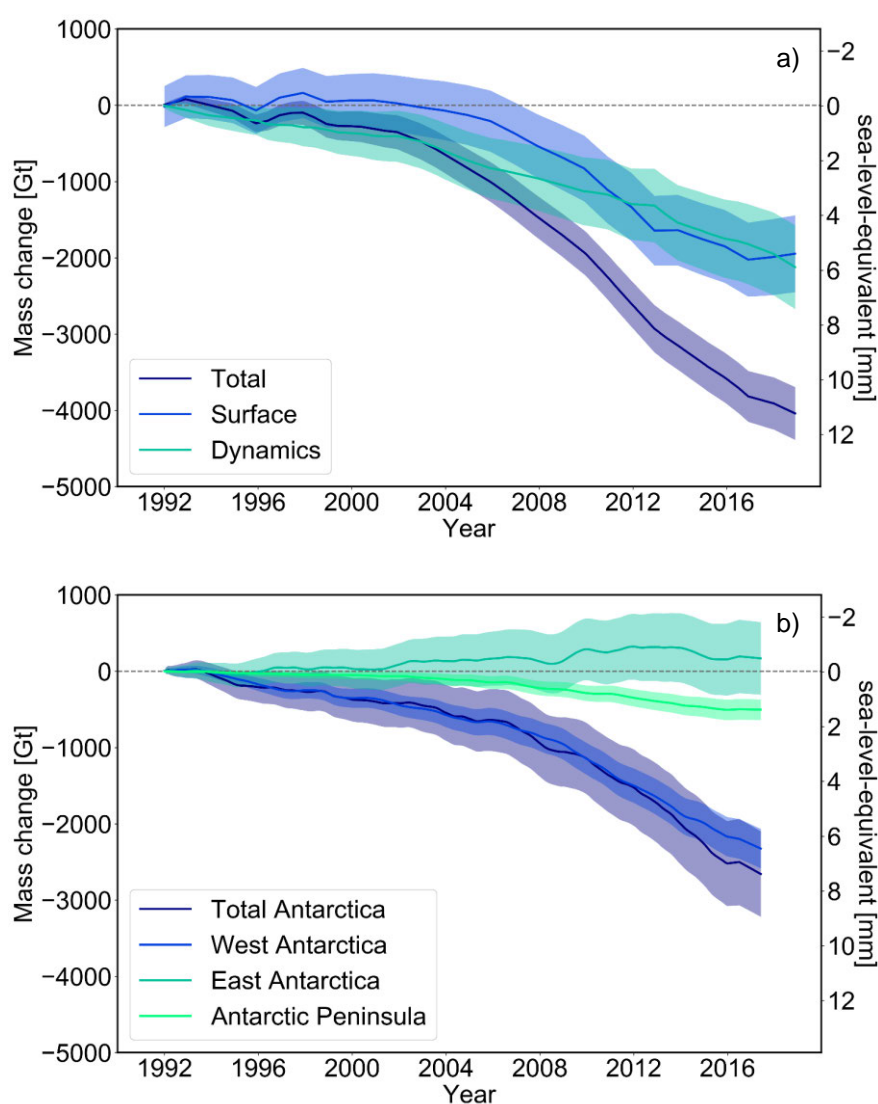


**Figure 1.1.** Cumulative mass changes and sea-level-equivalent over the Greenland (a) and Antarctic (b) ice sheets in 1992-2018 and 1992-2017, respectively. Data: (The IMBIE Team, 2018, 2020).





**Figure 1.2.** Overview map of Antarctica showing the three main sectors Antarctic Peninsula (API), West Antarctic Ice Sheet (WAIS) and East Antarctic Ice Sheet (EAIS) as well as major glaciers and ice shelves (blue). The background is a gridded bathymetry raster from the General Bathymetric Chart of the Oceans (GEBCO). BHS: Bellingshausen Sea. Data: (GEBCO Compilation Group, 2020; IMBIE, 2016; SCAR, 2019).

In agreement with overall Antarctic ice mass loss as well as the regional boundary conditions within the three Antarctic regions (Figure 1.2), changes on the AIS were spatially varying over the last decades (Figure 1.1b). In particular, Antarctic ice mass loss was dominated by the West Antarctic Ice Sheet (WAIS) accounting for ~2,340 Gt of the overall negative Antarctic mass balance in 1992-2017 (Figure 1.1b) (The IMBIE Team, 2018). Here, ocean thermal forcing led to the upwelling of warm Circumpolar Deep Water (CDW) onto the continental shelf (D, Figure 1.3), e.g. along the Amundsen Sea embayment and Bellingshausen Sea sector (see Figure 1.2), causing enhanced basal melting, ice shelf thinning, grounding line retreat and glacier acceleration which ultimately led to increased ice discharge through a reduction in ice shelf buttressing (e.g. Christianson et al., 2016; Depoorter et al., 2013; Jacobs et al., 2011; Jenkins et al., 2018; Martín-Español et al., 2016; Minchew et al., 2018; Mouginot et al., 2014; Pritchard et al., 2012; Rignot et al., 2019, 2013; The IMBIE Team, 2018). The second biggest contributor to Antarctic ice mass loss in 1992-2017 was with ~490 Gt the ice sheet

section of the Antarctic Peninsula (API) (Figure 1.1b) (The IMBIE Team, 2018). Besides ocean thermal forcing and dynamic thinning along the Bellingshausen Sea sector on the western API (see Figure 1.2) (Cook et al., 2016; Gardner et al., 2018; Hogg et al., 2017; Jenkins and Jacobs, 2008; Walker and Gardner, 2017; Wouters et al., 2015), mainly atmospheric warming (Turner et al., 2005) led to enhanced surface melting and meltwater ponding (H, I, Figure 1.3) resulting in the progressive retreat and disintegration of several API ice shelves as well as consequent ice flow accelerations and increased ice discharge (Doake and Vaughan, 1991; Pritchard and Vaughan, 2007; Rack et al., 1999; Rignot et al., 2019, 2004; Rott et al., 2007; Scambos et al., 2004, 2000; Seehaus et al., 2016; The IMBIE Team, 2018; Vaughan and Doake, 1996; Wuite et al., 2015). On the other hand, the East Antarctic Ice Sheet (EAIS) was indicated to be gaining mass (125 Gt) in 1992-2017 (Figure 1.1b) (The IMBIE Team, 2018). However, mass changes on the EAIS remain uncertain (Hanna et al., 2013; Martín-Español et al., 2017) with a recent study directly challenging the assumption of a growing EAIS and suggesting a significant negative contribution (1,211 Gt) from East Antarctica in 1979-2017 (Rignot et al., 2019). In this context, ice mass loss on the EAIS was associated with mainly ocean thermal forcing along Wilkes Land (see Figure 1.2) (Miles et al., 2018; Rignot et al., 2019; Rintoul et al., 2016; Roberts et al., 2018). To summarize, the main controlling factor on present-day Antarctic ice mass loss is dynamic thinning caused by the loss of the efficient buttressing force of ice shelves through ocean and atmospheric forcing. Other less prevalent controls on Antarctic ice dynamics include modified wind conditions that can temporally control oceanic heat supply through CDW upwelling (C, D, F, Figure 1.3) (Dutrieux et al., 2014; Friedl et al., 2018; Greene et al., 2017; Kimura et al., 2017; Walker and Gardner, 2017), changes in pre-frontal marine conditions that can destabilize glacier flow (G, Figure 1.3) (Fukuda et al., 2014; Greene et al., 2018; Khazendar et al., 2009; Lucchitta et al., 1994; Rott et al., 2018; Seehaus et al., 2015) as well as local or internal factors such as the glacier and bedrock geometry (Figure 1.3) (Christianson et al., 2016; Hogg et al., 2017; Rott et al., 2014; Seehaus et al., 2018) or changing marginal and basal conditions (P, Figure 1.3) (Hulbe et al., 2016; Stearns et al., 2008).

Despite the improved understanding of ice dynamical change on the AIS, the future of Antarctica remains difficult to predict with its contribution to SLR representing the largest uncertainty in current projections (Rintoul et al., 2018; Vaughan et al., 2013). If 21st century greenhouse gas (GHG) emissions are not contained, future climate scenarios yet suggest a further warming of the Antarctic until 2100 with temperature rises up to  $3.1 \pm 1.2$  °C compared to 1986-2005 (Collins et al., 2013). In particular, DeConto and Pollard (2016) state that Antarctica has the potential to raise global mean sea level by more than 1 m until 2100 and more than 15 m until 2500 if GHG emissions continue unabated. Additionally, Trusel et al. (2015) reveal a scenario-independent doubling of Antarctic surface melt until 2050 (Figure 1.4). Considering these scenarios,

atmospheric warming and melt intensification would soon become a dominant driver of Antarctic ice mass loss (DeConto and Pollard, 2016; Trusel et al., 2015).

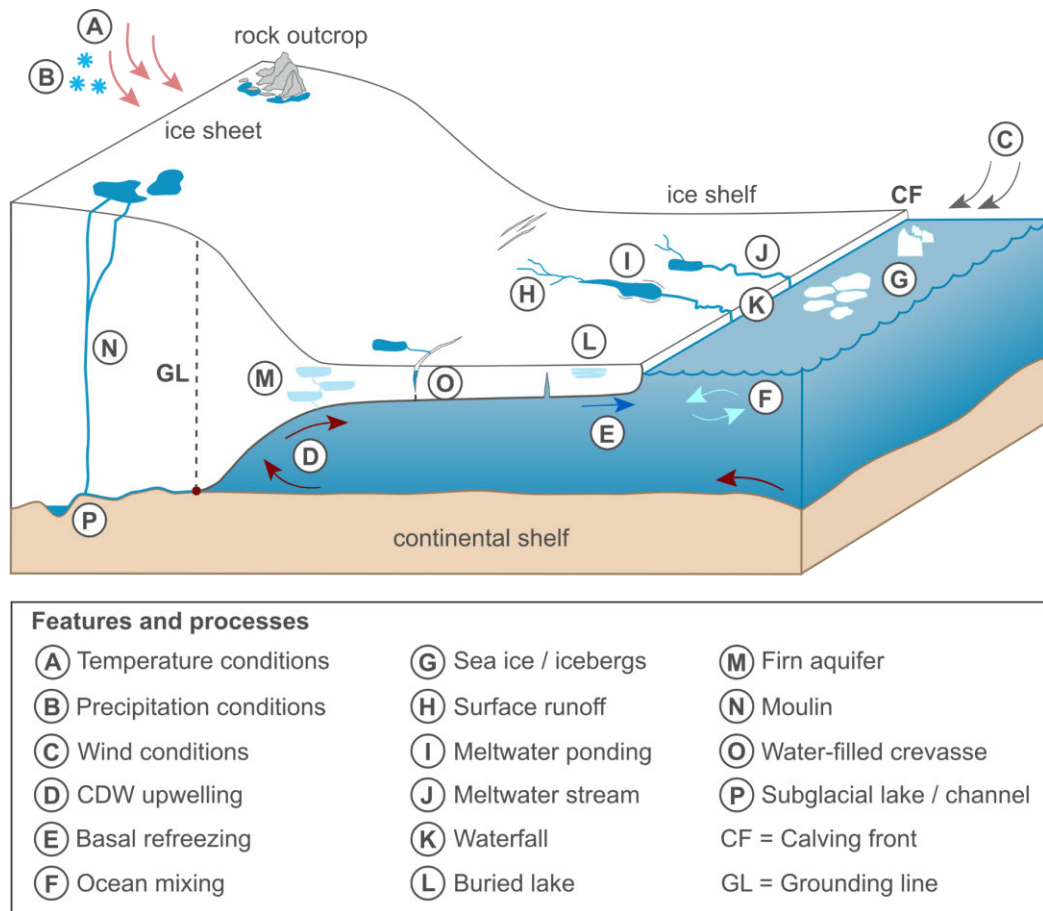


**Figure 1.3.** Sketch of features and processes (A-P) at an ocean-terminating outlet glacier in Antarctica with focus on hydrology. Modified after Dirscherl et al. (2021).

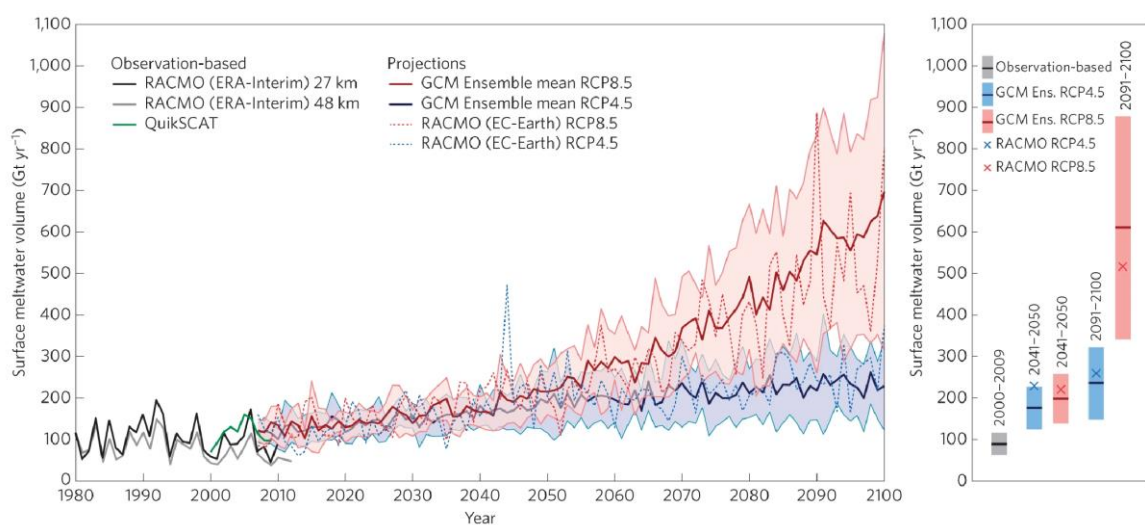


**Figure 1.4.** Antarctic surface meltwater volume from simulations of RACMO2 reanalysis data and QuikSCAT satellite observations under two climate projections. Right: Mean Antarctic surface meltwater volume ( $\pm\sigma$ ) per decade. Source: (Trusel et al., 2015). Reprinted with permission from Springer Nature and Copyright Clearance Center.

Apart from direct surface runoff and ice thinning, the main consequence of future intensified surface melting would be the increasing formation of supraglacial meltwater ponds in local surface depressions on the ice sheet or ice shelves (I, Figure 1.3) (Echelmeyer et al., 1991). As introduced above, supraglacial lakes are an important component in ice sheet hydrology through their impacts on ice dynamics and mass balance (Bell et al., 2018). First, an increasing presence of supraglacial lakes can intensify surface melting due to their low albedo initiating positive feedback mechanisms (Lüthje et al., 2006; Stokes et al., 2019; Tedesco et al., 2012). Second, the temporary drainage of supraglacial lakes to the glacier bed (N, Figure 1.3) can alter the basal conditions (P, Figure 1.3) and cause basal sliding as well as transient ice flow accelerations of grounded ice (Bell et al., 2018). While meltwater-induced basal sliding is a known driver for modified ice dynamics over the Greenland Ice Sheet (Bartholomew et al., 2010; Bell et al., 2018; Das et al., 2008; Hoffman et al., 2011; Schoof, 2010; Shepherd et al., 2009; Tedesco et al., 2013; Zwally et al., 2002), Tuckett et al. (2019) were the first to report of similar effects for glaciers along the API. The third mechanism involves a process called hydrofracturing resulting from the repeated filling and draining of supraglacial lakes into fractures and crevasses of an ice shelf as well as their downward propagation through the entire ice shelf thickness (O, Figure 1.3). As previously stated, hydrofracturing led to the disintegration of entire ice shelf sections along the API and caused rapid ice flow accelerations and dramatic ice mass loss through the loss of ice shelf buttressing (Banwell et al., 2019, 2013; Banwell and Macayeal, 2015; Bell et al., 2018; Fürst et al., 2016; Glasser and Scambos, 2008; Hulbe et al., 2016; Rignot et al., 2004; Rott et al., 2018, 1996; Scambos et al., 2004).

As ~75% of Antarctica's coastline is fringed by floating ice shelves that largely discharge and stabilize the AIS (Depoorter et al., 2013; Fürst et al., 2016; Rignot et al., 2013), detailed analyses of supraglacial lakes and their impacts on ice shelf stability and buttressing are of paramount importance, yet performed only scarcely. In this context, spaceborne remote sensing provides a valuable tool enabling the continuous monitoring of the Antarctic continent where ground-based mapping efforts are difficult to perform due to its vast size and remote geographical location. Only recently, advances in spaceborne remote sensing enabled more detailed research on Antarctic supraglacial lakes revealing far more widespread meltwater ponding than previously assumed (e.g. Bell et al., 2007; Dell et al., 2020; Kingslake et al., 2017; Langley et al., 2016; Lenaerts et al., 2017; Luckman et al., 2014, 2012; Stokes et al., 2019; Tuckett et al., 2019; Zheng and Zhou, 2019). Even though studies on Antarctic supraglacial lake dynamics are increasing, current research mainly focuses on local to regional-scale investigations of supraglacial lake abundance, e.g. along the API (e.g. Banwell et al., 2021; Glasser and Scambos, 2008; Kuipers Munneke et al., 2018; Leeson et al., 2020; Tuckett et al., 2019) or over individual drainage basins on the EAIS (e.g. Arthur et al., 2020b; Bell et al., 2017;

Dell et al., 2020; Halberstadt et al., 2020; Kingslake et al., 2015; Langley et al., 2016; Lenaerts et al., 2017; Moussavi et al., 2020; Stokes et al., 2019). At the same time, dense time series on supraglacial lake evolution, a circum-Antarctic assessment of supraglacial lake occurrence as well as an operational monitoring strategy are entirely missing. Additionally, current method developments (Dell et al., 2020; Halberstadt et al., 2020; Moussavi et al., 2020) are mostly semi-automated relying on optical multi-spectral satellite data only, thus are restricted to cloud-free imagery during austral summer (1 December to 1 March). Given the advantage of Synthetic Aperture Radar (SAR) data for detection of buried lakes as well as an illumination-independent monitoring of supraglacial lake dynamics, the lack of SAR-based supraglacial lake analyses additionally restricts current knowledge of Antarctic surface hydrology. In order to provide more detailed insight into Antarctic supraglacial lake distribution and evolution as well as to investigate associated drivers and impacts, the development of automated mapping strategies using multi-sensor remote sensing data from optical and SAR satellite sensors is of pressing need and overdue.

In particular, several key aspects should be addressed in future research on Antarctic meltwater ponding (Arthur et al., 2020a; Bell et al., 2018). First, a pan-Antarctic assessment of supraglacial lake distribution on ice shelves and grounded ice has to be enabled exploiting the growing archives of high-resolution satellite data. Second, the temporal evolution of supraglacial meltwater features throughout the year has to be evaluated, e.g. to reveal whether lakes refreeze or drain at the onset of Antarctic winter and whether lakes spread farther inland under the pressure of atmospheric warming. Third, the dominant control mechanisms on supraglacial lake formation need to be investigated more precisely. Finally, the impact of supraglacial meltwater ponding on Antarctic ice dynamics and ice shelf stability requires to be evaluated in more detail. In this context, the determination of critical meltwater thresholds indicating imminent ice shelf fracturing or collapse is of utmost importance (Arthur et al., 2020a; Bell et al., 2018). Dedicated analysis of these aspects is also relevant for an improved parametrization of meltwater processes in current climate models, e.g. on Antarctic SMB using RACMO (Regional Atmospheric Climate Model) (van Wessem et al., 2018). In parts, the above points are covered in the Scientific Committee on Antarctic Research (SCAR) Antarctic and Southern Ocean Science Horizon Scan that identified 80 key research questions to direct future Antarctic research (Kennicutt et al., 2015).

## 1.2 Research Motivation

Based on the scientific background information presented in Chapter 1.1, the main motivation of the present thesis is to exploit spaceborne remote sensing for an enhanced scientific understanding and knowledge of the Antarctic surface hydrological network

constraining (1) key characteristics of Antarctic supraglacial lake and stream formation and distribution, (2) underlying control mechanisms responsible for increased meltwater production and accumulation and (3) the vulnerability of ice shelves to enhanced surface melting under a warming climate. In this thesis, the term “supraglacial lake” is used to describe all surface meltwater that can be captured with spaceborne remote sensing including meltwater ponds and streams as well as partly frozen or buried lakes.

### 1.3 Research Objectives

As outlined in Chapter 1.1, the future of Antarctica largely depends on its ice dynamical response to changing boundary conditions including ocean and atmospheric forcing. In this context, the response of the AIS to atmospheric warming as well as an increasing meltwater production and accumulation on glaciers and ice shelves around the periphery of Antarctica is particularly crucial to assess (Bell et al., 2018). As previously mentioned, Antarctic meltwater ponding has the potential to initiate dramatic ice dynamic change and contribute significantly to global SLR (Doake and Vaughan, 1991; Leeson et al., 2020; Pritchard and Vaughan, 2007; Rignot et al., 2019; Scambos et al., 2004; The IMBIE Team, 2018; Tuckett et al., 2019; Wuite et al., 2015). However, the past and present distribution and evolution of Antarctic supraglacial lakes as well as underlying control mechanisms and impacts remain poorly understood.

In order to address this knowledge gap as well as to comply with the research motivation outlined in Chapter 1.2, the development of a novel framework for an automated mapping of Antarctic supraglacial lake extents in multi-sensor remote sensing data from optical and SAR satellite sensors is essential and represents a key objective of this thesis. In this regard, the open data archives of the European Space Agency (ESA) Copernicus Sentinel missions are particularly suitable providing substantial volumes of Earth Observation (EO) data for a continuous year-round monitoring of the Antarctic coastal zone where supraglacial lakes are clustered. More specifically, the four main research objectives of this thesis can be formulated as follows:

- **Objective 1.** The first research objective of this thesis is to conduct a literature review on existing studies on Antarctic supraglacial lakes including the assessment of fundamental controls and impacts of supraglacial lake distribution as well as of established supraglacial lake classification methods, used sensor types and the spatio-temporal coverage of studies.
- **Objective 2.** The second and central research objective of this thesis is the development of a novel and fully automated framework for circum-Antarctic supraglacial lake extent mapping in Sentinel-1 SAR and optical Sentinel-2 imagery. Combining observations from Sentinel-1 and Sentinel-2 is crucial to

allow continuous monitoring efforts also during polar darkness and cloud cover, limiting the visibility of supraglacial lakes in optical imagery, or when supraglacial lake detection is hindered in radar imagery.

- **Objective 3.** Following the successful implementation of methods, the third research objective addresses their application to the full Sentinel data archives over selected Antarctic regions for assessment of (1) the spatial distribution of Antarctic supraglacial lakes and (2) their seasonal and inter-annual evolution.
- **Objective 4.** Finally, a last research objective is associated with the linkage of supraglacial lake dynamics with underlying control mechanisms and drivers including the local glaciological setting, the regional near-surface climate and large-scale atmospheric modes.

In order to comply with the overarching objectives of this thesis, several key research questions have to be formulated and addressed. The first group of questions refers to the literature review on existing work on Antarctic supraglacial lakes. In particular, the following research questions shall be answered:

#### Research Questions 1

- Why are Antarctic supraglacial lakes of relevance?*
- What are known controls on supraglacial lake formation and how widespread are supraglacial lakes around Antarctica?*
- What are potential influences of supraglacial lakes on ice dynamics?*
- How many studies address Antarctic supraglacial lake dynamics and what is their spatio-temporal coverage and resolution?*
- What are the most frequently applied EO sensors and methods for supraglacial lake extent mapping?*
- Which research gaps exist and how can they be addressed?*

The second group of research questions focuses on the implementation of a novel framework for automated supraglacial lake extent mapping in Sentinel-1 SAR and optical Sentinel-2 satellite imagery. In this regard, specific focus is on the evaluation of potentials and challenges of satellite remote sensing as well as of state-of-the-art Machine Learning (ML) and Deep Learning (DL) techniques for an improved functionality and spatio-temporal transferability of methods.

#### Research Questions 2

- a. *What are potentials and challenges for mapping Antarctic supraglacial lake extents in optical and SAR satellite imagery and how can they be addressed and overcome?*
- b. *How can recent advances in EO, including innovative Artificial Intelligence (AI) approaches, support an improved monitoring and understanding of Antarctic supraglacial meltwater features?*
- c. *How can ML and DL support a fully automated mapping of Antarctic supraglacial lakes in Sentinel-1 SAR and optical Sentinel-2 imagery?*
- d. *What opportunities exist for the implementation of a holistic framework for circum-Antarctic supraglacial lake extent mapping?*

Next, the third group of research questions addresses the application of developed methods for retrieval of intra-annual and inter-annual supraglacial lake dynamics over selected Antarctic regions. In addition, supraglacial lake formation and evolution shall be linked to climate parameters and ice surface characteristics resulting in the following research questions:

#### Research Questions 3

- a. *What are intra-annual and inter-annual patterns and anomalies of supraglacial lake evolution?*
- b. *What are the properties of observed supraglacial lakes?*
- c. *Where do supraglacial lakes cluster on ice shelves and grounded ice and how often do they reoccur at the same locations?*
- d. *Are the observed ice shelf regions particularly vulnerable to ice shelf collapse and what are potential implications for future ice shelf stability?*
- e. *What are the dominant controls on supraglacial lake distribution and evolution? What are implications for other Antarctic regions?*



## 1.4 Thesis Outline

In Chapter 1.1, a brief introduction into the scientific relevance of the Antarctic Ice Sheet under a warming climate was given. Moreover, potential impacts of supraglacial meltwater accumulation on Antarctic ice dynamics and mass balance were highlighted and research gaps as well as future monitoring requirements were briefly introduced. Subsequently, Chapters 1.2 and 1.3 outlined the main research motivation and objectives of this thesis. Following this introductory chapter, the subsequent chapters can be summarized as follows:

**Chapter 2** briefly introduces Antarctica's political status and important background knowledge on the main physical properties and characteristics of ice sheets. In the following, Antarctica's glaciology, climatology and oceanography are described.

**Chapter 3** provides a review on fundamental characteristics of Antarctic surface hydrology. More specifically, details on Antarctic supraglacial lake distribution are given and current knowledge on controls and impacts of Antarctic supraglacial meltwater ponding is addressed.

**Chapter 4** first outlines the state-of-the-art of current research on Antarctic supraglacial lakes through application of spaceborne remote sensing. In the following, potentials and challenges of optical and SAR remote sensing for supraglacial lake extent delineation are summarized. Lastly, future research requirements with respect to spatial and temporal resolution standards as well as method developments are discussed.

**Chapter 5** presents the developed framework for automated supraglacial lake extent classification. Following a thorough description of used training and testing sites as well as the corresponding data basis, the methods for automated classification and fusion of Sentinel-1 SAR and optical Sentinel-2 data are introduced. In addition, mapping results are presented for independent test data and an accuracy assessment is performed. At last, the implementation of developed methods for large-scale processing over the entire Antarctic coastline is outlined and the results are discussed and summarized.

**Chapter 6** investigates the seasonal and inter-annual evolution of Antarctic supraglacial lake extents across multiple Antarctic regions in 2015-2021. In addition, the dominant control mechanisms on Antarctic supraglacial lake formation are investigated through correlation of supraglacial lake extents with environmental data at varying time lags.

**Chapter 7** summarizes the entire thesis and addresses the fulfilment of research questions and objectives outlined in Chapter 1.3. Moreover, an outlook into future challenges and opportunities is provided.



## CHAPTER 2

### 2 Physical Characteristics of Antarctica

All land and ocean between 60°S and the South Pole are considered Antarctic territory (see Figure 1.2). Within this region, the continental land mass of Antarctica stretches over an area of 14.2 million km<sup>2</sup> of which ~98% is covered by ice (CIA, 2021). Owing to these conditions, Antarctica is not inhabited. However, there are 112 permanent and seasonal Antarctic research stations operated by researchers and technicians from 30 different countries around the world (CIA, 2021; CONMAP, 2021). These countries are part of the Antarctic Treaty coming into force in 1961 for establishment of a legal system for international scientific cooperation and governance of Antarctica without sovereign claims or military actions (ATS, 2021; CIA, 2021; Dodds, 2010). Today, a total of 54 nations signed the Antarctic Treaty ensuring environmental protection, preservation and sustainability (ATS, 2021). Apart from its political status, Antarctica is also unique in terms of its physical properties and characteristics being the coldest, windiest, driest and most remote continent on Earth (CIA, 2021; Gossart et al., 2019). In the following, some fundamental glaciological background information is given and the main aspects of Antarctica's physical geography, including its glaciology, climatology and oceanography, are summarized. Being the central topic of this thesis, fundamental details on Antarctica's surface hydrology are given in Chapter 3.

#### 2.1 Glaciology

To provide some fundamental glaciological background information, Figure 2.1 outlines the main processes contributing to ice sheet formation. As can be seen, the formation and overall flow regime of an ice sheet is mainly controlled by snow accumulation and ablation as well as the regional geographical setting and gravity. More specifically, accumulated snow is gradually transformed into firn and ice through compaction of the snowpack with increasing precipitation, thus snow load. Under the impact of gravity, the formed ice column then flows seaward from regions of accumulation to regions of ablation (Figure 2.1). This relocation and metamorphosis of ice also results in the formation of different glacier zones (Benson, 1960; Braun et al.,

2000; Cuffey and Paterson, 2010; Rau et al., 2000). Within each of these zones, different snow, firn and ice conditions prevail (see Figure 2.1). In high altitudes of the ice sheet, the dry snow zone dominates as melting is absent throughout the entire year. The percolation zone is located directly below the dry snow zone and is characterized by occasional surface melting during summer. Here, meltwater percolates into the snowpack and refreezes at shallow depth forming ice pipes and lenses. In the wet snow zone adjacent to the percolation zone, sufficient melting takes place to permit runoff during summer. Next, the superimposed ice zone is located at the lower end of the wet snow zone. Here, refrozen meltwater forms a continuous layer of ice that is exposed at the surface through the loss of overlying snow. The upper boundary of the superimposed ice zone marks the snow line and the lower boundary the equilibrium line (Figure 2.1). The latter also represents the transition from accumulation to ablation zone where bare ice is visible during most of the year. Below the equilibrium line, ablation processes, including surface melt, sublimation and evaporation, prevail resulting in a constantly negative SMB within this zone. The net balance between mass gains in the accumulation zone and mass losses in the ablation zone then returns the overall SMB of the ice sheet. The net balance between mass gains in the accumulation zone and mass losses in the ablation zone then returns the overall SMB of the ice sheet. Together with mass losses through iceberg calving at the front, the overall mass balance can be calculated (Hanna et al., 2013; Rignot et al., 2013). The partitioning between mass gains through snow accumulation and mass losses due to ice dynamical discharge and ablation processes yet depends on the climatic and geographical setting as well as structure of the ice sheet. To provide more detail on the factors affecting mass balance partitioning in Antarctica, the following paragraphs and subchapters outline the structure, flow regime as well as recent ice dynamical change of the AIS.

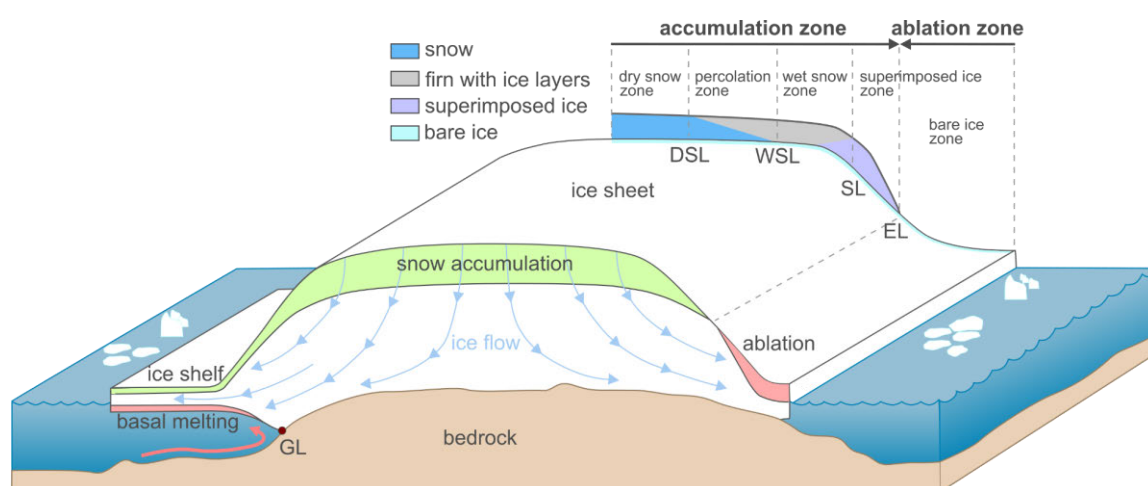


**Figure 2.1.** Idealized sketch of gravitational ice sheet flow from regions of snow accumulation to regions of ablation including the different glacier zones. The setting on the left shows typical ablation conditions at outlet glaciers with ice shelf in Antarctica. The setting on the right represents ablation conditions at outlet glaciers in Greenland. DSL: Dry Snow Line. WSL: Wet Snow Line. SL: Snow Line. EL: Equilibrium Line. GL: Grounding Line.

### 2.1.1 Ice Sheet Structure

In general, the AIS can be structured into slow-moving grounded ice, fast-moving ice streams and outlet glaciers as well as floating ice shelves (Figure 2.2a) (Bell and Seroussi, 2020). Slow-moving grounded ice can be found in the vast interior of the ice sheet where ice flow speeds typically do not exceed 1 m/a. Fast-moving ice streams and outlet glaciers drain the grounded inland ice towards the ocean and reach peak velocities of >4 km/a, as observed over Antarctica's fastest flowing Pine Island and Thwaites glaciers in West Antarctica (Figure 2.2b-d) (Mouginot et al., 2014). On the other hand, floating ice shelves fringe ~75% of Antarctica's 17,968 km long coastline (Figure 1.2) and act as the main stabilizing factor on Antarctic inland ice, thus have a slowing effect on overall ice flow (Bell and Seroussi, 2020; Rau et al., 2005; Rignot et al., 2013). The largest Antarctic ice shelves, including Ross, Filchner-Ronne and Amery, are on average 300 m thick (Figure 2.3c) providing considerable buttressing on the inland ice (Bell and Seroussi, 2020). The transition from grounded ice to floating ice is also referred to as the grounding zone and the location where the ice sheet loses contact to the underlying bedrock is called the grounding line (Figure 1.3, Figure 2.1) (Friedl et al., 2020).

In agreement with the spatial division of Antarctica into three major regions (see Figure 1.2), the Antarctic ice mass is not equally distributed across the continent. With an ice thickness up to 4,897 m above Astrolabe Subglacial Basin (see Figure 2.3b), the EAIS holds ~90% of all Antarctic inland ice making it the largest ice sheet worldwide (Fretwell et al., 2013; Rignot et al., 2019). Over East Antarctica, the Amery, Filchner and Ross-East ice shelves drain ~58% of all East Antarctic ice (Rignot et al., 2019). The highest elevation of the EAIS reaches more than 4,000 m over the Gamburtsev Mountains (Figure 2.3b,d) and the deepest point of the ice sheet can be found in a canyon below Denman Glacier at 3,500 m below sea level (see Figure 2.3b,e) (Morlighem et al., 2020). In coastal regions, the bedrock oftentimes breaches the ice surface in the form of rock outcrop whereat other parts of the EAIS are grounded well below sea level (see Figure 2.3b,d,e). Ice sheets that are largely grounded below sea level are also referred to as marine ice sheets and are most vulnerable to marine ice sheet instability through CDW intrusion and progressive basal melting (Bamber et al., 2009; Hughes, 1981; Joughin et al., 2014; Schoof, 2007).

The WAIS is separated from the EAIS through the Transantarctic Mountain Range (Figure 2.3b) and holds an ice mass equivalent to ~9% of all Antarctic inland ice (Rignot et al., 2019). The highest point of West Antarctica and of the entire Antarctic continent is Vinson Massif (4,892 m) in the Ellsworth Mountains (Figure 2.3b). At the same time, large parts of West Antarctica are grounded well below sea level making it particularly vulnerable to marine ice sheet instability (see Figure 2.3b,c). For example, the Amundsen Sea sector, including Pine Island and Thwaites glaciers (see Figure 2.2b),

drains most of West Antarctica (Rignot et al., 2019) of which ~80% is grounded on marine sediment below sea level (Fretwell et al., 2013; Morlighem et al., 2020). This sector is particularly vulnerable to marine ice sheet instability (Milillo et al., 2019) or even collapse (Scambos, 2017) also due to its retrograde bed slope declining towards the interior of the continent (Figure 2.3b,c). In addition, most ice in the Amundsen Sea sector is buttressed by only small ice shelves. On the contrary, substantial buttressing is provided by the larger Ross and Ronne ice shelves in the Ross and Weddell sea sectors, respectively (Figure 2.3b,c).

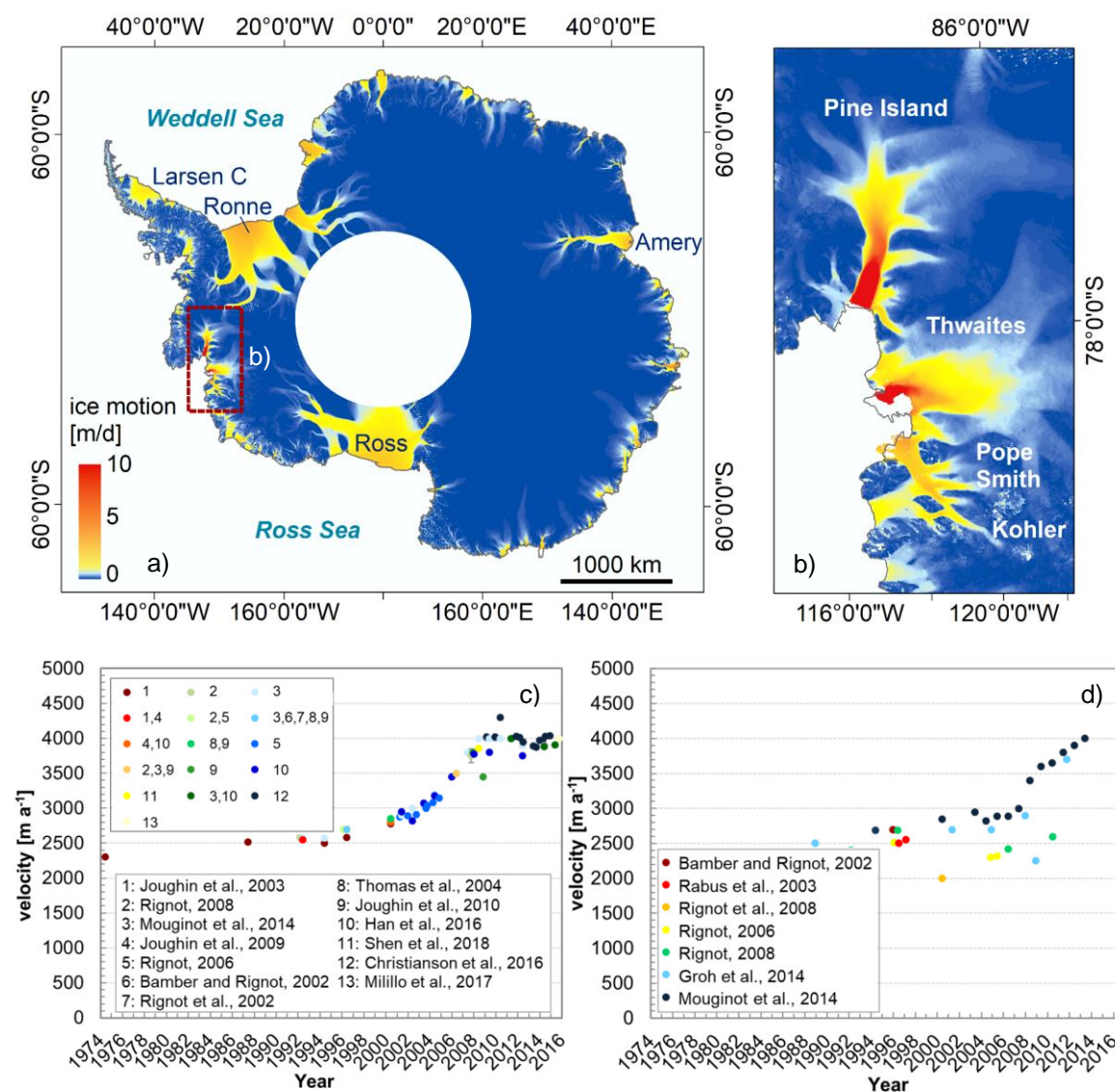


**Figure 2.2.** Spatio-temporal ice flow pattern over Antarctica. (a) Landsat 8 Ice Speed of Antarctica (LISA) during 2013-2017. (b) LISA inset for the Amundsen Sea sector. Central grounding line velocity trend over Pine Island (c) and Thwaites (d) glaciers, West Antarctica. The plots in c-d are modified after Dirscherl et al. (2020a). Data: (Fahnestock et al., 2016; Mouginot et al., 2017b; Rignot et al., 2013; Scambos et al., 2019).



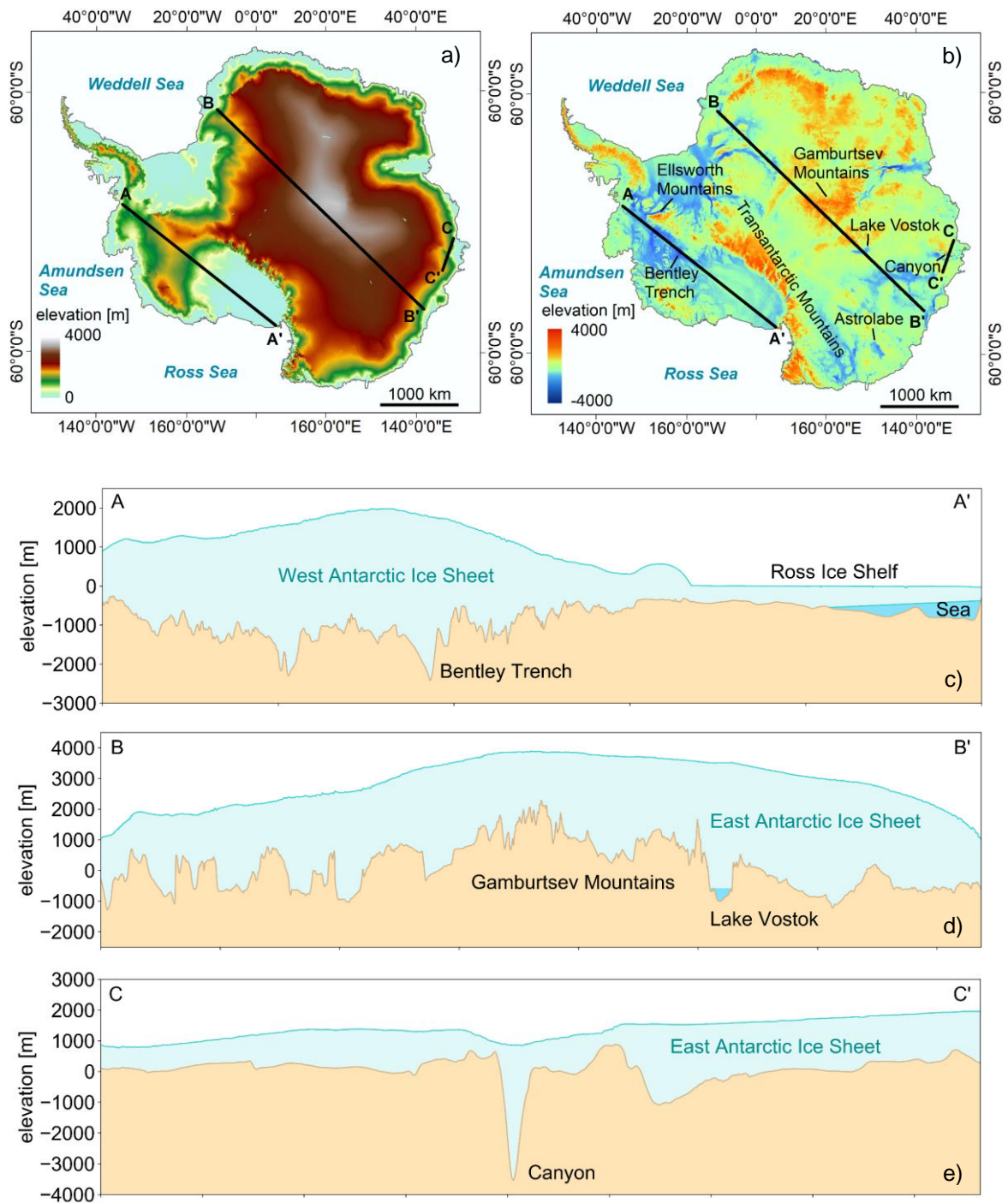


**Figure 2.3.** Surface (a) and bedrock (b) elevation of the Antarctic continent. (c) Elevation profile over West Antarctica. (d-e) Elevation profiles over East Antarctica. The ice thickness of Ross Ice Shelf in (c) as well as the water level in Lake Vostok in (d) were sketched. Data: (Morlighem, 2020; Morlighem et al., 2020; Mouginito et al., 2017b; Rignot et al., 2013; Wessel et al., 2021).

Holding  $\sim 0.5\%$  of the Antarctic ice mass (Rignot et al., 2019), the API is by far the smallest Antarctic ice sheet. Here, more than 500 glaciers drain from the central ice plateau onto small ice shelves along the north-western API and onto the larger Larsen ice shelves in the north-east (Bell and Seroussi, 2020). Along the south-western

Bellingshausen Sea sector, George VI Ice Shelf drains most of the adjacent inland ice, equivalent to ~54% of the overall API ice mass (see Figure 1.2).

### 2.1.2 Ice Dynamical Change

Changes of Antarctic ice dynamics can be measured by means of several key ice sheet parameters including the calving front, grounding line, ice motion, surface elevation as well as overall mass balance. Most of these parameters are in direct interaction with large interdependencies requiring a holistic view of overall Antarctic ice dynamical change as well as of associated drivers and impacts. For example, enhanced basal melting through CDW upwelling can cause ice shelf thinning and grounding line retreat inducing glacier acceleration as well as increased ice discharge and iceberg calving (Dirscherl et al., 2020; Hogg et al., 2017; Lilien et al., 2018; Shepherd et al., 2004). Similarly, atmospheric warming can induce ice shelf thinning and iceberg calving, both leading to grounding line retreat, glacier acceleration and increased ice discharge (Dirscherl et al., 2020; Rott et al., 2011; Scambos et al., 2004; Wuite et al., 2015). As mentioned in Chapter 1.1, local and internal instabilities control the magnitude and individual response of a glacier or ice shelf to external forcing. In the following, the main trends of circum-Antarctic ice dynamical change are summarized. Focus is on the last decades, where the AIS underwent dramatic change leading to considerable ice mass loss and an unprecedented contribution to global SLR (Figure 1.1b). Additionally, details on overall mass balance partitioning are given.

To start with, ocean-induced thinning of Antarctic ice shelves was extensive in 1994-2012 (Paolo et al., 2015). Within this period, by far the largest ice thickness changes were documented along the Amundsen and Bellingshausen sea sectors on the WAIS and API as well as over coastal sections along Wilkes Land on the EAIS (Paolo et al., 2015). This pattern is also confirmed by Rignot et al. (2013) reporting of particularly strong basal melt rates over the same coastal sections (Figure 2.4a). Similarly, ocean forcing caused Antarctic grounding lines to retreat significantly between 2010 and 2016 (Konrad et al., 2018). More specifically, 22%, 10% and 3% of all observed grounding lines on the WAIS, API and EAIS retreated during the observational period whereat largest retreat was revealed along the Amundsen Sea sector in West Antarctica as well as along the API (Konrad et al., 2018). Next, Antarctic calving front retreat was extensive in 1997-2018 leading to an areal loss of  $-22,510 \pm 116 \text{ km}^2$  for glaciers and ice shelves around Antarctica (Baumhoer et al., 2021). Within this period, most areal loss was found over the WAIS, closely followed by the API. At the same time, the only region with frontal advance exceeding frontal retreat was the EAIS (Baumhoer et al., 2021). Over the API, especially the disintegration of entire ice shelf sections, e.g. along Larsen B, Wilkins and Wordie ice shelves as well as of iceberg A-68 from Larsen C Ice Shelf, contributed to calving front retreat whereat in West Antarctica, mainly the Ross West, Ronne, Pine



Island, Thwaites, Getz and Abbot ice shelves accounted for retreat (Baumhoer et al., 2021). In this context, the dominant controls of calving front retreat were ocean and atmospheric forcing (Baumhoer et al., 2021). Furthermore, recent measurements of circum-Antarctic ice motion change revealed strong velocity increases in 2008-2015 particularly for glaciers along the API, the Amundsen Sea sector on the WAIS and Wilkes Land on the EAIS (Gardner et al., 2018; Shen et al., 2018). As expected, ice flow accelerations were found to be strongest in regions of strong ice shelf thinning as well as substantial grounding line or frontal retreat due to ocean and atmospheric warming, e.g. at Pine Island and Thwaites glaciers in the Amundsen Sea embayment (Figure 2.2c-d), over Getz Ice Shelf in the southern Amundsen Sea sector as well as around the former Larsen ice shelves and in Marguerite Bay on the API (Gardner et al., 2018). Additionally, Shepherd et al. (2019) investigated surface elevation change over the entire Antarctic continent in 1992-2017. As can be seen in Figure 2.4b, most of the interior of Antarctica remained stable over the observational period whereat ~1%, ~24%, and ~8% of the coastal EAIS, WAIS, and API were estimated to be in ice dynamical imbalance (Shepherd et al., 2019). In agreement with the imbalance of parameters introduced above as well as overall Antarctic ice mass loss, most elevation change was observed over the ice sheet sections along the Amundsen and Bellingshausen sea sectors of the WAIS and API as well as over Totten Glacier in Wilkes Land, EAIS (Figure 2.4b). Over Pine Island and Thwaites glaciers in the Amundsen Sea sector, ice drawdown reached peak values of 122 m (Shepherd et al., 2019).

As outlined in the previous paragraphs and in Chapter 1.1, overall Antarctic ice mass loss was extensive in 1992-2017 (Figure 1.1b) (Rignot et al., 2019; The IMBIE Team, 2018) and primarily resulted from ocean-induced basal melting as well as iceberg calving. In this context, Figure 2.4a gives insight into the approximate partitioning between iceberg calving (2007-2008) and melting (2003-2008). In contrast to the Greenland Ice Sheet, where ice mass loss is equally partitioned between atmospherically-induced surface runoff in the ablation zone (Fettweis et al., 2013; Khan et al., 2015; The IMBIE Team, 2020) and ocean warming leading to iceberg calving (Figure 1.1a) (Holland et al., 2008; Seale et al., 2011; Straneo and Heimbach, 2013; The IMBIE Team, 2020; Wood et al., 2021), overall Antarctic ice mass loss is dominated by ocean-induced basal melting of ice shelves being the main ablation mechanism in Antarctica (Figure 2.1, Figure 2.4a) (Fürst et al., 2016; Rignot et al., 2013). As stated in Chapter 2.1.1, this is mainly the result of Antarctica being drained through floating ice shelves compared to Greenland outlet glaciers that are mostly grounded at their front (CIA, 2021; Rau et al., 2005; Rignot et al., 2013; Wood et al., 2021).

## Physical Characteristics of Antarctica

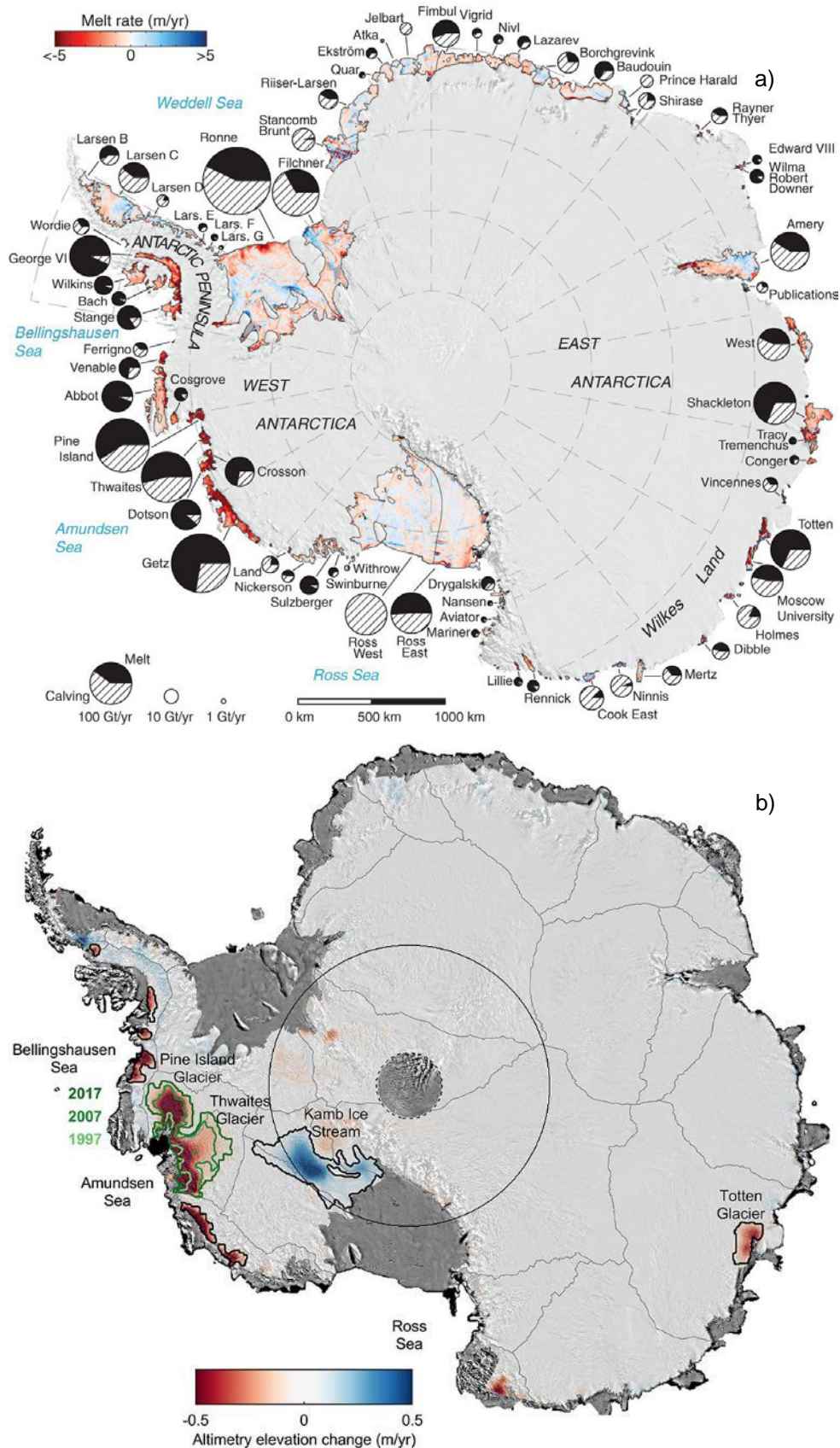


**Figure 2.4.** Antarctic ice dynamic change. (a) Basal melting (2003-2008) and iceberg calving (2007-2008) of Antarctic ice shelves. Source: (Rignot et al., 2013). Reprinted with permission from the American Association for the Advancement of Science and Copyright Clearance Center. (b) Antarctic surface elevation change from satellite altimetry in 1992-2017. Source: (Shepherd et al., 2019).

## 2.2 Climatology

In the following, the main aspects of Antarctica's climatic setting, including wind, air temperature and precipitation conditions as well as potential interactions, are summarized.

### 2.2.1 Wind

The main wind system circulating the Antarctic continent is a belt of strong Southern Westerly Winds (SWW) created through an atmospheric pressure gradient in Southern Hemisphere (SH) mid- to high-latitudes (Jones et al., 2016; Moreno et al., 2018). SWW form within the mid-latitude Ferrel cell, part of global atmospheric circulation, where air is moving poleward from high-pressure to low-pressure regions, while being diverted eastward by the Coriolis force (see Figure 2.5) (Moreno et al., 2018). Moreover, SWW are centered near the Polar front, the boundary between Ferrel and Polar cell. In the Polar cell, air moves from the high-pressure polar high above the South Pole towards low-pressure regions in the mid-latitudes. Together with the influence of Coriolis, the movement of air in the Polar cell forms the polar easterlies, also referred to as Easterly Winds (EW) (see Figure 2.5) (Stewart and Thompson, 2012). EW are dry, cold winds that are often weak and irregular. Yet, their impact on Antarctic coastal regions is meaningful as they circulate Antarctic ice shelf fronts and impact ocean circulation as well as sea ice concentration (Parish and Bromwich, 2007; Stewart and Thompson, 2012). Similarly, SWW and the ocean around Antarctica form a coupled climate system influencing the climate of the entire SH. More details on Antarctic wind-ocean interactions as well as implications for the AIS are given in Chapter 2.3.

The leading mode of Antarctic atmospheric circulation variability is the Southern Annular Mode (SAM), a measure for changes in atmospheric pressure between mid- and high-latitudes reflecting the strength and position of SWW (Jones et al., 2016). Different phases of SAM during summer and autumn affect Antarctic climate in various ways. During positive phases of SAM, atmospheric pressure over Antarctica is low intensifying the westerly wind belt and moving it poleward (Marshall, 2003). At the same time, anomalous air pressure in the mid-latitudes is high and winds tend to weaken (Moreno et al., 2018). A contraction of the SWW towards Antarctica affects ocean circulation and particularly the Antarctic Circumpolar Current (ACC) and CDW upwelling as well as Antarctic air temperature and precipitation, thus the overall state of the AIS (see following chapters) (Jones et al., 2016). On the other hand, negative phases of SAM move the wind belt towards the Equator affecting SH climate parameters in the opposite way (Moreno et al., 2018). Over the last decades, SAM has constantly been positive driving glacier and ice shelf recession over Antarctica (Abram et al., 2014; Rignot et al., 2019). Positive SAM trends have mostly been associated with stratospheric ozone

depletion, GHG emissions as well as tropical Pacific climate (Abram et al., 2014; Marshall et al., 2004; Moreno et al., 2018; Thompson et al., 2011) and might further influence the SH climate through effects such as a deepening of the Amundsen Sea Low being a regional low pressure region near the West Antarctic Coast (Mayewski et al., 2009). Depending on the future climate scenario (Rintoul et al., 2018), SAM will most likely strengthen even though opposite effects might arise from tropical Pacific climate change (Abram et al., 2014). Under a high-emission scenario, SAM could even strengthen to the degree that large parts of the AIS would be lost (Rintoul et al., 2018).

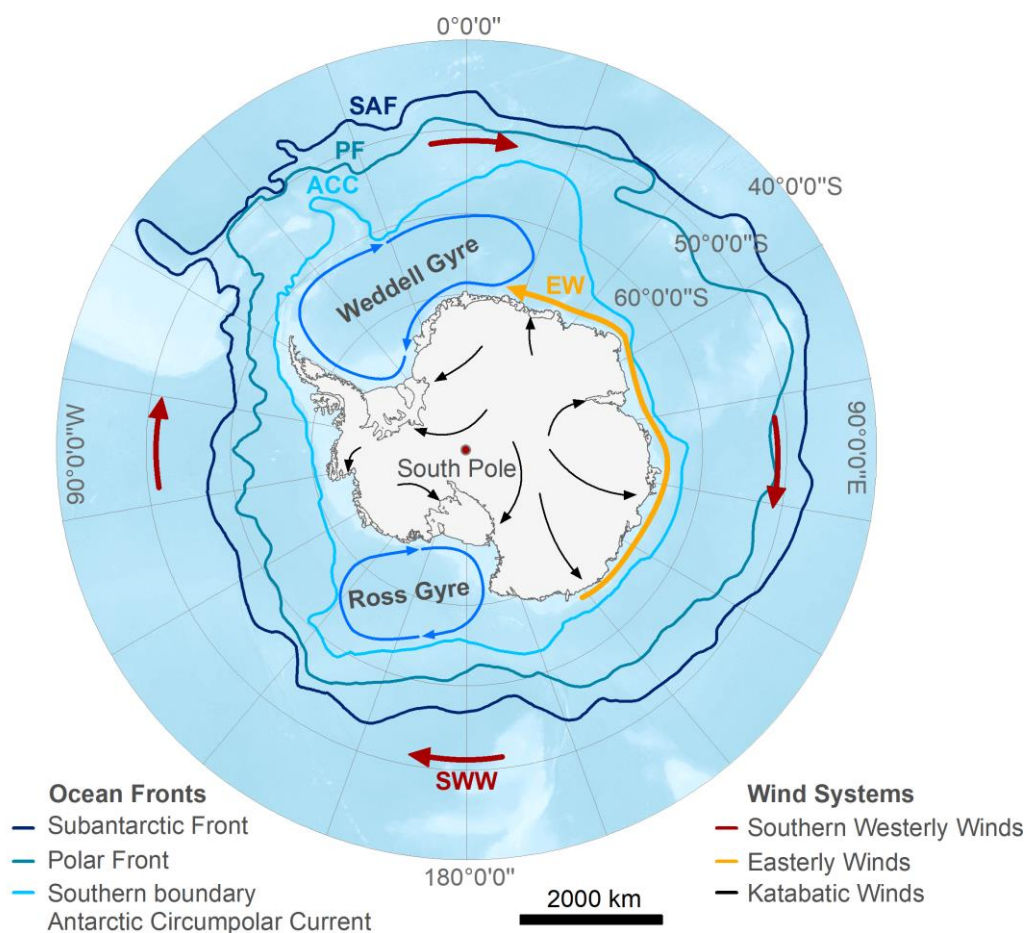


**Figure 2.5.** Antarctic ocean fronts and wind systems. The background image is a gridded bathymetry raster from GEBCO. Data: (AAD, 2021; GEBCO Compilation Group, 2020; Mougnot et al., 2017b; Rignot et al., 2013).

On the Antarctic continent, regional wind patterns play an equally important role for overall climate and ice dynamics. To start with, katabatic winds originate from cold and dry high-pressure regions in the interior of Antarctica and flow towards warmer low-pressure regions near the coast (see Figure 2.5) (Grazioli et al., 2017; Parish and Bromwich, 2007; Parish and Cassano, 2003). Katabatic winds flow downslope in the form of fall winds and can reach extreme wind speeds well above 300 km/h. In fact, the highest recorded wind speed over Antarctica was a measurement of 327 km/h

originating from katabatic winds at Dumont d'Urville station in 1972 (Hay, 2016). Similar to polar easterlies and SWW, katabatic winds may have important implications on sea ice formation as well as ocean and atmospheric circulation (Grazioli et al., 2017; Parish and Bromwich, 2007). Apart from cold katabatic winds, warm foehn winds are known to initiate enhanced surface melting around Antarctica (Cape et al., 2015; Datta et al., 2019; Lenaerts et al., 2017). While foehn winds over the API originate from episodic interaction of SWW with topography (Lenaerts et al., 2017), EAIS foehn winds mostly arise as adiabatically warmed katabatic winds flowing from the ice sheet's interior to the coast (Lenaerts et al., 2017). However, warm katabatic winds on the EAIS were also linked to westerly wind interaction with topography, as observed in the McMurdo Dry Valleys in the Transantarctic Mountain Range (Speirs et al., 2010). Figure 2.6a shows the overall pattern of maximum Antarctic wind speed in 2019 with highest speeds in coastal regions around the EAIS and WAIS.

### 2.2.2 Air Temperature

Until recently, the coldest recorded air temperature on Earth was a measurement of  $-89.2^{\circ}\text{C}$  made at Vostok Station, East Antarctica, in 1983 (see Figure 2.6c) (Turner et al., 2009). Satellite measurements during the 2004-2016 austral winters yet detected a frequent recurrence of snow surface temperatures well below  $-90^{\circ}\text{C}$  over the East Antarctic plateau (Figure 2.3d) (Scambos et al., 2018). These low-temperature snow surface conditions suggest air temperatures of around  $-94 \pm 4^{\circ}\text{C}$  over the same periods, as revealed through comparison with automated weather stations (Scambos et al., 2018). Around Antarctica, air temperature varies strongly with respect to geographical location and time. As can be seen in Figure 2.6c, the mean Antarctic air temperature in 1981-2020 was lowest above the central Antarctic plateau and highest around the coastal margins and the API (Figure 2.6c), whereat the overall Antarctic average air temperature was measured at  $-36.5^{\circ}\text{C}$ . Additionally, air temperatures are highest during austral summer and lowest during austral winter (Figure 2.6e,f). In this context, austral summer represents the months December to February and austral autumn, winter and spring represent the periods March to May, June to August and September to November, respectively. To provide more detail, Figure 2.6e shows monthly mean air temperatures for the period 1961-1990, measured at the German Antarctic Receiving Station (GARS) O'Higgins on the API (Figure 2.6c). As can be seen, the maximum average air temperature at O'Higgins Station was  $0.5^{\circ}\text{C}$  for the month of January whereat the lowest recorded monthly mean air temperature was  $-8.5^{\circ}\text{C}$  representing July (Figure 2.6e). A contrasting example is given in Figure 2.6f showing monthly mean air temperatures at Vostok Station in central East Antarctica (see Figure 2.6c). At Vostok Station, monthly mean air temperatures reached a maximum of  $-31^{\circ}\text{C}$  in austral summer and a minimum of  $-67.9^{\circ}\text{C}$  in austral winter.

Over recent decades, Antarctic air temperature underwent considerable change particularly along the API. At Vernadsky Station on the API west coast, a temperature rise of 2.8°C has been observed between 1951 and 2000 (Turner et al., 2016, 2005) most likely due to increased GHG emissions and stratospheric ozone depletion (Thompson and Solomon, 2002) leading to more positive phases of SAM (Marshall et al., 2006) but also due to teleconnections with El Niño–Southern Oscillation (ENSO) (Clem and Fogt, 2013) and local sea ice loss (Turner et al., 2013). However, since the late 1990s, the warming trend over the API receded and cooling (-0.47°C per decade) dominated the 1999-2014 summers. API cooling was mainly associated with natural decadal-scale climate variability and a strengthening mid-latitude jet leading to more cyclonic conditions in the Weddell Sea (Bozkurt et al., 2020; Turner et al., 2020, 2016). A recent study yet suggests an end of the API cooling phase since the mid-2010s (Carrasco et al., 2021). Similarly, the WAIS underwent significant warming over the last decades (Bromwich et al., 2013; Clem and Fogt, 2013; Ding et al., 2011; Steig et al., 2013, 2009). WAIS warming exceeded 0.1°C per decade since the late 1950s being particularly pronounced over the interior of the ice sheet (Bromwich et al., 2013; Turner et al., 2020) as well as during winter and spring (Ding et al., 2011; Schneider et al., 2012; Steig et al., 2009). In a more recent study, WAIS warming was also found to be significant during austral summer (Bromwich et al., 2013). The drivers for WAIS temperature increase remain uncertain with changes in tropical Sea Surface Temperature (SST) and sea ice (Ding et al., 2011; Schneider et al., 2012; Steig et al., 2013, 2009) being the most likely. More recently, WAIS temperature trends weakened (Clem et al., 2020). Over the EAIS, records of air temperature trends are inconsistent with slight cooling observed for the period 1979-1998 (Comiso, 2000). In contrast, significant EAIS warming of  $0.12 \pm 0.07$  °C per decade has been revealed for the period 1957-2006 (Steig et al., 2009). In agreement with the latter, Clem et al. (2020) report of significant warming at the South Pole with temperature increases up to  $0.61 \pm 0.34$  °C per decade over the last three decades. The EAIS warming trend was associated with the coupling of a positive SAM and increasing SST in the western tropical Pacific leading to a strong cyclonic anomaly in the Weddell Sea sector and allowing the penetration of warm moist air into the interior of Antarctica (Clem et al., 2020). Figure 2.6d summarizes Antarctic air temperature change over the last two decades similarly revealing the observed warming over the EAIS interior and cooling over parts of the WAIS and API. In detail, 2000-2010 mean air temperatures are compared to 2010-2020 mean air temperatures, as calculated from ERA5-Land reanalysis data.



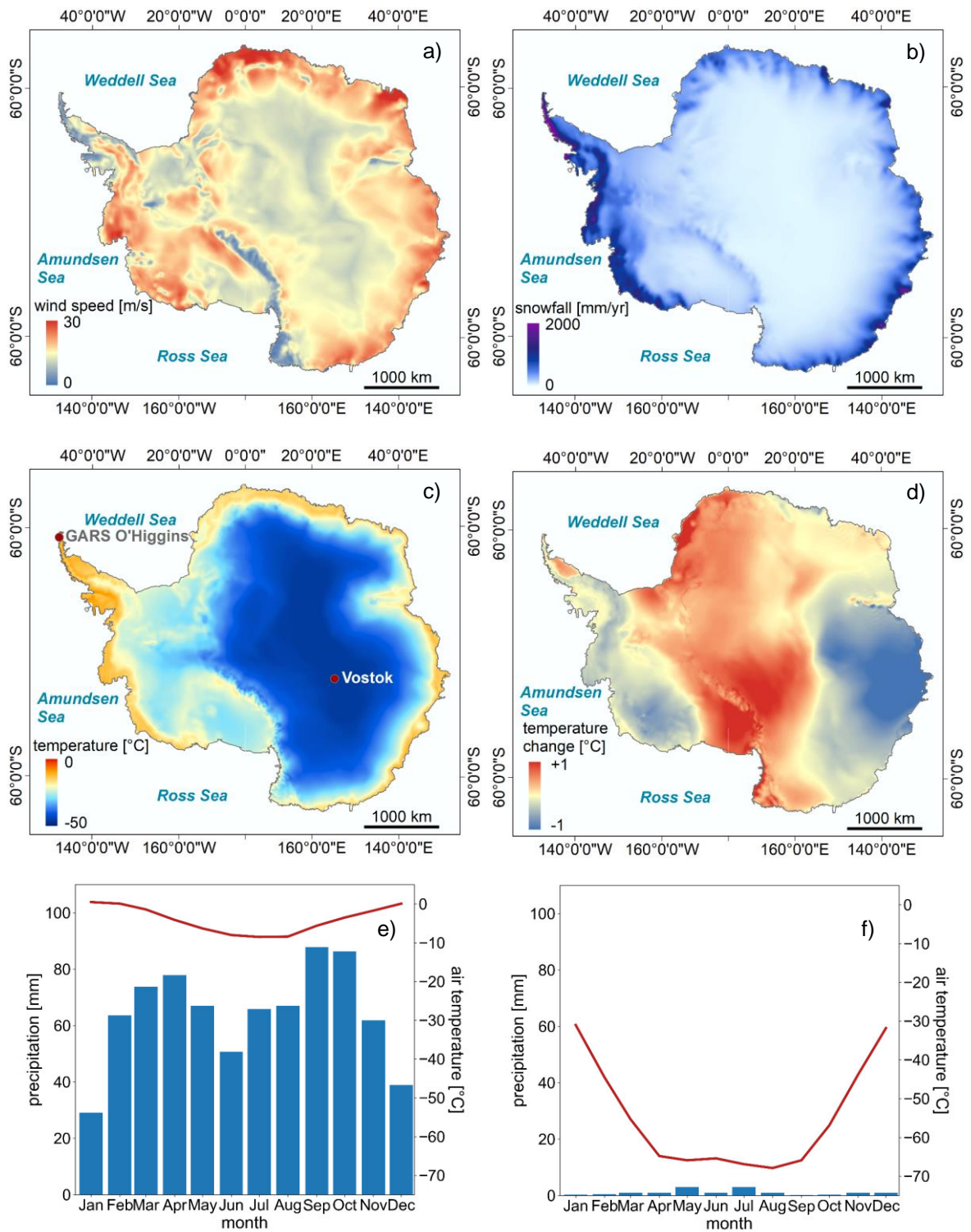


**Figure 2.6.** Antarctic climatic conditions calculated from ERA5-Land reanalysis (a-d) and station data (e-f). (a) Maximum Antarctic wind speed in 2019. (b) Average annual precipitation in 1981-2020. (c) Mean Antarctic air temperature in 1981-2020. (d) Mean Antarctic air temperature change between 2000-2010 and 2010-2020. Monthly mean temperature (red) and precipitation (blue) at O'Higgins (e) and Vostok (f) stations in 1961-1990. Data: (DWD, 2021; Mouginito et al., 2017b; Munoz Sabater, 2019a, 2019b; Rignot et al., 2013).

### 2.2.3 Precipitation

Antarctic precipitation conditions vary strongly across the continent with an average value of ~137 mm per year in 1981-2020. As shown in Figure 2.6b, precipitation is usually highest around the coastal margins of the EAIS and WAIS as well as along the API. In contrast, lowest precipitation rates can be found in the interior of Antarctica. This pattern is also reflected in Figure 2.6e-f showing constantly high monthly precipitation up to 88 mm at O'Higgins on the API (Figure 2.6e) and extremely low monthly precipitation up to 3 mm at Vostok station in central East Antarctica (Figure 2.6f).

In general, Antarctic precipitation conditions are influenced by four main SH climate parameters including the southern Baroclinic Annular Mode, the austral summer SAM as well as the two Pacific-South American teleconnection patterns (Marshall et al., 2017). Baroclinic Annular Mode is known to influence storm conditions over the Southern Ocean (SO) causing precipitation over East Antarctica to increase. At the same time, positive phases of summer SAM result in increased precipitation across West Antarctica and the western API as well as reduced precipitation over the eastern API and central EAIS, as revealed during 1979-2013 (Marshall et al., 2017). In contrast, Pacific-South American patterns mainly influence West Antarctic precipitation through meridional moisture fluxes into and out of the continent causing precipitation increases and decreases, respectively (Marshall et al., 2017).

During the 20th century, snowfall over the Antarctic continent increased by  $14 \pm 1$  Gt per decade and somewhat compensated SLR contributions from dynamic ice mass loss (Medley and Thomas, 2019; Thomas et al., 2017). Over the API, the overall increasing precipitation trend was rapid and accelerating. On the other hand, mass gains and losses from the eastern and western WAIS were close to balance (Medley and Thomas, 2019). Over the EAIS and particularly its coastal sections, snow accumulation increased until 1979 and then decreased (Medley and Thomas, 2019). In the coming decades, atmospheric warming is projected to further increase snow accumulation due to the enhanced moisture holding capacity of warmer air, thus will somewhat compensate future SLR contributions, e.g. from surface melting and enhanced runoff (Bell et al., 2018; Bengtsson et al., 2011; Krinner et al., 2007; Lenaerts et al., 2016).

## 2.3 Oceanography

The SO is directly coupled to the Antarctic climate system and is largely responsible for present-day Antarctic ice mass loss. The largest ocean current of the SO is the ACC encircling the Antarctic continent in eastward direction and being driven by SWW and ocean bathymetry (Figure 2.5) (Holland et al., 2020). The ACC is the largest and strongest current on Earth connecting all major oceans and providing substantial ocean



upwelling of North Atlantic Deep Water (Carter et al., 2008; Holland et al., 2020). Towards the north, the ACC creates a sharp boundary with the Polar Front (PF) and the Subantarctic Front (SAF) (Figure 2.5). The SAF is considered to be the northern end of the ACC whereas the PF lies within the ACC representing the transition between cold Antarctic and warmer Subantarctic water (Figure 2.7). At the PF, Antarctic ocean water generally sinks below warmer Subantarctic water driving ocean mixing and overturning. As shown in Figure 2.5, the southern end of the ACC lies directly south of the PF. During positive phases of SAM, the ACC intensifies and CDW is pushed onto the Antarctic continental shelf causing basal melting of ice shelves, as observed in the Bellingshausen and Amundsen sea sectors as well as along Wilkes Land and the western API (Cook et al., 2016; Rignot et al., 2019). CDW is a layer of warm, dense and high-saline ocean water located at ~500 m depth beneath the ocean surface (Holland et al., 2020). It is separated from surface water through a thermocline, a region of strong temperature change. The depth of CDW beneath the ocean surface, regional wind conditions as well as local bathymetry determine whether CDW upwelling and subsequent ice shelf basal melting can take place. The higher CDW sits within the ocean column, the more likely is CDW upwelling into ice shelf cavities close to the grounding line (Holland et al., 2020). In this context, EW may increase the depth of the thermocline and reduce the thickness of CDW. One component that can block CDW from penetration into ice shelf cavities is the impact of winter sea ice cover altering the salinity content of the ocean (Broecker and Peng, 1987; Holland et al., 2020). In detail, High Salinity Shelf Water forms through an increased sea ice abundance and wind transport away from the coast forming coastal polynyas. High Salinity Shelf Water effectively creates a barrier at the continental shelf break, the Antarctic Slope Front, hindering CDW from entering the ice shelf cavity (Holland et al., 2020). However, even in the case of High Salinity Shelf Water-blockage, melting can take place in a cold-water cavity due to the lower melting point of ice under increased pressure conditions at depth. At the same time, basal refreezing may take place as meltwater rises along the ice shelf base (E, Figure 1.3) (Holland et al., 2020). The cold, high-salinity shelf water may further cool through EW blowing across coastal polynyas and consequently descend into the deep ocean across the shelf break creating Antarctic Bottom Water (Gordon, 2001). Apart from these large-scale ocean circulations, two smaller-scale Antarctic ocean currents exist. In detail, the Ross and Weddell gyres rotate ocean water clockwise through interaction of ACC with regional seafloor topography (Figure 2.5).

Considering a strengthening of SAM in the future, wind-driven changes of the SO will further enhance the penetration of warm ocean water into ice shelf cavities (Rintoul et al., 2018). Moreover, changes in ocean circulation due to positive SAM events might affect eddy activity (Meredith and Hogg, 2006) as well as the CO<sub>2</sub> holding capacity of the SO (Quéré et al., 2007). Another aspect that could potentially impact future ocean

circulation results from a decreasing salinity of Antarctic Bottom Water, e.g. due to increased AIS freshwater discharge. In fact, freshening of Antarctic Bottom Water was observed in 1980-2012 (Purkey and Johnson, 2013) and may contribute to future enhanced basal melting through a reduction in Antarctic Bottom Water production allowing warmer ocean water to flow into ice shelf cavities (Silvano et al., 2018). Additionally, warming of the SO has been evident since the 1970s and may cause further perturbations to ocean circulation in the future (Meredith et al., 2019). At the same time, no significant changes in annual Antarctic sea ice extent have been observed in 1979-2018 (Ludescher et al., 2019; Meredith et al., 2019) despite large regional and seasonal variations, e.g. due to meridional winds (Holland, 2014; Holland and Kwok, 2012). Figure 2.7 illustrates the average SST for austral summers 1979-2019 as well as median spring and autumn sea ice extents in 1981-2010.

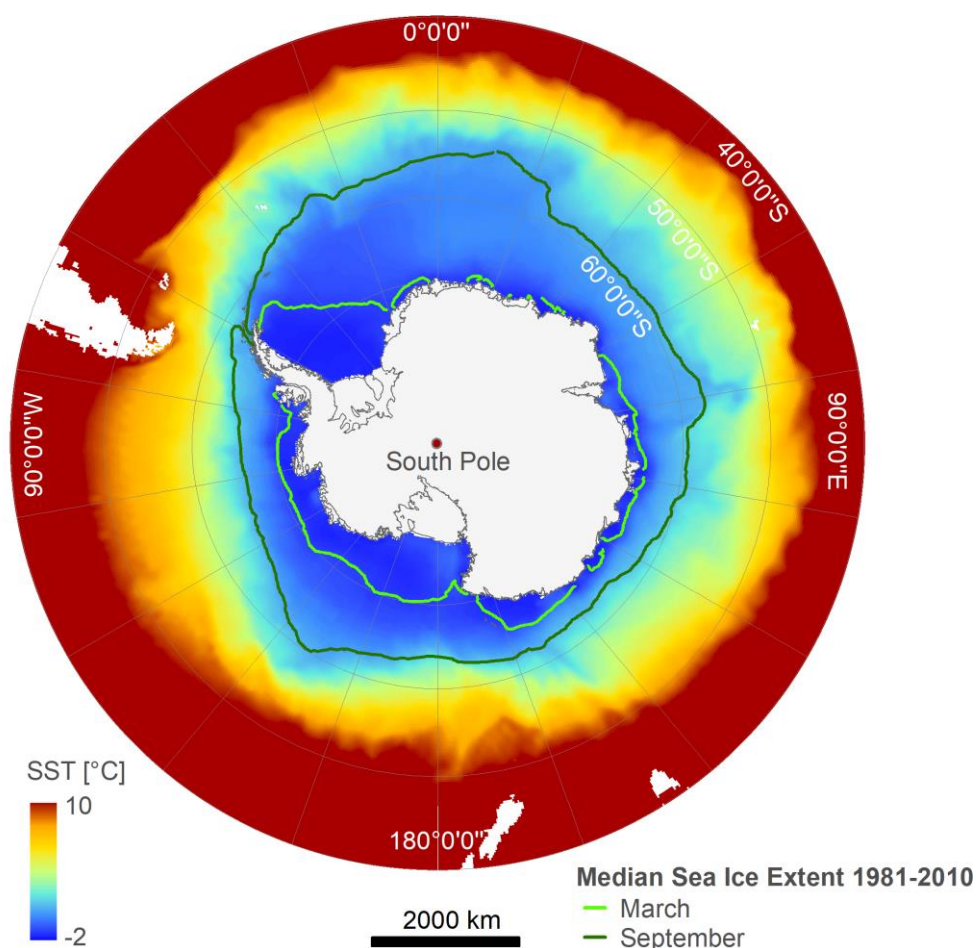


**Figure 2.7.** Average Antarctic Sea Surface Temperature (SST) for austral summers 1979-2019 and median sea ice extent for March and September 1981-2010. Data: (Fetterer et al., 2017; Hersbach et al., 2019; SCAR, 2019).

## CHAPTER 3

### 3 A Review on Fundamentals of Antarctic Surface Hydrology

The Antarctic hydrological network plays an important role in overall ice dynamics and mass balance and can be divided into a supraglacial, an englacial as well as a subglacial component. Antarctic supraglacial hydrology consists of meltwater streams, ponds and frontal waterfalls (I-K, Figure 1.3) forming through enhanced meltwater production above an impermeable snow/ice layer on top of glaciers, ice shelves and the ice sheet (Echelmeyer et al., 1991). Surface hydrological features are often interconnected and develop extensive drainage systems that transport meltwater across the ice shelves and the ice sheet (Figure 3.1) (Dell et al., 2020; Spergel et al., 2021). The Antarctic surface hydrological network is directly connected to englacial hydrological features within the ice sheet and ice shelves comprising firn aquifers, moulins, buried lakes and water-filled fractures and crevasses (Bell et al., 2018; Chu, 2014; Fountain and Walder, 1998). Buried lakes form through freezing of supraglacial lakes as well as their subsequent coverage in snow (L, Figure 1.3) (Bell et al., 2018; Lenaerts et al., 2017) and perennial firn aquifers store water in a porous matrix of ice crystals within the firn column of an ice sheet (M, Figure 1.3) (Bell et al., 2018). On the other hand, meltwater can be stored in fractures and crevasses of an ice shelf (O, Figure 1.3) (Bell et al., 2018; Rott et al., 2011; Scambos et al., 2004) whereat vertical meltwater drainage through grounded ice via moulins can connect the englacial and basal hydrological systems (N, Figure 1.3) (Bell et al., 2018; Chu, 2014; Tuckett et al., 2019). Lying at the base of the Antarctic Ice Sheet, the subglacial hydrological system (P, Figure 1.3) consists of an extensive network of interconnected lakes and channels forming in local depressions of the bedrock (Figure 2.3d). Apart from meltwater inflow through englacial drainage systems, basal meltwater is produced from pressure melting, frictional heating as well as subglacial geothermal activity (Ashmore and Bingham, 2014; Remy and Legresy, 2004; Sergienko and Hulbe, 2011; Siegert and Dowdeswell, 1996). One remarkable feature of Antarctic subglacial hydrology is Lake Vostok. Situated in a topographic trough east of the Gamburtsev Mountains in East Antarctica, Lake Vostok reaches a depth of >1 km at

its deepest point with the thickness of overlying ice exceeding 4 km (Figure 2.3b,d) (Siegert et al., 2001).

Despite recent progress in the understanding of Antarctic ice sheet hydrology, detailed knowledge of Antarctic surface hydrological features, including meltwater ponds and streams, is still limited. To summarize the state-of-the-art of knowledge on Antarctic surface hydrology, the following chapters provide a comprehensive review on the main factors controlling supraglacial lake formation on ice sheets (Chapter 3.1), the spatio-temporal distribution of Antarctic supraglacial lakes (Chapter 3.2) as well as potential impacts on Antarctic ice dynamics (Chapter 3.3). Chapter 3.4 summarizes the entire Chapter 3.

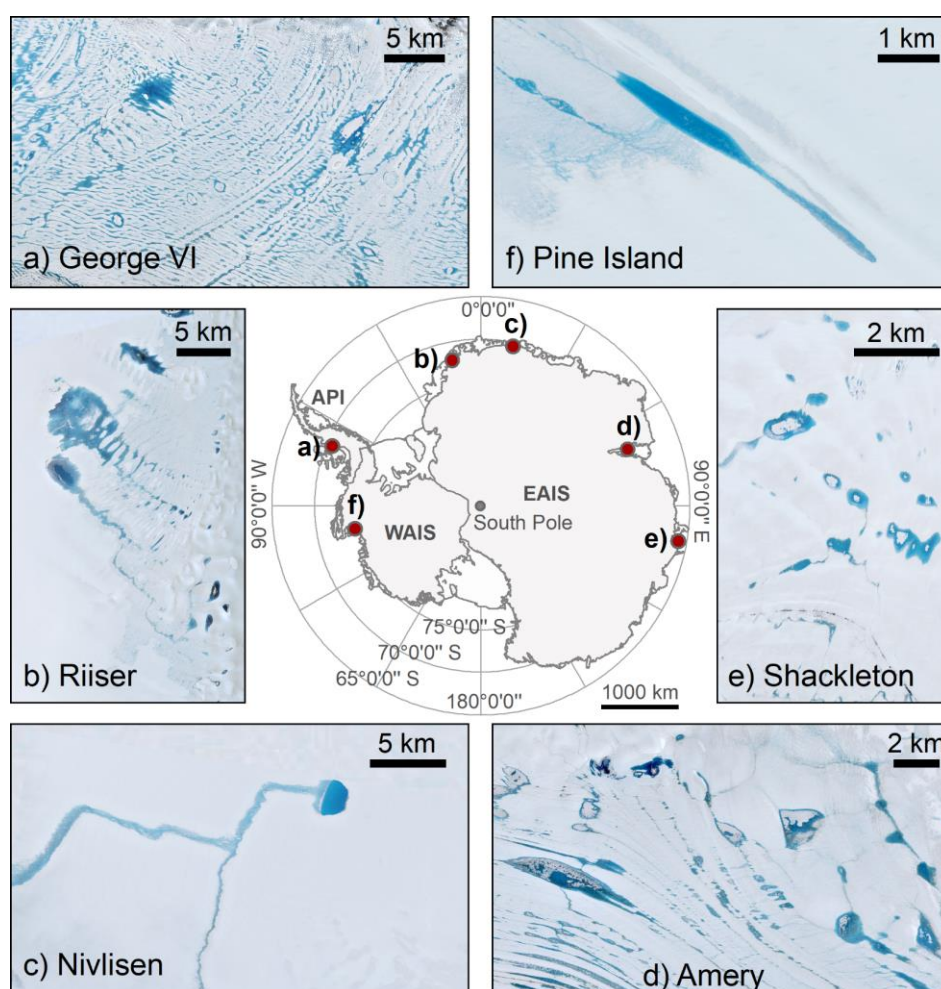


**Figure 3.1.** Appearance of Antarctic supraglacial lakes in Sentinel-2 image extracts of (a) 19 January 2020 on George VI Ice Shelf, (b) 2 February 2017 on Riiser-Larsen Ice Shelf, (c) 21 January 2019 on Nivlisen Ice Shelf, (d) 2 January 2019 on Amery Ice Shelf, (e) 29 January 2019 on Shackleton Ice Shelf and (f) 27 December 2019 on Pine Island Ice Shelf. API: Antarctic Peninsula. EAIS: East Antarctic Ice Sheet. WAIS: West Antarctic Ice Sheet. Data: (Copernicus Sentinel-2 data; IMBIE, 2016; Mouginot et al., 2017b; Rignot et al., 2013).

## 3.1 Controls on Supraglacial Lake Formation and Appearance

### 3.1.1 Local Controls

Local controls on the spatio-temporal evolution of surface hydrological features include topographic and ice flow conditions, ice surface characteristics as well as melt-albedo feedbacks. To start with, supraglacial lakes tend to pond above an impermeable snow and ice layer in local surface depressions on grounded and floating ice (Echelmeyer et al., 1991). Meltwater ponding on grounded ice is closely connected to the subglacial bedrock topography translating into ice surface depressions and permitting lakes to reform in the same location annually (Banwell et al., 2014; Echelmeyer et al., 1991; Gudmundsson, 2003; Ignéczi et al., 2018; Lampkin and VanderBerg, 2011; Langley et al., 2016; Stokes et al., 2019). Annual lake clustering on grounded ice can also be found in glacier confluence zones where lateral shear stress induces strain and glacier deformation (see Figure 3.2b). An important implication of frequent recurrence times of lakes in fixed locations is enhanced basal ablation driving lakes on grounded ice to grow larger and deeper than lakes on floating ice where they are more transient (Law et al., 2020; Lüthje et al., 2006; Tedesco et al., 2012). In particular, lakes on thinner floating ice accumulate in migrating ice shelf surface depressions generated by spatio-temporal variations in ice flow (Figure 3.1) (Arthur et al., 2020b; Glasser and Gudmundsson, 2012; LaBarbera and MacAyeal, 2011; Macdonald et al., 2018; Spergel et al., 2021). Ice shelf surface depressions may also form in response to channelized basal melting causing the ice shelf to subside (Dow et al., 2018; McGrath et al., 2012). Over both grounded and floating ice, supraglacial lake formation tends to be more prevalent on slow-moving ice at low elevations and low surface slopes (Arthur et al., 2020b; Bell et al., 2018; Dell et al., 2020; Kingslake et al., 2017; Stokes et al., 2019).

Another important control on supraglacial meltwater ponding are ice surface characteristics and particularly the firn air content (FAC) (Arthur et al., 2020a; Stokes et al., 2019). Supraglacial lake formation is suggested to be promoted over snow and firn with a reduced FAC impeding an infiltration of meltwater into the firn column, e.g. due to firn air depletion and densification caused by firn over-saturation, meltwater refreezing in firn pore space or reduced snowfall (Alley et al., 2018; Arthur et al., 2020a; Kuipers Munneke et al., 2014; Lenaerts et al., 2017; Spergel et al., 2021; Stokes et al., 2019). Contrarily, an increased FAC is suggested to allow the percolation of meltwater into the low-density firn layer, thus reduces the likelihood of ponding (Bell et al., 2018; Kuipers Munneke et al., 2014; van Wessem et al., 2021). At the same time, an increasing FAC may support the formation of firn aquifers (Bell et al., 2018; van Wessem et al., 2021).

Melt-albedo feedbacks can contribute to intensified surface melting and ponding near low-albedo features such as blue ice, exposed bedrock or surface debris (see Figure



3.2) (Arthur et al., 2020a; Bell et al., 2018; Kingslake et al., 2017; Lenaerts et al., 2017; Tedesco, 2015; Winther et al., 1996). In detail, surface features with a low albedo enhance melting through an increased absorption of solar radiation leading to intensified heat exchange with the adjacent ice column (Arthur et al., 2020a; Lenaerts et al., 2017). Around Antarctica, melt-albedo feedbacks are assumed to control supraglacial lake clustering close to and upstream of the grounding line where blue ice and rock outcrop are most abundant (Bell et al., 2018; Kingslake et al., 2017; Stokes et al., 2019). In very high elevations, melt-albedo feedbacks near rock and blue ice could even be a first-order control on supraglacial lake formation due to air temperatures being too low to initiate melting under normal conditions (Figure 3.2a,c) (Stokes et al., 2019). Likewise, supraglacial lakes themselves can initiate positive melt-albedo feedbacks. Depending on their depth, the albedo of supraglacial lakes is around 50% lower than that of snow-covered and bare ice leading to intensified melting and a further growth of supraglacial meltwater features (Malinka et al., 2018; Stokes et al., 2019; Tedesco, 2015).

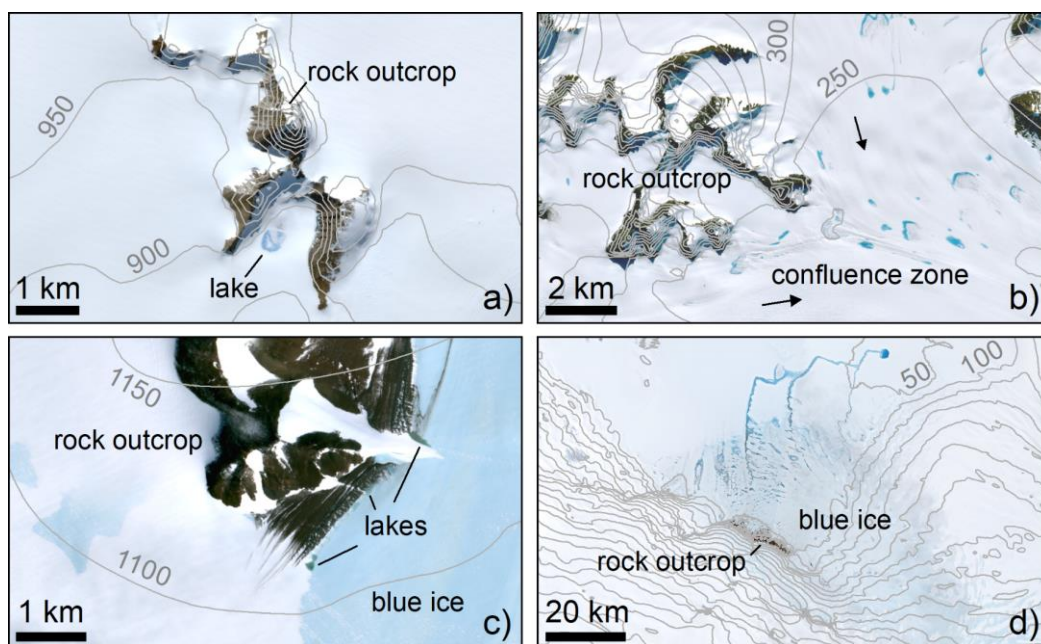


**Figure 3.2.** Supraglacial lake formation near rock outcrop and blue ice on (a) 19 January 2020 upstream of George VI Ice Shelf, (b) 23 January 2021 near Wilkins Ice Shelf, (c) 2 January 2019 upstream of Amery Ice Shelf and (d) 21 January 2019 around Nivlisen Ice Shelf. The black arrows in (b) indicate the direction of ice flow. The grey contour lines in (a-d) show the elevation in meters. Data: (Copernicus Sentinel-2 data; Howat et al., 2019).

### 3.1.2 Regional Controls

Regional controls on supraglacial meltwater ponding result from the near-surface climate including the amount of incoming solar radiation, air temperature, wind and precipitation conditions. To start with, the amount of incoming shortwave radiation has important implications on lake ponding providing the necessary energy required for melt

(Leppäranta et al., 2016, 2013; Rowley et al., 2020). As mentioned, this particularly applies to regions where melt-albedo feedbacks promote supraglacial lake formation through an enhanced absorption of solar radiation (Bell et al., 2018; Lenaerts et al., 2017). Moreover, the availability of solar radiation was stated to play an important role during foehn-induced melt on the south-western API (Laffin et al., 2021).

In agreement with seasonal increases of incoming solar radiation, air temperature is suggested to be a first-order control on supraglacial lake formation during summer (Banwell et al., 2021; Bevan et al., 2020; Dell et al., 2020; Langley et al., 2016). Summer surface melting and ponding primarily occurs on low-lying ice shelves around the margin of Antarctica, where air temperatures are higher (Stokes et al., 2019). Depending on the geographical location and temperature conditions, supraglacial meltwater features may yet persist into Antarctic winter (Kuipers Munneke et al., 2018).

Furthermore, changes in air temperature and surface melting are directly linked to regional wind conditions. For example, episodic foehn wind occurrence was shown to drive increased air temperatures and melting on the API (Datta et al., 2019; Laffin et al., 2021; Luckman et al., 2014; Turton et al., 2020) and adiabatically warmed katabatic winds were revealed to drive meltwater ponding across the grounding zones of several EAIS ice shelves (Arthur et al., 2020b; Kingslake et al., 2017; Lenaerts et al., 2017). Due to their high wind speeds particularly near rock outcrop, katabatic winds lead to wind scouring and blue ice exposure that can further promote melt-albedo feedbacks (Das et al., 2013; Kingslake et al., 2017; Lenaerts et al., 2017; Stokes et al., 2019).

As mentioned in Chapter 3.1.1, regional precipitation conditions determine the FAC and can be another important control on supraglacial meltwater ponding (Arthur et al., 2020a; Lenaerts et al., 2017; Stokes et al., 2019). High snow accumulation and FAC can be found in coastal regions near the ice front enabling the percolation of meltwater into the firn and hindering meltwater ponding on the surface (Arthur et al., 2020a; Kuipers Munneke et al., 2014; Lenaerts et al., 2017; Stokes et al., 2019). In contrast, reduced snowfall leads to firn densification and is suggested to promote meltwater ponding near ice shelf grounding zones (Arthur et al., 2020b; Bell et al., 2018; Leeson et al., 2020).

### **3.1.3 Large-Scale Controls**

Large-scale controls on Antarctic supraglacial lakes include SH atmospheric modes and teleconnections with the tropics. Over recent decades, the leading mode of SH atmospheric circulation variability (SAM) shifted towards more positive values causing regional atmospheric warming and enhanced melting on the API (Chapter 2.2.1) (Bell et al., 2018; Marshall, 2003; Marshall et al., 2017; Thompson et al., 2011; Turner et al., 2006). For example, SAM-induced atmospheric warming is suggested to be linked to enhanced surface ponding preceding recent ice shelf disintegration events on the north-

east API (Kwok and Comiso, 2002; Scambos et al., 2003; Vaughan and Doake, 1996). At the same time, positive SAM years can have opposite climate effects on air temperature and melt over East Antarctica (Abram et al., 2014; Kwok and Comiso, 2002). Further, teleconnections between the tropics and high latitudes can influence Antarctic surface melt (Bell et al., 2018; Nicolas et al., 2017; Nicolas and Bromwich, 2011; Tedesco and Monaghan, 2009). For example, linkage with ENSO was shown to influence West Antarctic melt (Nicolas et al., 2017; Nicolas and Bromwich, 2011) and variations in Indian Ocean Dipole (IOD) API melt (Bevan et al., 2020).

## **3.2 Supraglacial Lake Distribution**

Around Antarctica, surface ponding is more widespread than previously assumed (Figure 3.1, Figure 3.3). In the following, supraglacial lake observations from ground-based, airborne and spaceborne mapping efforts are briefly summarized.

### **3.2.1 Antarctic Peninsula**

Due to regional atmospheric warming between 1951 and 2000 (Turner et al., 2005), supraglacial meltwater features were numerous over multiple API ice shelves and glaciers (Figure 3.3). On the north-east API, most research focused on the area around the Larsen ice shelves where supraglacial lake formation had partly catastrophic effects on ice shelf stability and dynamics (see Chapter 3.3) (Banwell et al., 2014, 2013; Leeson et al., 2020; Rott et al., 2018; Scambos et al., 2003). For example, supraglacial lakes have been observed on the surface of Prince Gustav and Larsen A ice shelves preceding their collapse in 1995 (Glasser et al., 2011; Rott et al., 1996; Scambos et al., 2003). Likewise, surface ponding was extensive on Larsen B Ice Shelf in the decades preceding its collapse in 2002 with a continuous southward migration of lakes between 1979 and 2002 (Banwell et al., 2014; Glasser and Scambos, 2008; Leeson et al., 2020). A more recent study by Tuckett et al. (2019) also documented supraglacial lake occurrence over tributaries of the former Larsen A and Larsen B ice shelves during 2014-2016. Supraglacial meltwater features on Larsen C Ice Shelf were repeatedly documented in several inlets close to the grounding line (Bell et al., 2018; Holland et al., 2011; Hubbard et al., 2016; Kuipers Munneke et al., 2018; Luckman et al., 2014). Further south, lakes have been sporadically observed on the former Wordie Ice Shelf in Marguerite Bay (Doake and Vaughan, 1991) as well as over George VI and Wilkins ice shelves in the Bellingshausen Sea sector (Banwell et al., 2021; Bell et al., 2018; Braun and Humbert, 2009; Kingslake et al., 2017; LaBarbera and MacAyeal, 2011; Lucchitta and Rosanova, 1998; Reynolds, 1981; Scambos et al., 2009, 2003; Vaughan et al., 1993). Over some API ice shelves, including George VI and Larsen A, surface drainage across the ice shelves has been observed (Kingslake et al., 2017; Rott et al., 1996).



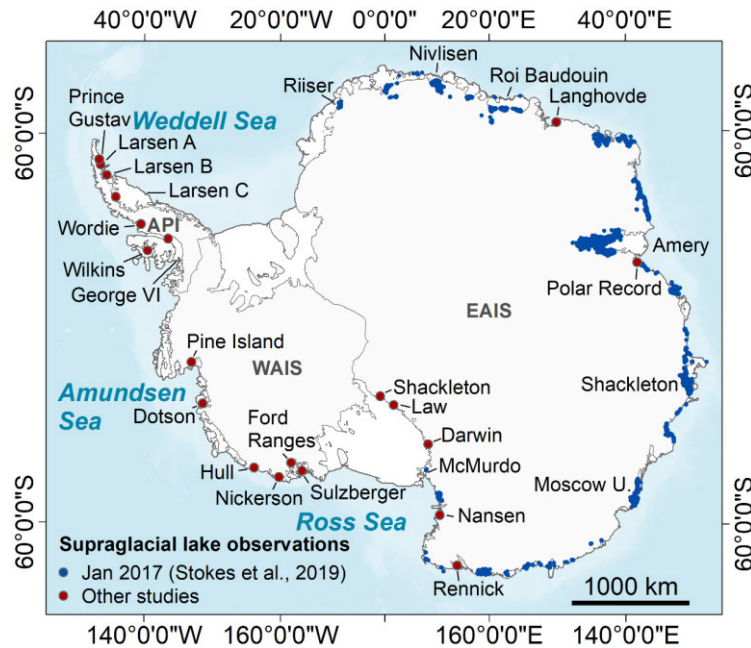


**Figure 3.3.** Geospatial distribution of Antarctic supraglacial lake observations. The point layer (blue) shows supraglacial lakes across East Antarctica during January 2017 (Stokes et al., 2019). Additional sightings of supraglacial lakes are marked in red. API: Antarctic Peninsula. WAIS: West Antarctic Ice Sheet. EAIS: East Antarctic Ice Sheet. Data: (IMBIE, 2016; Morlighem, 2020; Morlighem et al., 2020; Mouginit et al., 2017b; Rignot et al., 2013; Stokes et al., 2019).

### 3.2.2 East Antarctica

Around East Antarctica, supraglacial lakes have been observed on several glaciers and ice shelves around the periphery of the ice sheet. These include observations over Riiser-Larsen, Nivlisen, Roi Baudouin, Amery, Shackleton, Moscow University, Nansen and McMurdo ice shelves as well as over Langhovde, Polar Record, Rennick, Darwin, Law and Shackleton glaciers (Figure 3.3) (e.g. Arthur et al., 2020b; Banwell et al., 2019; Bell et al., 2018, 2017; Dell et al., 2020; Kingslake et al., 2015; Langley et al., 2016; Lenaerts et al., 2017; Liang et al., 2019; Moussavi et al., 2020; Phillips, 1998; Spergel et al., 2021; Winther et al., 1996; Zheng and Zhou, 2019). Meltwater streams terminating as waterfalls at the calving front have been observed on Nansen Ice Shelf only but may have important implications for future ice shelf stability through meltwater export to the ocean (Bell et al., 2017). The first large-scale assessment of East Antarctic supraglacial lakes was performed only recently revealing widespread EAIS surface ponding since at least 1947 as far south as 85°S and at elevations up to 1,300 m (Kingslake et al., 2017). Similarly, a recent study by Stokes et al. (2019) documented >65,000 supraglacial lakes around the margin of East Antarctica during January 2017 (Figure 3.3).

### 3.2.3 West Antarctica

Observations on West Antarctic surface hydrological features are so far scarce. Yet, Kingslake et al. (2017) report of isolated supraglacial lake occurrence on Pine Island Ice

Shelf as well as in the Ford Ranges near Ross Ice Shelf (Figure 3.3). Furthermore, Arthur et al. (2020a) report of sporadic supraglacial meltwater features on Sulzberger, Nickerson and Dotson ice shelves as well as on Hull Glacier. Supraglacial lakes on the WAIS are generally smaller than lakes on the EAIS and API.

### 3.3 Supraglacial Lake Impacts on Ice Dynamics

As mentioned in Chapter 1.1, surface ponding may impact Antarctic ice dynamics and mass balance through four main processes. To start with, direct surface runoff (Figure 3.4a) can lead to accelerated ice thinning and a negative SMB (Bell et al., 2018; Enderlin et al., 2014; The IMBIE Team, 2020). Around Antarctica, surface runoff mainly affects peripheral ice shelves due to the higher abundance of melt around the margin of the ice sheet (Kingslake et al., 2017). However, Antarctic surface melt is currently low resulting in a negligible contribution of ice thinning to overall Antarctic ice mass loss (Bell et al., 2018). This stands in contrast to Greenland, where surface runoff accounts for ~50% of all ice mass loss (Khan et al., 2015; The IMBIE Team, 2020).

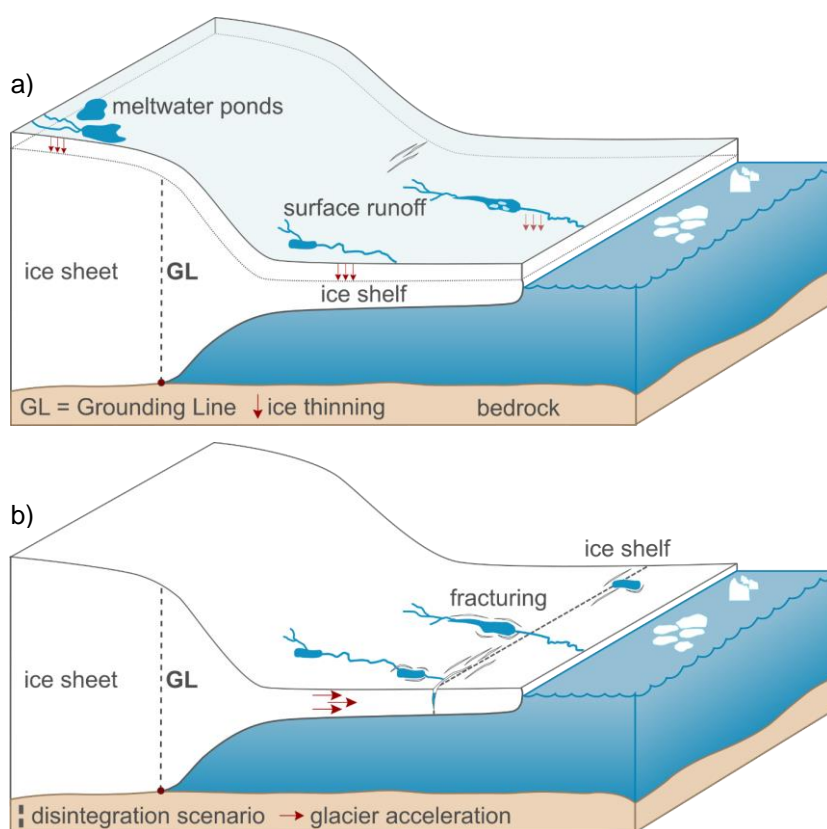


**Figure 3.4.** Supraglacial lake impacts on ice sheet dynamics. (a) Direct surface runoff leading to ice thinning. (b) Meltwater-induced fracturing leading to ice shelf collapse. (c) Basal injection of meltwater causing glacier acceleration and frontal melting. (d) Modified ice surface albedo initiating melt-albedo feedbacks and accelerated melting and thinning. GL: Grounding Line.

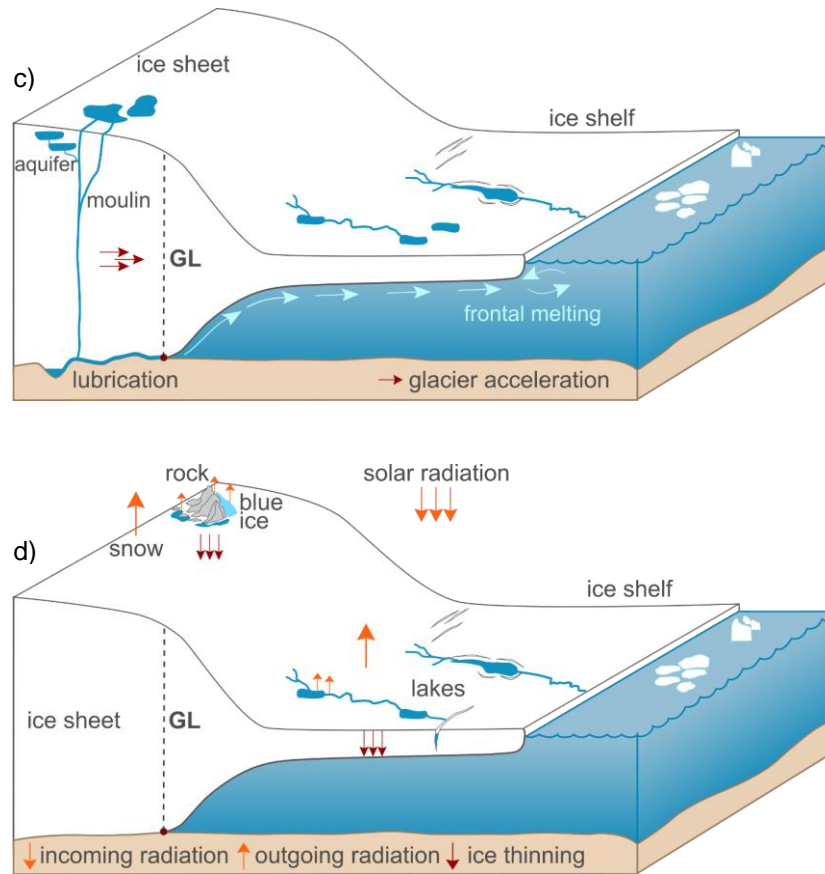


**Figure 3.4.** Continuation.

A more dramatic consequence of present-day Antarctic surface hydrology are supraglacial lakes causing ice shelf collapse through hydrofracturing, as observed along the API (Figure 3.4b) (Glasser et al., 2011; Leeson et al., 2020; Rott et al., 1996; Scambos et al., 2009). Hydrofracture results from the englacial drainage and penetration of meltwater through ice shelves via fractures that either arise due to the downward propagation of surface meltwater or the repeated infill and drainage of lakes (Banwell et al., 2013; Banwell and Macayeal, 2015; Bell et al., 2018; Braun et al., 2009; Glasser and Scambos, 2008; Langley et al., 2016; Lenaerts et al., 2017; Luckman et al., 2014; MacAyeal and Sergienko, 2013; Scambos et al., 2009). In this context, the repeated filling of lakes on ice shelves results in increased gravitational loading, while lake drainage causes the hydrostatic rebound of the ice shelf (Banwell et al., 2013; Banwell and Macayeal, 2015). In consequence, the ice shelf bends and flexes triggering radial and ring fracturing around supraglacial lakes (Figure 3.4b) (Banwell et al., 2019; Banwell and Macayeal, 2015; Bell et al., 2018; Langley et al., 2016; Scambos et al., 2009). Depending on the spatial density of water-filled fractures and whether they intersect with lakes, a chain reaction of lake drainage is triggered causing the ice shelf to fragment and collapse (Banwell et al., 2013; Bell et al., 2018; LaBarbera and MacAyeal, 2011). This process is suggested to have occurred preceding the collapse of Larsen B in 2002, where the near-synchronous drainage of >2,000 lakes has been associated with fracture

propagation and ice shelf fragmentation (Banwell et al., 2013; Glasser and Scambos, 2008; Scambos et al., 2003). The occurrence of such drainage events yet depends on the local glaciological setting of an ice shelf. For example, the compressive flow regime over George VI Ice Shelf (Hambrey et al., 2015; Holt et al., 2013; Reynolds and Hambrey, 1988) currently hinders fracturing despite the widespread abundance of lakes each year (Banwell et al., 2021; LaBarbera and MacAyeal, 2011; Reynolds, 1981). The dominant impact of meltwater-induced ice shelf collapse on Antarctic ice dynamics results from a reduction in ice shelf buttressing initiating glacier acceleration and enhanced ice discharge (Rignot et al., 2004; Rott et al., 2018, 2002; Scambos et al., 2004; Seehaus et al., 2018; Shen et al., 2018; Vaughan and Doake, 1996; Wuite et al., 2015). Changes in glacier dynamics due to ice shelf collapse can persist over multiple years. Over tributaries of the former Prince-Gustav-Channel and Larsen ice shelves on the northern API, ice flow velocities were still considerably higher in 2014-2016 than in pre-collapse conditions (Figure 3.5) (e.g. Gardner et al., 2018; Rott et al., 2018; Seehaus et al., 2018; Shen et al., 2018). Apart from surface lakes, englacial meltwater drainage can originate from buried lakes and firn aquifers even though knowledge on the distribution of Antarctic firn aquifers and buried lakes is so far scarce (Dunmire et al., 2020; Hubbard et al., 2016; Lenaerts et al., 2017; Liston et al., 1999; MacDonell et al., 2020; Montgomery et al., 2020) and mostly results from modelling studies (van Wessem et al., 2021, 2016).

Similarly, the temporary injection of meltwater to the glacier bed results from the percolation of surface or subsurface meltwater into fractures and crevasses on grounded ice and their subsequent penetration through the entire ice sheet thickness (Figure 3.4c) (Bell et al., 2018; Poinar et al., 2017; Willis et al., 2015). Additionally, meltwater can be delivered to the glacier bed via moulins (Smith et al., 2015). Meltwater that reaches the base of a grounded glacier can affect ice dynamics through frontal ocean melting (Bell et al., 2018) or basal lubrication encouraging basal sliding through a reduction in basal shear stress (Figure 3.4c) (Siegert et al., 2018). The latter is a known driver for transient ice flow accelerations and increased ice discharge over the Greenland Ice Sheet (Bartholomew et al., 2010; Bell et al., 2018; Das et al., 2008; Hoffman et al., 2011; Schoof, 2010; Tedesco et al., 2013), while Antarctic ice flow change due to a connection of the surface and basal hydrological networks was reported for isolated glaciers on the north-east API only (Tuckett et al., 2019). Here, meltwater penetration to the glacier bed led to short-lived ice flow accelerations up to 100% greater than the annual mean (Tuckett et al., 2019). With accelerated global warming and Antarctic surface melting expected to double until 2050 (Trusel et al., 2015), the Antarctic surface and basal hydrology may further connect and contribute to future enhanced ice mass loss (Bell et al., 2018). This may also arise due to meltwater delivery to the basal hydrological environment leading to growing subglacial hydrological features and the consequent

redistribution of basal meltwater to influence Antarctic ice dynamics. For example, subglacial meltwater is a known factor controlling the ice flow of the Ross and Filchner-Ronne ice streams (Bell et al., 2007; Carter et al., 2013; Siegert et al., 2016; Stearns et al., 2005). Here, processes such as the emergence of sticky spots (i.e. localized regions of higher basal friction and traction) in the confluence zone of the Ross ice streams, subglacial water transport along their shear margins as well as basal meltwater depletion were associated with ice dynamic change (Hulbe et al., 2016, 2013; Joughin et al., 2005, 2002; Stearns et al., 2005). Moreover, drainage of active subglacial lakes can initiate transient ice flow accelerations, as observed below Byrd (Stearns et al., 2008) and Cook glaciers, EAIS (Miles et al., 2018).

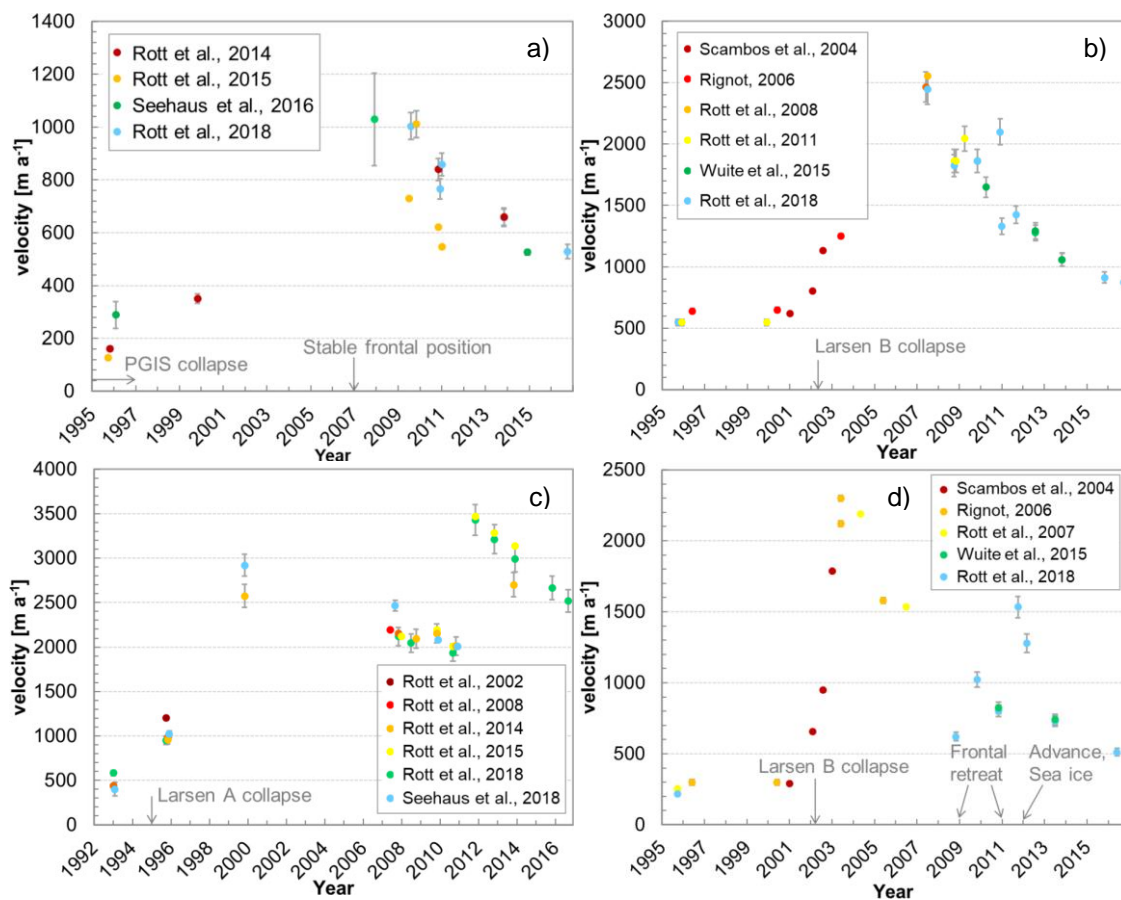


**Figure 3.5.** Temporal trends of central calving front velocity over tributaries of former ice shelves including (a) Sjögren, (b) Crane, (c) Drygalski and (d) Hektor Glacier. PGIS: Prince-Gustav-Channel Ice Shelf. Modified after Dirscherl et al. (2020a).

Furthermore, an increasing presence of surface hydrological features leads to a modified ice surface albedo causing positive melt-albedo feedbacks through an enhanced absorption of incoming solar radiation (Figure 3.4d) (Bell et al., 2018; Lenaerts et al., 2017; Lüthje et al., 2006). On the one hand, the low albedo of surface lakes can lead to enhanced lake bottom ablation and the warming of the adjacent ice column

causing a deepening (Bell et al., 2018; Tedesco et al., 2012) and growth of supraglacial lakes (Arthur et al., 2020a; Lenaerts et al., 2017). On the other hand, an overall reduced ice surface albedo leads to intensified melting across the whole ice sheet which further promotes ice thinning and runoff. In this regard, ice thinning leads to a further exposure of rock triggering additional surface melting due to its low albedo (Kingslake et al., 2017; Stokes et al., 2019). Apart from elevated melt, the higher abundance of rock outcrop also causes locally increased wind speeds leading to snow removal by wind erosion and the expansion of low-albedo blue ice areas (Das et al., 2013; Kingslake et al., 2017; Lenaerts et al., 2017; Winther et al., 1996). These can trigger further melting and ice thinning, thus rock outcrop to expand initiating a continuous coupling between melting, ice thinning, rock exposure and blue ice formation (Kingslake et al., 2017). In consequence, already existing drainage systems are enlarged and can contribute to meltwater delivery to ice shelves that are vulnerable to collapse. Ice shelf collapse then leads to glacier acceleration and upstream ice thinning initiating further melt-albedo feedbacks (Kingslake et al., 2017). Even though future increased precipitation conditions due to the enhanced moisture holding capacity of warmer air may partly compensate this (Bell et al., 2018; Bengtsson et al., 2011; Krinner et al., 2007; Lenaerts et al., 2016), melt-albedo feedbacks will play a crucial role for future ice shelf and ice sheet stability.

### 3.4 Summary

In this chapter, the state-of-the-art of Antarctic surface hydrology, including known controls on Antarctic supraglacial lake formation as well as their distribution and potential impacts on ice dynamics, was summarized. To start with, the predominant control mechanisms on Antarctic supraglacial lake formation were found to be the local setting, the regional near-surface climate and large-scale atmospheric circulation patterns. Moreover, the literature review revealed that Antarctic supraglacial lakes are numerous over the API and EAIS and scarce over the WAIS. Potential impacts of Antarctic supraglacial lakes on ice dynamics were shown to result from direct surface runoff, a changing albedo, basal meltwater injection and hydrofracture.

At the same time, current knowledge on Antarctic supraglacial lakes mostly results from theoretical considerations, e.g. in comparison to knowledge from the Greenland Ice Sheet, or from individual observations over selected ice shelves only. This highlights the need for more sophisticated research on Antarctic supraglacial lakes including detailed analyses on predominant control mechanisms driving lake formation and evolution as well as on potential impacts on Antarctic ice dynamics. For this purpose, the spatio-temporal distribution of supraglacial lakes is required to be investigated in more detail.



## CHAPTER 4

### **4 A Review on Spaceborne Remote Sensing of Antarctic Supraglacial Lake Extents \***

This chapter summarizes recent developments and advancements of spaceborne remote sensing for Antarctic supraglacial lake classification (Chapter 4.1). In addition, potentials and challenges of earth observation for Antarctic supraglacial lake extent delineation are introduced (Chapter 4.2) and future requirements are discussed (Chapter 4.3). As part of Chapter 4.1, a systematic literature review on the state-of-the-art of existing studies on spaceborne remote sensing of Antarctic supraglacial lakes was performed on the basis of all available publications (n=43) between January 1980 and June 2021. For this purpose, studies were investigated for applied satellite sensors and mapping techniques (Chapter 4.1.1, Chapter 4.1.2) as well as their geospatial coverage and temporal resolution (Chapter 4.1.3, Chapter 4.1.4). For an improved evaluation of studies investigating the influence of meltwater ponding on Antarctic ice dynamics, a second review was performed on the basis of 201 publications within the period 1984-2018. The results of Chapter 4.1 and Chapter 4.2 form the basis for the identification of future requirements in Chapter 4.3. Finally, Chapter 4.4 summarizes the entire chapter.

#### **4.1 Results of the Literature Review on Spaceborne Remote Sensing of Antarctic Supraglacial Lakes**

With accelerating global climate change, the monitoring of Antarctic ice dynamics received an ever-increasing attention. Historical measurements of the Antarctic Ice Sheet were performed with ground-based measurement devices such as theodolites or Global Positioning System (GPS) receivers (Bindschadler et al., 2003; Whillans and Van Der Veen, 1993). However, due to the remote geographical location, harsh environment and vast size of Antarctica, ground-based mapping efforts are difficult to perform and time-consuming resulting in incomplete mapping records (Joughin et al., 2010; Rignot et al., 2011). In the advent of spaceborne remote sensing, the monitoring of the Antarctic Ice Sheet was revolutionized allowing for detailed mapping efforts at unprecedented

---

\*Parts of this chapter are based on Dirscherl et al. (2020a) and Dirscherl et al. (2021a).

spatial coverage. Apart from the mapping of Antarctic surface features, including supraglacial lakes (Kingslake et al., 2017; Stokes et al., 2019), blue ice (Hui et al., 2014; Rivera et al., 2014; Winther et al., 2001), rifts and crevasses (Marsh et al., 2021; Rivera et al., 2014) or rock outcrop (Kang et al., 2018), measurements with optical, SAR and Light Detection and Ranging satellite sensors enabled the monitoring of ice sheet elevation (Seehaus et al., 2015; Shepherd et al., 2019), ice motion (Mouginot et al., 2017a; Rignot et al., 2011), sea ice and iceberg conditions (Fraser et al., 2020; Zibordi and Van Woert, 1993) as well as of grounding line (Fricker et al., 2009; Friedl et al., 2020) and calving front dynamics (Baumhoer et al., 2019) (see Figure 4.1).

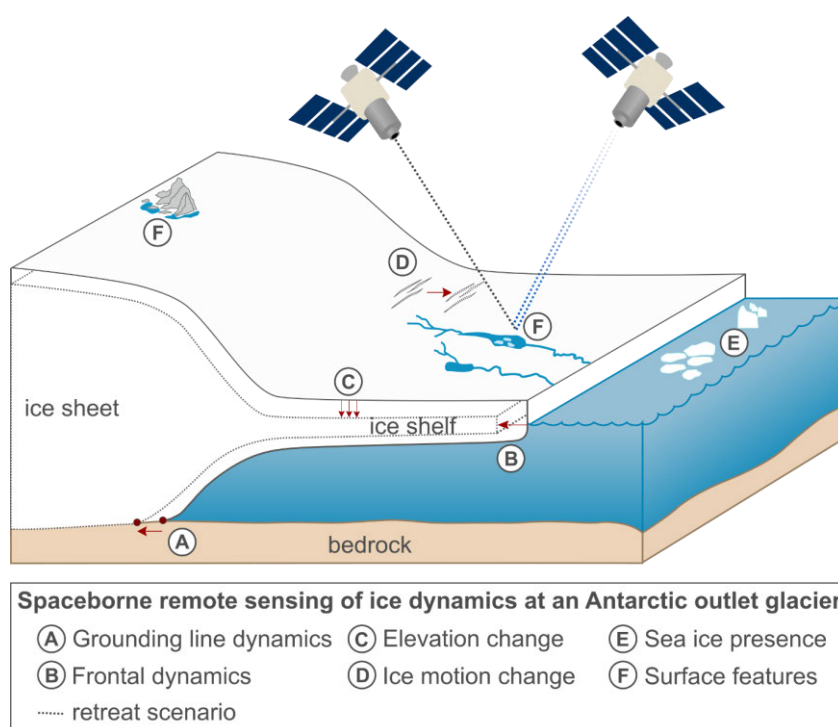


**Figure 4.1.** Potentials of EO for the monitoring of Antarctic ice sheet dynamics.

#### 4.1.1 Applied Satellite Sensors

The history of spaceborne observations of Antarctic supraglacial lakes dates back to the 1970s and 1980s, when the launch of the Landsat satellites led to an increase of studies using optical remote sensing data (Figure 4.2a). Early studies on Antarctic supraglacial lakes in the 1980s and 1990s were performed only sporadically with most studies relying on the use of publicly available optical satellite data from Landsat 1-5. During the 1990s, also the use of SAR data, e.g. from the European Remote Sensing Satellites (ERS-1/-2), became more popular. In the following decades, studies greatly increased peaking in the 2010s as well as in 2020. These peaks were related to the recent launches of the Landsat 8 and Sentinel-1/-2 satellite missions in 2013 and 2014-2017, respectively, but also to the increasing awareness for potential supraglacial lake impacts on ice shelf stability following the collapse of several Antarctic ice shelves in the



1990s and 2000s (Figure 4.2a-b). In detail, the highest number of studies was found for years 2019 and 2020, where multiple algorithms for large-scale derivation of lake extents and volumes in optical imagery were tested (Halberstadt et al., 2020; Moussavi et al., 2020) and where the first large-scale assessment of East Antarctic supraglacial lakes during January 2017 was performed on the basis of optical Landsat 8 and Sentinel-2 data (Stokes et al., 2019). Over the full investigation period 1980 to 2021, ~77% of all studies used optical satellite data for evaluation of Antarctic supraglacial lakes, while only 11% of all studies were SAR-based. At the same time, ~12% of all studies employed a combination of optical and SAR data (Figure 4.2a).

Figure 4.3 presents a more detailed analysis of used sensor types as well as the frequency of use of data from specific satellite missions during the investigation period 1980-2021. In agreement with the predominant use of optical satellite data (~89%), the most commonly used sensors for Antarctic supraglacial lake extent mapping were from the optical Landsat satellite mission. With their launches in 1999 and 2013 (see Figure 4.2a), data from Landsat 7 and Landsat 8 were most frequently used. Also, data from Landsat 1 as well as from Landsat 4-5 were applied in numerous studies. As mentioned, these sensors were launched in the 1970s and 1980s providing important data for historical supraglacial lake analyses. First results using Landsat data for Antarctic supraglacial lake identification were published in the late 1980s (Orheim and Lucchitta, 1987; Swithinbank, 1988), but also recent studies rely on the use Landsat 1-5 data for long-term analyses of supraglacial lake evolution (Arthur et al., 2020b; Kingslake et al., 2017; Leeson et al., 2020; Spergel et al., 2021). Despite the medium spatial resolution of Landsat data, their large scene cover is particularly useful for large-scale assessments of Antarctic supraglacial lakes. Further, data from Sentinel-2 and Aqua/Terra were frequently used. Due to their launches in 1999 and 2002 (see Figure 4.2a), the Moderate-resolution Imaging Spectroradiometer (MODIS) sensors aboard Terra and Aqua were used for assessments of past supraglacial lake evolution (e.g. Hubbard et al., 2016; Kingslake et al., 2015; Spergel et al., 2021). On the other hand, Sentinel-2 data were used for more recent investigations of Antarctic supraglacial lakes (e.g. Arthur et al., 2020b; Banwell et al., 2021; Moussavi et al., 2020; Stokes et al., 2019; Tuckett et al., 2019). All other optical sensors listed in Figure 4.3 were used <5 times each.

Data from SAR sensors were employed less frequently (~11%). The most commonly used data were from ERS-1/-2 (Figure 4.3). With their launches in the early 1990s (Figure 4.2a), ERS-1/-2 were the first operational SAR missions in space and therefore of great value for early investigations of Antarctic supraglacial lakes (Lucchitta and Rosanova, 1998; Phillips, 1998; Rott et al., 1996). Moreover, data from the Advanced Synthetic Aperture Radar (ASAR) sensor aboard the Environmental Satellite (ENVISAT) (Holland et al., 2011; Luckman et al., 2014) as well as from the recently launched Sentinel-1 satellite mission (Kuipers Munneke et al., 2018; Spergel et al., 2021) were

used in two studies each. Similarly, data from RADARSAT-1/2 and the Advanced Land Observing Satellite (ALOS) were used in one study each.

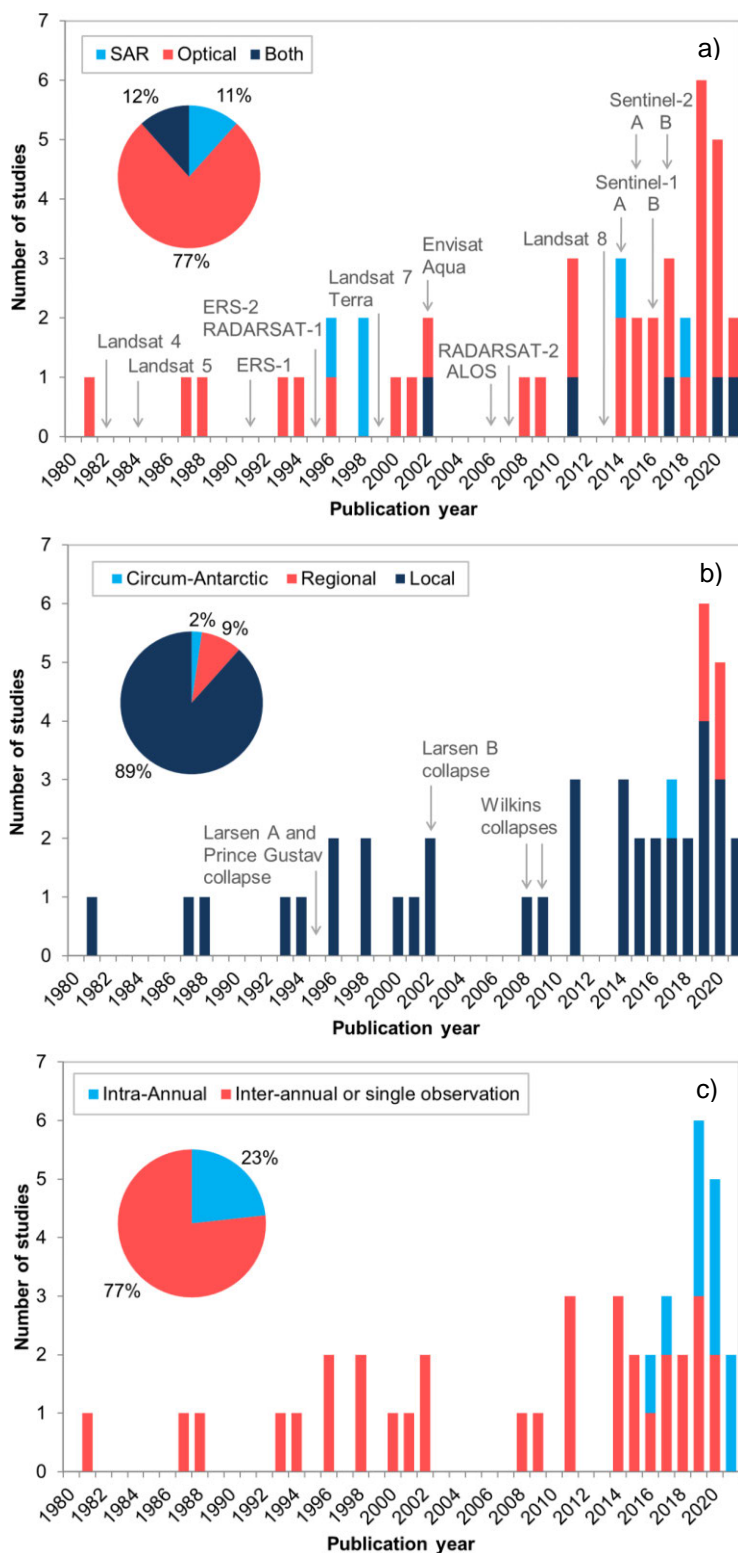


**Figure 4.2.** Temporal evolution of studies on spaceborne remote sensing of Antarctic supraglacial lakes between January 1980 and June 2021 with respect to the (a) used sensor types, (b) spatial coverage and (c) temporal resolution. The launch years of important satellite missions are marked in grey (a).

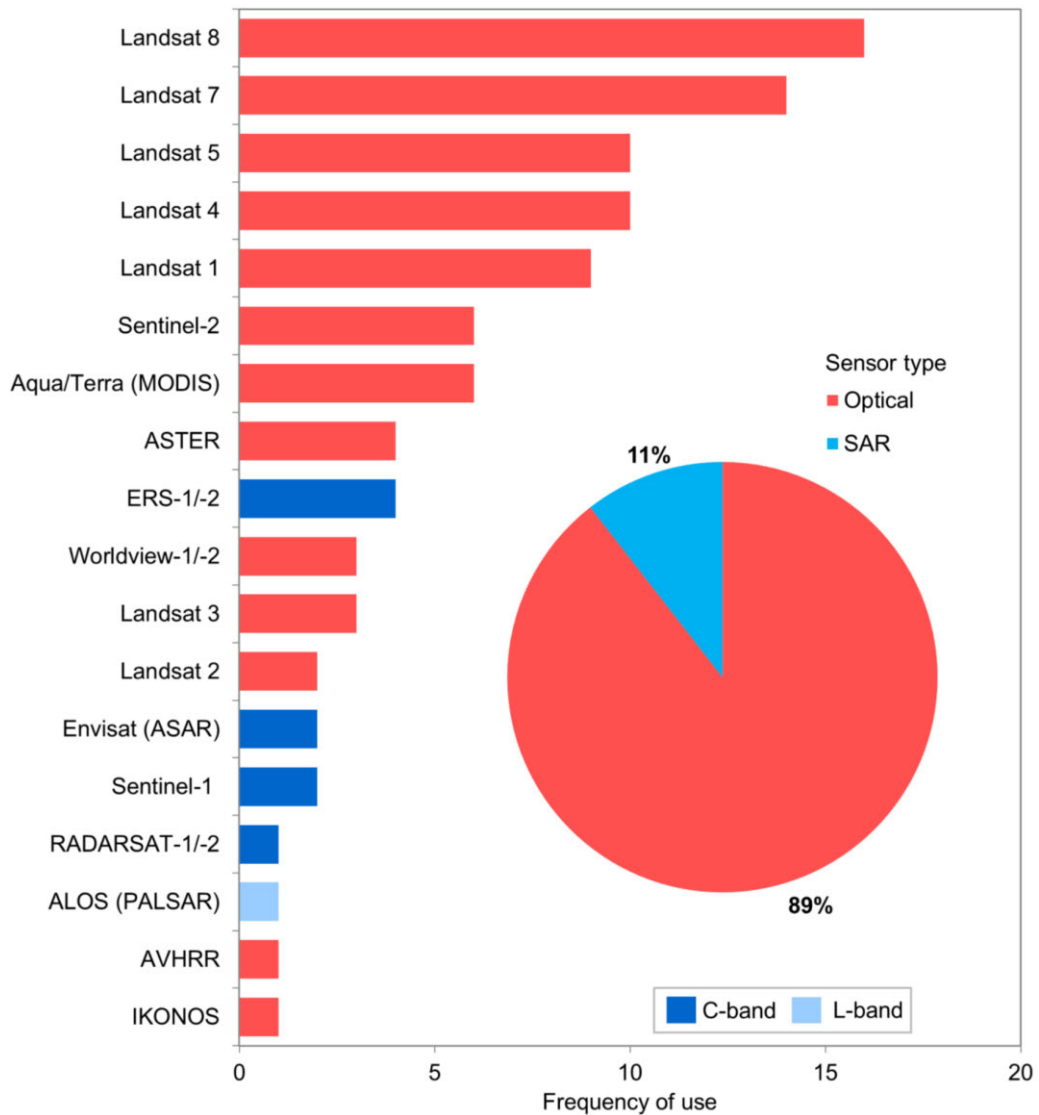


**Figure 4.3.** Distribution of used sensor types and frequency of use of data from specific satellite missions for the mapping of Antarctic supraglacial lakes in 1980-2021.

#### 4.1.2 Applied Mapping Techniques

Over the past decades, the mapping of Antarctic supraglacial lake extents in optical satellite imagery was performed through visual identification, manual delineation or semi-automated mapping techniques. Purely visual identification of lakes was mainly done in early studies on Antarctic supraglacial lake occurrence during the 1980s and 1990s, but also in more recent work (e.g. Kingslake et al., 2015; Lucchitta and Rosanova, 1998; Orheim and Lucchitta, 1987; Rott et al., 1996; Swithinbank, 1988; Tuckett et al., 2019; Winther et al., 1996). Similarly, the manual delineation of lakes in optical satellite imagery was a frequently applied method until the mid-2010s (e.g. Glasser et al., 2011; Kingslake et al., 2017; LaBarbera and MacAyeal, 2011; Langley et al., 2016; Vaughan et al., 1993). In more recent years, supraglacial lake extent mapping was performed through semi-automated Normalized Difference Water Index (NDWI) thresholding in

combination with manual post-processing (Arthur et al., 2020a; Leeson et al., 2020; Stokes et al., 2019). In particular,  $NDWI_{ice}$  represents a modified version of NDWI with enhanced water detection capabilities over glaciated regions (Yang and Smith, 2013) and was frequently applied for classification of Antarctic meltwater ponds, e.g. in Sentinel-2 or Landsat 8 imagery (Arthur et al., 2020b; Banwell et al., 2019; Bell et al., 2017; Dell et al., 2020).  $NDWI_{ice}$  is calculated as the normalized ratio of blue and red reflectance bands:

$$NDWI_{ice} = \frac{blue-red}{blue+red} \quad (1)$$

Even though no universal  $NDWI_{ice}$  threshold exists, a value of 0.25 was commonly used for pixel-based classification of deep water bodies (Bell et al., 2017; Dell et al., 2020). Likewise, values between 0.14 and 0.25 were used for medium deep water classification and values between 0.12 and 0.14 for shallow water classification and slush detection (Bell et al., 2017). Only recently, also threshold-based methods using multiple normalized difference indices, including NDWI and Normalized Difference Snow Index (NDSI), as well as selected reflectance bands were proposed for future pan-Antarctic assessments using Landsat 8 and Sentinel-2 (Moussavi et al., 2020). Moreover, Halberstadt et al. (2020) tested unsupervised k-means clustering for derivation of supraglacial lake extents in Landsat 8 imagery. Semi-automated supraglacial lake extent mapping techniques (Box and Ski, 2007; Howat et al., 2013; Miles et al., 2017; Moussavi et al., 2016) as well as adaptive thresholding were also applied for supraglacial lake extent mapping in satellite imagery over the Greenland Ice Sheet (Johansson and Brown, 2013; Liang et al., 2012; Selmes et al., 2011; Sundal et al., 2009; Williamson et al., 2017). Yet, these methods were found to be far less accurate than manual delineation techniques (Leeson et al., 2013).

Furthermore, the enhanced spatial and spectral resolution of recent optical satellite missions enables the derivation of lake depths and volumes using radiative transfer models (Arthur et al., 2020a; Moussavi et al., 2020; Pope et al., 2016; Sneed and Hamilton, 2007). These calculate lake depths and volumes based on the rate of light attenuation with depth due to absorption and scattering mechanisms (Moussavi et al., 2020). As these models underly several assumptions that are not always met in Antarctica, including the absence of wind-induced surface roughening, an accurate discrimination between ice-covered and ice-free lake areas as well as a homogeneous lake-bottom albedo (Arthur et al., 2020a; Banwell et al., 2019; Moussavi et al., 2016; Pope et al., 2016; Sneed and Hamilton, 2007), lake depths and volumes were not considered as part of this thesis and a more in-depth description of physical-based models for lake volume derivation is not provided.

On the other hand, the detection of Antarctic supraglacial lakes in SAR imagery was so far mainly visual (Fricker et al., 2002; Holland et al., 2011; Kuipers Munneke et al., 2018; Lucchitta and Rosanova, 1998; Phillips, 1998; Rott et al., 1996) or manual (Leeson et al., 2020; Lenaerts et al., 2017; Spergel et al., 2021). In addition, a recent study employed pixel-based thresholding on Envisat ASAR imagery (Luckman et al., 2014). Similar work was done for supraglacial lake extent mapping over the Greenland Ice Sheet, where a combination of optical and adaptive SAR thresholding was employed on optical Landsat 8 and Sentinel-1 SAR imagery (Miles et al., 2017). Besides, polarimetric SAR from Sentinel-1 was used for detection of perennial supraglacial lakes across the Greenland Ice Sheet (Schröder et al., 2020).

### 4.1.3 Geospatial Coverage of Studies

Studies on Antarctic supraglacial lakes were also categorized into “local”, “regional” and “circum-Antarctic” investigations. In this context, local-scale refers to investigations over a single glacier, ice shelf or drainage basin and regional-scale describes studies that stretch over multiple glaciers, ice shelves or drainage basins. Circum-Antarctic studies include drainage basins that are distributed across all three Antarctic regions.

Figure 4.2b illustrates the spatial coverage of studies on Antarctic supraglacial lakes over time. As can be seen, ~89% of all studies were local-scale investigations, while only ~9% of all studies represented regional-scale analyses. At the same time, ~2% of all investigations on Antarctic supraglacial lakes were performed at circum-Antarctic spatial scale. While local-scale investigations increased constantly over time (e.g. Bell et al., 2017; Dell et al., 2020; Fricker et al., 2002; Kingslake et al., 2015; Orheim and Lucchitta, 1987; Winther et al., 1996), the first regional-scale analyses were published in 2019 and 2020. With more detail, regional-scale analyses were mainly performed on the basis of optical Landsat 8 and Sentinel-2 data and focusing on ice shelves and drainage basins across East Antarctica (Halberstadt et al., 2020; Moussavi et al., 2020; Stokes et al., 2019) and the API (Tuckett et al., 2019). Similarly, the only circum-Antarctic supraglacial lake investigation was published in 2017 identifying meltwater drainage systems in Landsat, ASTER and WorldView satellite imagery as well as in aerial photography across multiple AIS ice shelves (Kingslake et al., 2017). Even though the investigation by Kingslake et al. (2017) primarily focused on the detection of surface meltwater features on individual ice shelves and time steps, their analysis was the first to report of Antarctic meltwater features to be more widespread than previously assumed.

Moreover, local- and regional-scale investigations were subdivided according to their spatial coverage across the three Antarctic regions. As can be seen in Figure 4.4, local-scale investigations on Antarctic supraglacial lakes focused on drainage basins on the API (~42%) and EAIS (~47%). Likewise, regional studies were conducted for glaciers,

ice shelves or drainage basins on the API (~2%) and EAIS (~7%) only. As previously mentioned, the remaining 2% of all studies covered regions on the API, WAIS and EAIS.

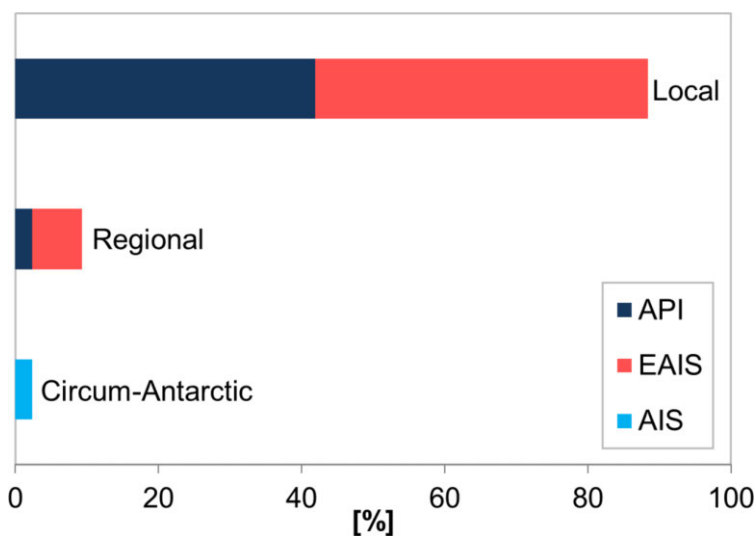


**Figure 4.4.** Spatial extent and focus regions of spaceborne investigations on Antarctic supraglacial lakes. API: Antarctic Peninsula. WAIS: West Antarctic Ice Sheet. EAIS: East Antarctic Ice Sheet. AIS: Antarctic Ice Sheet.

To provide more detail on the spatial distribution of studied drainage basins and ice shelves, geospatial heat maps were created (Figure 4.5). At this point it has to be noted, that EAIS supraglacial lakes that were detected during January 2017 by Stokes et al. (2019) (purple points in Figure 4.5) are not included in the study count. As can be seen in Figure 4.5, ice shelves on the API and EAIS were studied 21 and 24 times, respectively. At the same time, only one study investigated an ice shelf on the WAIS, where surface melt is generally less abundant. More specifically, Amery Ice Shelf on the EAIS was by far the most frequently studied ice shelf appearing in a total of seven studies. Amery is the largest East Antarctic ice shelf and was the first where supraglacial lakes were documented to be widespread (Mellor and McKinnon, 1960; Phillips, 1998; Swithinbank, 1988). Other frequently studied ice shelves include Larsen C and George VI ice shelves on the API with six and five studies each. The large interest in supraglacial lakes on George VI Ice Shelf results from the presence of an extensive surface hydrological network since at least the 1980s (Reynolds, 1981). On the other hand, Larsen C Ice Shelf was frequently studied due to the repeated presence of supraglacial lakes having important implications for future ice shelf stability (Buzzard et al., 2018a). Besides, Larsen B, Nivlisen and Roi Baudouin ice shelves appeared in four studies each and Wilkins and Shackleton ice shelves were studied three times each. Supraglacial lakes on Larsen B Ice Shelf were of particular interest due to their suggested influence on the collapse of Larsen B in 2002 (Banwell et al., 2014; Glasser and Scambos, 2008; Leeson et al., 2020; Scambos et al., 2000). On the other hand, Nivlisen, Wilkins, Shackleton and Roi Baudouin ice shelves were revealed to be covered in substantial

amounts of surface melt during summer resulting in an increased scientific interest as well as their frequent use as test regions during recent method developments using Landsat 8 and Sentinel-2 data (Arthur et al., 2020b; Dell et al., 2020; Halberstadt et al., 2020; Kingslake et al., 2017, 2015; Lenaerts et al., 2017; Moussavi et al., 2020; Stokes et al., 2019; Vaughan et al., 1993; Zheng and Zhou, 2019). Ice shelves that were studied only two times include Larsen A on the API as well as Riiser-Larsen, McMurdo and Nansen ice shelves on the EAIS. On the WAIS, Pine Island Ice Shelf was analyzed only once as part of the circum-Antarctic mapping effort by Kingslake et al. (2017).

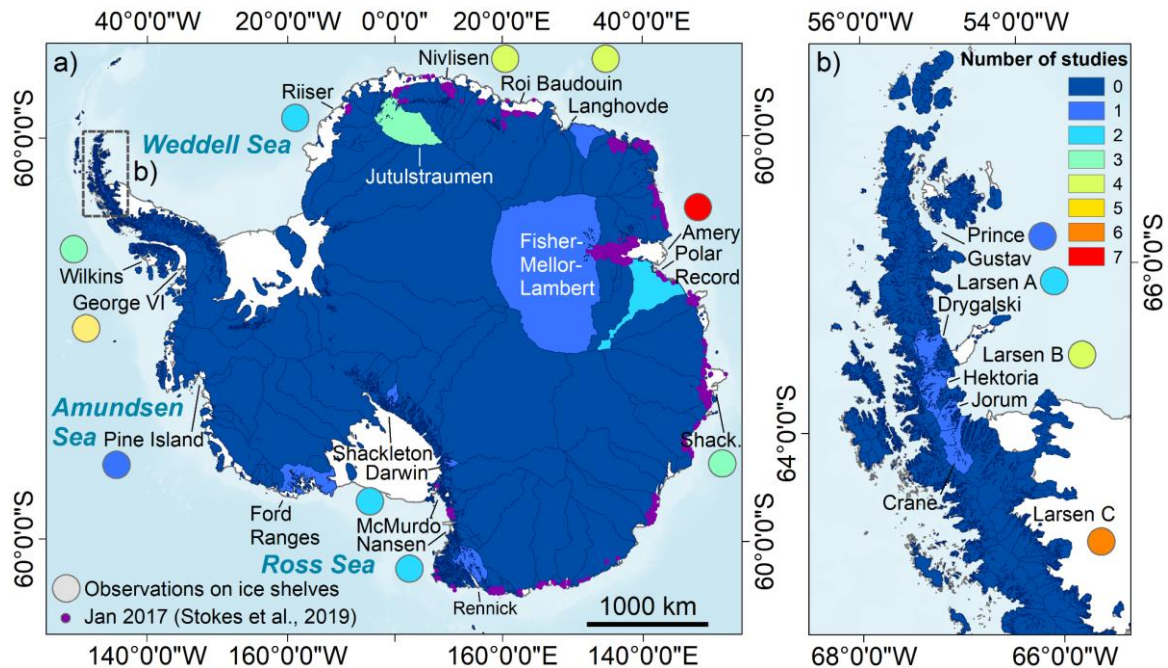


**Figure 4.5.** (a) Geospatial distribution of spaceborne studies on Antarctic supraglacial lakes over individual drainage basins and ice shelves (circles). Purple points are lakes identified by Stokes et al. (2019). (b) Magnification over the northern Antarctic Peninsula. Data: (Morlighem, 2020; Morlighem et al., 2020; SCAR, 2019).

Studies on supraglacial lake occurrence over individual drainage basins are so far scarce (Figure 4.5). The most frequently studied drainage basins include Jutulstraumen in Queen Maud Land appearing in three studies (Orheim and Lucchitta, 1987; Winther et al., 2001, 1996) as well as Polar Record Glacier near Amery Ice Shelf being studied twice (Jawak and Luis, 2014; Liang et al., 2019). Several glaciers draining into Ross Ice Shelf as well as into the embayments of the former Larsen A and Larsen B ice shelves on the API were analyzed in one study each (Kingslake et al., 2017; Tuckett et al., 2019). Further, one study analyzed seasonal supraglacial lake dynamics on Langhovde Glacier in East Antarctica (Langley et al., 2016) and one investigation dealt with lakes in the Fisher-Mellor-Lambert Glacier System feeding Amery Ice Shelf (Hambrey and Dowdeswell, 1994). Apart from supraglacial lakes identified in EAIS drainage basins as

part of the mapping campaign by Stokes et al. (2019), all other glaciers and ice shelves still lack a detailed supraglacial lake mapping record from spaceborne remote sensing.

#### **4.1.4 Temporal Resolution of Studies**

Apart from spatial characteristics of studies on Antarctic supraglacial lakes, also their temporal resolution was investigated. In detail, studies were categorized in agreement with their focus on either intra-annual or inter-annual supraglacial lake dynamics. In the following, intra-annual refers to the evolution of supraglacial lakes within an individual melting season and inter-annual refers to the consideration of supraglacial lake dynamics between years or at individual time steps only.

As shown in Figure 4.2c, ~77% of all studies on Antarctic supraglacial lakes were performed at inter-annual temporal resolution or using single satellite observations only. This particularly applies to early studies on Antarctic supraglacial lakes that primarily dealt with supraglacial lake observations at individual time steps (e.g. Fricker et al., 2002; Orheim and Lucchitta, 1987; Reynolds, 1981; Swithinbank, 1988; Vaughan et al., 1993). On the other hand, ~23% of all studies investigated seasonal characteristics of Antarctic supraglacial lakes. In particular, seasonal investigations on the evolution of Antarctic supraglacial lakes increased strongly since 2016, when the availability of spaceborne observations, e.g. from the optical Landsat 8 or Sentinel-2 satellite missions, started to improve (Arthur et al., 2020b; Banwell et al., 2021; Dell et al., 2020; Kingslake et al., 2017; Langley et al., 2016; Liang et al., 2019; Moussavi et al., 2020; Spergel et al., 2021; Tuckett et al., 2019). In fact, recent studies on Antarctic supraglacial lakes predominantly investigated intra-annual supraglacial lake extent dynamics with a total share of 50%, 60% and 100% in 2019, 2020 and 2021, respectively (Figure 4.2c). At the same time, also inter-annual or single observations of Antarctic supraglacial lakes are still of great interest for the glaciological community, e.g. for large-scale or continent-wide investigations of Antarctic supraglacial lakes (Kingslake et al., 2017; Stokes et al., 2019).

## **4.2 Potentials and Challenges of Spaceborne Remote Sensing for Antarctic Supraglacial Lake Extent Mapping**

Spaceborne remote sensing greatly supports the mapping of Antarctic supraglacial lake extents enabling the continuous monitoring of the AIS at unprecedented spatial coverage and detail. The extraction of Antarctic supraglacial lake extents from optical and SAR imagery yet requires detailed knowledge and understanding of the individual advantages and disadvantages of passive optical and active SAR sensors. Additionally, the spectral properties and backscattering characteristics of ice sheet surface features, clouds and open ocean are required to be considered. Table 4.1 summarizes the key



characteristics and limitations of recently launched optical and SAR satellite sensors with specific focus on the recently launched Sentinel-1/-2 and Landsat 8 satellite missions.

**Table 4.1.** Main characteristics of recently launched optical and SAR satellite sensors for supraglacial lake extent mapping in Antarctica. Specific focus is on the Sentinel and Landsat satellite missions. S2: Sentinel-2. L8: Landsat 8.

Properties	SAR	Optical
Spatial accuracy	Medium	High (S2, L8)
Pixel spacing $\leq 10$ m	Yes	Yes (S2)
Spatial coverage $\geq 10,000$ km <sup>2</sup>	Yes	Yes (S2, L8)
Revisit time $\leq 6$ days	Yes	Yes (S2)
Dependence on illumination	No	Yes (S2, L8)
Dependence on weather conditions	No	Yes (S2, L8)
Features that are difficult to discriminate from surface lakes	<ul style="list-style-type: none"> <li>• Slush</li> <li>• Wet snow</li> <li>• Dry snow</li> <li>• Radar shadow</li> <li>• Blue / bare ice</li> <li>• Ocean</li> </ul>	<ul style="list-style-type: none"> <li>• Slush</li> <li>• Shadow</li> <li>• Blue ice</li> <li>• Icebergs and sea ice in the ocean</li> </ul>
Other limitations	<ul style="list-style-type: none"> <li>• Seasonal changes</li> <li>• Wind roughening</li> <li>• Speckle noise</li> </ul>	<ul style="list-style-type: none"> <li>• Seasonal changes</li> </ul>

#### 4.2.1 Optical Remote Sensing

As visible in Table 4.1, the recent launch of passive optical satellite sensors such as Sentinel-2 or Landsat 8 is of great relevance for supraglacial lake extent mapping in Antarctica. The high spatial accuracy, coverage and repeat interval of these sensors allows for a detailed, large-scale monitoring of the AIS. For example, Sentinel-2 records the sunlight reflected from the earth’s surface in 13 spectral bands in the visible and infrared regions of the electromagnetic spectrum. Sentinel-2 provides data at 10 m spatial resolution covering an area of  $\sim 10,000$  km<sup>2</sup> at up to daily revisit frequencies over polar regions. Due to the open data policy of the Copernicus programme, Sentinel-2 data are free of use highlighting their value for Antarctic research. Also, data of the Landsat 8 satellite mission are relevant for supraglacial lake extent mapping. Landsat 8 OLI (Operational Land Imager) images the earth every 16 days in nine spectral bands in the visible and infrared regions. The high spatial coverage ( $\sim 33,000$  km<sup>2</sup>) and resolution (30 m) of a single Landsat 8 scene is particularly suitable for large-scale ice sheet monitoring efforts. However, passive satellite sensors depend on meteorological and illumination conditions restricting the use of Sentinel-2 or Landsat 8 data to cloud-free daytime acquisitions during Antarctic summer (Table 4.1).

For an accurate delineation of supraglacial lake extents in optical satellite imagery, the discrimination of different ice sheet surface features, clouds and open ocean is required. Figure 4.6 provides details on the reflectance and spectral albedo of snow, ice,

rock, meltwater ponds and the open ocean in the visible and near-infrared regions. As can be seen, the transition and metamorphism from fresh snow to firn and glacier ice can be easily tracked through their varying spectral reflectance at different wavelengths. Fresh snow shows highest reflectance, oftentimes similar to clouds, while progressively older granular snow shows reduced reflectance values (Dietz et al., 2012). Lowest reflectance of 10-30% can be found over polluted snow and glacier ice, rock outcrop as well as the open ocean (Figure 4.6) (Tedesco, 2015).

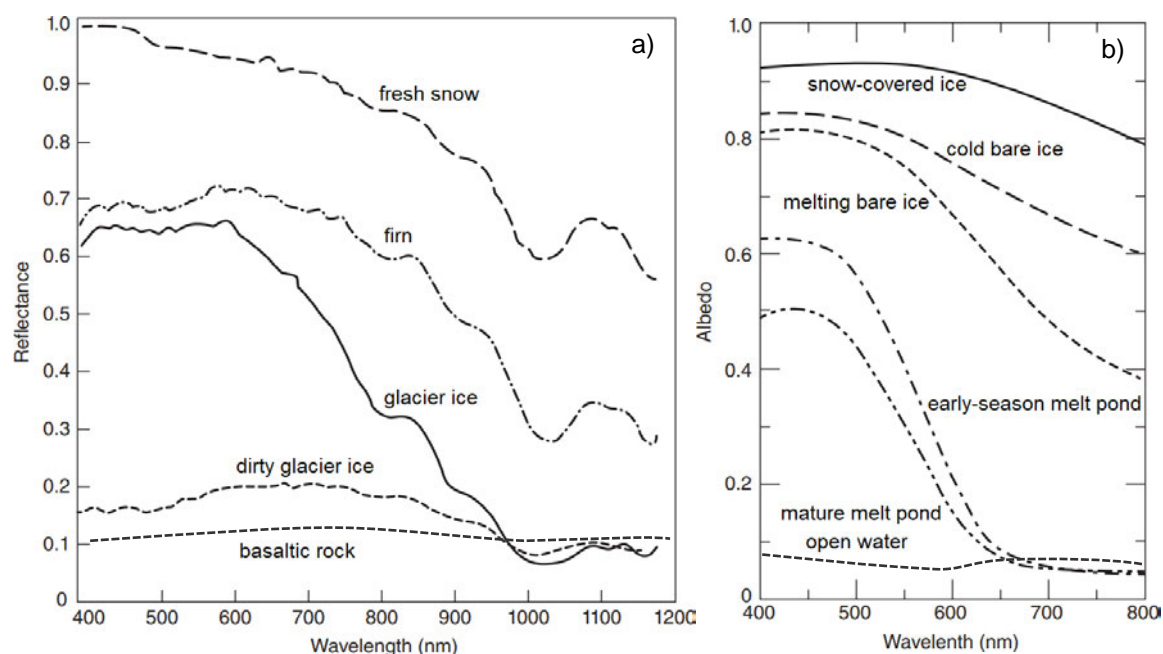


**Figure 4.6.** (a) Reflectance properties of basaltic rock and different snow and ice types. (b) Spectral albedo of different snow and ice types, open ocean and meltwater ponds. Modified after Tedesco (2015). Reprinted with permission from John Wiley and Sons and Copyright Clearance Center.

On the other hand, supraglacial lakes can be easily identified through the low albedo of surface ponds creating a sharp boundary with surrounding snow and ice of higher reflectance as well as with exposed bedrock and open ocean of considerably lower reflectance (Figure 4.6) (Tedesco, 2015). Likewise, also frozen lakes can be detected as long as the ice cover is clear and no fresh snow is overlying the ice. However, the correct discrimination between supraglacial lakes and features with similar spectral reflectance such as blue ice (Figure 4.7a,d), slush (Figure 4.7f), shadow (Figure 4.7a-c), melting sea ice (Figure 4.7d-e) or icebergs in the ocean (Figure 4.7e) represents a challenging task (Table 4.1). In particular, shadowing on snow, blue ice as well as in crevasses, rifts or at the calving front (Figure 4.7a-e) is difficult to discriminate from supraglacial meltwater in optical imagery. Similarly, partly submerged icebergs increase the spectral signature of the overlying ocean which complicates a correct differentiation from Antarctic supraglacial lakes (Figure 4.7e). Another challenge to overcome is the varying spectral signature of lakes, snow, ice and shadowing over the course of a year (Figure 4.6b)

(Dietz et al., 2012; Tedesco, 2015). For example, shallow meltwater ponds during the early melting season show a comparatively high albedo and reflectance, similar to that of blue ice or slush, while deep, late-season meltwater ponds show lower reflectance values comparable to shadow (Figure 4.6b) (Moussavi et al., 2020). In turn, the transition to refreezing lakes towards the end of a summer melting season again leads to higher reflectance values similar to blue ice or slush as long as no snow is overlying the ice.

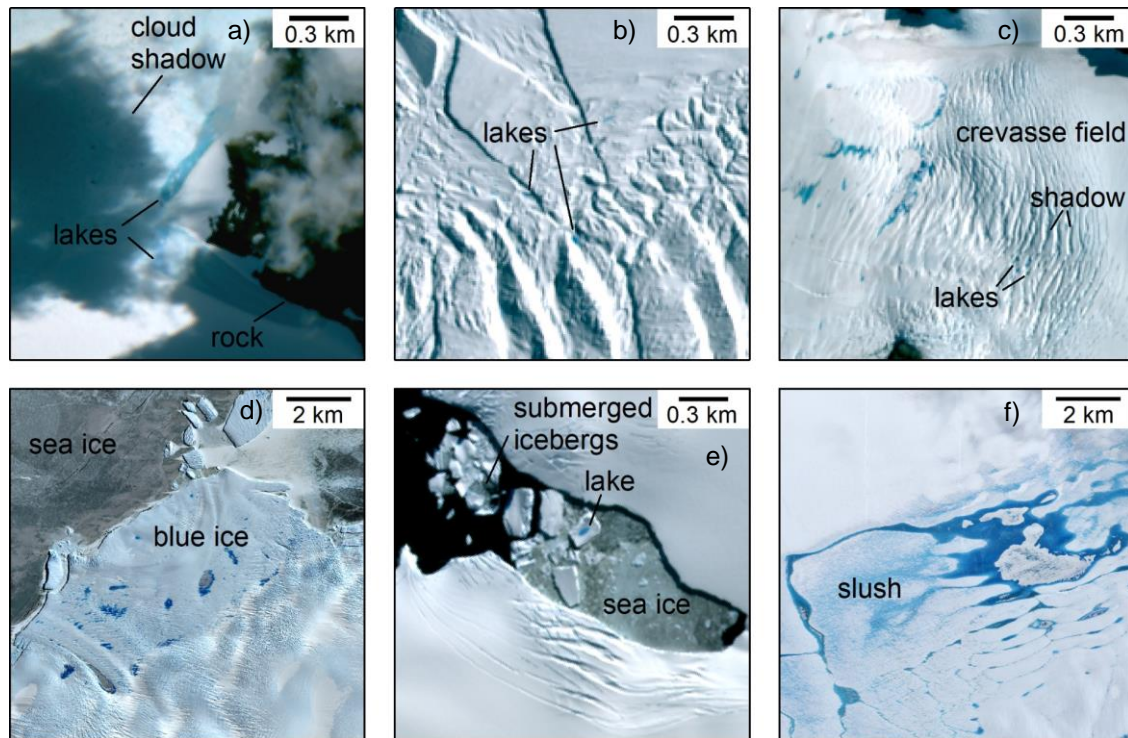


**Figure 4.7.** Appearance of Antarctic supraglacial lakes and ice sheet surface features with similar spectral reflectance in Sentinel-2 imagery. Lakes adjacent to (a) rock outcrop and cloud shadow, (b) topographic shadow on ice, (f) slush as well as within a (c) crevasse and (d) blue ice field or (e) atop and around submerged icebergs. Data: (Copernicus Sentinel-2 data).

#### 4.2.2 SAR Remote Sensing

Emitting electromagnetic signals in the microwave frequency domain, active SAR sensors are of equal importance for Antarctic supraglacial lake extent mapping. In detail, the emitted electromagnetic signal interacts with features at the earth's surface and is scattered back to the satellite antenna providing phase and amplitude information. While phase-based information describes the distance between the satellite platform and scattering object, the amplitude represents the intensity of the backscattered signal. Over polar regions, phase-based remote sensing is mostly employed for surface elevation, deformation, grounding line or ice velocity derivation through application of interferometric SAR (e.g. Fricker et al., 2009; Rack et al., 2000; Rott et al., 2018; Young and Hyland, 2002), while backscattering intensity images are commonly used for

Antarctic calving front (Baumhoer et al., 2019; Mohajerani et al., 2019; Zhang et al., 2019) or supraglacial lake extent delineation (Luckman et al., 2014; Miles et al., 2017).

One major advantage of microwave remote sensing is the independence of meteorological and illumination conditions enabling continuous data acquisition also during cloud cover and Antarctic polar night (Table 4.1). Similar as for optical sensors, SAR delivers imagery at high spatial and temporal coverage. For example, Sentinel-1 images the Earth every 6 days at a swath width and pixel spacing of 250 km and 10 m in Interferometric Wide (IW) swath mode. Even higher spatial coverage of 400 km can be achieved in Extra Wide (EW) swath mode providing data at a reduced spatial resolution of 40 m. Although Sentinel-1 has a revisit time of 6 days, the overlapping orbit tracks in high latitudes enable polar regions to be revisited up to daily. Another advantage of C-band SAR sensors such as C-SAR aboard Sentinel-1 is their increased penetration capability improving the detection of subsurface features including buried and partly frozen lakes on ice sheets.

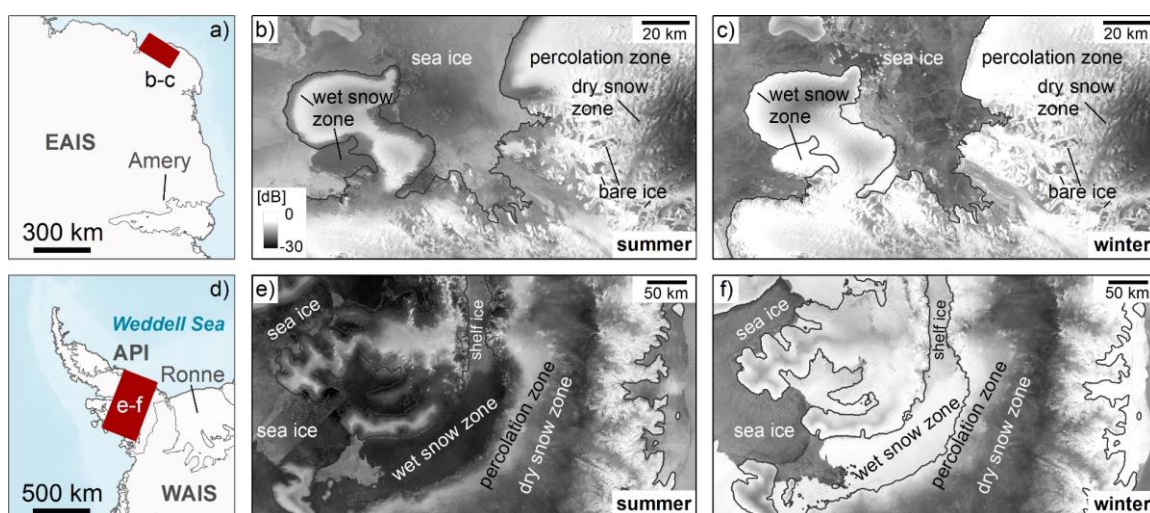


**Figure 4.8.** Radar backscattering characteristics of different radar glacier zones and sea ice in Antarctica. Overview maps (a,d) showing the locations of the mean SAR intensity images over the East Antarctic Ice Sheet (EAIS) (b-c) and the Antarctic Peninsula (API) (e-f) during austral summer (b,e) and winter (c,f). The grounding line is illustrated in grey. WAIS: West Antarctic Ice Sheet. Data: (Copernicus Sentinel-1 data; IMBIE, 2016; Morlighem, 2020; Morlighem et al., 2020; Mouginot et al., 2017b; Rignot et al., 2013).

Despite the great potentials of SAR remote sensing, the similar backscattering characteristics of ice sheet surface features make their correct discrimination difficult. This particularly applies to different snow and ice types showing varying dielectric properties throughout the year or across different glacier elevation zones, thus leading to strongly fluctuating backscattering values (Figure 4.8, Figure 4.9). In detail, high moisture contents as well as open water result in particularly low backscattering values and low moisture contents result in high backscattering intensities (Kwok et al., 1992; Mätzler,



1987; Stiles and Ulaby, 1980). In agreement with the dielectric properties of snow, the ice sheet can be divided into different radar glacier zones (see Figure 2.1). As mentioned in Chapter 2.1, the dry snow zone can be found in high altitudes where melting is absent (Figure 4.8). Here, the radar signal penetrates several meters into the snowpack resulting in volume scattering and low backscattering throughout the whole year (Figure 4.9) (Liu et al., 2006). The percolation zone is located directly below the dry snow zone returning high backscattering values due to scattering from ice pipes and lenses that form within the snowpack and firn as a result of occasional melting and refreezing during summer (Figure 2.1, Figure 4.8, Figure 4.9) (Liu et al., 2006). In the glacier zones stretching over lower altitudes, seasonal variations in surface air temperature lead to more substantial fluctuations in radar backscatter. As can be seen in Figure 4.8 and Figure 4.9, the wet snow zone undergoes substantial melting during summer leading to very low radar penetration and low backscattering values, while radar intensity during winter is usually intermediate due to reduced scattering from refrozen ice lenses within the high-density firn (Liu et al., 2006). Meltwater ponds and streams are present within the wet snow zone having very low radar backscattering values similar to that of wet snow due to the specular reflection of microwaves over smooth water (Figure 4.8, Figure 4.10e) (Bernier, 1987; Stiles and Ulaby, 1980). In the superimposed and bare ice zones, a continuous layer of ice is exposed at the surface leading to comparatively low winter backscattering values similar to that in the wet snow zone (Liu et al., 2006). During summer, the superimposed and bare ice zones generally return higher radar intensity values than the wet snow zone (Fahnestock et al., 1993).

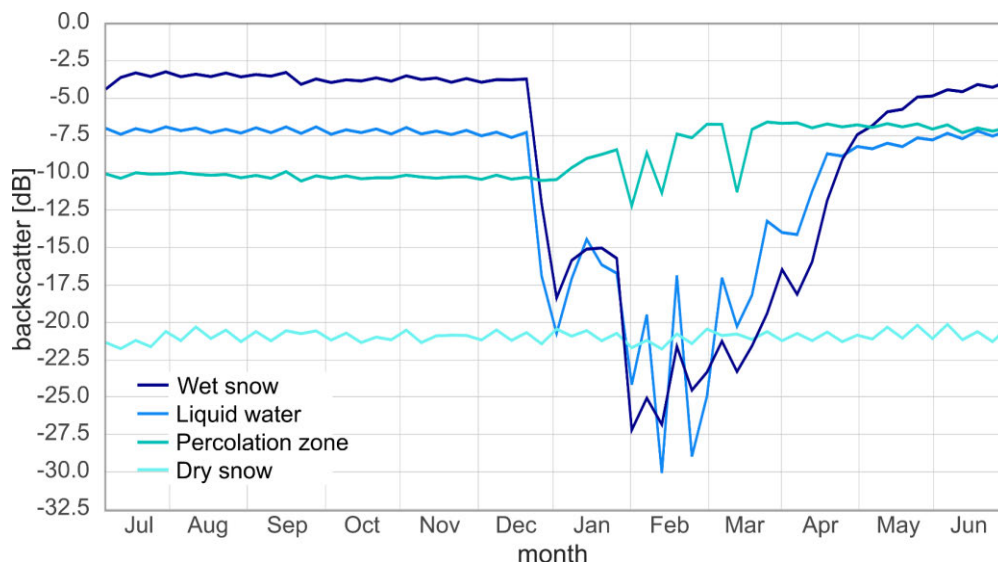


**Figure 4.9.** Exemplary backscattering signature of different snow and ice types as well as of liquid water throughout the course of a year, as extracted from single-polarized Sentinel-1 imagery over a selected test site on the Antarctic Peninsula. Data: (Copernicus Sentinel-1 data).

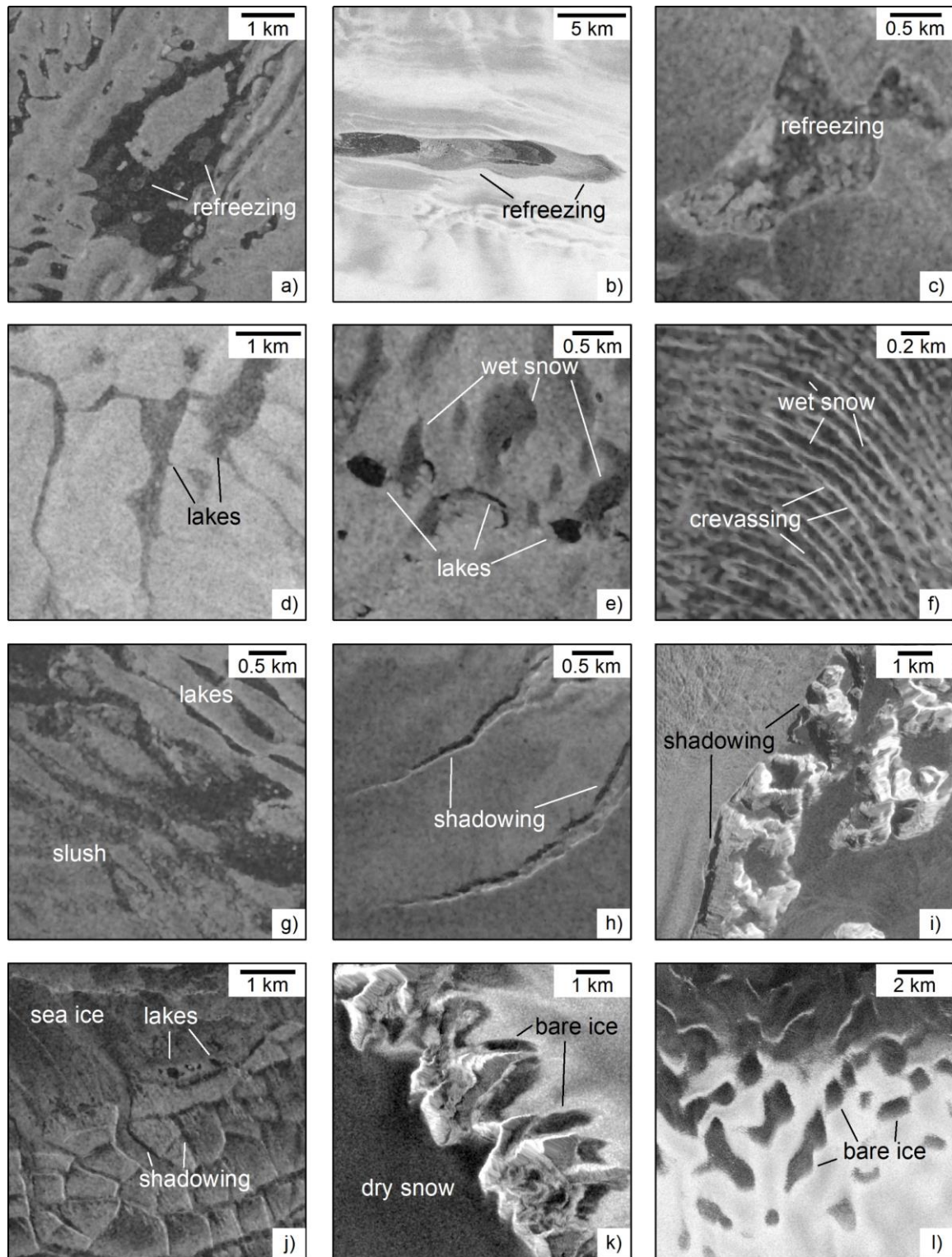
In agreement with these properties, supraglacial lakes are particularly difficult to discriminate from low backscatter wet or dry snow in SAR imagery even if temporal

image metrics are available (Figure 4.8, Figure 4.9, Figure 4.10e,f,k) (Liu and Jezek, 2004). Similarly, the low backscattering signature of open ocean or radar shadow (Figure 4.10h-j) can be a challenge for supraglacial lake identification (Liu and Jezek, 2004). Due to the frequent occurrence of wind across the Antarctic continent, also wind roughening of lake surfaces or the ocean has to be considered (Liu and Jezek, 2004). Here, diffuse radar reflection results in increased backscattering intensities than under calm weather conditions making a correct discrimination between ice and water even more difficult. In particular, wind roughened water surfaces can be easily confused with ice sheet surface features of slightly higher backscattering values such as bare ice or blue ice (Figure 4.8, Figure 4.10k,l). Furthermore, shallow slushy lakes or the strong refreezing of lakes lead to higher backscattering values and speckle noise results in inhomogeneous backscattering values (Figure 4.10a,b,c,d,g). Additionally, these properties can lead to fuzzy lake edges and low visual contrast. Finally, the seasonally varying sea ice cover or meltwater accumulation on sea ice (Figure 4.10j) complicates an accurate differentiation between land and ocean as well as between lakes on sea ice and lakes on ice shelves or the ice sheet (Figure 4.8) (Kwok et al., 1992).

### **4.2.3 Optical versus SAR**

To summarize, each sensor type has different potentials and limitations. While supraglacial lake detection in optical satellite imagery is primarily affected by the similar appearance of supraglacial lakes and surface features such as shadow, blue ice or slush as well as the lack of data during cloud cover and Antarctic polar night, SAR remote sensing is subject to speckle noise, surface roughening, e.g. due to wind or lake refreezing, as well as the similar backscattering signature of surface lakes, wet snow, dry snow, bare ice, radar shadow and the open ocean (Table 4.1). At the same time, SAR remote sensing provides continuous data coverage and improves the detection of slightly frozen and buried lakes whereas optical remote sensing is particularly advantageous due to the possibility of mapping lakes at high spatial accuracy. In addition, optical data enable the mapping of lakes that are subject to strong wind roughening or refreezing in case of the overlying ice being clear and snow-free.

Due to these sensor-specific characteristics, optical and SAR data of the same date oftentimes do not reflect the same supraglacial lake extents (Figure 4.11). For example, severe wind roughening of lake surfaces as well as the occurrence of strongly frozen lakes leads to a greatly reduced visibility of lakes in SAR imagery, as shown in Figure 4.11. Here, lakes either appear bright or are considerably smaller in extent than in optical imagery, where they are clearly visible also during wind roughening and refreezing as long as the overlying ice is clear and snow-free. In this context, also different acquisition times during a day could be responsible for differences in supraglacial lake visibility, e.g. due to short-term refreezing or melting events.



**Figure 4.10.** Appearance of Antarctic supraglacial lakes and resembling ice sheet surface features in Sentinel-1 imagery. Lakes and lake refreezing on George VI (a) and Amery ice shelves (b-c). (d) Lakes with low visual contrast on Amery Ice Shelf. (e-f) Lakes and wet snow on George VI Ice Shelf. (g) Shallow lakes adjacent to slush on George VI Ice Shelf. Shadowing in ice shelf fractures on Shackleton Ice Shelf (h) as well as near rock outcrop (i) and at a fractured ice tongue (j) close to Larsen C Ice Shelf. Bare ice and dry snow near rock on Rennick Ice Shelf (k) and bare ice near Nivlisen Ice Shelf (l). Data: (Copernicus Sentinel-1 data).

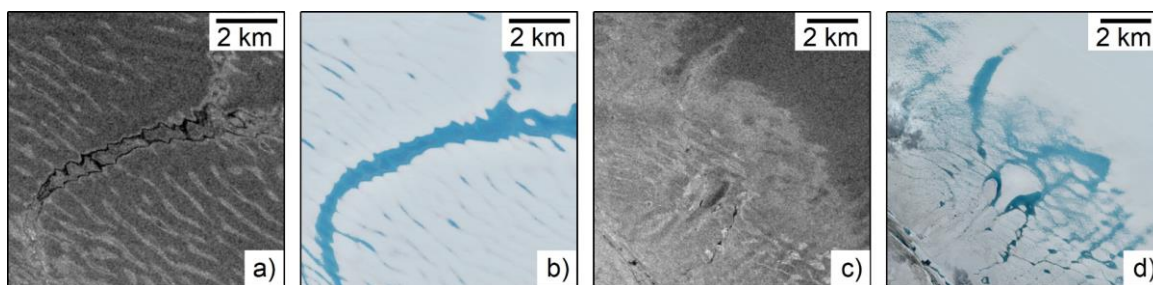


**Figure 4.11.** Appearance of supraglacial lakes in SAR (a,c) and optical (b,d) satellite imagery of 19 January 2020 over George VI Ice Shelf. (a-b) and (c-d) show the same locations. Data: (Copernicus Sentinel data).

### 4.3 Discussion of Requirements of Spaceborne Remote Sensing of Antarctic Supraglacial Lakes

Despite the shown potentials and advances in the mapping and understanding of Antarctic surface hydrology using EO, current knowledge on Antarctic supraglacial lakes is still restricted. In agreement with the results of the literature review outlined in Chapter 4.1 as well as the potentials and challenges of optical and SAR remote sensing (Chapter 4.2), several key challenges and requirements of future research on Antarctic surface hydrology were defined, as summarized in the following. In particular, future requirements were formulated in order to enable the answering and addressing of the following overarching key research questions:

- What are the drivers of Antarctic supraglacial lake occurrence?
- How do supraglacial lakes evolve spatially and temporally?
- What are the impacts of meltwater ponding on Antarctic ice dynamics?
- Which ice shelves are vulnerable to hydrofracture and meltwater-induced ice shelf collapse?

#### 4.3.1 Requirement of a Higher Temporal and Spatial Coverage of Studies on Antarctic Supraglacial Lakes

As summarized in Chapter 4.1, studies on Antarctic supraglacial lake extents are so far scarce with only limited spatial and temporal coverage and resolution. In particular, past studies primarily focused on local-scale investigations at low temporal resolution, oftentimes restricted to observations from single satellite scenes (Figure 4.2b-c). At the same time, existing large-scale investigations focused on image snapshots over individual drainage basins (Kingslake et al., 2017) or during individual melting seasons only (Stokes et al., 2019), thus did not provide complete mappings of the spatio-temporal distribution and evolution of Antarctic supraglacial lakes. Future investigations on Antarctic surface hydrology should therefore capture the full picture of Antarctic



supraglacial lake dynamics and focus on analyses at regional or circum-Antarctic spatial scale if data coverage is sufficient. In fact, sophisticated mapping efforts are needed over regions where no or only incomplete supraglacial lake extent mapping records exist. This includes most glaciers and ice shelves on the WAIS, where only one ice shelf and drainage basin were investigated, but also large coastal sections along the EAIS and API, respectively (see Figure 4.5). In particular, drainage basins on the EAIS, the biggest potential contributor to global sea-level-rise (Rignot et al., 2019) call for increased monitoring efforts. Moreover, also the API and surrounding islands should be studied in more detail considering their maritime climate and increased vulnerability to climate change and surface melting (Hock et al., 2009). Given the potential consequences that supraglacial lakes can have on ice shelf stability (Alley et al., 2018; Banwell et al., 2019, 2013; Lai et al., 2020; Leeson et al., 2020) as well as on overall ice dynamics and mass balance, as revealed over the Greenland Ice Sheet (e.g. Bartholomew et al., 2010; Bell et al., 2018; Das et al., 2008; Khan et al., 2015; Tedesco et al., 2013; The IMBIE Team, 2020), detailed mapping efforts are in fact overdue. In this regard, the availability of spatially complete mapping products is of utmost importance since varying micro-climatic conditions on ice shelves and grounded ice may result in supraglacial lake evolution to vary down- and upstream of the grounding line (see Chapter 3.1) (Stokes et al., 2019). Likewise, an inland migration of lakes due to regional atmospheric warming, as observed over the Greenland Ice Sheet (Howat et al., 2013), can only be captured with large-scale supraglacial lake extent mapping products.

Apart from large-scale mapping efforts, time series on supraglacial lake evolution at intra-annual and inter-annual temporal resolution are required for an improved evaluation and understanding of Antarctic supraglacial lake extent dynamics. This particularly applies to seasonal investigations of Antarctic surface hydrology during a summer melting season but also to analyze the exact onset of supraglacial lake formation and whether lakes refreeze or drain during Antarctic autumn or winter (Arthur et al., 2020b; Dell et al., 2020; Langley et al., 2016). Seasonal investigations of Antarctic surface hydrology are of particular relevance also for an improved understanding of environmental drivers of meltwater ponding as well as of potential impacts on Antarctic ice dynamics. Even though a trend towards more frequent analyses of seasonal supraglacial lake extent dynamics exists (Figure 4.2c), links to associated drivers and impacts were investigated only sporadically. For example, the influence of supraglacial lake drainage on the motion of grounded ice remains understudied (Arthur et al., 2020a; Tuckett et al., 2019), as most investigations on Antarctic ice motion focus on tributaries of former ice shelves along the API (e.g. Rott et al., 2018; Scambos et al., 2004; Seehaus et al., 2018, 2016) or drainage basins that experience ice motion change due to factors such as CDW upwelling (e.g. Groh et al., 2014; Han et al., 2016; Jenkins et al., 2010; Mougnot et al., 2014; Rignot, 2006; Shepherd et al., 2004). This is also reflected

in the geospatial heat maps in Figure 4.12 showing the distribution of spaceborne remote sensing studies on Antarctic ice motion. Likewise, investigations on drivers of Antarctic surface ponding are so far scarce with most knowledge resulting from theoretical considerations or studies on the Greenland Ice Sheet (Chapter 3). Accurate representations of Antarctic meltwater ponding are also required in the light of the poor performance of current model simulations of Antarctic supraglacial lakes revealing their influence on ice shelf stability and calving (Arthur et al., 2020a; Banwell et al., 2013; Buzzard et al., 2018a, 2018b; Lenaerts et al., 2018; Stokes et al., 2019).

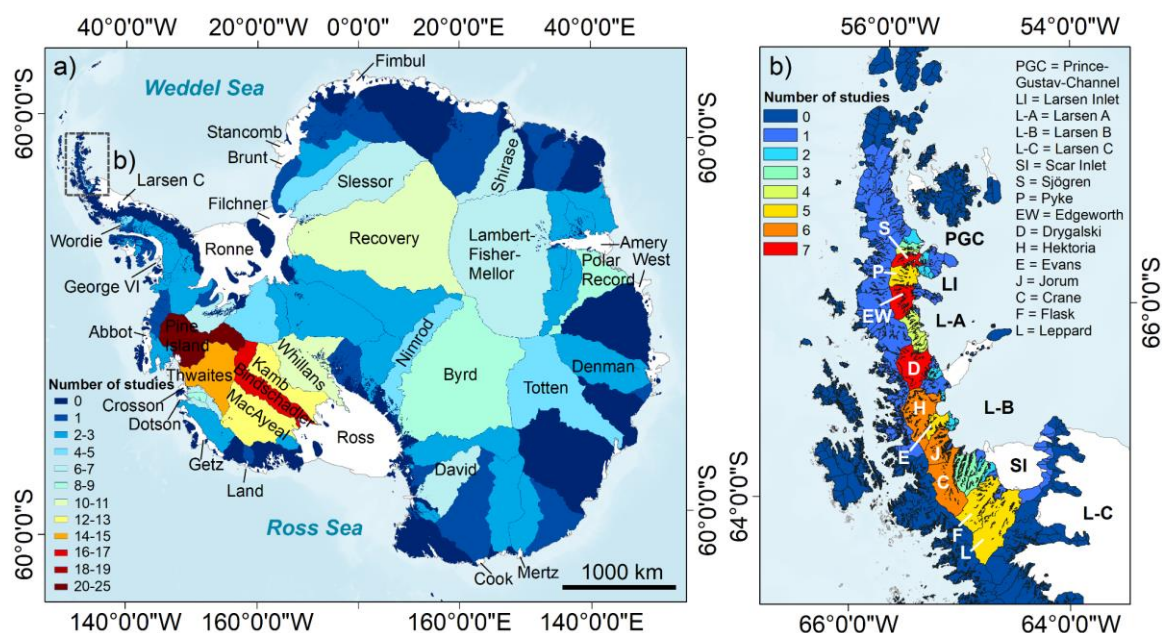


**Figure 4.12.** (a) Geospatial distribution of spaceborne studies on Antarctic ice motion over individual drainage basins. (b) Magnification over the northern Antarctic Peninsula. The heat maps are assembled from 201 scientific papers published in 1984-2018. Modified after Dirscherl et al. (2020a). Data: (Morlighem, 2020; Morlighem et al., 2020; SCAR, 2019).

To enable the comparison of supraglacial lake extent mapping products from different studies or satellite sensors, temporal resolution standards for intra-annual and inter-annual supraglacial lake extent mappings should be defined within the feasibility of available satellite missions. For example, inter-annual supraglacial lake extent mapping products should be composed of data from consistent time spans, e.g. covering the peak of a summer melting season, as performed by Stokes et al. (2019), and intra-annual supraglacial lake extent mappings should be produced at the highest possible temporal resolution providing full spatial coverage (e.g. bi-weekly). For circum-Antarctic supraglacial lake investigations, the generation of intra-annual mapping records might still be challenging as full spatial coverage can presently be achieved at inter-annual resolution only. However, with the increasing availability of satellite data, e.g. from the

Sentinel satellites, future circum-Antarctic supraglacial lake extent mappings should equally be produced at intra-annual temporal resolution.

#### **4.3.2 Future Method Requirements for Antarctic Supraglacial Lake Extent Mapping**

Over recent years, research on Antarctic supraglacial lakes increasingly exploited data of the optical Landsat 8 and Sentinel-2 satellite missions (Figure 4.2a, Figure 4.3). Due to its increased radiometric precision, higher signal-to-noise ratio and narrower spectral bands compared to Landsat 1–7, Landsat 8 enabled major advances in the mapping of Antarctic supraglacial lake extents. Likewise, the availability of Sentinel-2 data at unprecedented 10 m spatial resolution offered new opportunities for the mapping of Antarctic supraglacial lake extents. To date, data from Landsat 8 and particularly Sentinel-2 remain underexploited (Figure 4.3) and no time-efficient mapping method has been implemented for a systematic and automated review of Antarctic supraglacial lake extents. In fact, current methods for supraglacial lake extent mapping in optical satellite imagery were shown to be purely manual, visual or semi-automated being subject to substantial misclassifications and requiring time-consuming manual post-processing. Therefore, future method developments should exploit advanced image classification techniques including ML in order to provide an automated mapping method for supraglacial lake extent derivation in optical satellite data at full ice sheet coverage, thus with spatio-temporal transferability.

As optical satellite data will always be restricted to the use of cloud-free daytime acquisitions, SAR imagery represents a valuable additional data source for supraglacial lake extent mapping. Apart from the possibility of delineating buried lakes as well as a continuous data acquisition during cloud cover and night-time, SAR sensors operate during Antarctic winter allowing for more detailed investigations of intra-annual supraglacial lake dynamics including lake refreezing or drainage events (see Table 4.1). So far, only few studies employed SAR data for supraglacial lake extent derivation (Figure 4.2a). In this context, SAR-based method developments were either visual, manual or semi-automated (Chapter 4.2.2). Therefore, future work should equally focus on the implementation of advanced mapping methods for automated supraglacial lake extent derivation in SAR satellite imagery over Antarctica. In this context, the detected potentials and challenges outlined in Chapter 4.2 are required to be exploited and overcome. Regarding SAR, particularly data of the recently launched Sentinel-1 mission should be used but also data of other missions such as the C-band RADARSAT Constellation Mission (RCM) of the Canadian Space Agency could be of interest. These sensors are so far understudied with Sentinel-1 SAR being applied in only two studies (Figure 4.3).

Furthermore, the combination of mapping products from optical and SAR sensors would enable a more complete mapping of Antarctic supraglacial lake extent dynamics during a given time period and allow to exploit and overcome sensor-specific advantages and limitations (see Chapter 4.2.3). In particular, the exploitation of advantages of both sensor types is particularly crucial in Antarctica where a frequent cloud coverage as well as polar darkness during austral winter oftentimes restrict the availability of optical satellite data and where SAR data may be limited due to the frequent occurrence of wind. For this purpose, spatial and temporal resolution standards should be defined within the feasibility of the individual optical and SAR satellite sensors. The development of a global mapping method for supraglacial lake extent derivation using both SAR and optical data would greatly support the fulfilment of requirements identified in Chapter 4.3.1 and enable an improved understanding of environmental drivers of Antarctic supraglacial meltwater ponding as well as of potential influences on overall Antarctic ice dynamics.

### **4.4 Summary**

This chapter summarized the state-of-the art of spaceborne remote sensing for Antarctic supraglacial lake extent delineation and discussed potentials and challenges of supraglacial lake classification in optical and SAR satellite imagery. Despite recent progress in the understanding of Antarctic surface hydrology using EO, current mappings of Antarctic supraglacial lakes are still restricted in terms of their spatial and temporal coverage and resolution. In addition, data of high-resolution satellite sensors including the Sentinels remain underexploited and method developments were mostly visual, manual or semi-automated. In agreement with the shown potentials and challenges of optical and SAR remote sensing, future requirements therefore include the combination of data from high-resolution optical and SAR satellite sensors for derivation of fused supraglacial lake extent classifications as well as the development of automated mapping methods with spatio-temporal transferability. In addition, the results showed that future studies should address historical, present-day and future supraglacial lake evolution using intra-annual and inter-annual supraglacial lake extent mappings at regional to circum-Antarctic spatial scale.

## CHAPTER 5

### 5 A Novel Framework for Antarctic Supraglacial Lake Extent Mapping \*

As outlined in Chapter 4, current knowledge on Antarctic supraglacial lakes is mainly restricted by the lack of an automated, time-efficient classification technique with pan-Antarctic mapping capabilities. Considering the increasing availability of satellite data over the Antarctic coastline since the launch of Landsat 8, Sentinel-1 and Sentinel-2, the development of an automated processing chain for supraglacial lake identification in optical and SAR data is overdue.

In order to address the lack of an adequate mapping technique and thus the identified potentials, challenges and future requirements of spaceborne remote sensing of Antarctic supraglacial lakes (Chapter 4), a novel framework for automated supraglacial lake extent mapping was developed as part of this thesis. The developed workflow combines recent advances in artificial intelligence with data from the Sentinel-1 SAR and optical Sentinel-2 satellite sensors of the Copernicus programme for an improved monitoring of Antarctic supraglacial lake extents. In order to obtain most accurate classification results for each sensor type as well as to comply with sensor-specific advantages and limitations and thus the varying visibility of supraglacial lakes in optical and SAR satellite data (Figure 4.11), two separate machine learning and deep learning mapping methods were developed. In this context, the use of state-of-the-art image classification techniques from supervised machine learning and deep learning was particularly important given that traditional image classification techniques, including thresholding or unsupervised learning (e.g. clustering), were not suitable in the light of the difficulties outlined in Chapter 4.2. In fact, it is well known that methods from computer vision including supervised learning outperform conventional classification techniques when it comes to an automated or large-scale processing of extensive amounts of image data with varying characteristics (Hoeser and Kuenzer, 2020). To provide more detail, a Random Forest (RF) classifier (Breiman, 2001) from supervised learning was implemented for optical Sentinel-2 data, while a Deep Convolutional Neural Network (DCNN) based on a modified U-Net (Ronneberger et al., 2015) was found to

---

\*Parts of this chapter are based on Dirscherl et al. (2020b) and Dirscherl et al. (2021a).

perform best for classification of Sentinel-1 SAR imagery (Chapter 5.3). The two methods were combined through decision-level fusion of optical and SAR classification results at bi-weekly temporal intervals allowing for detailed seasonal investigations of supraglacial lake evolution.

The following chapters first introduce the study sites selected for training and testing the machine learning models (Chapter 5.1) to then outline the corresponding data basis including all data required for pre- and post-processing (Chapter 5.2). Next, Chapter 5.3 presents the methodological framework developed for automated supraglacial lake extent classification in Sentinel-1 SAR and optical Sentinel-2 imagery and Chapter 5.4 shows selected classification results from automated mapping. In Chapter 5.5, the outcome of a comprehensive performance evaluation of both classifiers is outlined and Chapter 5.6 describes the implemented steps for a fully automated processing of the satellite data. Finally, Chapter 5.7 discusses the main advantages and remaining limitations of the developed workflow and Chapter 5.8 provides a summary of the entire Chapter 5.

### **5.1 Training and Testing Sites**

As a sub-discipline of artificial intelligence, supervised machine learning and deep learning are commonly used for remote sensing image classification (Baumhoer et al., 2019; Hoeser and Kuenzer, 2020; Ji et al., 2019; Wang et al., 2016; Zhong et al., 2019) and are based upon the use of labeled data for training of machine learning models that can accurately predict unlabeled imagery. For machine learning models to perform well on unlabeled data, a sensible choice of training data is of fundamental importance. In the context of remote sensing, training data should include imagery of varying dates and locations to ensure an appropriate representation of different land surface types and conditions during model training as well as to allow for an accurate recognition of image objects in data that were not presented to the model before. For evaluation of the performance of trained classifiers, unlabeled or labeled test data can be used. In this context, another prerequisite for an accurate and representative evaluation of the trained model is to ensure a different spatial and temporal coverage of training and testing sites.

In agreement with the outlined specifications as well as to fulfil the requirement of a spatially and temporally transferable mapping method for supraglacial lake extent delineation across the whole Antarctic continent, the training sites had to be selected to cover (1) multiple dates throughout a summer melting season in order to capture the temporally varying signature of supraglacial lakes and of different snow and ice types and (2) the entire variety of surface features and conditions on the AIS including rock outcrop, bare ice, blue ice, dry snow, wet snow, polluted snow, slush as well as shallow, deep and slightly frozen supraglacial lakes (Dirscherl et al., 2020b, 2021a). In addition,

locations with extensive shadowing around rock outcrop or in fractures and crevasses had to be included to ensure an accurate discrimination from lakes. On the other hand, the independent test sites had to be chosen to cover locations different to the selected training data (Figure 5.1, Figure 5.2) as well as regions that are particularly difficult to differentiate from supraglacial lakes in Sentinel-1 or Sentinel-2 satellite imagery.

In detail, the training and test sites were equally distributed around the Antarctic continent and across different elevation zones (Figure 5.1), in agreement with previously documented supraglacial lake locations (Kingslake et al., 2017; Lenaerts et al., 2017; Stokes et al., 2019; Zheng and Zhou, 2019) as well as lakes that were visually identified in spaceborne remote sensing imagery on Google Earth Engine (Dirscherl et al., 2020b, 2021a). To ensure the temporal transferability of developed algorithms, the selection of training and testing sites was further restricted by the occurrence of supraglacial lakes during specific summer seasons with particularly strong melting events, e.g. during January 2020 over the API and WAIS or during 2016-2017 and 2018-2019 over the EAIS (Dirscherl et al., 2021a). In detail, supraglacial lake occurrences during the summer melting seasons of years 2018-2019 and 2019-2020 were considered as Sentinel-1 training regions and supraglacial lake observations during 2016-2017, 2017-2018 and 2019-2020 were chosen as Sentinel-1 testing regions (Table 5.1, Figure 5.3a) (Dirscherl et al., 2021a). In contrast, Sentinel-2 training regions were determined in agreement with supraglacial lake abundance during melting seasons 2016-2017, 2017-2018 and 2018-2019 and Sentinel-2 testing regions capture lake occurrences during 2016-2017, 2017-2018 and 2019-2020 (Table 5.3, Figure 5.3b) (Dirscherl et al., 2020b). Overall, this resulted in 13 training and 10 test sites for Sentinel-1 and 14 training and 14 test sites for Sentinel-2 (Table 5.1, Table 5.3, Figure 5.1).

For an improved evaluation of the spatio-temporal transferability of the developed classification workflows, additional test sites covering George VI and Amery ice shelves were selected and analyzed for intra-annual and inter-annual supraglacial lake dynamics, respectively (Figure 5.1, Figure 5.2). In detail, George VI Ice Shelf was used for assessment of the Sentinel-1 classification workflow. Here, rock outcrop, blue ice, dry snow, wet snow, slush as well as shallow and deep supraglacial lakes are widespread (Figure 3.1a, Figure 3.2a, Figure 4.8) which greatly supports the assessment of the classifier. On the other hand, Amery Ice Shelf was used for evaluation of the developed Sentinel-2 classification method. Over Amery Ice Shelf, meltwater accumulation is particularly widespread (Spergel et al., 2021; Stokes et al., 2019) and rock outcrop and blue ice (e.g. Figure 3.2c) can be found adjacent to both wet and dry snow in low and high elevations, respectively. In addition, both ice shelves were used as exemplary test regions to create fused Sentinel-1 and Sentinel-2 classification products highlighting the relevance of multi-sensor mappings. Finally, two independent test sites on the Greenland Ice Sheet were defined for evaluation of the methods in regions beyond Antarctica.



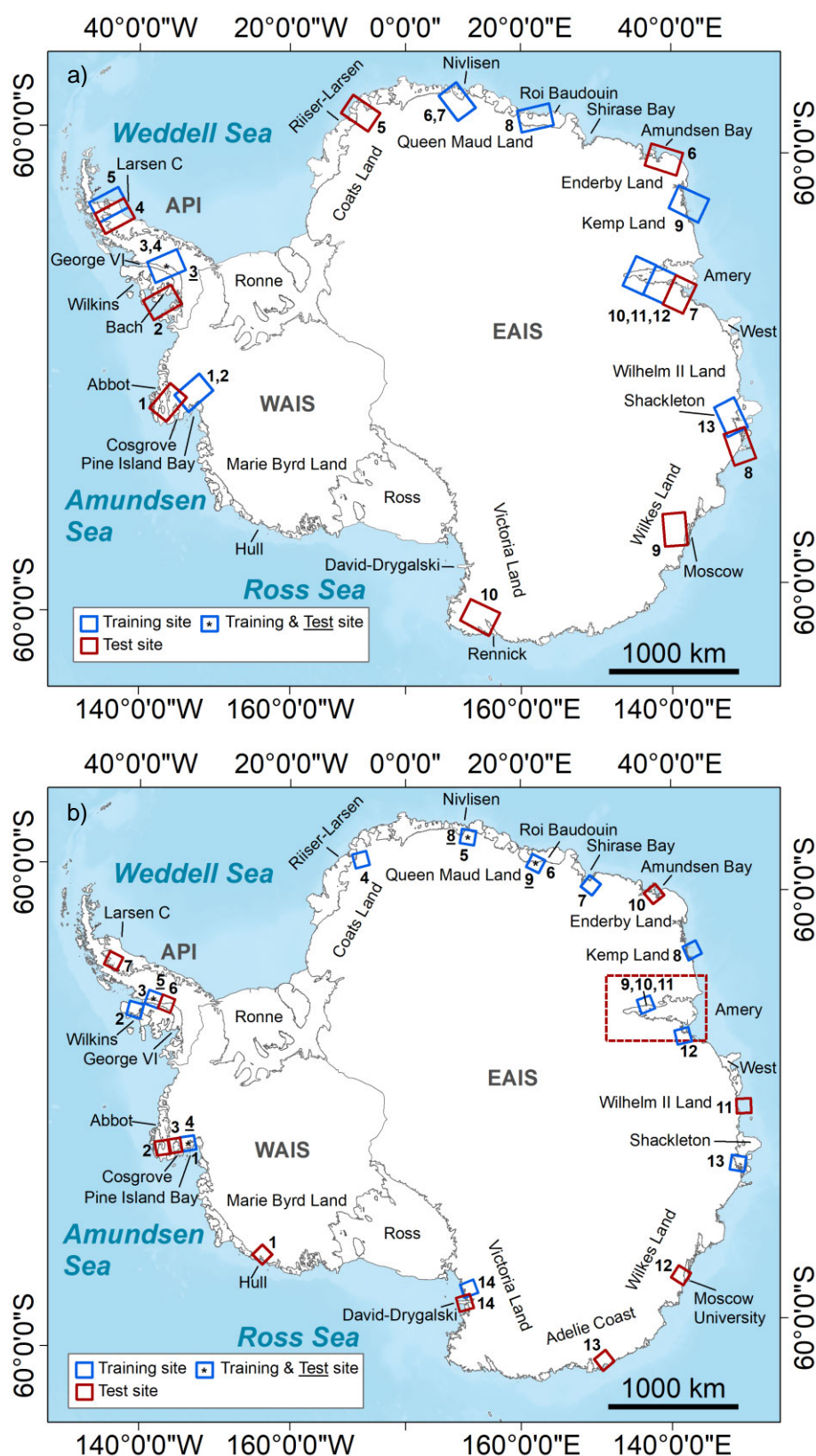


**Figure 5.1.** Spatial distribution of training and testing regions for Sentinel-1 (a) and Sentinel-2 (b). Stars highlight regions where training and testing data of different dates were overlapping. The dashed red line in (b) shows the test site over Amery Ice Shelf (Figure 5.2). API: Antarctic Peninsula. WAIS: West Antarctic Ice Sheet. EAIS: East Antarctic Ice Sheet. Modified after Dirscherl et al. (2020b) and Dirscherl et al. (2021a). Data: (IMBIE, 2016; Morlighem, 2020; Morlighem et al., 2020; Mouginito et al., 2017b; Rignot et al., 2013).



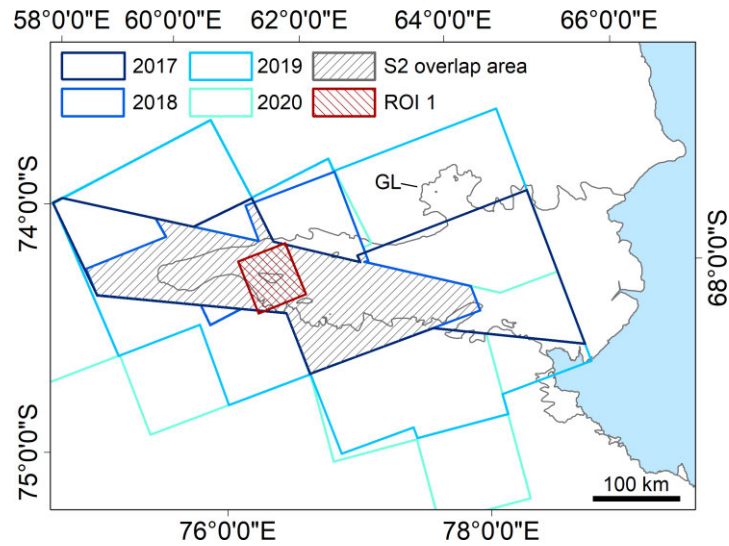


**Figure 5.2.** Geospatial coverage of Sentinel-2 data over Amery Ice Shelf during melting seasons 2016-2017 to 2019-2020. The grey area shows the overlap area of all years and the red area shows the region of interest (ROI) that was analyzed in Figure 5.21. GL: Grounding Line. Modified after Dirscherl et al. (2020b). Data: (Mouginot et al., 2017b; Rignot et al., 2013).

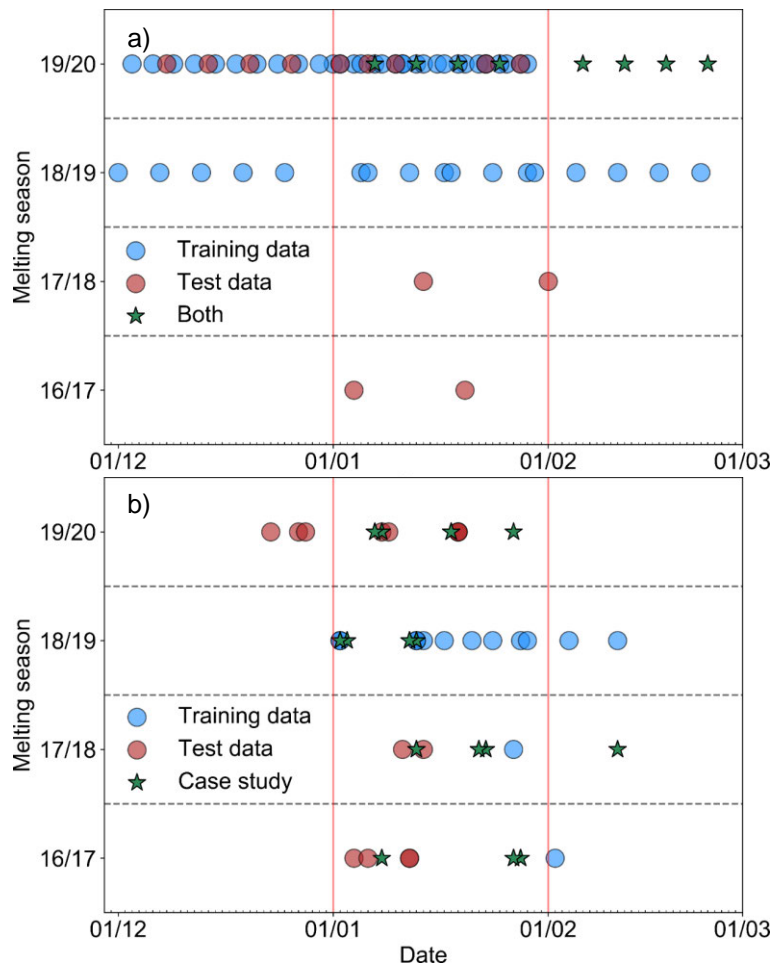


**Figure 5.3.** Temporal availability of Sentinel-1 (a) and Sentinel-2 (b) training and test data during melting seasons 2016-2017 to 2019-2020. The green stars in (a) highlight acquisitions that were used for training and testing despite training data being aggregated monthly data products. The green stars in (b) highlight additional test data over Amery. Modified after Dirscherl et al. (2021a).

## 5.2 Input Data

The following chapters summarize the required input data used for model training and testing over the regions described in Chapter 5.1. These include satellite imagery from Sentinel-1 and Sentinel-2 (Chapter 5.2.1, Chapter 5.2.2) as well as corresponding ground truth labels (Chapter 5.2.3). For Sentinel-1, labels were created for land surface classes “water” and “non-water”, while Sentinel-2 data were labeled in agreement with classes “water”, “snow/ice”, “rock” and “shadow”. A more detailed categorization, e.g. in agreement with varying lake depths or different snow and ice types, was not performed as the main aim during method development was to derive supraglacial lake extents. In addition, lake depths can only be retrieved over completely ice-free lakes in optical satellite data being a condition that is rarely met in Antarctica. Finally, the data needed for pre- and post-processing are introduced in Chapter 5.2.4 and Chapter 5.2.5.

### 5.2.1 Sentinel-1 Data

The Sentinel-1 constellation consists of two polar-orbiting satellites, Sentinel-1A and Sentinel-1B, that were launched in 2014 and 2016, respectively (Figure 4.2a). Sentinel-1 operates in the microwave frequency domain at C-band (5.405 GHz center frequency) enabling data acquisition during day and night and independent of meteorological conditions (ESA, 2021a). The continuous data availability from Sentinel-1 offers new opportunities for the monitoring of the Earth’s surface at unprecedented spatial and temporal coverage and resolution compared to its predecessors ERS-1/-2 and ENVISAT (ESA, 2021a). As outlined in Chapter 4.2.2, the two-satellite constellation allows for a revisit time of 6 days at the Equator with up to daily revisit frequencies in high latitudes due to overlapping orbit tracks (Figure 5.4a). Over the Antarctic coastline, Sentinel-1 acquires data in either IW or EW swath mode (Figure 5.4b). While IW products are provided at 10 m pixel spacing in single polarization (HH), EW products can also be retrieved in dual polarization (HH-HV) at a spatial resolution of 40 m (Figure 5.4b). In addition, both data products can be obtained in either Single Look Complex (SLC) or Ground Range Detected (GRD) format. Due to the advanced pre-processing of GRD data, including focusing, multi-looking and ground range projection, GRD data are to be preferred over SLC data when only amplitude information is required (ESA, 2021a).

In order to achieve the highest possible resolution standard for Antarctic supraglacial lake extent mapping as well as to resolve even small or elongated supraglacial lakes and streams (e.g. Figure 3.1, Figure 4.7f), the Sentinel-1 data used in this thesis were acquired in IW acquisition mode and GRD format. Even though dual-polarized EW data allow for a more accurate discrimination between different ice types (Wesche and Dierking, 2014), the use of higher-resolution IW data was preferred as the main aim during method development was to discriminate between water and non-water. To

provide more detail, the IW acquisition mode delivers data at a swath width of 250 km (Figure 5.1a) with incidence angles in the range between 29° and 46° (ESA, 2016). Each IW data product is assembled from three sub-swaths captured using the Progressive Scans SAR technique whereat each sub-swath consists of a series of bursts. To obtain the final IW image product, all bursts and sub-swaths are merged (ESA, 2016). Figure 5.5a shows an exemplary 14-day acquisition coverage of Sentinel-1 IW data.

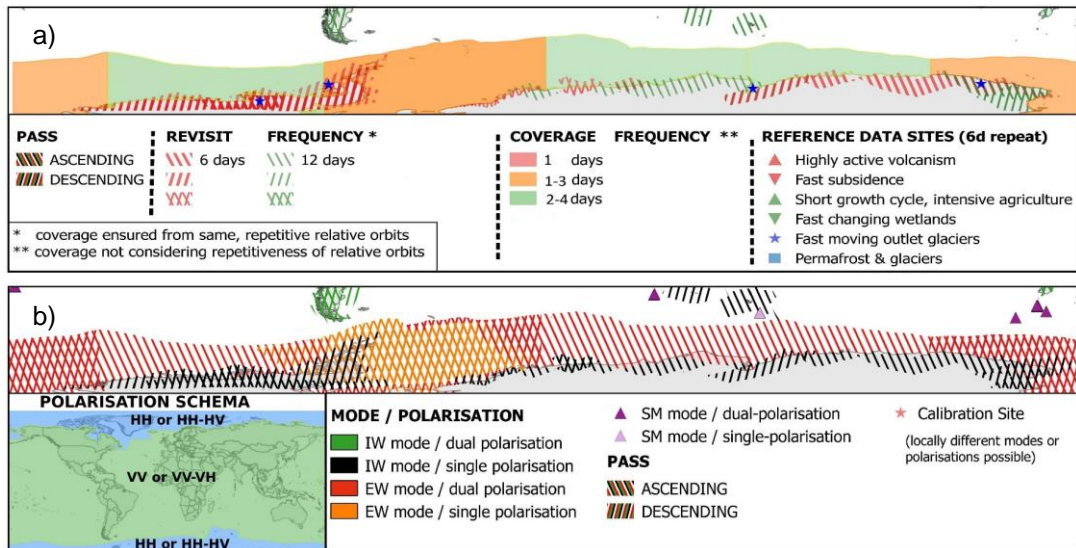


**Figure 5.4.** Sentinel-1 observation scenario over the Antarctic coastline. (a) Revisit and coverage frequency. (b) Acquisition modes and polarization scheme. Modified after ESA (2021a).

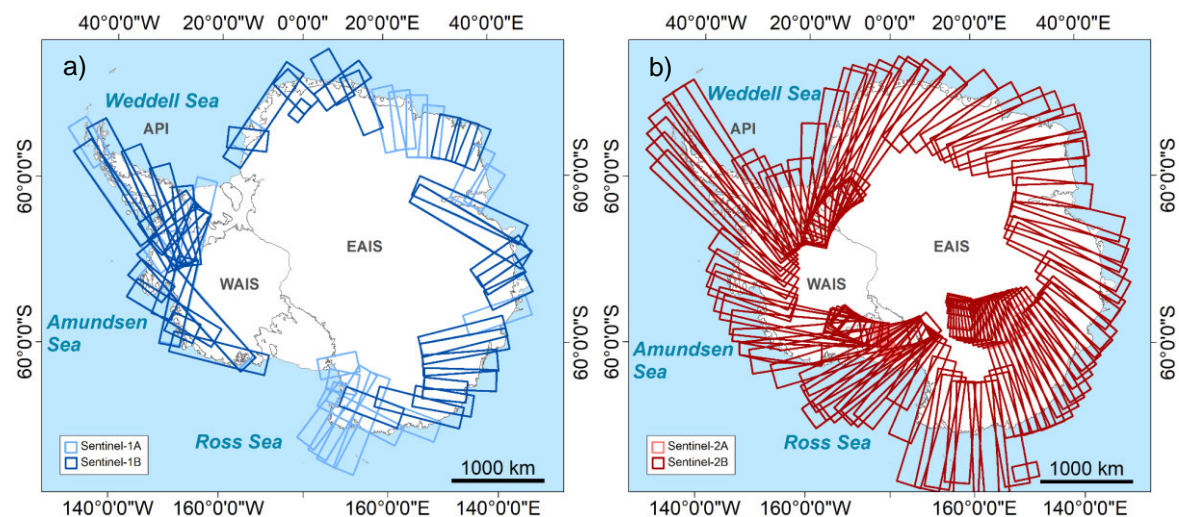


**Figure 5.5.** Sentinel-1A/B (a) and Sentinel-2A/B (b) acquisition segments during exemplary 14-day intervals. API: Antarctic Peninsula. WAIS: West Antarctic Ice Sheet. EAIS: East Antarctic Ice Sheet. Data: (ESA, 2021b; IMBIE, 2016; Mouginit et al., 2017b; Rignot et al., 2013).

For deep learning model training and testing over the regions shown in Figure 5.1a, a total of 70 Sentinel-1 image products was retrieved (Figure 5.3a). Of these, 57 were used for model training and nine were selected for testing the model in spatially and

temporally independent regions. In detail, training acquisitions were filtered to include the maximum number of available acquisitions in either ascending or descending orbit for a given study region and month in order to compute the monthly backscattering minimum product for each region in the following (Table 5.1, Chapter 5.3). Regarding the acquisitions used for testing, no further processing to temporally aggregated products was performed. For the additional test site over George VI Ice Shelf, the eight individual training acquisitions covering January and February 2020 (green stars in Figure 5.3a) as well as four additional Sentinel-1 scenes for December 2019 were used for derivation of intra-annual supraglacial lake extents to highlight the potential of the developed workflow for time series analyses (Table 5.1) (Dirscherl et al., 2021a). Moreover, the January 2020 acquisitions over George VI Ice Shelf (Figure 5.3a) as well as all available Sentinel-1 acquisitions covering early January 2019 over Amery Ice Shelf (not shown in Figure 5.3a, Chapter 5.3.3) were used for derivation of fused classification products. Finally, the Sentinel-1 scene covering Greenland was acquired on 28 July 2018 (Table 5.1).

**Table 5.1.** Training and testing regions used for method developments with Sentinel-1. Each training region corresponds to an aggregated monthly backscattering minimum raster and each testing region corresponds to one Sentinel-1 IW acquisition except for region 3, where multiple data products were evaluated. API: Antarctic Peninsula. WAIS: West Antarctic Ice Sheet. EAIS: East Antarctic Ice Sheet. Modified after Dirscherl et al. (2021a).

ID	Time period/Date	Study area	Region	Relative orbit	Orbit direction
Training regions Antarctica					
1	December 2019	Pine Island Bay	WAIS	53	Descending
2	January 2020	Pine Island Bay	WAIS	53	Descending
3	January 2020	George VI Ice Shelf	API	169	Descending
4	February 2020	George VI Ice Shelf	API	169	Descending
5	January 2020	Larsen Ice Shelf	API	38	Descending
6	December 2019	Nivlisen Ice Shelf	EAIS	93	Descending
7	January 2020	Nivlisen Ice Shelf	EAIS	93	Descending
8	January 2020	Roi Baudouin Ice Shelf	EAIS	59	Ascending
9	January 2019	Mawson Coast	EAIS	72	Ascending
10	December 2018	Amery Ice Shelf	EAIS	3	Descending
11	January 2019	Amery Ice Shelf	EAIS	3	Descending
12	February 2019	Amery Ice Shelf	EAIS	3	Descending
13	January 2020	Shackleton Ice Shelf	EAIS	85	Ascending
Testing regions Antarctica					
1	06 January 2020	Abbot and Cosgrove ice shelves	WAIS	68	Descending
2	28 January 2020	Bach Ice Shelf	API	38	Descending
3	Dez/Jan/Feb 2019-2020	George VI Ice Shelf	API	169	Descending
4	14 January 2018	Larsen C Ice Shelf	API	38	Descending
5	20 January 2017	Riiser-Larsen Ice Shelf	EAIS	50	Descending
6	02 January 2020	Enderby Land	EAIS	14	Ascending
7	04 January 2017	Amery Ice Shelf	EAIS	3	Descending
8	01 February 2018	Shackleton Ice Shelf East	EAIS	41	Ascending
9	23 January 2020	Moscow University Ice Shelf	EAIS	55	Ascending
10	10 January 2020	Rennick Ice Shelf	EAIS	43	Descending
Testing regions Greenland					
1	28 July 2018	Nordenskiöld Glacier	West	90	Ascending

### 5.2.2 Sentinel-2 Data

Likewise, the high spatial resolution and coverage of Sentinel-2 offers new opportunities for Antarctic supraglacial lake extent mapping (Table 4.1). In detail, the Sentinel-2 constellation consists of two polar-orbiting satellites, Sentinel-2A and Sentinel-2B, enabling the monitoring of the Earth’s surface every 5 days under cloud-free conditions. Due to overlying orbit tracks, polar regions can be monitored up to daily. Figure 5.5b shows exemplary acquisition segments of Sentinel-2 during a 14-day period in December 2020 and January 2021 over the Antarctic coastline.

Both Sentinel-2A and Sentinel-2B carry a passive Multispectral Instrument (MSI) recording the sunlight reflected from the Earth’s surface in 13 spectral bands in the visible and infrared regions (ESA, 2015). Of these, four provide data at 10 m spatial resolution, six at 20 m spatial resolution and three at 60 m spatial resolution (Table 5.2). Sentinel-2 data are provided as Level-1C Top-of-Atmosphere products covering 100 x 100 km granules on the Earth’s surface (see Figure 5.1b) (ESA, 2015).

The Sentinel-2 granules used for model training and testing are shown in Table 5.3 and Figure 5.3b. In agreement with the study sites in Figure 5.1b, 14 training and 14 testing scenes were selected. In particular, only acquisitions with a cloud cover  $\leq 10\%$  and a sun elevation angle  $\leq 20^\circ$  were considered. For the additional study site on Amery Ice Shelf, all available Sentinel-2 data during January 2017-2020 were retrieved for evaluation of inter-annual supraglacial lake dynamics. Further, the data covering Amery Ice Shelf during early January 2019 as well as all available January 2020 data over George VI Ice Shelf (not shown in Figure 5.3b) were used for the derivation of fused mappings. Finally, the Sentinel-2 scene covering Greenland was from 10 August 2019.

**Table 5.2.** Sentinel-2 MSI spectral bands. NIR: Near-Infrared. SWIR: Shortwave Infrared. S2A: Sentinel-2A. S2B: Sentinel-2B. Modified after Dirscherl et al. (2020b).

Band number	Band description	Central wavelength S2A / S2B (nm)	Bandwidth S2A / S2B (nm)	Spatial resolution (m)
1	Aerosols	442.7 / 442.2	21 / 21	60
2	Blue	492.4 / 492.1	66 / 66	10
3	Green	559.8 / 559.0	36 / 36	10
4	Red	664.6 / 664.9	31 / 31	10
5	Red Edge 1	704.1 / 703.8	15 / 16	20
6	Red Edge 2	740.5 / 739.1	15 / 15	20
7	Red Edge 3	782.8 / 779.7	20 / 20	20
8	NIR	832.8 / 832.9	106 / 106	10
8A	Red Edge 4	864.7 / 864.0	21 / 22	20
9	Water vapor	945.1 / 943.2	20 / 21	60
10	Cirrus	1373.5 / 1376.9	31 / 30	60
11	SWIR1	1613.7 / 1610.4	91 / 94	20
12	SWIR2	2202.4 / 2185.7	175 / 185	20

**Table 5.3.** Training and testing regions used for method developments with Sentinel-2. API: Antarctic Peninsula. WAIS: West Antarctic Ice Sheet. EAIS: East Antarctic Ice Sheet. Modified after Dirscherl et al. (2020b).

ID	Date	Study area	Region	Relative orbit	Orbit direction
Training regions Antarctica					
1	27 January 2018	Pine Island Bay	WAIS	139	Descending
2	24 January 2019	Wilkins Ice Shelf	API	95	Descending
3	28 January 2019	George VI Ice Shelf	API	9	Descending
4	02 February 2017	Riiser-Larsen Ice Shelf	EAIS	7	Descending
5	21 January 2019	Nivlisen Ice Shelf	EAIS	49	Descending
6	14 January 2019	Roi Baudouin Ice Shelf	EAIS	91	Descending
7	04 February 2019	Shirase Bay	EAIS	105	Descending
8	17 January 2019	Mawson Coast	EAIS	133	Descending
9	02 January 2019	Amery Ice Shelf	EAIS	61	Descending
10	13 January 2019	Amery Ice Shelf	EAIS	75	Descending
11	11 February 2019	Amery Ice Shelf	EAIS	61	Descending
12	13 January 2019	Publications Ice Shelf	EAIS	75	Descending
13	29 January 2019	Shackleton Ice Shelf	EAIS	17	Descending
14	02 January 2019	Nordenskjöld Ice Tongue	EAIS	71	Descending
Testing regions Antarctica					
1	08 January 2020	Hull Glacier	WAIS	83	Descending
2	12 January 2017	Abbott Ice Shelf	WAIS	139	Descending
3	12 January 2017	Cosgrove Ice Shelf	WAIS	139	Descending
4	27 December 2019	Pine Island Bay	WAIS	53	Descending
5	19 January 2020	George VI Ice Shelf	API	95	Descending
6	19 January 2020	George VI Ice Shelf	API	95	Descending
7	19 January 2020	Larsen C Ice Shelf	API	95	Descending
8	11 January 2018	Nivlisen Ice Shelf	EAIS	49	Descending
9	09 January 2020	Roi Baudouin Ice Shelf	EAIS	91	Descending
10	04 January 2017	Amundsen Bay (Enderby Land)	EAIS	19	Descending
11	14 January 2018	Wilhelm II Coast	EAIS	89	Descending
12	28 December 2019	Moscow University Ice Shelf	EAIS	59	Descending
13	23 December 2019	Adelie Coast	EAIS	1	Descending
14	06 January 2017	Drygalski Ice Tongue	EAIS	57	Descending
Testing regions Greenland					
1	10 August 2019	Nordenskiöld Glacier	West	68	Ascending

### 5.2.3 Training Labels

For supervised machine learning classifiers to learn from training data, ground truth labels are required. As no circum-Antarctic lake inventory exists to date and as ground-based measurements of Antarctic supraglacial lakes are difficult to perform, labels were created manually on the basis of the underlying Sentinel-1 and Sentinel-2 imagery (Table 5.1, Table 5.3).

As mentioned, Sentinel-1 training labels were created for land surface classes “water” and “non-water” only. Due to the similar backscattering characteristics of different ice sheet surface features (Figure 4.10) in the absence of additional image information, e.g. from multiple polarizations, a more detailed categorization was not performed. As Sentinel-1 data were classified by means of a deep learning model, all training data had to be labelled at full extent meaning that each image pixel is required to be assigned a

land surface class (see Figure 5.11). To support the labelling of particularly difficult image regions, optical Landsat-8 and Sentinel-2 data were used for comparison.

On the other hand, training labels for Sentinel-2 were created for classes “water”, “snow/ice”, “rock” and “shadow” (Dirscherl et al., 2020b). Here, the availability of multi-spectral information enabled to differentiate between a larger number of classes supporting a more accurate discrimination between “water” and “non-water”. In addition, the classification of “rock” is particularly useful for geoscientific analyses, e.g. on melt-albedo feedbacks (see Chapter 6). Due to the use of a pixel-based RF classifier for classification of Sentinel-2 data, the labeling of image subsets was sufficient which greatly reduced the time required for manual labeling. Depending on their visibility in the corresponding Sentinel-1 or Sentinel-2 imagery, training labels for the “water” class were drawn for open water, slightly frozen lakes and buried lakes. Lakes in Sentinel-1 SAR imagery that were subject to speckle noise or wind roughening leading to fuzzy lake edges and low contrast were delineated as accurate as possible.

#### **5.2.4 Topographic Data**

To provide the RF model with additional input variables during model training as well as to support the pre- and post-processing of Sentinel-1 and Sentinel-2 data, the TanDEM-X PolarDEM 90 m of Antarctica (Figure 2.3a) (Wessel et al., 2021) and thereof derived topographic variables were used (Dirscherl et al., 2020b, 2021a). In detail, the TanDEM-X PolarDEM is generated from SAR data covering the period between April 2013 and October 2014. Due to erroneous elevation values over sea ice and icebergs close to the Antarctic calving front, the DEM was refined by clipping it to a TanDEM-X coastline product and by manually editing it subsequently. Due to its complete coverage over the Antarctic continent, the TanDEM-X PolarDEM is superior to the higher-resolution Reference Model of Antarctica (REMA) being subject to substantial data gaps across large parts of the Antarctic continent (Howat et al., 2019). An accuracy assessment of the TanDEM-X PolarDEM over blue ice areas additionally revealed its low mean vertical height error of  $-0.3 \pm 2.5$  m (Wessel et al., 2021).

#### **5.2.5 Coastline Data**

In addition, the post-processing of Sentinel-1 and Sentinel-2 classifications was supported by a Sentinel-1 coastline product (Chapter 5.3) (Baumhoer et al., 2021, 2019). In particular, the circum-Antarctic coastline was derived through semantic segmentation of single- and dual-polarized Sentinel-1 imagery covering the period between June and August 2018 (Baumhoer et al., 2021). For improvement of the Sentinel-1 coastline product, morphological erosion and topographic masking was performed, while remaining minor errors were corrected manually (Baumhoer et al., 2021).

## 5.3 Methodological Framework

This chapter describes the full classification workflow for supraglacial lake extent delineation in Sentinel-1 (Chapter 5.3.1) and Sentinel-2 imagery (Chapter 5.3.2). In addition, the criteria for the fusion of classification products from both sensor types are outlined (Chapter 5.3.3).

### 5.3.1 Sentinel-1

In order to comply with the stated future method requirements for Antarctic supraglacial lake extent mapping in SAR imagery (Chapter 4.3.2), the development of a fully automated processing chain with pan-Antarctic mapping capabilities was required. Due to the limitations outlined in Chapter 4.2.2 (Figure 4.9, Figure 4.10), conventional image classification techniques, including pixel-based thresholding, unsupervised learning or time series analysis, could not be employed for classification of supraglacial lake extents in SAR imagery and advanced image classification techniques from machine learning were exploited (Dirscherl et al., 2021a). Being a sub-discipline of machine learning, deep learning outperforms common machine learning classifiers, including RF or Support Vector Machines, in the solving of complex image classification problems (Hoeser and Kuenzer, 2020) and was therefore employed for supraglacial lake identification in SAR imagery.

To provide more detail, deep learning uses Artificial Neural Networks (ANN) with multiple hidden layers to extract complex information from large datasets. ANNs are usually fully connected where all input, hidden and output layers, the neurons, are connected through weights and non-linear activations. The weights are learned during model training and allow to extract complex features from an input dataset that support an accurate prediction of a previously unknown output. With an increasing number of hidden layers, the model gets deeper and more complex features can be extracted. In this context, Convolutional Neural Networks (CNN) belong to the class of ANNs and are particularly suitable for the processing of 2D image data (Krizhevsky et al., 2012), e.g. for image recognition, image segmentation or object detection tasks (Hoeser and Kuenzer, 2020). CNNs outperform traditional image classification techniques due to the consideration of the spatial image context via convolutional extraction of feature maps from a given input image. Considering the shift towards growing data volumes from satellite sensors and increasingly complex image classification problems to solve, the use of CNNs considerably gained in popularity also in EO and remote sensing (e.g. Baumhoer et al., 2019; Hoeser et al., 2020; Ji et al., 2019; Mohajerani et al., 2019; Zhang et al., 2019, 2018).



Accordingly, the deep learning workflow developed for automated supraglacial lake extent mapping in Sentinel-1 SAR imagery is based upon a CNN (Chapter 5.3.1.2) and can be subdivided into (1) pre-processing and data preparation, (2) deep learning model training, (3) post-processing and (4) accuracy assessment (see Dirscherl et al., 2021a). While the methods employed for the accuracy assessment are outlined in Chapter 5.5, the following chapters provide details on all remaining steps. In addition, the full classification workflow is summarized in Figure 5.6.

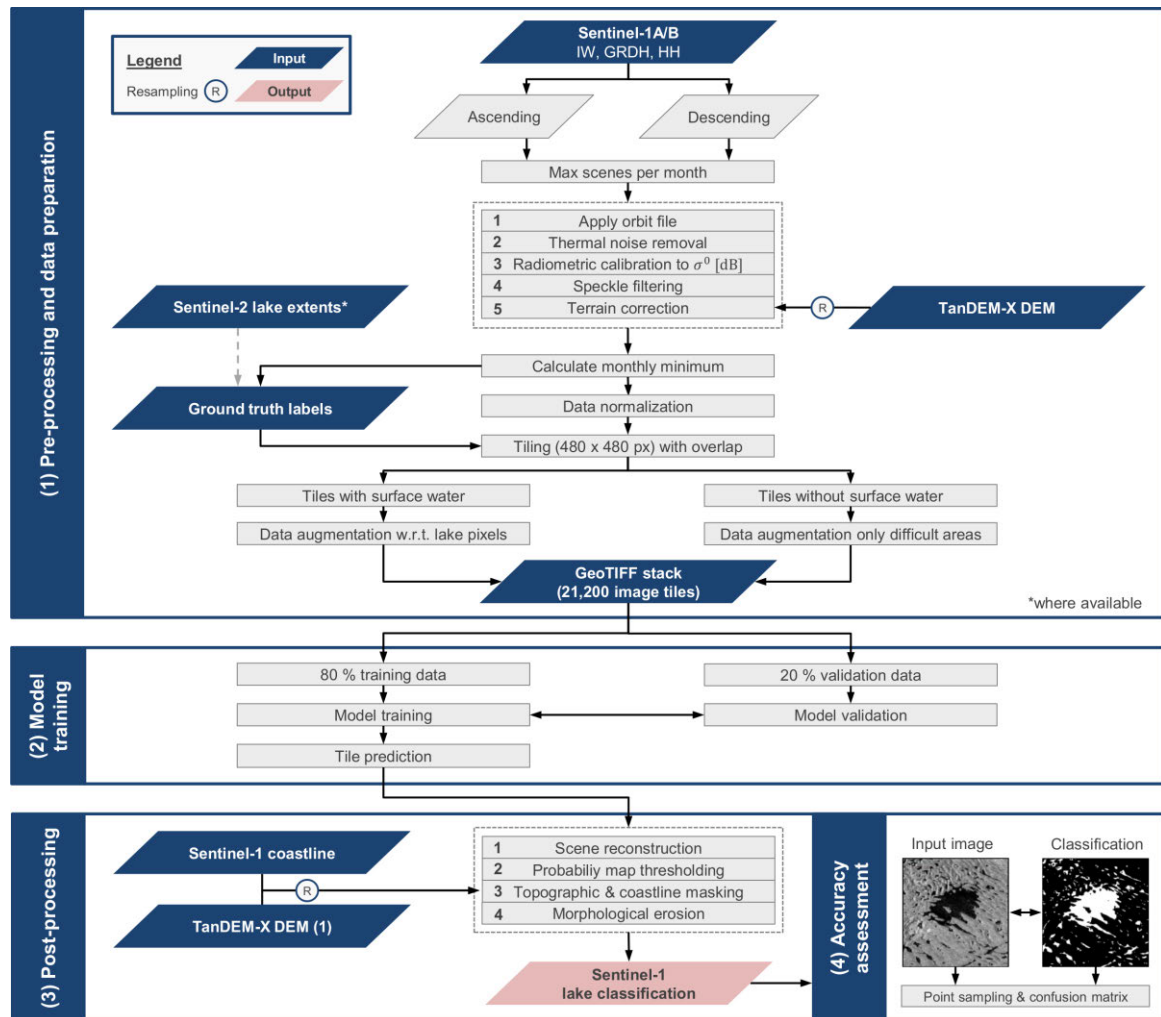


**Figure 5.6.** Workflow for Antarctic supraglacial lake extent classification in Sentinel-1 SAR imagery using deep learning. Modified after Dirscherl et al. (2021a).

### 5.3.1.1 Data Preparation and Pre-Processing

Before ingesting the Sentinel-1 IW data to the implemented deep learning pipeline (Chapter 5.3.1.2), the data were required to be pre-processed using sensor-specific processing tools. For this purpose, the open-source ESA Sentinel Application Platform (SNAP) was used. At first, the orbit metadata was updated with restituted orbit files and thermal noise was removed. In the following, the data were radiometrically calibrated to

retrieve the backscattering coefficient sigma naught ( $\sigma^0$ ) and speckle noise was removed. Finally, the calibrated data were corrected for topographic distortions using the TanDEM-X PolarDEM 90 m of Antarctica (Figure 5.6).

The pre-processed Sentinel-1 training data were then aggregated to monthly backscattering minimum products covering the 13 training regions shown in Figure 5.1a. In this context, the calculation of backscattering minimum products allowed to reinforce model training on low backscatter regions that are particularly difficult to discriminate from surface lakes with a comparatively low amount of data. The backscattering minimum products were then normalized to standardize all data to the same range. Z-score normalization was performed by subtracting the mean of the entire dataset from each backscattering minimum product and by dividing the result by the standard deviation. To increase the training dataset as well as to reduce border effects during scene prediction, the normalized data were tiled into 480 x 480-pixel patches (see Figure 5.11) with 200-pixel overlap. This patch size was found to capture both small and large supraglacial lakes. At the same time, sufficient spatial image context was included and GPU (Graphics Processing Unit) memory was kept low.

For an efficient training of the deep learning network, an even larger training dataset was yet required (Ronneberger et al., 2015). For this purpose, artificial data augmentation was performed through tile flipping, rotating and shifting. To achieve an improved consideration of the less representative “water” class, patches with particularly numerous water pixels were augmented at an increased rate. Here, patches with numerous lake pixels are defined as the upper quartile of all image patches sorted by their overall count of water pixels. In particular, tile flipping was performed down- and sideward, rotating was implemented for angles in the range of 45-315 degrees at 45-degree intervals and shifting was performed by moving the image patches by 100 pixels side- and downward. For the latter, the created empty space was filled through reflection of the adjacent image area. Overall, this resulted in 11 augmentation steps and reinforced model training on supraglacial meltwater. Pixels with fewer lake pixels, thus the remaining three quarters of all patches, were augmented only eight times. Here, tile rotation was performed at angles of 90, 180 and 270 degrees only. Likewise, patches covering difficult ice sheet surface features, including shadow, wet snow or blue ice, were augmented eight times, while patches covering non-water features were included at a low random selection rate. Overall, this augmentation strategy resulted in 21,200 Sentinel-1 image patches of which 64% covered the “water” class and 36% the “non-water” class. To support model calibration, the training dataset was further split into a random training (80%) and validation (20%) subset, to be fed to the deep learning network described below (Figure 5.7, Figure 5.8) (Dirscherl et al., 2021a). In this context,

the validation data are used to evaluate the loss and support the model in updating its parameters.

### 5.3.1.2 Deep Learning Model Training

The deep learning architecture used for semantic segmentation of supraglacial lakes in Sentinel-1 SAR imagery is based upon U-Net, a Fully Convolutional Network (FCN) that was originally developed for biomedical image segmentation (Ronneberger et al., 2015). In detail, U-Net was implemented with the aim of obtaining increased segmentation accuracies with only few training samples through the extensive use of data augmentation. The architecture of U-Net follows an encoder-decoder design where a contracting path with successive image convolutions and pooling operations captures the spatial image context and where a symmetrical expansion path with upsampling and convolution operations restores the original image size enabling localization (Figure 5.7) (Ronneberger et al., 2015). In addition, skip connections pass information from each downsampling block in the encoder to the decoder allowing to maintain fine-grained details. Besides the requirement of only few training samples, U-Net outperforms other DL networks due to its low training time and the consideration of the spatial image context. The latter can be improved through integration of additional modules such as Atrous Spatial Pyramid Pooling (ASPP) (Figure 5.7) (Hoeser et al., 2020). Encoder-decoder designs such as U-Net are commonly used for EO applications and are superior to naïve-decoder models due to the improved consideration and preservation of image detail (Hoeser et al., 2020). Approaches from object detection, including multi-task instance segmentation, were not considered as the main aim during method development was to extract pixel-based classifications.

In detail, the modified U-Net designed in this thesis consists of four downsampling blocks and four upsampling blocks that were adapted in order to fit the classification task at hand. As shown in Figure 5.8, each downsampling block consists of two successive image convolutions with a 3 x 3 filter and one-pixel-width padding for patch size conservation, a residual connection to the original input layers as well as a max pooling operation. In addition, a 0.3 dropout of input features is performed to prevent overfitting, thus to make the model more robust to different input data by training it by means of different reduced versions of it. The dropout value of 0.3 outperformed higher and lower values, respectively.

To provide more detail, the 3 x 3 image convolutions are performed to double the number of feature maps in each downsampling block starting with 32 in the first block and reaching 512 in the deepest block. In this context, the weights of the 3 x 3 convolutions are randomly initialized and updated during training. For activation, the Leaky non-linear Rectified Linear Unit (LeakyReLU) activation function was used.

LeakyReLU was chosen over the default ReLU activation function due to the broader range of accepted values that are passed to the following operation (Figure 5.9). Moreover, one specific feature of the designed architecture is the implementation of each downsampling block with residual connections (Figure 5.7, Figure 5.8). Residual connections combine the convoluted output of each downsampling unit with the original input images allowing deep architectures to perform considerably better than shallow networks (He et al., 2016). Before adding the input images to the convoluted output, the depth of the input images first had to be increased by convolution and activated with LeakyReLU (Figure 5.8, Figure 5.9). Residual connections were first introduced with the ResNet architecture (He et al., 2016) and were frequently employed in combination with CNNs such as U-Net due to the enhanced preservation of fine-grained detail being particularly relevant in EO (Chu et al., 2019; Diakogiannis et al., 2020; Miao et al., 2018; Sun et al., 2018; Zhang et al., 2018). As a last step, max pooling was performed with a 2 x 2 kernel in order to halve the image size before passing the data to the next downsampling block where an increasing number of feature maps is created.

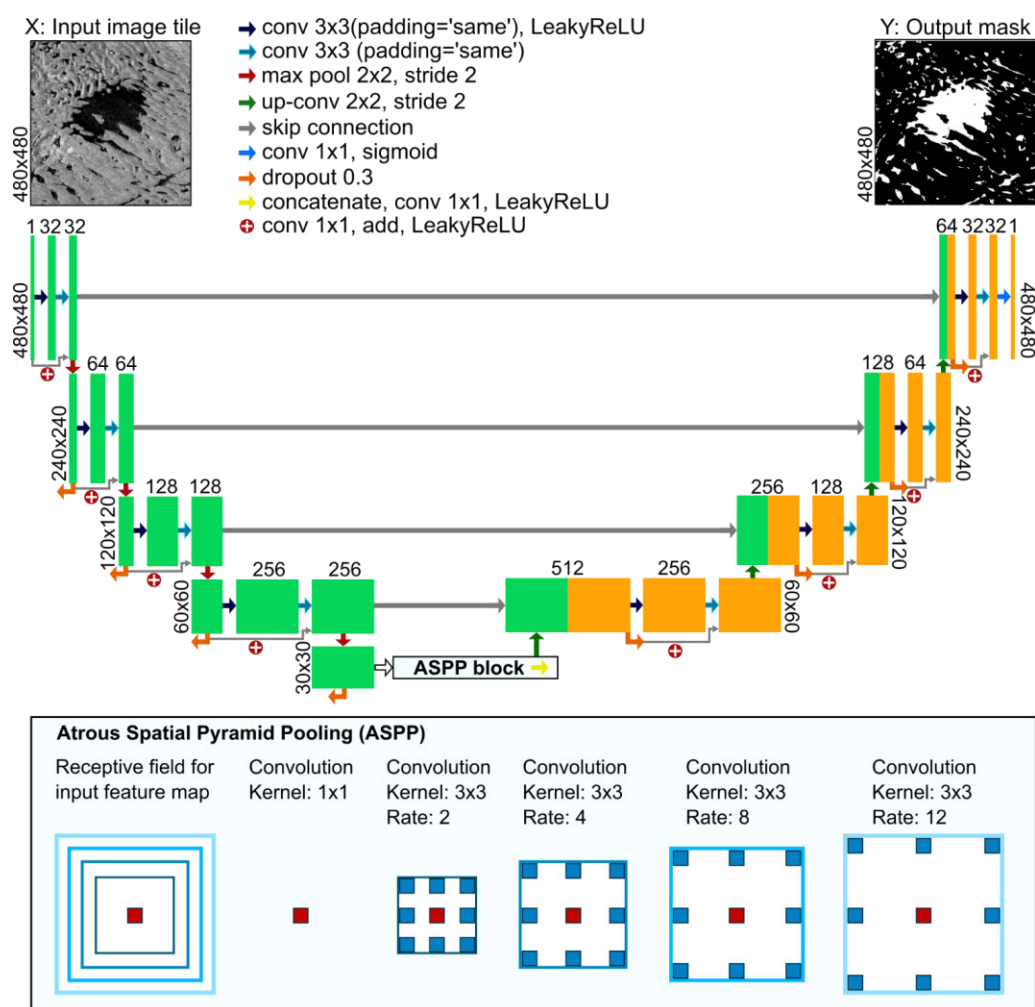


**Figure 5.7.** Deep learning architecture based on residual U-Net used for semantic segmentation of Sentinel-1 SAR imagery. Modified after Dirscherl et al, (2021a).

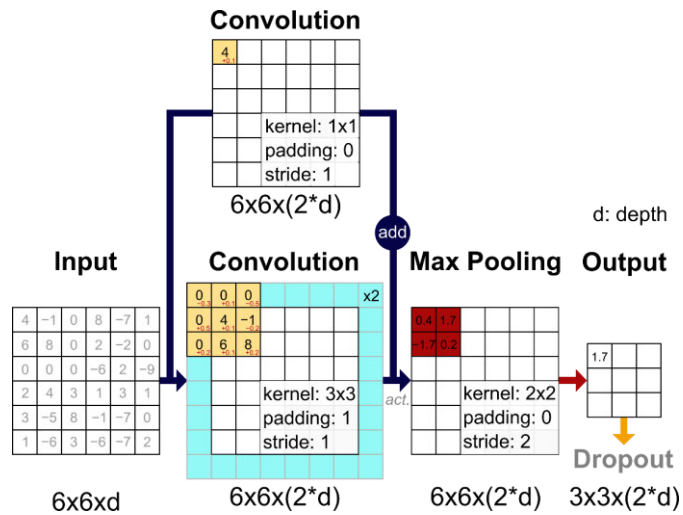


**Figure 5.8.** Sketch of a single downsampling unit with a residual connection and dropout. To simplify, no activation function (act.) is applied. Modified after Dirscherl et al. (2021a).

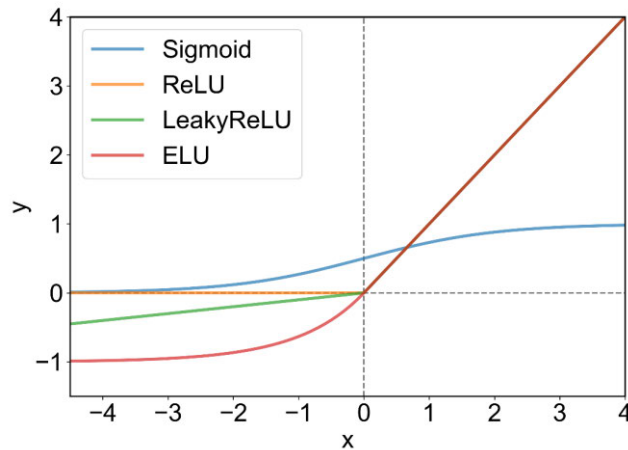


**Figure 5.9.** Exemplary functions available for activation of convoluted layers. ReLU: Rectified Linear Unit. LeakyReLU: Leaky non-linear Rectified Linear Unit. ELU: Exponential Linear Unit.

In contrast to the conventional U-Net, the bottleneck of the designed deep learning architecture is an ASPP module. ASPP was first introduced with the DeepLab family (Chen et al., 2016) and uses dilated convolution kernels to increase the receptive field of the filters for extraction of multiscale information at constant image resolution (Figure 5.7) (Chen et al., 2017, 2018a). The use of ASPP greatly improves the consideration of the spatial image context and enables the detection of image features with varying sizes making it particularly suitable for the extraction of Antarctic supraglacial lakes in Sentinel-1 SAR imagery (e.g. Figure 3.1a). In addition, ASPP reduces the occurrence of blobby segmentation results and further improves the detection of fine-grained detail (Hoeser et al., 2020). Due to its numerous advantages, the integration of ASPP in CNNs such as U-Net was frequently performed (e.g. Baheti et al., 2020; He et al., 2019; Liu et al., 2019; P. Zhang et al., 2018). Apart from a simple  $1 \times 1$  convolution, ASPP was implemented with atrous rates of 2, 4, 8 and 12 (Figure 5.7) enabling an improved detection of image

features of varying sizes and high density (Baheti et al., 2020) compared to the originally proposed rates of 6, 12, and 18 in DeepLabV3+ (Chen et al., 2018b). Before passing the multiscale feature maps to the following upsampling block, the results were concatenated and convoluted.

On the other hand, the decoder of the modified U-Net restores the original patch size through successive  $2 \times 2$  upsampling operations as part of four residual blocks designed symmetrical to the downsampling units (Figure 5.7). At each convolutional block in the decoder, the up-sampled output is combined with feature maps from the encoder via skip connections enabling precise localization and improving the preservation of image detail. The last 32 feature maps are finally converted to a  $480 \times 480$ -pixel prediction probability map for the “water” class (see Figure 5.11) using a  $1 \times 1$  convolution that is activated with the sigmoid activation function (Figure 5.9). For model compilation, the Adamax optimizer, the binary crossentropy loss function as well as an initial learning rate of 0.001 was used. In this context, the learning rate can be regarded as one of the most crucial hyperparameters for model calibration. For this reason, an additional callback was set to automatically multiply the learning rate by 0.1 if the validation loss did not improve over three epochs. The deep learning model finally converged after 30 epochs (Figure 5.10a) and outperformed shallow and deep versions of the modified U-Net as well as architectures without ASPP or residual connections. The final model consists of 10.6 million trainable parameters and was trained with a batch size of 2 on a GeForce GTX 1,080 GPU using the (Python) Keras Application Programming Interface built on top of TensorFlow 2.2. Figure 5.10 provides details on the performance of the full training process including loss and accuracy metrics. Moreover, Figure 5.11 shows an exemplary prediction outcome for a  $480 \times 480$ -pixel input patch.

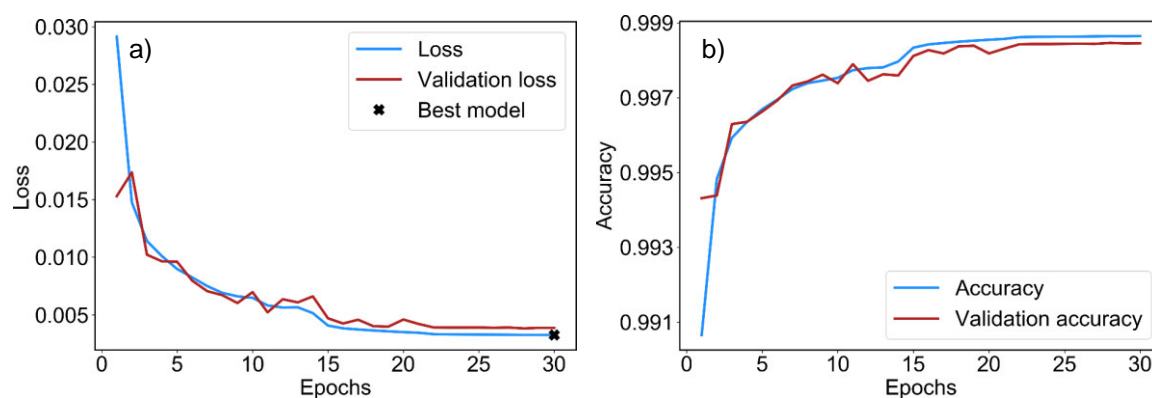


**Figure 5.10.** Performance metrics of the training process. (a) Loss obtained from the training (blue) and validation (red) subset with the best model performance marked at epoch 30 (black cross). (b) Accuracy obtained from the training (blue) and validation (red) subset.

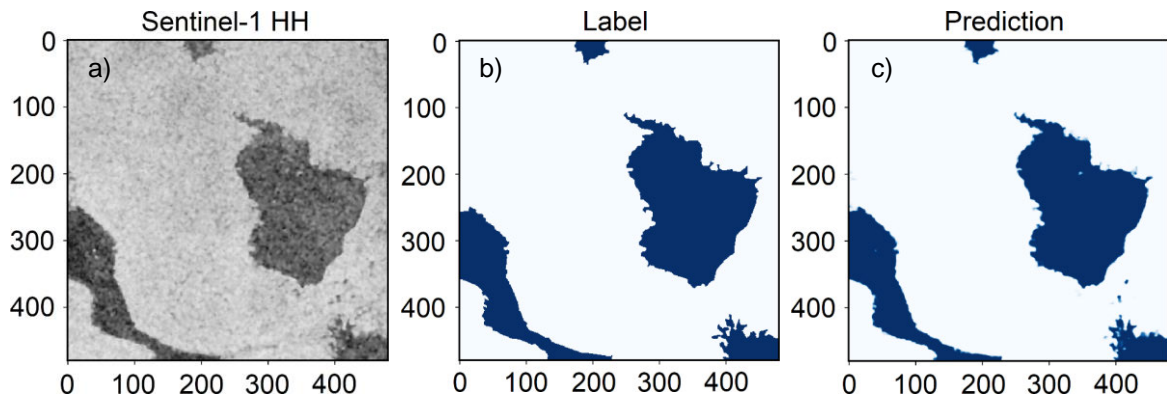


**Figure 5.11.** Prediction results for an exemplary 480 x 480-pixel patch. (a) Original Sentinel-1 input patch. (b) Manually drawn label. (c) Prediction outcome for the input patch in (a). The x- and y-axes show the number of pixels in both directions. Data: (Copernicus Sentinel-1 data)

### 5.3.1.3 Post-Processing

In order to obtain the final classification products, the model was used to predict the Sentinel-1 testing data and the corresponding outcomes were refined as part of post-classification. As can be seen in Figure 5.6, four main post-processing steps were implemented. At first, the image patches had to be reshaped into the original image size of the Sentinel-1 scenes whereat overlap regions between adjacent image patches were averaged. Next, the reshaped prediction probability maps had to be thresholded in order to retrieve binary classification products. For this purpose, all pixels above a threshold of 0.5 were assigned to the “water” class and all pixels below that threshold were assigned to the “non-water” class. Higher and lower thresholds were also tested but resulted in increased rates of false negatives and positives, respectively. In a next step, the thresholded classification maps were masked using the TanDEM-X PolarDEM as well as a buffered version of the 2018 Sentinel-1 coastline (Chapter 5.2). For the latter, buffering was necessary in order to mask classification errors over open ocean where the coastline strongly retreated inland since the acquisition of the coastline data. On the other hand, topographic masking allowed to exclude remaining misclassifications in high altitudes  $>1,500$  m as well as over particularly steep terrain ( $>5\%$ ). Here, supraglacial lake formation is usually not promoted, as shown in previous work (Stokes et al., 2019). In addition, surface slopes greater than the radar look angle may cause image regions to appear in shadow, thus with backscatter values as low as surface lakes (Figure 4.10i). Finally, a last step involved morphological erosion for elimination of lake area  $<300$  m<sup>2</sup>. During the same step, isolated islands within the boundary of surface lakes were removed. The final classification rasters were provided at 10 m pixel spacing.



### 5.3.2 Sentinel-2

Similar as for Sentinel-1, the development of an automated supraglacial lake extent mapping technique for Sentinel-2 had to fulfil the requirements outlined in Chapter 4.3.2. In this context, particularly the limitations stated in Chapter 4.2.1 were required to be overcome. These mainly include difficulties in discriminating between supraglacial lakes and ice sheet surface features such as shadow, blue ice or slush but also the similar appearance of supraglacial lakes and submerged icebergs in frontal embayments. Due to these challenges as well as the requirement of a mapping technique with spatio-temporal transferability to the entire Antarctic Ice Sheet, simple thresholding, clustering or time series methods were not suitable and a supervised machine learning classifier was employed (Dirscherl et al., 2020b). As mentioned, supervised machine learning is commonly employed for remote sensing image classification and is based upon the categorization of training data with prior information. In contrast to Sentinel-1, method developments with Sentinel-2 did not require the use of more advanced image classification techniques, e.g. from deep learning, due to the availability of multi-spectral information as well as the less complex classification task (Table 4.1). In fact, deep learning model training is far more time-consuming and computationally intensive and should only be applied if the classification problem at hand cannot be solved with conventional machine learning techniques.

To provide more detail, the Sentinel-2 data were classified by means of a RF classifier. RF belongs to the family of decision trees aiming at the deduction of rule sets from a set of input variables (Breiman, 2001). The full workflow for classification of Antarctic supraglacial lakes in optical Sentinel-2 data is outlined in Figure 5.12 consisting of (1) pre-processing and data preparation, (2) RF model training, (3) post-classification and (4) accuracy assessment. While the methods for the accuracy assessment are outlined in Chapter 5.5, the following chapters provide details on the remaining steps.

#### 5.3.2.1 Data Preparation and Pre-Processing

To start with, the Sentinel-2 data were pre-processed to correct for atmospheric effects. For this purpose, Sen2Cor, a processing tool enabling the conversion from Level-1C Top-of-Atmosphere products to Level-2A Bottom-of-Atmosphere reflectance data, was used (ESA, 2015; Louis et al., 2016). Following atmospheric correction, a discrimination analysis between land surface classes “water”, “snow/ice”, “rock” and “shadow” was performed on the basis of the Sentinel-2 training data revealing the high suitability of Sentinel-2 reflectance bands 2, 3, 4 and 8 as input variables for RF image classification (Figure 5.13). In addition, the selected bands, together with the available shortwave infrared bands (Table 5.2), were used to calculate a range of spectral indices as additional input variables for RF model training. In total, 10 spectral indices were

derived (Table 5.4, Figure 5.13) for an improved identification of water (Ding, 2009; Feyisa et al., 2014; Kauth and Thomas, 1976; McFeeters, 1996; Schwatke et al., 2019; Williamson et al., 2017; Yang and Smith, 2013), rock (ESA, 2019; Huete, 1988), snow/ice (Hall et al., 1995; Keshri et al., 2009; Xu, 2006) and shadow (Feyisa et al., 2014; Li et al., 2016).

Furthermore, the TanDEM-X topographic data, including elevation, slope, relief and roughness information, as well as the rasterized training labels were resampled to the highest resolution of Sentinel-2 (10 m) using the nearest neighbor algorithm (Figure 5.12). In this context, the four topographic variables were included to test their suitability for an improved discrimination between “water” and “non-water” in high altitudes or steep terrain where supraglacial meltwater usually does not accumulate. Finally, the 18 training variables were clipped to the extent of the training labels and split into a random training (70%) and validation (30%) subset used for model calibration (Chapter 5.3.2.2).

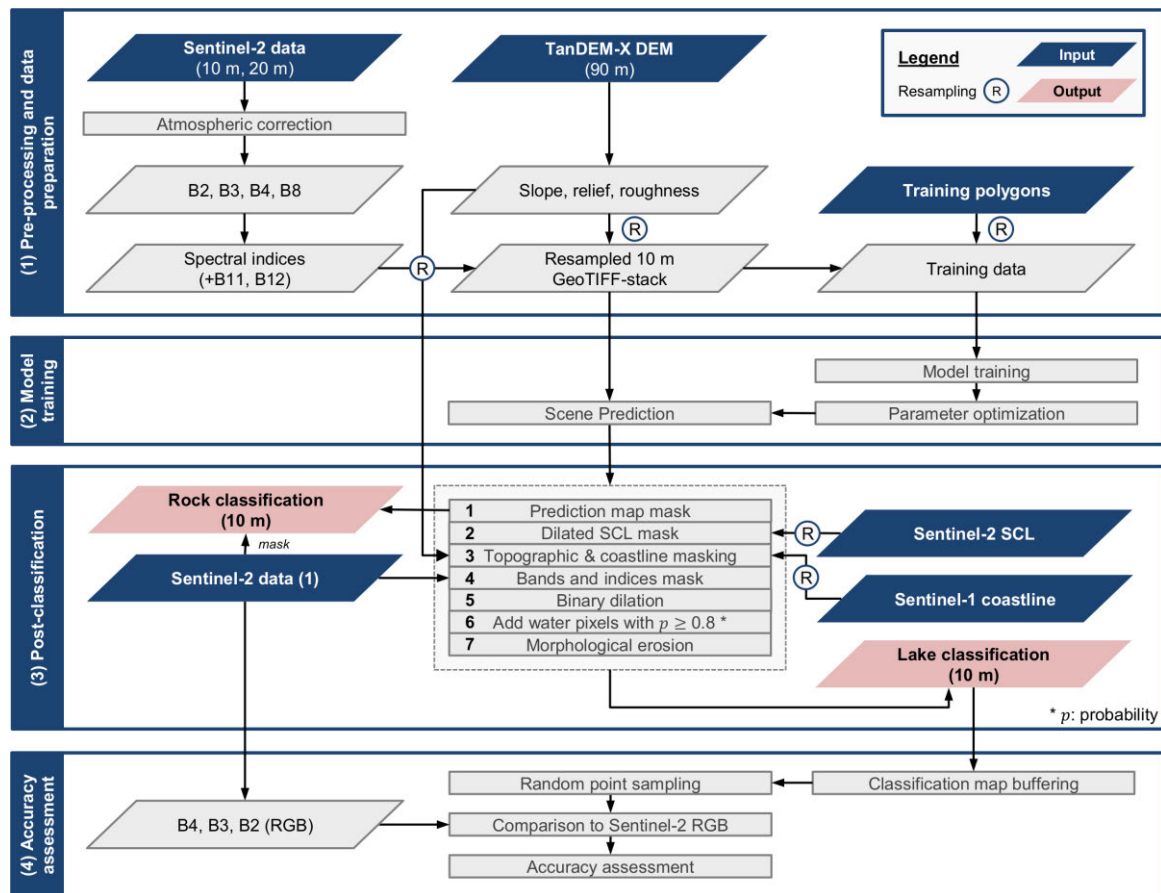


**Figure 5.12.** Workflow for Antarctic supraglacial lake extent classification in optical Sentinel-2 imagery using machine learning. Modified after Dirscherl et al. (2020b).

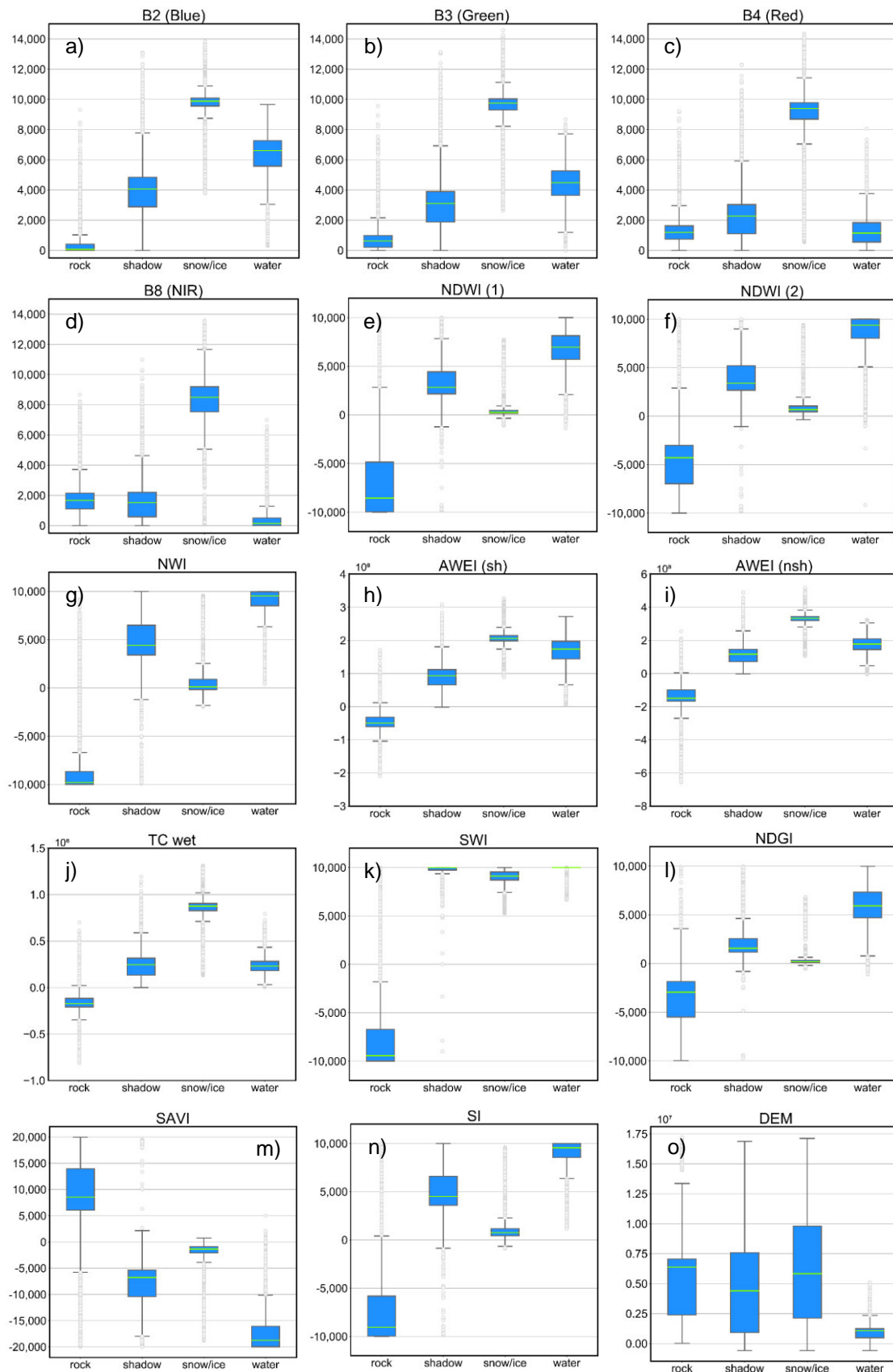


**Figure 5.13.** Discrimination analysis for classes “rock”, “shadow”, “snow/ice” and “water”. Sentinel-2 bands 2, 3, 4 and 8 (a-d), normalized indices (e-n) and scaled topographic variables (o-r). The boxplots show the interquartile ranges, the median, the full data range and outliers. Modified after Dirscherl et al. (2020b).

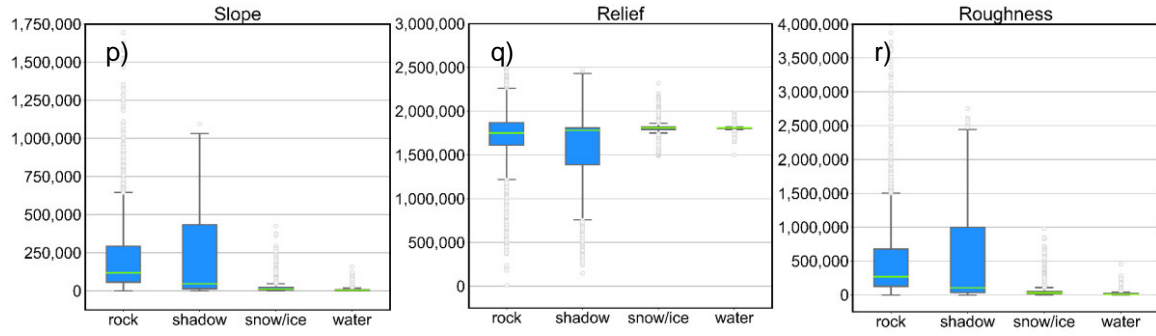


**Figure 5.13.** Continuation.

**Table 5.4.** Selected spectral indices for supraglacial lake classification with a RF classifier. See Table 5.2 for more detailed information on the spectral bands used for index calculation. NDWI: Normalized Difference Water Index. NWI: New Water Index. AWEI<sub>sh</sub>: Automated Water Extraction Index with shadow removal. AWEI<sub>nsh</sub>: AWEI with dark area removal. TC<sub>wet</sub>: Tasseled Cap for wetness. SWI: Soil/Water Index. NDGI: Normalized Difference Glacier Index. SAVI<sub>mod</sub>: modified Soil Adjusted Vegetation Index. SI<sub>mod</sub>: modified Shadow Index.  $\rho$ : surface reflectance. Modified after Dirscherl et al. (2020b).

Index	Mathematic Formulation	References
NDWI <sub>1</sub>	$(\rho_{blue} - \rho_{red}) / (\rho_{blue} + \rho_{red})$	(Williamson et al., 2017; Yang and Smith, 2013)
NDWI <sub>2</sub>	$(\rho_{green} - \rho_{NIR}) / (\rho_{green} + \rho_{NIR})$	(McFeeters, 1996)
NWI	$(\rho_{blue} - (\rho_{NIR} + \rho_{SWIR1} + \rho_{SWIR2})) / (\rho_{blue} + (\rho_{NIR} + \rho_{SWIR1} + \rho_{SWIR2}))$	(Ding, 2009)
AWEI <sub>sh</sub>	$\rho_{blue} + (2.5 \times \rho_{green}) - (1.5 \times (\rho_{NIR} + \rho_{SWIR1})) - (0.25 \times \rho_{SWIR2})$	(Feyisa et al., 2014)
AWEI <sub>nsh</sub>	$4 \times (\rho_{green} - \rho_{SWIR1}) - ((0.25 \times \rho_{NIR}) + (2.75 \times \rho_{SWIR2}))$	(Feyisa et al., 2014)
TC <sub>wet</sub>	$(0.1509 \times \rho_{blue}) + (0.1973 \times \rho_{green}) + (0.3279 \times \rho_{red})$ $+ (0.3406 \times \rho_{NIR}) - (0.7112 \times \rho_{SWIR1})$ $- (0.4572 \times \rho_{SWIR2})$	(Kauth and Thomas, 1976; Schwatke et al., 2019)
SWI	$(\rho_{blue} - \rho_{SWIR1}) / (\rho_{blue} + \rho_{SWIR1})$	(ESA, 2019)
NDGI	$(\rho_{green} - \rho_{red}) / (\rho_{green} + \rho_{red})$	(Keshri et al., 2009)
SAVI <sub>mod</sub>	$((\rho_{NIR} - \rho_{green}) / (\rho_{NIR} + \rho_{green} + 1)) \times 2$	(Huete, 1988)
SI <sub>mod</sub>	$(\rho_{blue} - \rho_{NIR}) / (\rho_{blue} + \rho_{NIR})$	(Li et al., 2016)

### 5.3.2.2 Random Forest Model Training

RF is a frequently employed classifier for remote sensing image classification (Berhane et al., 2018; Immitzer et al., 2012; Son et al., 2018; Tsai et al., 2019) and is superior to other classification algorithms (e.g. Support Vector Machines) due to its easy implementation, simple parameter tuning, low risk of overfitting, low computational time and parallel processing capabilities (Belgiu and Drăguț, 2016; Breiman, 2001; Pal, 2005; Sazonau, 2012). RF is based upon the use of multiple uncorrelated decision trees that are trained on random subsets of the original training data (Figure 5.14). This random selection strategy is referred to as bootstrap aggregating or bagging whereat each subset accounts for two thirds of the training data (Belgiu and Drăguț, 2016; Breiman, 2001). The remaining data, the Out-Of-Bag samples, are used for internal cross-validation. To obtain the final classification outcome, the predictions of all uncorrelated

decision trees are aggregated and the class with the maximum votes is assigned (Figure 5.14) (Breiman, 2001). Furthermore, RF enables the deduction of variable importance plots describing the relevance of each input dataset provided to the classifier. These are particularly beneficial for further model testing and selection with restricted input variables. To retrieve the average variable importance for all training regions and classes, the mean decrease in Gini, a metric for retrieval of the best split at each node of a decision tree (Breiman, 2001), is calculated during training. Figure 5.14 shows a sketch of a RF decision tree classifier with multiple decision trees.

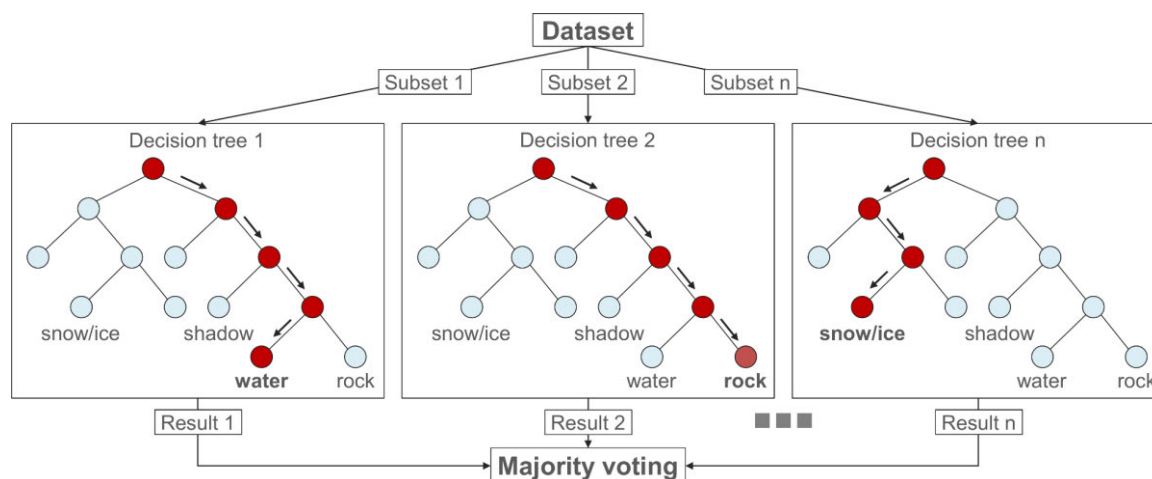


**Figure 5.14.** Sketch of Random Forest with multiple decision trees and majority voting.

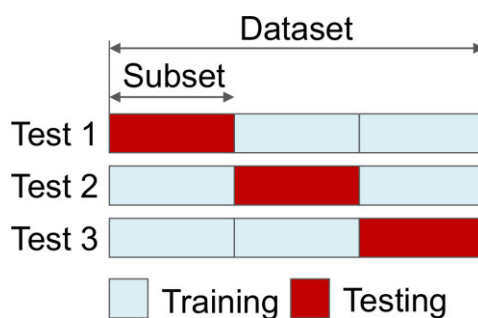


**Figure 5.15.** Sketch of 3-fold cross-validation for robust Random Forest model training.

For implementation of RF, Python’s scikit-learn library was used (Pedregosa et al., 2011). In particular, the “RandomizedSearchCV” and “GridSearchCV” functionalities were employed for hyperparameter tuning ensuring a suitable use of model parameters during training (Pedregosa et al., 2011). First, “RandomizedSearchCV” was used to narrow down a randomly created grid of initial parameter inputs that were defined in agreement with the default parameters of scikit-learn (Table 5.5). Here, 50 random iterations were performed with 3-fold cross-validation resulting in a total number of 150 tested combinations. Cross-validation is a frequently employed method to prevent an overfitting of the model to the training data. For 3-fold cross-validation, the training

dataset is split into three instances (or folds) and each parameter combination is iteratively trained on two random subsets (Figure 5.15). The remaining subset is used for internal cross-validation. Cross-validation is performed until all possible combinations are tested allowing to obtain more robust parameter estimations (Figure 5.15). The results of the random parameter search were then used to present a refined parameter grid to “GridSearchCV” testing all possible parameter combinations on three folds and returning the final optimum parameter combination. Table 5.5 provides details on the initial random parameter grid, the refined parameter grid as well as the final parameter selection. In this context, the optimized model parameters include the total number of trees in the forest, the maximum depth of a single tree, the number of features to consider when looking for the best split, the minimum number of samples required to split a node as well as the minimum number of samples required at leaf node (Table 5.5). Furthermore, an additional parameter was set in order to train the model with balanced class samples, thus to avoid an overfitting of the model to the class representing most data points in the training data.

**Table 5.5.** Hyperparameter tuning for supraglacial lake extent classification in Sentinel-2 imagery with the RF classifier. sqrt: square root. n\_features: number of features.

Parameter	Initial random search grid	Refined search grid	Final parameters
Number of trees	[200, 400, 600]	[400, 600, 800]	[600]
Maximum depth of a tree	[60, 80, None*]	[80, None*]	[80]
Number of features for best split	[sqrt(n_features), 4, 6, 8]	[sqrt(n_features), 4]	[sqrt(n_features)]
Minimum number of samples to split a node	[2, 5, 10]	[2, 5]	[2]
Minimum number of samples at leaf node	[1, 2, 4]	[1, 2]	[1]

\*nodes are expanded until all leaves are pure or until all leaves contain less than the minimum number of samples required to split a node

In addition to model training with all 18 input variables (Figure 5.16a), three further models were calibrated on the basis of restricted input data. In detail, one model was trained without topographic variables (Figure 5.16b) and one model was trained without topographic variables and with 10 m Sentinel-2 bands and indices only (Figure 5.16c). A final model was trained with only half of all features (Figure 5.16d). Here, only variables with importance weights above the median of all feature importances were considered. In this context, the training of different versions of the original RF model allowed to evaluate the influence of different variable combinations and whether topographic data can adequately support model training.

As can be seen in Figure 5.16a, the included topographic variables in fact returned lowest importance values (<3), thus are not informative for overall image classification. On the other hand, the feature importances of Sentinel-2 surface reflectance bands were

comparatively high with bands 3-4 showing importance values >5 in all four model versions. Comparatively high importance values were also computed for various indices including SWI, NWI, AWEI<sub>sh</sub>, AWEI<sub>nsh</sub>, TC<sub>wet</sub> and NDGI. Lower importance values were found for indices NDWI<sub>1</sub>, NDWI<sub>2</sub>, SI and SAVI with the exception of the model trained on 10 m variables only. Here, also indices SI and SAVI returned high importance values.

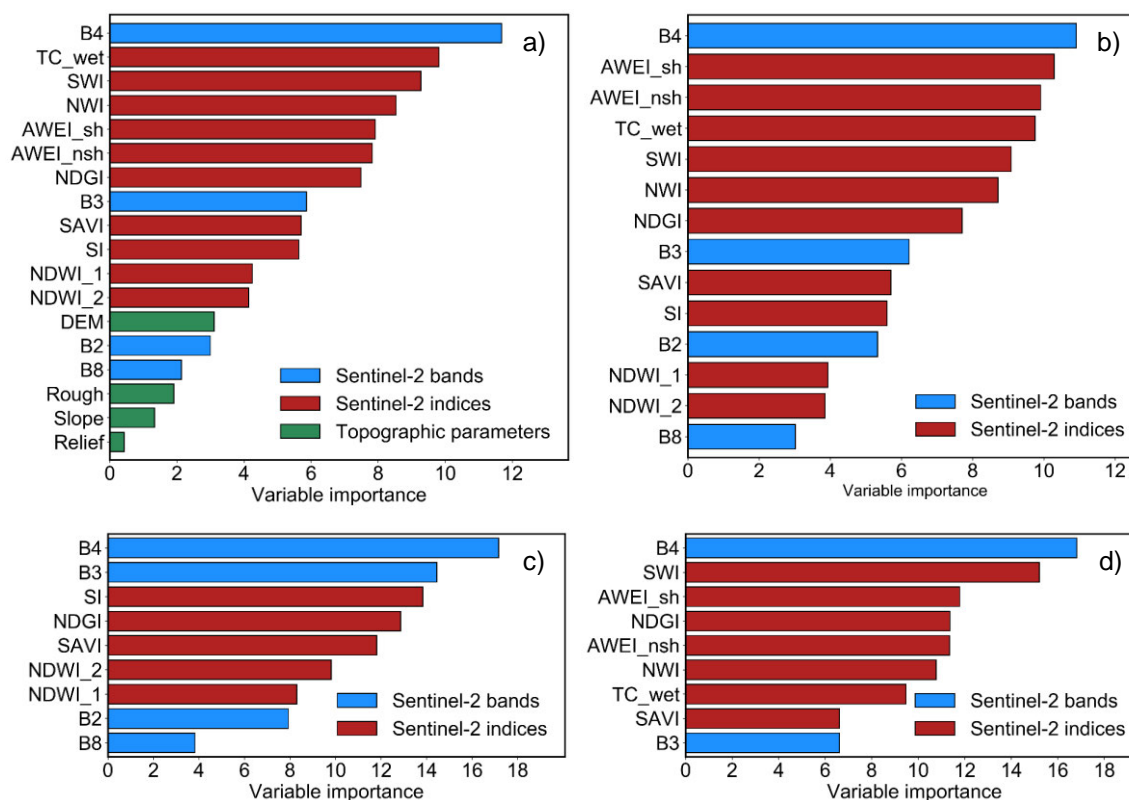


**Figure 5.16.** Variable importance plots obtained from training the Random Forest model (a) with all features, (b) without topographic variables, (c) with 10 m bands and indices only and (d) with variables representing the upper median of all importance values only. Importance values represent the mean of all classes and training regions. Modified after Dirscherl et al. (2020b).

### 5.3.2.3 Post-Processing

Following model training and test scene prediction, the obtained classification results were further refined using a range of universal post-processing steps (Figure 5.12) (Dirscherl et al., 2020b). At first, the prediction probabilities were converted to class values. For this purpose, the probability values of all four classes were aggregated over each pixel and the class with the highest probability was assigned. During this step, a rock classification map was extracted as side-product. The remaining post-classification steps were mainly performed to mask remaining misclassifications, e.g. over shadow, blue ice or slush (Chapter 4.2.1). For this purpose, a dilated version of the Scene Classification Layer (SCL), an automated output of data pre-processing, was used to mask defective pixels, dark area pixels and cloud shadow. Moreover, a dilated version of

the Sentinel-1 coastline of 2018 (Baumhoer et al., 2021) was used for the masking of pixels seaward of the coastline where submerged icebergs or meltwater atop calved icebergs might have introduced false positive classifications. Another step involved topographic masking. Similar as for Sentinel-1 (Chapter 5.3.1.3), pixels in high altitudes >1,500 m and in particularly steep terrain >5% were excluded. In contrast to Figure 5.13p suggesting the use of a lower slope threshold, this value was set rather conservative due to the TanDEM-X PolarDEM being from a different time step as well as its lower spatial resolution compared to Sentinel-2. In fact, lower slope thresholds were found to cause the masking of true positive supraglacial lake pixels, e.g. where steep crevasses or fractures used to be present during the acquisition of the underlying SAR data. Following this, a range of band and index thresholds were employed to further improve the masking of misclassifications over shadow, blue ice and slush. As this resulted in the final classification maps to be rather conservative estimates of supraglacial lake occurrence, the final classification layers were additionally buffered by 12 pixels and all pixels above a “water” probability threshold of 0.8 within that boundary were accepted as supraglacial lake pixels. Finally, a last step involved morphological erosion in order to eliminate lake area and isolated islands <300 m<sup>2</sup>. The final Sentinel-2 classification products were provided at 10 m pixel spacing.

### **5.3.3 Fusion of Sentinel-1 and Sentinel-2 Classifications**

Following Sentinel-1 and Sentinel-2 scene prediction and post-classification, the obtained classification results covering George VI Ice Shelf during January 2020 as well as Amery Ice Shelf during January 2019 were combined through decision-level fusion. Decision-level fusion describes the process of mosaicking all obtained classification results within a given time period to maximum supraglacial lake extent mapping products considering all classified supraglacial lake pixels in a single satellite scene as valid. In particular, a bi-weekly temporal interval of approximately 14 days was chosen for data fusion. This interval allows the analysis of time series at intra-annual temporal resolution while ensuring a sufficient amount of data to be included. At the same time, the selected time span keeps potential errors due to the movement of lakes with ice flow at minimum. In fact, regions with particularly fast ice flow can lead to overestimations of supraglacial lake coverage when particularly long observational periods (>1 month) are considered. For George VI Ice Shelf, two fused mappings were derived, one covering early January 2020 and one covering late January 2020. Over Amery Ice Shelf, only the first half January 2019 was considered. As stated in Chapter 4.3.2, fused classification products allow to obtain a more complete mapping of supraglacial lakes and are of particular importance to exploit and overcome sensor-specific advantages and limitations.



## 5.4 Results

In the following chapters, the classification results for the Sentinel-1 and Sentinel-2 test data are presented. In addition, the results of the intra-annual and inter-annual analysis of supraglacial lake dynamics on George VI and Amery ice shelves are shown. Finally, Chapter 5.4.3 presents the fused supraglacial lake extent classification products for George VI and Amery ice shelves at sub-monthly temporal resolution.

### 5.4.1 Sentinel-1

For Sentinel-1, a total of 10 test scenes (Figure 5.1a, Table 5.1) was classified for evaluation of the implemented deep learning framework. Figure 5.17 shows extracts of the final classification results highlighting the good functionality of the developed workflow. In particular, lakes with low visual contrast (Figure 5.17a-c), roughened lake surfaces (Figure 5.17b-c) as well as lakes of strongly varying sizes (Figure 5.17b) were classified correctly. As can be seen in Figure 5.17, also the differentiation between supraglacial lakes and open ocean (Figure 5.17c,f), shadowing (Figure 5.17d,g) or different snow and ice types (Figure 5.17a,c,d,f,h,j) was successful. At the same time, particularly large or elongated lakes, e.g. on Riiser-Larsen or Rennick ice shelves (Figure 5.17e,i), showed minor gaps in the lake classifications. Moreover, the results reveal highly fluctuating lake extents with particularly numerous and large lakes (diameter or length  $\geq 1$  km) over George VI (Figure 5.17b), Bach (Figure 5.17c), Riiser-Larsen (Figure 5.17e), Amery (Figure 5.17g), Moscow University (Figure 5.17i) and Rennick ice shelves (Figure 5.17j). Fewer lakes with diameters  $\leq 1$  km were observed over Abbot (Figure 5.17a), Larsen C (Figure 5.17d) and Shackleton ice shelves (Figure 5.17h) as well as in Enderby Land (Figure 5.17f).

Furthermore, Figure 5.18 shows intra-annual supraglacial lake extent dynamics over northern George VI Ice Shelf. In detail, months December 2019 and February 2020 are represented by monthly supraglacial lake extent mapping products and January 2020 classifications result from single Sentinel-1 acquisitions. While supraglacial lake coverage during December 2019 was comparatively low ( $\sim 5$  km<sup>2</sup>), lake extents started to increase significantly during January 2020. On 7 January 2020, supraglacial lakes on George VI Ice Shelf covered an area of 93 km<sup>2</sup> and further expanded until 13 January, when the peak of supraglacial lake coverage was reached. Here, a total area of  $\sim 341$  km<sup>2</sup> was covered by supraglacial lakes. Six days later, on 19 January 2020, lakes stretched over an area of  $\sim 30$  km<sup>2</sup> and again expanded until 25 January, when a total ice shelf area of  $\sim 102$  km<sup>2</sup> was covered by surface meltwater. Overall, the maximum lake extent during January 2020 was computed at  $\sim 385$  km<sup>2</sup>. In February 2020, supraglacial lakes were found to extend over an ice shelf area of  $\sim 107$  km<sup>2</sup> only.

Finally, an additional study region covering the south-west Greenland Ice Sheet on 28 July 2018 was evaluated in order to highlight the spatio-temporal transferability of the developed method to regions beyond Antarctica (Figure 5.19). Here, supraglacial lakes were comparatively large with well-defined boundaries. This is also reflected in the automated classification results where lakes appear distinctively and well-delineated.

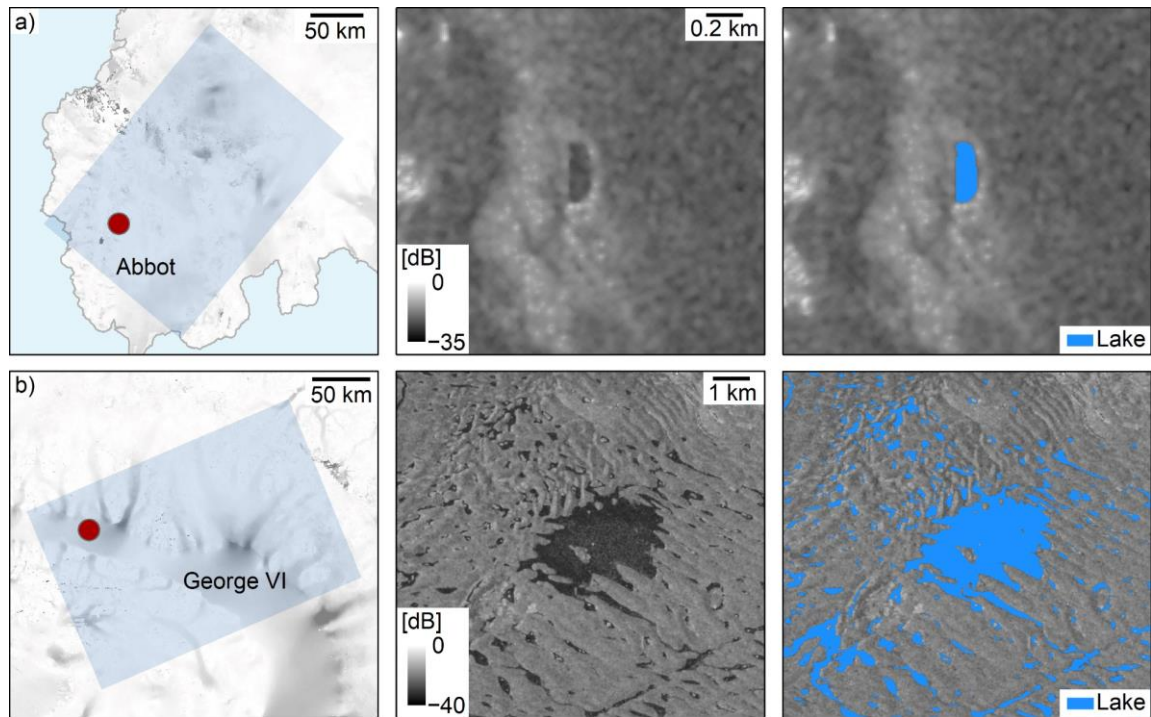


**Figure 5.17.** Classification results for the Sentinel-1 test data. From left to right, each sub-plot in (a-j) shows an overview map of the location of the Sentinel-1 test scene (blue shading), an extract of the Sentinel-1 test scene at the location of the red circle in (a-j) as well as the automated classification result for the image extract. (a) Abbot, (b) Bach, (c) George VI, (d) Larsen C, (e) Riiser-Larsen, (g) Amery, (h) Shackleton and (i) Moscow University ice shelves. (f) Enderby Land. (j) Rennick Glacier. The red line in (c,f) shows the 2018 Sentinel-1 coastline. The background in (a-j) is the LISA velocity mosaic. Modified after Dirscherl et al. (2021a). Data: (Copernicus Sentinel-1 data; Fahnestock et al., 2016; Mouginot et al., 2017b; Rignot et al., 2013; Scambos et al., 2019).

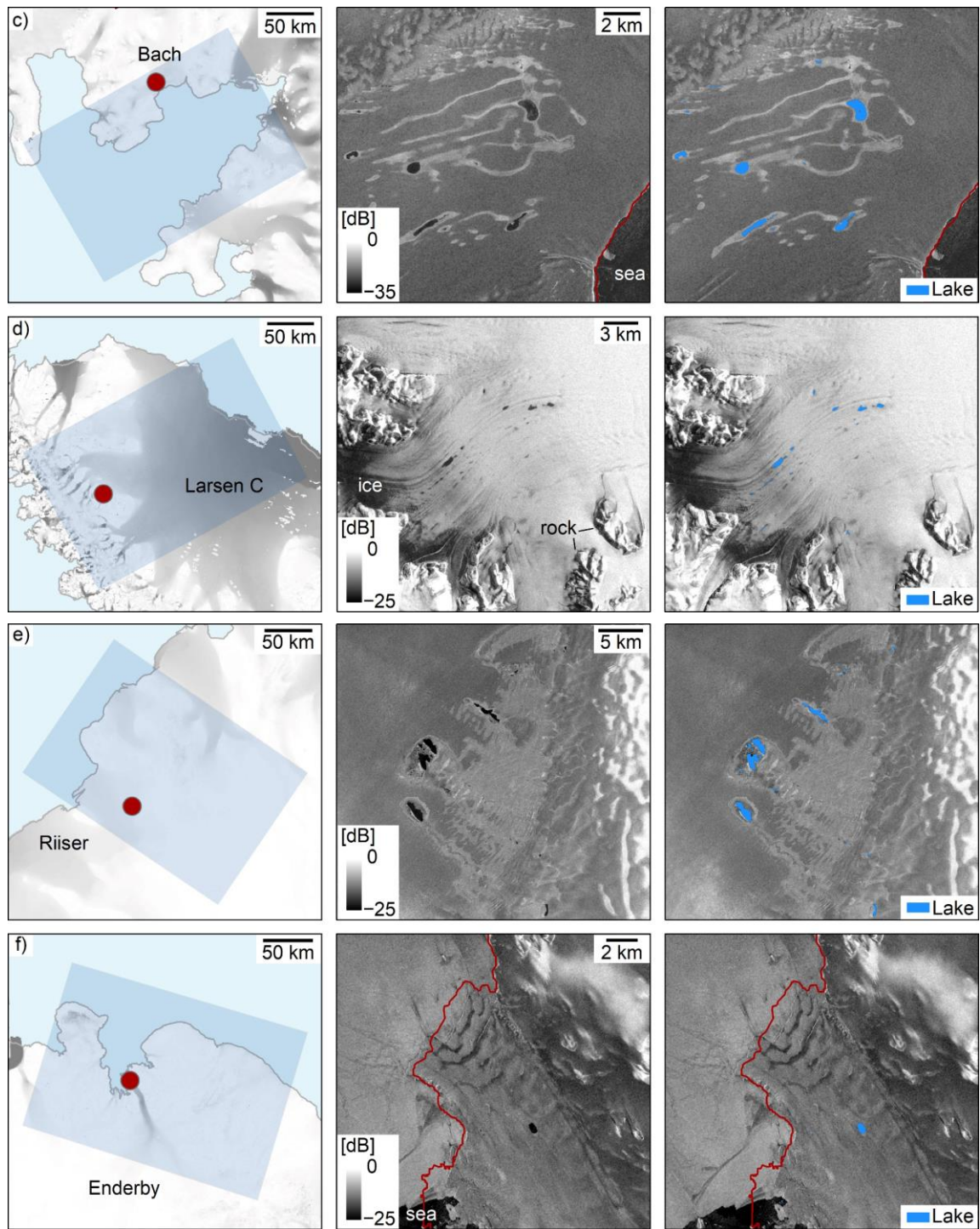


Figure 5.17. Continuation.



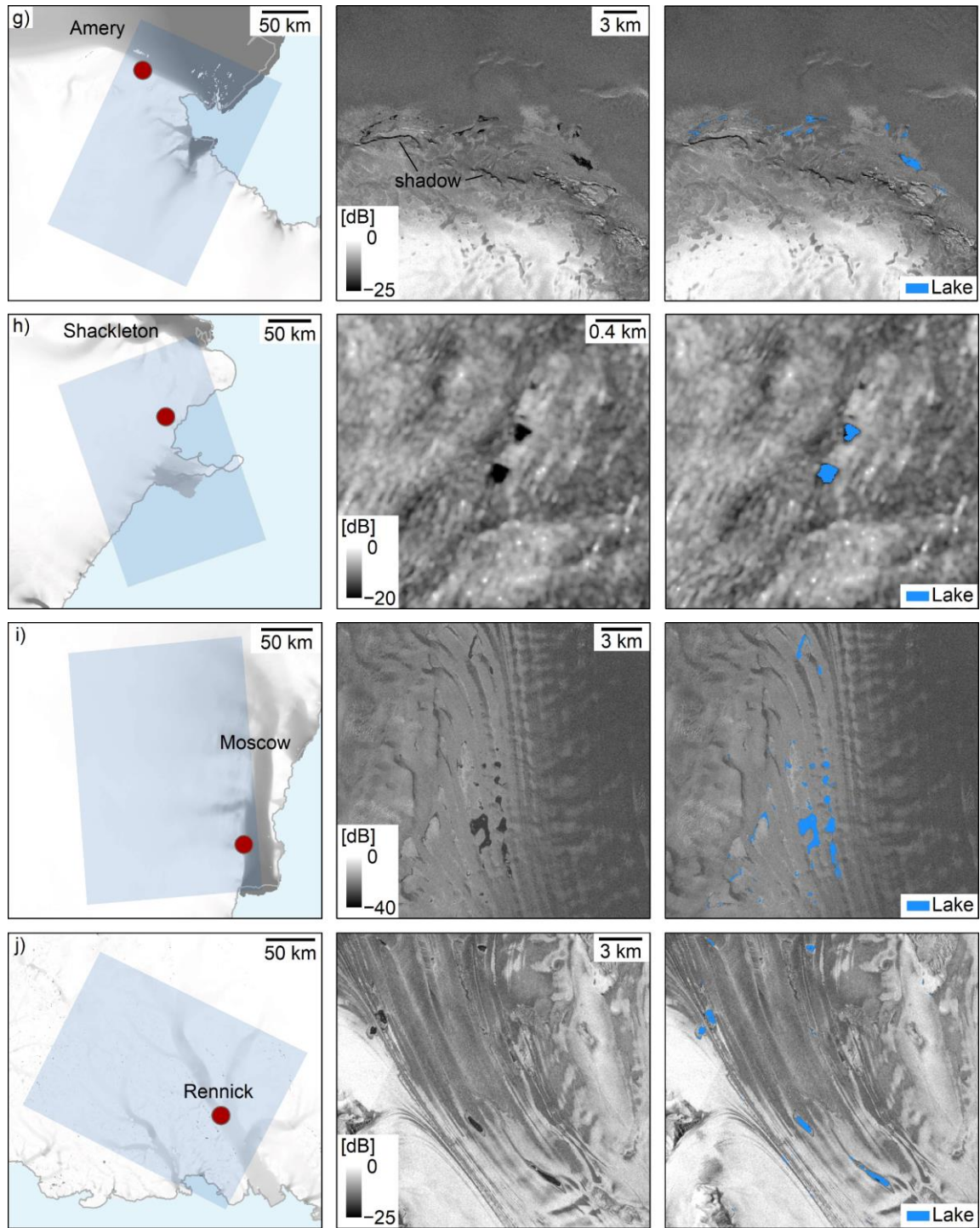
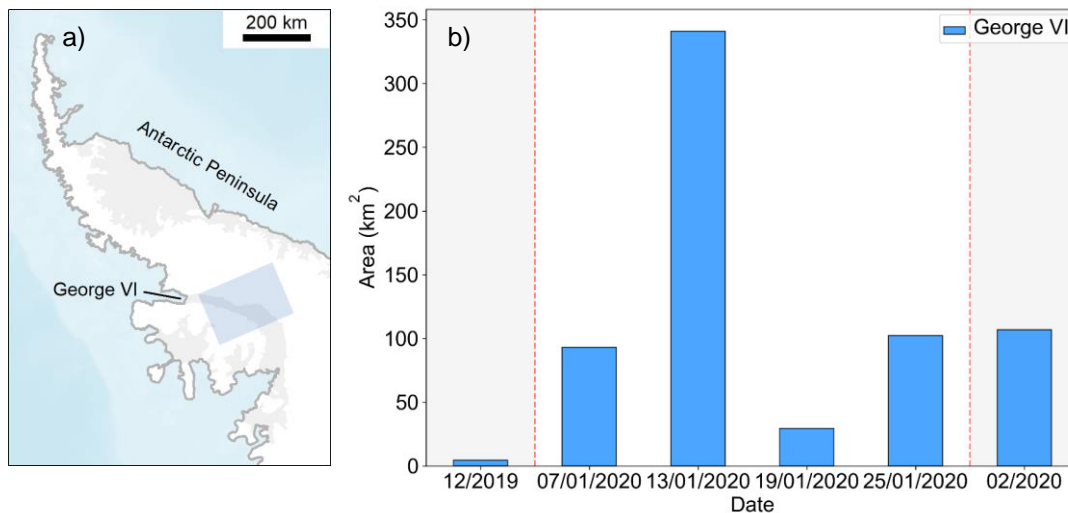
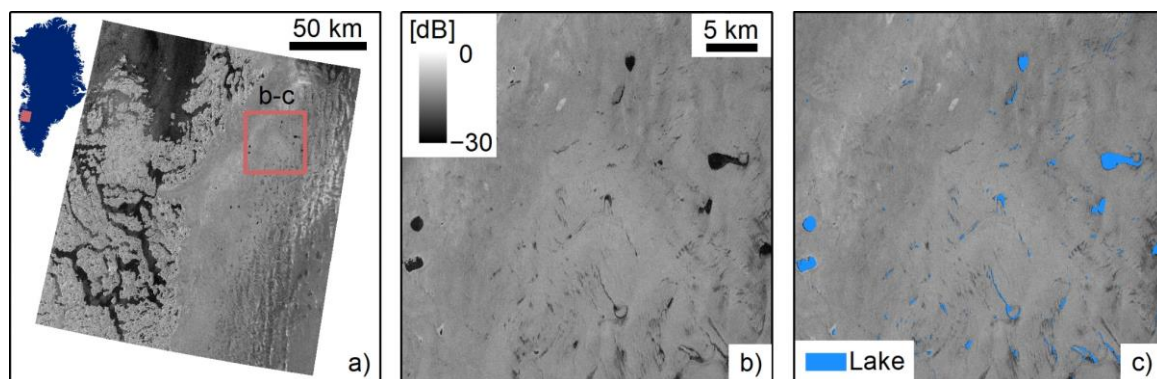


Figure 5.17. Continuation.



**Figure 5.18.** (a) Overview map of the study region covering northern George VI Ice Shelf (blue shading). (b) Intra-annual supraglacial lake evolution during summer 2019-2020. December 2019 and February 2020 represent maximum lake extent mapping products and January 2020 represents four individual Sentinel-1 acquisitions. Modified after Dirscherl et al. (2021a). Data: (Morlighem, 2020; Morlighem et al., 2020; Mougnot et al., 2017b; Rignot et al., 2013).



**Figure 5.19.** Automated classification result (c) for an image extract (b) of a Sentinel-1 acquisition of 28 July 2018 over the south-west Greenland Ice Sheet (a). Modified after Dirscherl et al. (2021a). Data: (Copernicus Sentinel-1 data; GEUS, 2020).

### 5.4.2 Sentinel-2

For evaluation of the RF classifier, 14 independent Sentinel-2 test scenes were acquired and classified (Table 5.3, Figure 5.1b). At this point it has to be noted that the classification of the test scenes was performed with the 10 m bands and indices model only due to its superior performance compared to all other tested model versions (see Chapter 5.5). As shown in Figure 5.20, supraglacial lakes appear well delineated in the automated classification results, yet with strongly varying shapes and sizes ranging from small and round lakes, e.g. on Abbot and Cosgrove ice shelves (Figure 5.20b-c), to extensive meltwater streams as part of inter-connected surface hydrological networks, e.g. on George VI, Nivlisen or Roi Baudouin ice shelves (Figure 5.20f,h,i). In addition, some lake features were frozen at their surface or started to freeze over making an accurate delineation more difficult. As can be seen in Figure 5.20h and Figure 5.20n, partly frozen lakes were still classified correctly highlighting the suitability of the developed classifier. Furthermore, difficult image features, including blue ice (Figure 5.20k-n), slush (Figure 5.20i), shadow (Figure 5.20a,g,h,i), melt on sea ice (Figure 5.20a,j,k) and submerged icebergs (Figure 5.20a), were accurately differentiated from supraglacial lakes.

For an improved evaluation of the spatio-temporal transferability of the developed classification method, Amery Ice Shelf was investigated for inter-annual supraglacial lake dynamics. Figure 5.21 and Figure 5.22 highlight the dynamic nature of supraglacial lake formation over Amery Ice Shelf with January 2017 (Figure 5.21b) and January 2019 (Figure 5.21d) showing particularly high supraglacial lake coverage and January 2018 (Figure 5.21c) and January 2020 (Figure 5.21e) showing comparatively low supraglacial lake coverage. This applies to the small region of interest in the center of the ice shelf (Figure 5.21b-e), the Sentinel-2 overlap area for all years (see Figure 5.2) as well as the total ice shelf area (Figure 5.22). As can be seen in Figure 5.22, peak lake coverage was detected during January 2019 (see Figure 5.21a), when meltwater features reached a total areal coverage of  $\sim 1,356 \text{ km}^2$ . In comparison, lake coverage over the full ice shelf area in years 2017, 2018 and 2020 was calculated at  $\sim 927 \text{ km}^2$ ,  $\sim 475 \text{ km}^2$  and  $\sim 366 \text{ km}^2$ , respectively. During all four years, meltwater was most abundant in the southern section of Amery as well as along its eastern grounding line (Figure 5.21a).

Similar as for Sentinel-1, an additional study region covering the south-west Greenland Ice Sheet was analyzed for improved evaluation of the spatio-temporal transferability of the classification algorithm to regions beyond Antarctica. Figure 5.23 shows the classification result for an extract of the Sentinel-1 scene of 10 August 2019. As can be seen, lakes appear well delineated and comparatively large in extent. Yet, it has to be noted that small parts of particularly deep lakes were missed in the classification.

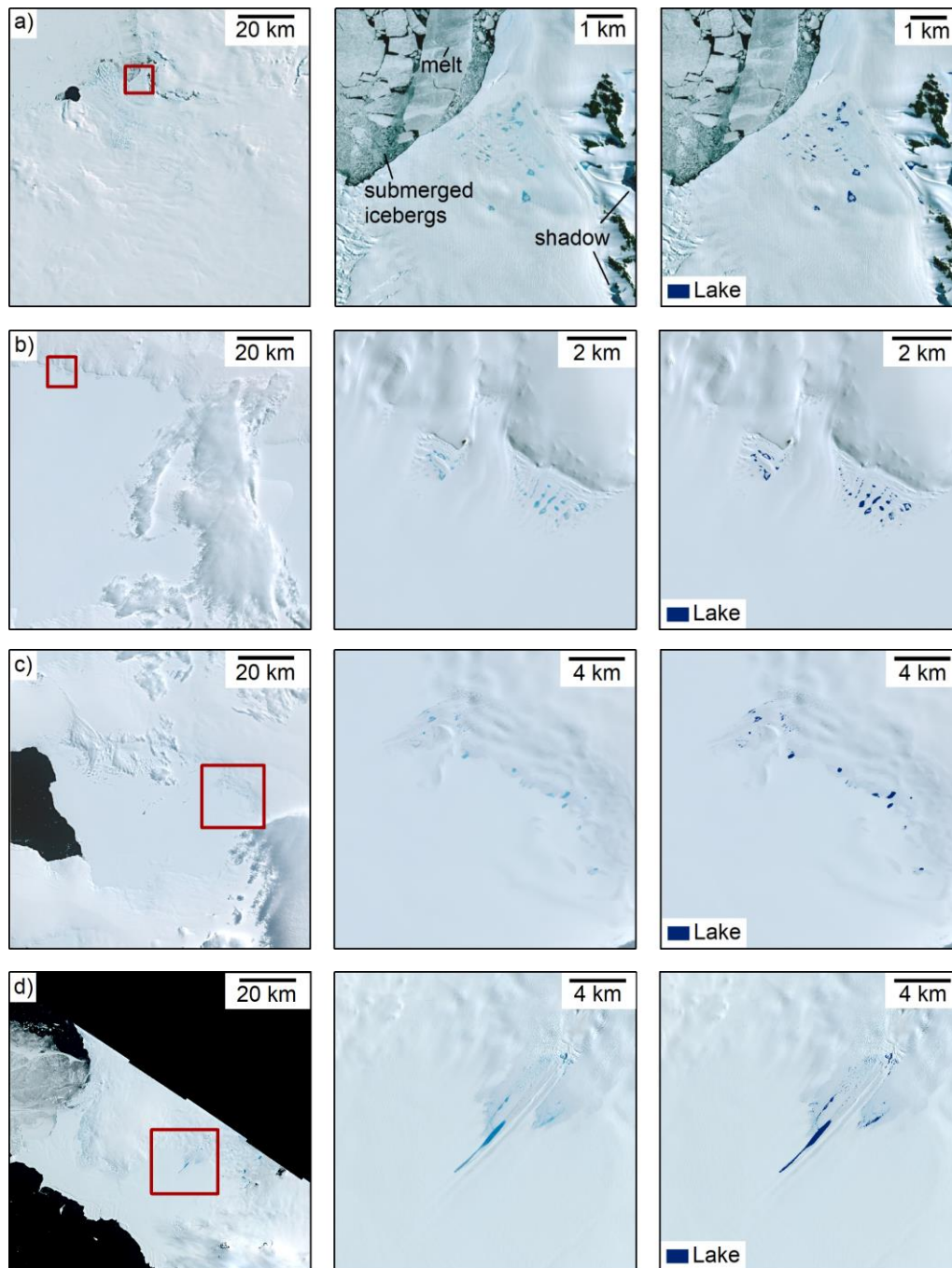


**Figure 5.20.** Automated classification results for the Sentinel-2 test data. From left to right, the sub-plots in (a-n) show the Sentinel-2 test scene, an extract at the location of the red outline in (a-n) as well as the automated classification result for the image extract. (a) Hull Glacier. (b) Abbot, (c) Cosgrove, (e-f) George VI, (g) Larsen C, (h) Nivlisen, (i) Roi Baudouin and (l) Moscow University ice shelves. (d) Pine Island Bay. (j) Enderby Land. (k) Wilhelm II and (m) Adelie Coast. (n) Drygalski Ice Tongue. Modified after Dirscherl et al. (2020b). Data: (Copernicus Sentinel-2 data).



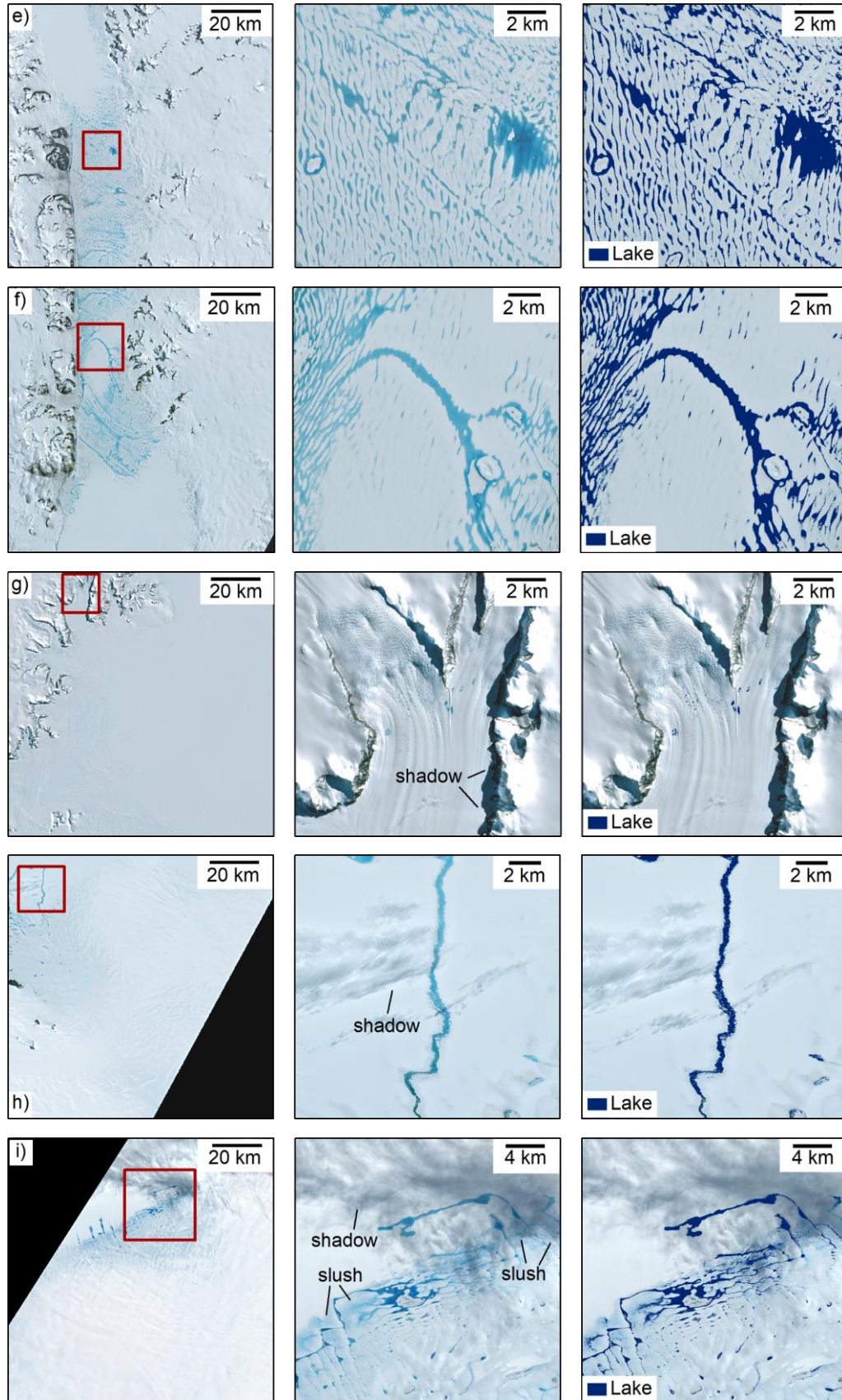


Figure 5.20. Continuation.

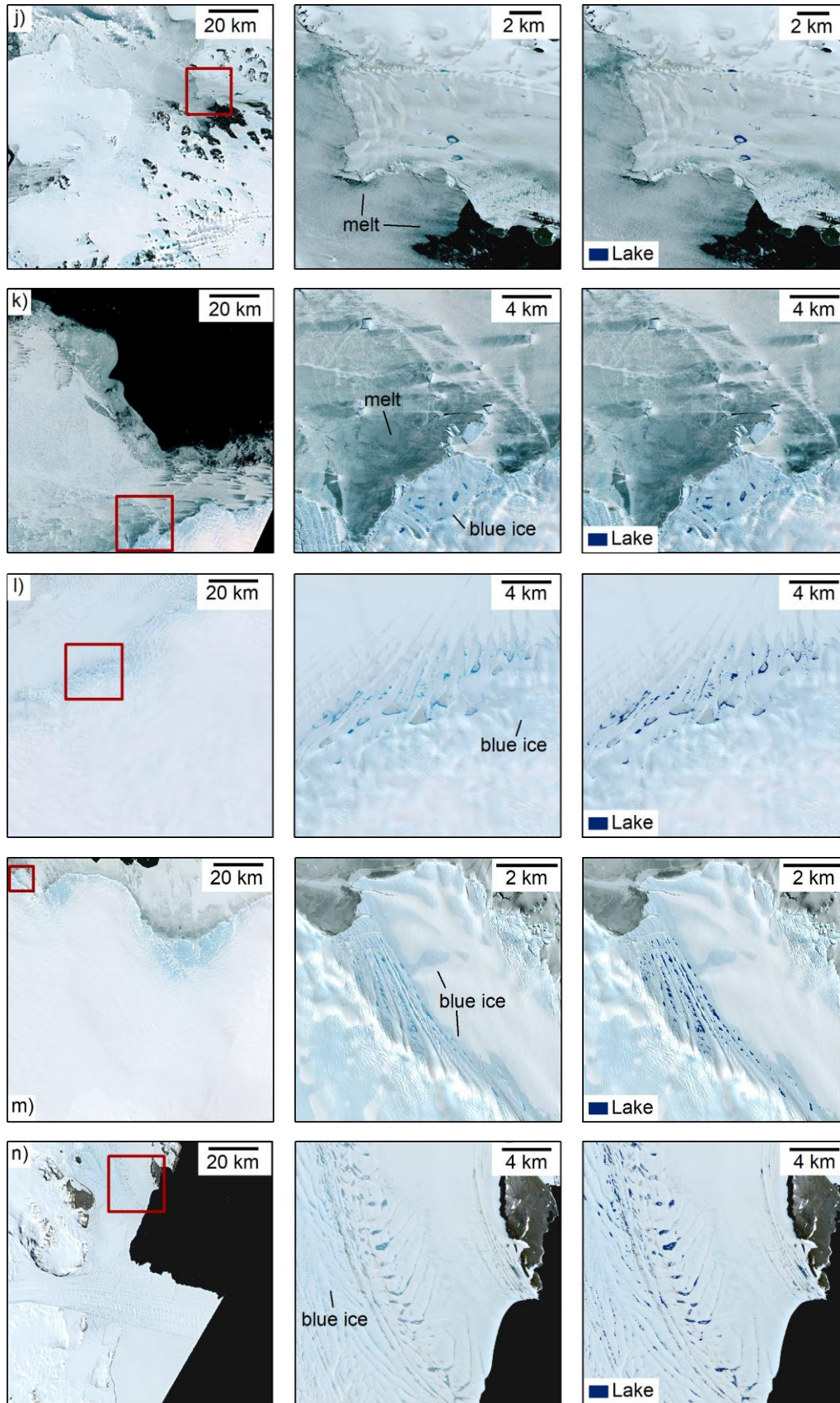
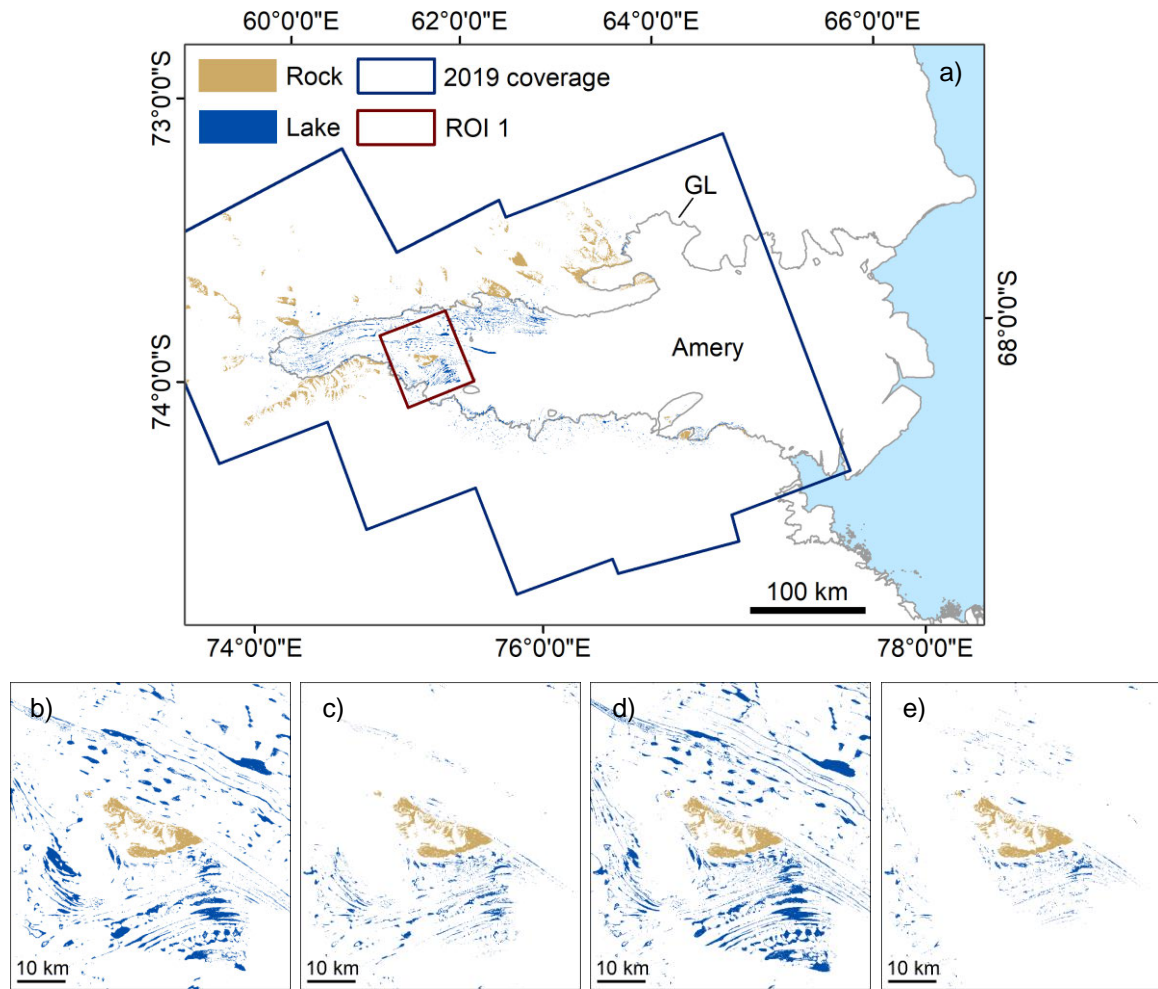
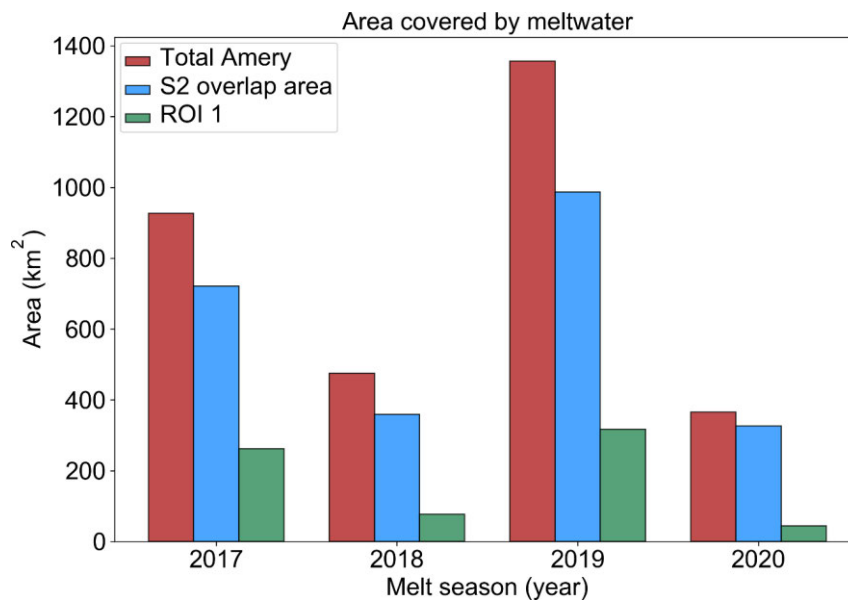


Figure 5.20. Continuation.





**Figure 5.21.** Maximum lake extent in January 2019 over Amery Ice Shelf (a). Mappings over region of interest (ROI) 1 for January 2017 (b), 2018 (c), 2019 (d) and 2020 (e). Modified after Dirscherl et al. (2020b). Data: (Dirscherl et al., 2020b; Mouginit et al., 2017b; Rignot et al., 2013).



**Figure 5.22.** Inter-annual evolution of maximum supraglacial lake extents during January 2017-2020 over Amery Ice Shelf. See Figure 5.2 for the outlines of the spatial units. Modified after Dirscherl et al. (2020b).

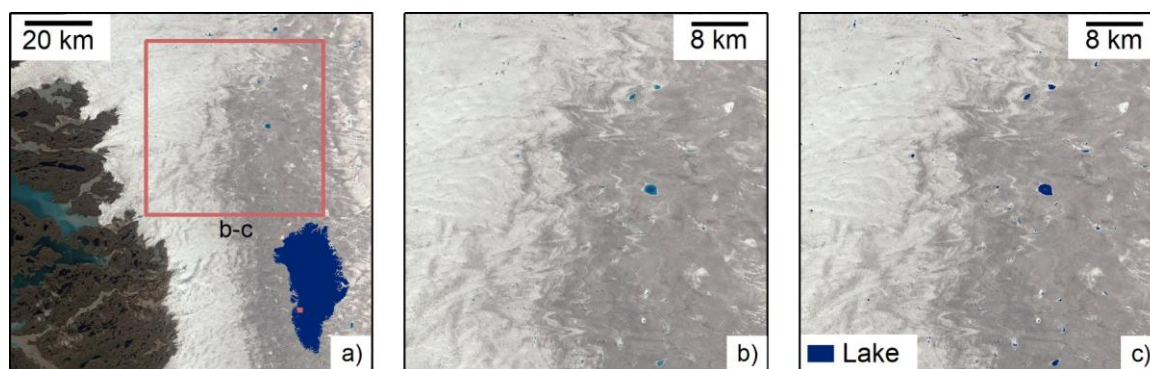


**Figure 5.23.** Classification result (c) for an image extract (b) of the additional Sentinel-2 test scene of 10 August 2019 over Greenland (a). Data: (Copernicus Sentinel-2 data; GEUS, 2020).

### 5.4.3 Fused Classification Products

In addition to single-sensor classification products, fused supraglacial lake extent mappings were derived for George VI and Amery ice shelves. To start with, Figure 5.24 shows a fused classification product covering northern George VI Ice Shelf during a 2-week period in early January 2020. As can be seen, supraglacial lakes were widespread across the entire ice shelf ranging from small, elongated lakes to larger surface meltwater features with diameters  $>10$  km (Figure 5.24a). During the two-week interval, only Sentinel-1 SAR imagery delivered input data for supraglacial lake extent mapping as optical Sentinel-2 data were subject to continuous cloud cover (e.g. Figure 5.24d). During the considered period, total lake coverage reached  $\sim 379$  km<sup>2</sup>.

Figure 5.25 shows that supraglacial lakes were widespread on George VI Ice Shelf during the second half of January 2020. During the 2-week period, both satellite sensors delivered valuable information on supraglacial lake coverage. As shown in Figure 5.25a, the southern section of George VI Ice Shelf was mostly covered by Sentinel-2, while the northern ice shelf section was covered by both satellite sensors. Over some isolated regions, only Sentinel-1 classifications were available. In particular, SAR data were advantageous where slightly frozen and buried lakes could not be detected in optical Sentinel-2 imagery (Figure 5.25b-d). To provide more detail,  $\sim 629$  km<sup>2</sup> of all lake area was classified in Sentinel-2 imagery only,  $\sim 10$  km<sup>2</sup> was classified in SAR imagery only and 166 km<sup>2</sup> was detected with both Sentinel-1 and Sentinel-2. Overall, this resulted in a total supraglacial lake coverage of 805 km<sup>2</sup> during the 2-week interval.

On the other hand, Figure 5.26 shows the fused supraglacial lake extent mapping product covering Amery Ice Shelf during the first two weeks of January 2019. Similar as in Figure 5.21, supraglacial lakes were widespread in the southern and eastern sections of the ice shelf. In the central ice shelf section, particularly large lakes with lengths  $>25$  km were detected. Overall, most supraglacial lake classifications are from optical Sentinel-2 data, while only few mappings represent overlap regions or data from

Sentinel-1 (Figure 5.26a,b). In particular,  $\sim 16 \text{ km}^2$ ,  $\sim 1,232 \text{ km}^2$  and  $\sim 124 \text{ km}^2$  of all classified lake pixels result from Sentinel-1, Sentinel-2 and both sensors, respectively.

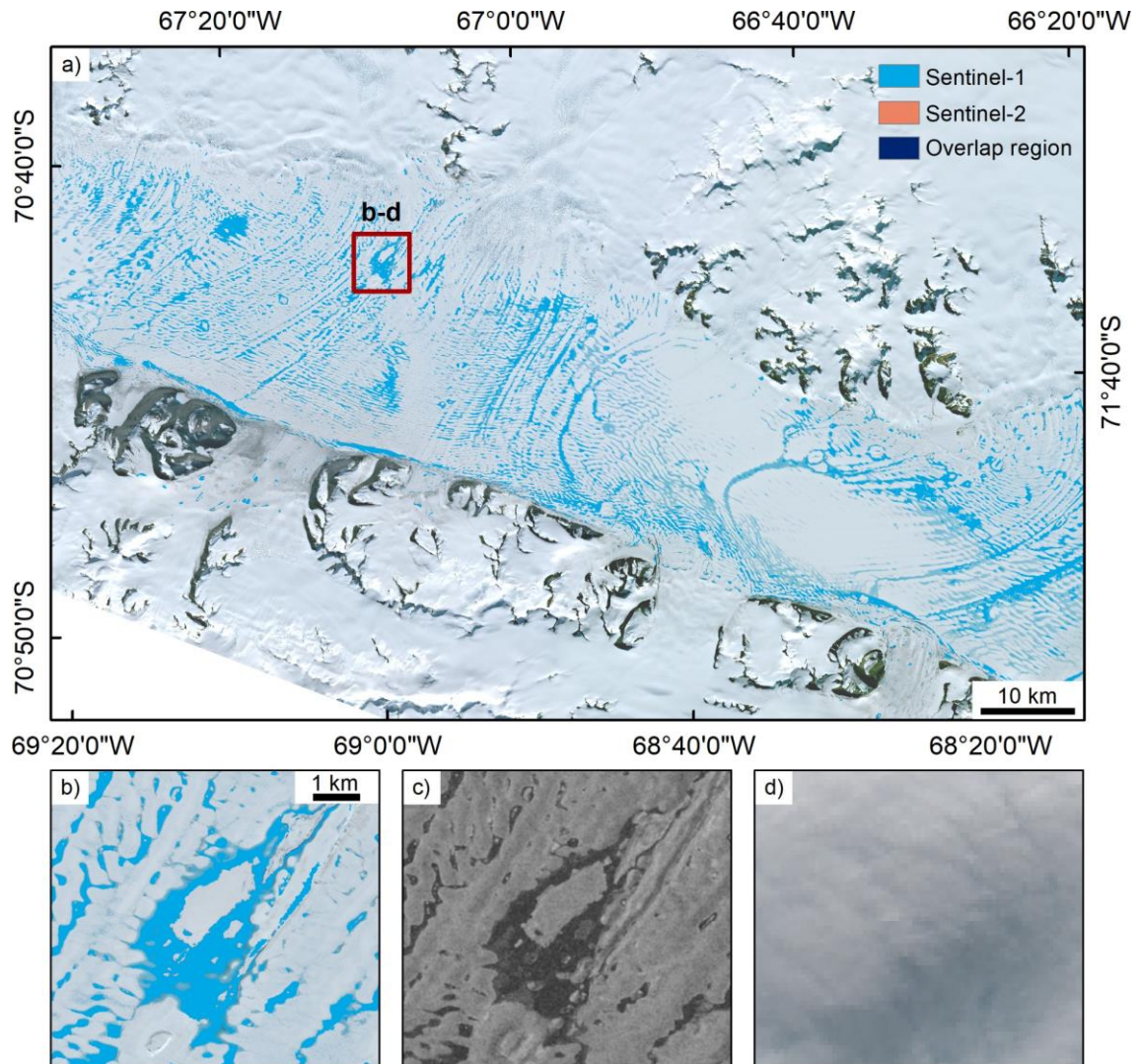


**Figure 5.24.** Decision-level fusion of automatically generated Sentinel-1 and Sentinel-2 maximum lake extent classification products covering the first half of January 2020 over George VI Ice Shelf (a). (b) Inset over the region outlined in (a) (red). (c) Sentinel-1 SAR backscattering minimum product for January 2020. (d) Sentinel-2 imagery of 9 January 2020. The fused classification product is shown as an overlay with Sentinel-2 data of 19 January 2020. Data: (Copernicus Sentinel data).



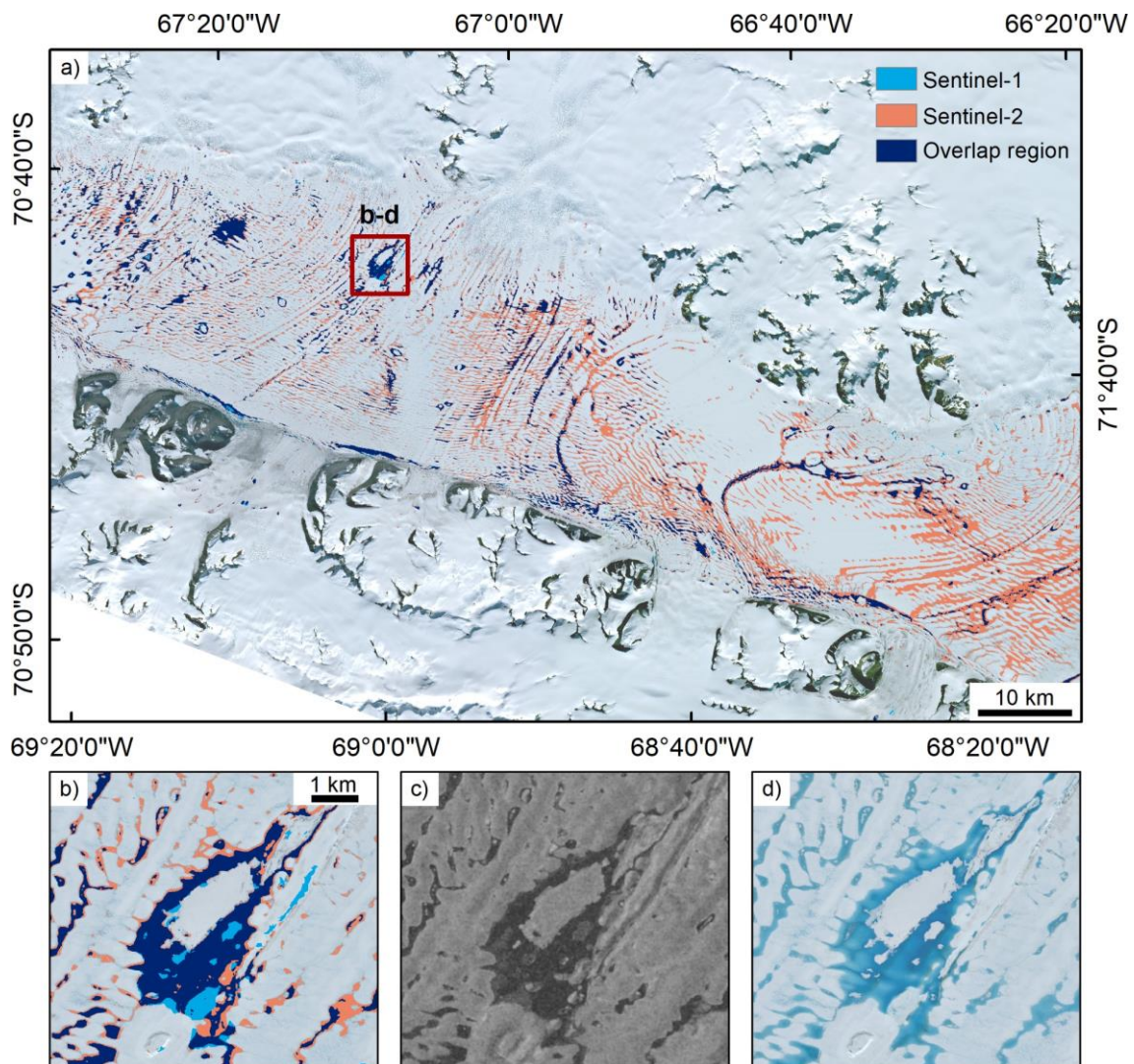


**Figure 5.25.** Decision-level fusion of automatically generated Sentinel-1 and Sentinel-2 maximum lake extent classification products covering the second half of January 2020 over George VI Ice Shelf (a). (b) Inset over the region outlined in (a) (red). (c) Sentinel-1 SAR backscattering minimum product for January 2020. (d) Sentinel-2 imagery of 19 January 2020. The fused classification product is shown as an overlay with Sentinel-2 data of 19 January 2020. Modified after Dirscherl et al. (2021a). Data: (Copernicus Sentinel data).

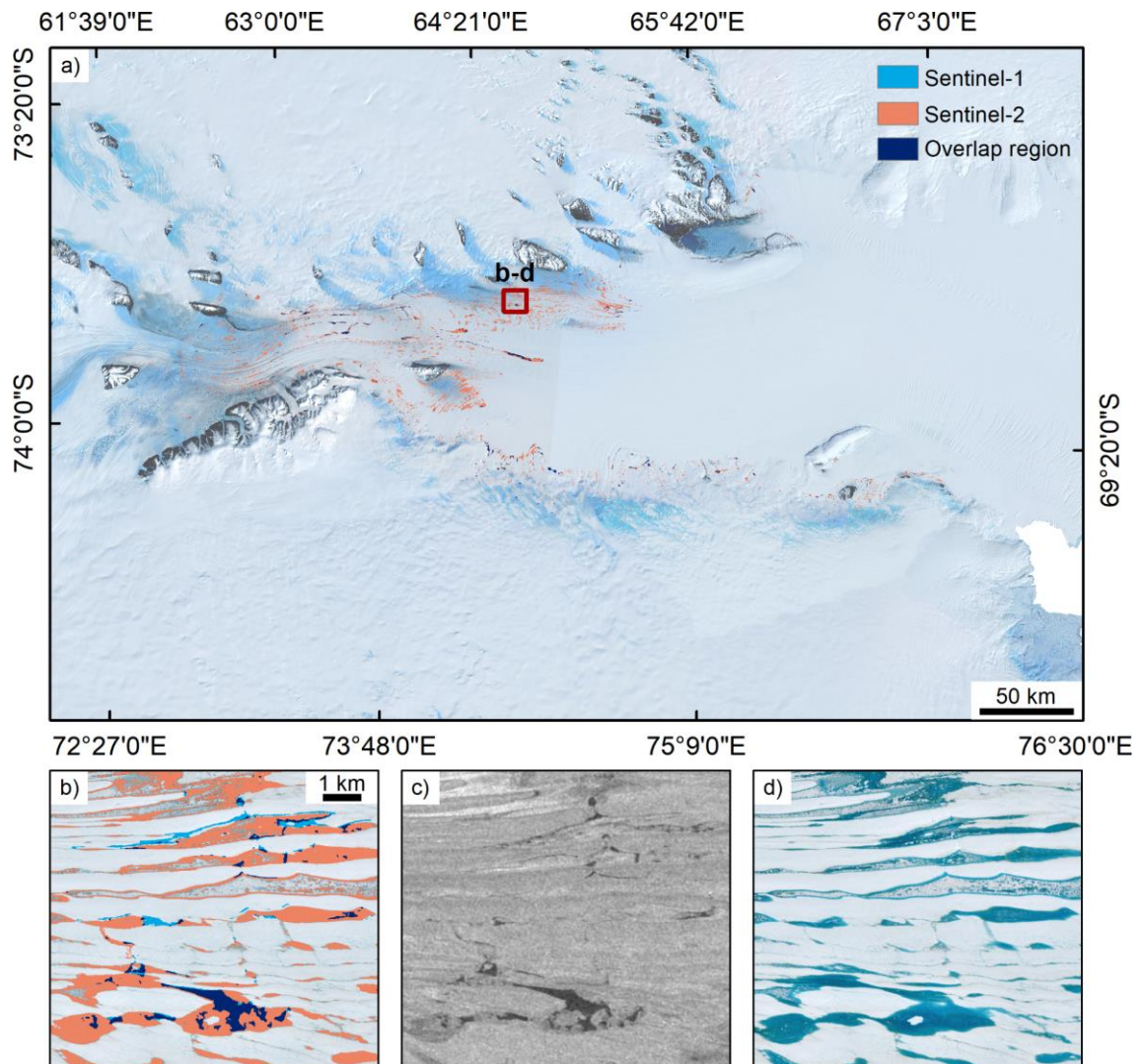


**Figure 5.26.** Decision-level fusion of automatically generated Sentinel-1 and Sentinel-2 maximum lake extent classification products covering the first half of January 2019 over Amery Ice Shelf (a). (b) Inset over the region outlined in (a) (red). (c) Sentinel-1 SAR imagery of 12 January 2019. (d) Sentinel-2 imagery of 2 January 2019. The fused classification product is shown as an overlay with the Landsat Image Mosaic of Antarctica (LIMA). The data basis for the additional Sentinel-1 scenes over Amery Ice Shelf is outlined in Chapter 6.2. Data: (Copernicus Sentinel data; Bindschadler et al., 2008).



## 5.5 Accuracy Assessment

For evaluation of the obtained classification results, an accuracy assessment was performed for the "water" and the "non-water" class. In this context, the "water" class comprises all supraglacial meltwater features and the "non-water" class refers to all remaining ice sheet surface features. As no reference data on Antarctic supraglacial lakes exist to date, the accuracy assessment was carried out on the basis of the original Sentinel-1 and Sentinel-2 test data. In detail, random point samples were created for all classified test imagery. To focus on regions that are particularly difficult to discriminate from surface meltwater as well as to obtain an adequate sampling rate in regions where misclassifications may exist, a buffer of 250 m around each water pixel in the corresponding classification maps was introduced. For evaluation of the Sentinel-1 classification algorithm, point sampling was performed for all nine independent test scenes as well as the 13 January 2020 acquisition covering George VI Ice Shelf (see Table 5.1). In total, 23,000 points were sampled within the buffered "water" class of all test scenes and labeled in agreement with their true class membership, as visually determined in the underlying SAR data. As supraglacial lake coverage in some Sentinel-1 test scenes was comparatively low, the number of point samples per scene was defined in agreement with the areal share of classified lake pixels compared to all other test data. Similarly, a total of 28,000 points was sampled in the buffered "water" class of the classified Sentinel-2 test data. Here, point labeling was performed on the basis of the underlying Sentinel-2 RGB imagery.

Following point sampling and labeling, the point data of each test scene were compared to the corresponding classification results and the number of true and false positives and negatives was extracted and evaluated as part of a confusion matrix. In this context, a confusion matrix allows deriving common statistical accuracy metrics including Precision (P), Recall (R), F-score ( $F_1$ ), error of omission (ERO), error of commission (ERC) and Cohen's Kappa (K) (Cohen, 1960; Jolly, 2018; Landis and Koch, 1977; Müller and Guido, 2016). To start with, Precision and Recall are calculated dividing the number of true positive (TP) classifications by the number of predicted class samples and the number of true class samples, respectively:

$$P = \frac{TP}{TP+FP} \quad (2)$$

$$R = \frac{TP}{TP+FN} \quad (3)$$

where FN is the rate of false negatives and FP is the rate of false positives.

Next, the harmonic mean of Recall and Precision was calculated to retrieve the F-score, an overall quality measure on both statistical accuracy metrics:

$$F_1 = \frac{2 \times (R \times P)}{(R+P)} \quad (4)$$

On the other hand, the errors of omission and commission capture the rate of false negatives and false positives with respect to all true class samples and all predicted class samples, respectively. Finally, the Kappa coefficient is an overall quality measure on the similarity between classification results and ground truth. Kappa is derived from the overall accuracy (OA) and the expected accuracy (EA):

$$OA = \frac{TP + TN}{TS} \quad (5)$$

$$EA = \frac{(TN + FP) \times (TN + FN) + (FN + TP) \times (FP + TP)}{TS \times TS} \quad (6)$$

$$K = \frac{OA - EA}{1 - EA} \quad (7)$$

where TN are the true negatives and TS are the total samples (Cohen, 1960; Jolly, 2018; Landis and Koch, 1977; Müller and Guido, 2016). The Kappa coefficient returns values in the range of 0-1 where values close to one represent a high agreement between classification results and ground truth and values close to zero a low agreement between classifications and ground truth. In contrast to P, R, F<sub>1</sub>, ERO and ERC, Cohen's Kappa measures the accuracy of both classes conjointly.

### 5.5.1 Sentinel-1

The results of the accuracy assessment for the Sentinel-1 test data are shown in Table 5.6. In addition, Figure 5.27a visualizes the results of the calculation of Cohen's Kappa. As can be seen, the average ERC and ERO across all test sites were slightly higher for the "water" class than for the "non-water" class. At the same time, both error rates were comparatively low revealing the high accuracy of the classification results. In agreement with this, the average Precision (88.9%) and Recall (98.83%) returned an average F-score of 93% for the "water" class compared to values of 99.86%, 99.17% and 99.51% for Precision, Recall and F-score of the "non-water" class. In this context, the slightly reduced Precision and F-score of the "water" class mostly result from classification errors over Enderby Land, Shackleton Ice Shelf and Rennick Glacier (Table 5.6). In agreement with this, these regions show lowest values of Kappa (Figure 5.27a). The average Kappa coefficient across all test sites was computed at 0.925.

**Table 5.6.** Results of the accuracy assessment for the Sentinel-1 test data. From left to right, the columns for each class represent the Precision, Recall, F-score, error of commission and error of omission. Modified after Dirscherl et al. (2021a).

Classes	Water					Non-water				
	P [%]	R [%]	F <sub>1</sub> [%]	ERC [%]	ERO [%]	P [%]	R [%]	F <sub>1</sub> [%]	ERC [%]	ERO [%]
Abbot	100.0	100.0	100.0	0.0	0.0	100.0	100.0	100.0	0.0	0.0
Bach	99.32	99.32	99.32	0.68	0.68	99.9	99.9	99.9	0.1	0.1
George VI	98.88	99.13	99.0	1.12	0.87	99.83	99.79	99.81	0.17	0.21
Larsen C	93.1	99.39	96.14	6.9	0.61	99.95	99.44	99.7	0.05	0.56
Riiser-Larsen	90.84	99.13	94.8	9.16	0.87	99.83	98.09	98.95	0.17	1.91
Enderby Land	69.81	100.0	82.22	30.19	0.0	100	97.96	98.97	0.0	2.04
Amery	100.0	96.32	98.13	0.0	3.68	99.54	100.0	99.77	0.46	0.0
Shackleton	77.78	100.0	87.5	22.22	0.0	100.0	99.48	99.74	0.0	0.52
Moscow U.	98.99	98.2	98.59	1.01	1.8	99.72	99.84	99.72	0.28	0.16
Rennick	60.29	86.85	74.32	39.71	3.15	99.86	97.19	98.5	0.14	2.81
<b>Average</b>	<b>88.90</b>	<b>98.83</b>	<b>93.0</b>	<b>11.1</b>	<b>1.17</b>	<b>99.86</b>	<b>99.17</b>	<b>99.51</b>	<b>0.14</b>	<b>0.83</b>

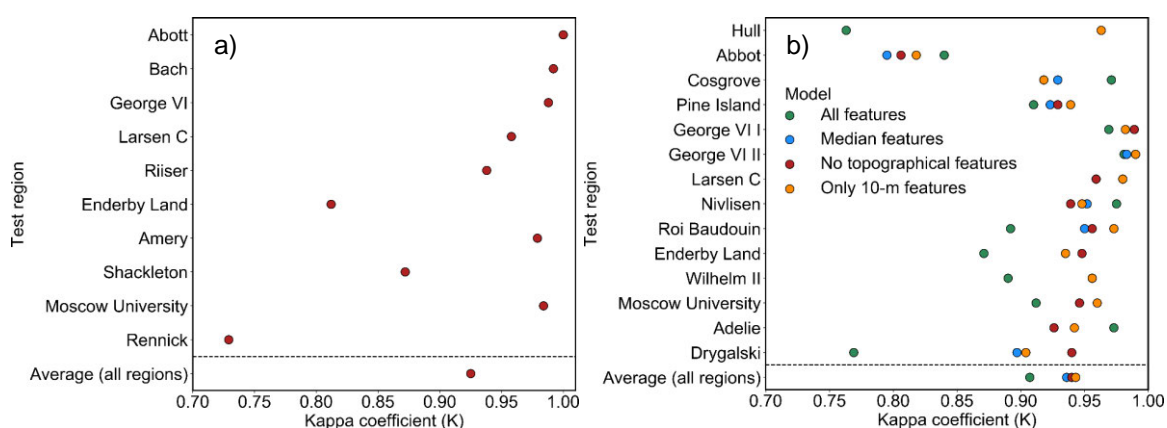


**Figure 5.27.** Kappa coefficient for the Sentinel-1 (a) and Sentinel-2 (b) test data.

## 5.5.2 Sentinel-2

The classification accuracies and error rates for the Sentinel-2 test data are presented in Table 5.7 and Figure 5.27b. As the model version with 10 m bands and indices returned the highest average Kappa coefficient (0.943) across all test sites (Figure 5.27b), the accuracy metrics in Table 5.7 refer to this model version only.

As can be seen in Table 5.7, the average Precision, Recall and F-score of the “water” and the “non-water” class were computed at comparatively high values of 95.71%, 93.95% and 94.71% as well as of 99.8%, 99.89% and 99.84%, respectively. In agreement with this, the corresponding error rates were comparatively low reaching maximum values of 4.3% and 6.05% for the false positive (ERC) and false negative (ERO) rate of the “water” class. Lowest accuracy values and highest error rates were detected for the “water” class over Abbot Ice Shelf, Cosgrove Ice Shelf and Drygalski Glacier. Similarly, these regions returned lowest values of Kappa (Figure 5.27b).

**Table 5.7.** Results of the accuracy assessment for the Sentinel-2 test data. From left to right, the columns for each class represent the Precision, Recall, F-score, error of commission and error of omission. Modified after Dirscherl et al. (2020b).

Classes	Water					Non-water				
	P [%]	R [%]	F <sub>1</sub> [%]	ERC [%]	ERO [%]	P [%]	R [%]	F <sub>1</sub> [%]	ERC [%]	ERO [%]
Hull	100.0	92.86	96.3	0.0	7.14	99.95	100.0	99.97	0.05	0.0
Abbot	100.0	69.84	82.24	0.0	30.16	99.03	100.0	99.51	0.97	0.0
Cosgrove	97.87	86.79	92.0	2.13	13.21	99.64	99.95	99.8	0.36	0.05
Pine Island Bay	88.68	100.0	94.0	11.32	0.0	100.0	99.69	99.85	0.0	0.31
George VI	98.04	98.68	98.36	1.96	1.32	99.89	99.84	99.86	0.11	0.16
George VI	99.57	98.73	99.15	0.43	1.27	99.83	99.94	99.89	0.17	0.06
Larsen C	96.15	100.0	98.04	3.85	0.0	100.0	99.95	99.97	0.0	0.05
Nivlisen	98.57	92.0	98.17	1.43	8.0	99.36	99.89	99.63	0.64	0.11
Roi Baudouin	95.83	99.14	97.46	4.17	0.86	99.95	99.73	99.84	0.05	0.27
Enderby Land	88.1	100.0	93.67	11.9	0.0	100.0	99.75	99.87	0.0	0.25
Wilhelm II Land	94.29	97.06	95.65	5.71	2.94	99.95	99.9	99.92	0.05	0.1
Moscow U.	100.0	92.5	96.1	0.0	7.5	99.85	100.0	99.92	0.15	0.0
Adelie Coast	97.06	91.67	94.29	2.94	8.33	99.85	99.95	99.9	0.15	0.05
Drygalski	85.71	96.0	90.57	14.29	4.0	99.95	99.8	99.87	0.05	0.2
<b>Average</b>	<b>95.71</b>	<b>93.95</b>	<b>94.71</b>	<b>4.3</b>	<b>6.05</b>	<b>99.8</b>	<b>99.89</b>	<b>99.84</b>	<b>0.2</b>	<b>0.12</b>

## 5.6 Implementation of Methods for Circum-Antarctic Processing

In order to enable the fully automated classification of supraglacial lake extents in Sentinel-1 SAR and optical Sentinel-2 imagery over the Antarctic continent, the developed methods were implemented as part of the High-Performance Computing (HPC) infrastructure of the German Remote Sensing Data Center at the German Aerospace Center (DLR). The final implementation of the developed framework combines all method developments outlined in Chapter 5.3 and can be easily applied to other glaciated regions such as the Greenland Ice Sheet (Figure 5.19, Figure 5.23). The following paragraphs outline the individual tools and processes of the full methodological framework encompassing study site selection as well as automated data retrieval, pre-processing, image classification and post-processing.

As can be seen in Figure 5.28, the first step towards fully automated supraglacial lake extent delineation comprises the creation of a shapefile for a given Area of Interest (AOI). In the following, the shapefile is ingested into DLR’s Internal Data Access (IDA) and all available Sentinel-1 and Sentinel-2 data meeting a pre-defined set of criteria (e.g. temporal resolution, product specifications) are automatically retrieved and stored on IDA. For facilitated data access, IDA is mounted on DLR’s Calvalus Hadoop cluster where the data can be readily processed. Therefore, the next step involves the automated pre-processing of all satellite data on Calvalus. For this purpose, Extensible Markup Language (XML) scripts are used to open docker containers comprising all required pre-processing tools for each sensor type. Within the docker containers, the pre-processing tools are launched using shell scripts. For Sentinel-1, the SNAP command line Graph Processing Tool (GPT) is used (Chapter 5.3.1.1). On the other

hand, Sentinel-2 data are pre-processed using the SNAP Sen2Cor plugin (Chapter 5.3.2.1). Following automated data pre-processing, further shell and XML scripts are executed for Sentinel-1 and Sentinel-2, respectively. In particular, these scripts open docker containers where Python scripts are launched with further shell scripts in order to prepare, classify and post-process all Sentinel-1 and Sentinel-2 imagery. As Sentinel-1 data are classified on the Calvalus GPU cluster, the prepared data first need to be transferred to cvtensorflow, one of the core processors of the cluster. Similar as for IDA and Calvalus, this is achieved through the GPU cluster being mounted on Calvalus. Following the automated processing of all satellite imagery, the same Python scripts can be used for an automated fusion of Sentinel-1 and Sentinel-2 classification results whereat the parameter settings for data fusion, including the temporal aggregation interval, can be adjusted in agreement with the user requirements. Therefore, either single classification maps for each satellite scene or temporally aggregated supraglacial lake extent mapping products can be retrieved with the implemented workflow. The final classification results are automatically stored on Calvalus. More detailed examples of automatically derived supraglacial lake extent mapping products are shown in Chapter 6.

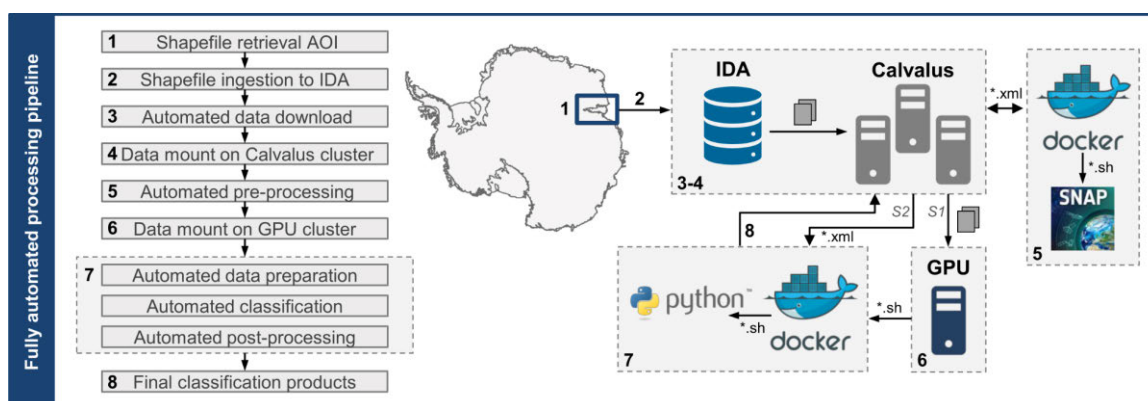


**Figure 5.28.** Sketch of the automated processing pipeline for classification of Sentinel-1 and Sentinel-2 imagery on DLR's High-Performance Computing infrastructure. AOI: Area of Interest. IDA: Internal Data Access. SNAP: Sentinel Application Platform. GPU: Graphics Processing Unit. S1: Sentinel-1. S2: Sentinel-2. The copyright of the logos belongs to the respective institutions.

## 5.7 Discussion

This chapter discusses the main advantages and remaining limitations of the developed classification workflow for Antarctic supraglacial lake extent delineation in Sentinel-1 SAR and optical Sentinel-2 satellite imagery. In detail, Chapter 5.7.1 discusses the obtained classification results for Sentinel-1, Sentinel-2 and fused mappings. In the following, Chapter 5.7.2 addresses the results of the accuracy assessment and Chapter 5.7.3 summarizes future research requirements on the basis of remaining limitations.

### 5.7.1 Mapping Results

#### 5.7.1.1 Sentinel-1

As shown in Chapter 5.4.1, the classification results for the Sentinel-1 test data reveal reliable lake extent delineations as well as an accurate differentiation from image features such as wet snow, dry snow, bare ice, shadowing or the open ocean. In addition, the delineation of lakes being subject to refreezing, wind roughening or speckle noise was successful. Across the AIS, supraglacial lakes appeared to be widespread with strongly varying shapes and sizes in agreement with previous documentations of Antarctic supraglacial lakes (Kingslake et al., 2017; Moussavi et al., 2020; Stokes et al., 2019). Furthermore, an intra-annual analysis on supraglacial lake evolution over George VI Ice Shelf during 2019-2020 was performed (Figure 5.18). Being the first SAR-based analysis on intra-annual supraglacial lake dynamics, the results reveal strongly fluctuating supraglacial lake extents throughout the melting season which highlights the value of the developed method for time series analyses. Even though the results do not reflect the detected peak of lake coverage on 19 January 2020 in Banwell et al. (2021), likely due to the corresponding SAR acquisition being affected by severe wind roughening, the results similarly reveal lake coverage to be peaking during mid-January. At the same time, the comparatively low lake extents in the Sentinel-1 scene of 19 January 2020 (Figure 5.18b) highlight the importance of fused supraglacial lake extent mapping products, where also optical data are considered. In addition, the classification result for the additional test site covering the south-west Greenland Ice Sheet (Figure 5.19) highlights the spatio-temporal transferability of the method to other glaciated regions.

#### 5.7.1.2 Sentinel-2

Similarly, the mapping results for the Sentinel-2 test data (Figure 5.20) reveal strongly varying supraglacial lake extents across Antarctica, in agreement with the results for Sentinel-1 as well as previous investigations (e.g. Kingslake et al., 2017;



Moussavi et al., 2020; Stokes et al., 2019). In particular, the differentiation between supraglacial meltwater and shadow, slush, blue ice, submerged icebergs, melt on sea ice and the open ocean was successful. In addition, the classification results over Amery Ice Shelf emphasize the potential of the developed method for multi-temporal analyses on supraglacial lake coverage. Here, inter-annual analyses were performed revealing varying supraglacial lake coverage during January 2017-2020. The obtained results are in good agreement with other investigations. For instance, Moussavi et al. (2020) used Landsat 8 data to calculate supraglacial lake extents over Amery Ice Shelf during January 2017 and January 2018. In detail, their threshold-based approach revealed lake extents of 720 km<sup>2</sup> and 380 km<sup>2</sup> for January 2017 and 2018 being in excellent agreement with the obtained results of ~721 km<sup>2</sup> and ~359 km<sup>2</sup> for the Sentinel-2 overlap area. Minor differences most likely result from the use of different satellite data and mapping methods as well as different temporal and areal coverages. Furthermore, the classification results for the additional study region over the Greenland Ice Sheet highlight the good functionality and spatio-temporal transferability of the developed classification workflow even though few pixels over particularly deep lakes were missed in the classification.

### 5.7.1.3 Fused Classification Products

Furthermore, the derivation of fused supraglacial lake extent classification products over Amery and George VI ice shelves demonstrates the value of multi-sensor remote sensing data for a more detailed mapping of Antarctic supraglacial lakes. To start with, the fused mapping product covering George VI Ice Shelf during early January 2020 (Figure 5.24) revealed supraglacial lake classifications to result from Sentinel-1 SAR imagery only. Here, optical data were subject to continuous cloud cover highlighting the importance of SAR-based mappings due to their independence of meteorological and illumination conditions. On the other hand, Figure 5.25 shows the fused classification product for George VI Ice Shelf during the second half of January 2020. In contrast to Figure 5.24, the fusion of optical and SAR classifications revealed a large number of lake pixels to result from optical Sentinel-2 data as well as a comparatively large overlap area between optical and SAR classifications. At the same time, few classifications, e.g. over buried and slightly frozen lakes, resulted from Sentinel-1 data only. Therefore, the combination of data from both sensor types enabled a more complete mapping of supraglacial lake coverage which again emphasizes the benefits of multi-sensor mappings. Comparing the maximum supraglacial lake extent over George VI Ice Shelf during the second half of January 2020 (805 km<sup>2</sup>) to the estimate of ~1,200 km<sup>2</sup> on 19 January 2020 in Banwell et al. (2021), the presented result is slightly lower. This likely results from the use of different sensor data, mapping techniques as well as AOI sizes. In fact, Banwell et al. (2021) use optical Landsat 8 data of coarser spatial resolution (30

m) as well as a threshold-based mapping technique that was calibrated over East Antarctica, thus can be subject to substantial misclassifications when applied without an appropriate adaption of thresholds. Finally, Figure 5.26 presented a bi-weekly supraglacial lake extent mapping product covering the first half of January 2019 over Amery Ice Shelf. Similar as in Figure 5.25, optical classifications were of great relevance, while overlap area and Sentinel-1 classifications occurred less frequently.

To summarize, fused supraglacial lake extent mapping products from Sentinel-1 SAR and optical Sentinel-2 classifications are of great relevance in order to capture a more complete picture of Antarctic supraglacial lake formation. In this context, optical Sentinel-2 data deliver important information on supraglacial lake coverage during wind roughening and cloud-free conditions in Antarctic summer. Contrarily, Sentinel-1 SAR data are of particular relevance in order to enable data acquisition during cloud cover, nighttime and polar darkness. Furthermore, Sentinel-1 SAR has the ability to detect subsurface meltwater including partly frozen and buried lakes (Figure 5.25b-c).

## **5.7.2 Accuracy Assessment**

### **5.7.2.1 Sentinel-1**

The results of the accuracy assessment for the Sentinel-1 test data (Chapter 5.5.1) revealed overall high accuracy values and low error rates confirming the functionality and performance of the developed classification algorithm. Through application of a modified CNN for an improved consideration of the spatial image context, it was possible to reliably extract supraglacial lakes of varying appearances, as reflected in the overall high accuracy metrics for Kappa and the F-score (Table 5.6, Figure 5.27). This includes small to large meltwater features that are either round or elongated as well as lakes with fuzzy edges or strongly fluctuating backscattering values, e.g. due to wind roughening or speckle noise. Despite the excellent performance of the overall classification workflow, some test scenes returned comparatively low accuracy values. Reduced classification accuracies mainly occurred due to false positive lake classifications resulting in increased values for the error of commission. In particular, misclassifications affected the test scenes covering Enderby Land, Shackleton Ice Shelf and Rennick Glacier but also Riiser-Larsen and Larsen C ice shelves (Table 5.6). One reason for false positive lake classifications is the use of the Sentinel-1 coastline product of 2018 for ocean masking. In fact, the use of a static coastline product for temporally varying data can lead to misclassifications over open ocean where the calving front strongly retreated since the acquisition date of the coastline data. This effect is enhanced where ocean polynyas (i.e., small patches of open ocean within sea ice) are present or where rifts form close to the calving front. In fact, the deviating date of the used coastline product was found to be responsible for some of the misclassifications and increased errors of commission in

Enderby Land as well as over Riiser-Larsen Ice Shelf and Rennick Glacier (Table 5.6). Furthermore, false positive lake classifications occurred due to remaining weaknesses of the classifier over dark area patches caused by shadow, bare ice or wet snow. Through investigation of the full classification maps, dark area patches similar to lakes were found to account for increased error rates over Rennick Glacier, Enderby Land as well as Riiser-Larsen and Moscow University ice shelves. At this point it has to be noted that Rennick Glacier and Moscow University Ice Shelf are located most distant from training regions (Figure 5.1a) which can potentially explain the lower performance of the classifier over these regions. As mentioned in Chapter 5.4.1, small patches of particularly large lakes were missed in the classifications resulting in slightly increased false negative rates (ERO), e.g. over Amery and Rennick ice shelves. In detail, large lakes were underrepresented in the training data requiring extensive augmentation. This likely resulted in an overfitting of the model towards the training data causing the described underestimations (Figure 5.17).

### 5.7.2.2 Sentinel-2

Likewise, the accuracy assessment for the Sentinel-2 test data revealed an excellent performance of the developed classification workflow. In fact, the F-score was above 90% for most test sites with the exception of the study region covering Abbot Ice Shelf returning a value of ~82% for the “water” class. At the same time, multiple regions were subject to false positive lake classifications and multiple regions returned increased rates of false negatives. To start with, false positive lake classifications were present over the test regions covering Pine Island Bay, Enderby Land and Drygalski Ice Tongue (Table 5.7). Similar as for Sentinel-1, the deviating date of the used coastline product for the masking of pixels seaward of the calving front introduced false positive classifications over melt on sea ice in Pine Island Bay despite being successfully masked in the image extracts in Figure 5.20. Moreover, false positive lake classifications over Pine Island Bay resulted from the widespread presence of slush being misclassified as surface lakes. In contrast to that, false positive lake classifications over Enderby Land can be explained by mixed ice and water pixels at the edges of refreezing lakes. Similarly, misclassifications at lake edges as well as near the calving front explain the increased rate of false positives over Drygalski Ice Tongue. On the contrary, false negative lake classifications mainly influenced the performance of the classifier over Abbot and Cosgrove ice shelves as well as in Adelie Land. In all three regions, false negative classifications resulted from mixed pixels at lake edges as well as lake regions that were obscured by cloud shadow.

### 5.7.3 Future Requirements

Despite the shown potential of the automated classification workflow, the Sentinel-1 and Sentinel-2 classification algorithms could be further refined. For Sentinel-1, the most important method refinement would be to increase the dataset used for deep learning model training. In this context, more training samples covering lakes of varying appearances as well as ice sheet surface features that are difficult to discriminate from lakes would be helpful. Apart from increasing the availability of training samples over shadow, wet snow, dry snow, bare ice and the open ocean, one important measure would be to include more samples covering large lakes. As small lake features are more widespread around Antarctica, training data covering large lakes could be collected over Greenland which would also contribute to a further improved spatio-temporal transferability of the method. When increasing the training dataset, particular focus should be on regions that are most distant from current training regions (Figure 5.1a) in order to support future pan-Antarctic mapping strategies. This applies to large parts of Victoria Land on the EAIS as well as to Marie Byrd Land on the WAIS.

Furthermore, variations of the model architecture and training parameters could be tested. In this context, the use of a weighted loss function (Lu et al., 2019; Sun et al., 2018) or of sample weights could be of interest. However, due to the high accuracy of the classification results obtained with the current deep learning architecture and parameter settings, weighted loss functions were not considered as part of this thesis. In this context, the implemented data augmentation strategy with focus on patches with numerous lake pixels and difficult regions as well as the use of backscattering minimum products certainly contributed to the obtained high classification accuracies. Furthermore, the extension of U-Net with suitable modules, including ASPP for multi-scale feature extraction and residual connections for optimized performance, was of particular advantage for an improved consideration of the spatial image context. Apart from that, the model could be trained with a larger number of input bands. In this regard, dual-polarized SAR data, temporal image metrics or DEM data could be fed to the deep learning pipeline. As dual-polarized Sentinel-1 data are currently available at a spatial resolution of 40 m only, it would greatly reduce the visibility of small or elongated lakes and was therefore not considered. On the other hand, the integration of temporal image metrics or of DEM data would drastically increase the computational load. At the same time, high-resolution topographic data, e.g. from the REMA DEM, are still restricted in terms of their incomplete spatial coverage. Furthermore, the temporal acquisition interval of the REMA DEM deviates from the Sentinel-1 acquisitions which would likely result in further inaccuracies.

On the other hand, the accuracy of classifications from Sentinel-2 could be further improved through consideration of additional training data covering Adelie Coast and

Wilkes Land on the EAIS as well as Marie Byrd Land on the WAIS (Figure 5.1b). These regions are so far underrepresented in the training data and could be of great help to improve the classification accuracies for future pan-Antarctic assessments. In particular, more training data covering slush, lake edges and lakes affected by cloud shadow could be included. However, as the integration of more training data covering slush or lake edges might lead to reduced classification accuracies, e.g. over shallow lake area, alternative methods (Chapter 5.3.2.3) should also be considered. Similar as for Sentinel-1, also the consideration of temporal image metrics during model training could improve the accuracy of the classifier, while being at the cost of an increased computational load. Another aspect to consider in future research is the use of more up-to-date coastline and DEM data during post-processing. In fact, this applies to both Sentinel-1 and Sentinel-2 being subject to misclassifications, e.g. where the coastline retreated inland since the acquisition of the underlying data (Chapter 5.7.2). For example, more up-to-date coastline data could be retrieved from the acquisitions themselves through application of automated coastline extraction methods (e.g. Baumhoer et al., 2019). Furthermore, the integration of more up-to-date DEM data, e.g. from the REMA DEM, would allow for less conservative thresholds during post-classification (Chapter 5.3.1.3, Chapter 5.3.2.3). In fact, lower elevation and slope thresholds could potentially support a further masking of misclassifications around rock outcrop. As mentioned, this step would be at the cost of an increasing computational load.

Apart from method improvements, future efforts should consider the collection and integration of ground truth data, e.g. from field measurements or flight campaigns. This would allow for a more representative evaluation of the obtained classification results. However, as reference data are difficult to collect over the Antarctic Ice Sheet, alternative locations over glaciated regions beyond Antarctica could be considered. Furthermore, velocity mappings could be beneficial in order to account for overestimations due to the movement of lakes with ice flow. This is particularly relevant when fused supraglacial lake extent mappings are derived at temporal intervals greater than one month.

## 5.8 Summary

In this chapter, a novel framework for automated supraglacial lake extent mapping in multi-sensor remote sensing data was introduced. As outlined in Chapter 5.3, the novel framework for Antarctic supraglacial lake extent derivation combines recent advances in artificial intelligence with the increasing availability of open access satellite data provided by the European Copernicus programme. In particular, a combination of Sentinel-1 SAR and optical Sentinel-2 data was chosen in order to exploit and overcome sensor-specific advantages and limitations (Chapter 4.2) for retrieval of more complete mapping products. To provide more detail, Sentinel-1 SAR imagery were classified by means of a

convolutional neural network based on residual U-Net that was trained on 21,200 single-polarized Sentinel-1 SAR image patches covering 13 Antarctic regions. Similarly, optical Sentinel-2 data were collected over 14 Antarctic regions and used for training of a pixel-based RF classifier. The two methods were combined through decision-level fusion of optical and SAR classification products and implemented as part of DLR's internal HPC infrastructure allowing for an automated processing of large amounts of satellite data over the entire Antarctic continent. The combination of optical and SAR classification products was shown to be of particular relevance over Antarctica where optical data are often limited by cloud cover (Figure 5.24d) and polar darkness and where SAR data can be subject to effects such as severe wind roughening. In addition, SAR-based mappings are of particular importance in order to capture both surface and subsurface meltwater accumulation. As an efficient large-scale mapping technique for supraglacial lake extent derivation is so far lacking, the developed approach is of great relevance for the scientific community allowing for detailed intra-annual and inter-annual analyses on Antarctic supraglacial lake formation. In particular, the developed mapping technique for the first time enables an automated mapping of Antarctic supraglacial lake extents without the requirement of manual post-processing or user intervention (Chapter 5.6). In addition, the developed framework can be easily applied to other glaciated regions such as Greenland (Chapter 5.4) highlighting its potential for spatio-temporal transferability.

Furthermore, the obtained mapping results and accuracy metrics revealed the good functionality of the developed classification methods for both Sentinel-1 and Sentinel-2. With an average F-score of ~93% for the "water" class in all Sentinel-1 test data, the performance of the deep learning pipeline was shown to be particularly robust. In this regard, the design of the data augmentation strategy as well as the extension of U-Net with suitable modules for an improved consideration of the spatial image context was particularly beneficial. On the other hand, the main remaining limitations of the SAR-based mapping technique include (1) the lack of high-resolution and up-to-date topographic and coastline data, (2) the underrepresentation of large lakes and several Antarctic regions in the training data, (3) misclassifications over radar shadow and small bare ice and wet snow patches and (4) the lack of ground truth data for an improved evaluation of the classification results. Likewise, the accuracy metrics of the developed Sentinel-2 classification method reveal the good functionality and spatio-temporal transferability of the RF classifier. Here, the average F-score of the "water" class across all test sites was computed at ~95%. Similar as for Sentinel-1, remaining limitations of the implemented RF algorithm include the lack of high-resolution and up-to-date topographic and coastline data as well as of ground truth data. Furthermore, misclassifications over slush and lake edges as well as an underrepresentation of individual ice sheet regions in the training data contributed to increased errors rates.

Considering the defined future requirements in Chapter 4.3, the developed workflow greatly contributes to their fulfilment. In particular, the stated future requirement of intra-annual and inter-annual supraglacial lake extent mappings at regional to circum-Antarctic scale was shown to be fulfilled through derivation of multi-temporal supraglacial lake extent mapping products over Amery and George VI ice shelves as well as the implementation of developed methods for large-scale processing. Furthermore, the stated requirement of a multi-sensor classification technique with pan-Antarctic mapping capabilities is equally fulfilled through combination of Sentinel-1 SAR and optical Sentinel-2 satellite data as well as the training and testing of the classifiers across multiple independent regions including locations on the Greenland Ice Sheet. Additionally, the requirement of spatial and temporal resolution standards was formulated. As stated in Chapter 5.3.3, the implemented methodological framework suggests the use of bi-weekly observational periods in order to capture intra-annual supraglacial lake extent dynamics at sufficient spatial coverage whilst avoiding overestimations of lake area due to their movement with ice flow. Furthermore, a spatial resolution of 10 m was chosen for the final classification products, in agreement with the pixel spacing of the used sensor data.

To summarize, the developed workflow presents the first automated mapping method for Antarctic supraglacial lake extent derivation in multi-sensor remote sensing data from the Sentinel-1 SAR and optical Sentinel-2 satellite missions. In detail, the main benefits of the developed mapping technique include (1) the efficient and fast processing of large amounts of satellite data from Sentinel-1 and Sentinel-2 through implementation of the developed methods on a High-Performance Computing infrastructure, (2) the automated and highly accurate classification of supraglacial lake extents in optical and SAR satellite imagery through application of supervised machine learning, (3) the spatio-temporal transferability of the developed algorithm to regions across the entire Antarctic continent as well as to regions beyond Antarctica and (4) the possibility of an automated extraction of high resolution classification maps from single satellite scenes as well as of fused optical and SAR classification products at flexible temporal intervals ensuring continuous mapping efforts during Antarctic winter, cloud coverage or wind roughening. Through the mentioned advantages and benefits, the developed mapping technique will greatly support future research on Antarctic surface hydrology and improve current knowledge on Antarctic supraglacial lake formation, evolution and impacts. In this context, automated mapping products will also contribute to an improved representation of meltwater transport across Antarctic ice shelves in modelling efforts being crucial for future assessments of Antarctica's contribution to global sea-level-rise.



## CHAPTER 6

### **6 Environmental Controls on Antarctic Supraglacial Lake Formation in 2015-2021 \***

Recent ice shelf disintegration events along the Antarctic Peninsula were driven by atmospheric warming resulting in an increased presence of meltwater ponds on ice shelves to cause hydrofracturing and ice shelf collapse (Cook and Vaughan, 2010; Leeson et al., 2020; Scambos et al., 2004). Ice shelf collapse leads to a reduction in buttressing forcing glacier acceleration and increased ice discharge (Rott et al., 2018; The IMBIE Team, 2018). Considering that Antarctic surface melting and ponding is expected to increase under future atmospheric warming (Bell et al., 2018; Gilbert and Kittel, 2021; Kingslake et al., 2017; Meredith et al., 2019; Trusel et al., 2015), further Antarctic ice shelves will likely become unstable triggering ice shelf collapse and ice dynamic change. This particularly applies to regions that are classified as vulnerable to hydrofracture (Alley et al., 2018; Fürst et al., 2016; Lai et al., 2020) or are structurally weakened by fractures and crevasses (Lhermitte et al., 2020) or firn air depletion (Kuipers Munneke et al., 2014; Lenaerts et al., 2017; Spergel et al., 2021). As mentioned in Chapter 3.3, also an inland migrating of lakes under global warming can result in the connection of surface and basal hydrological systems causing basal lubrication and sliding to initiate ice flow accelerations (Bartholomew et al., 2010; Bell et al., 2018; Siegert et al., 2018; Tuckett et al., 2019). Further, the low albedo of rock, blue ice and supraglacial lakes themselves can trigger enhanced melting contributing to a more frequent occurrence of the described impacts (Bell et al., 2018; Lenaerts et al., 2017; Lüthje et al., 2006). In this context, other suggested control factors on supraglacial lake distribution and evolution include the local glaciological setting, the regional near-surface climate as well as large-scale atmospheric modes (Chapter 3.1) (Arthur et al., 2020a; Cape et al., 2015; Laffin et al., 2021; Lenaerts et al., 2017; Stokes et al., 2019).

Despite recent progress in the understanding of Antarctic surface hydrology, the spatio-temporal distribution of Antarctic supraglacial lakes as well as associated environmental drivers and impacts remain poorly constrained. To improve the understanding of present-day Antarctic surface hydrology as well as to constrain the

---

\*Parts of this chapter are based on Dirscherl et al. (2021b).

dominant control factors on supraglacial lake formation, the monitoring of Antarctic supraglacial lake extent dynamics is of utmost importance. Therefore, the implemented framework for automated supraglacial lake extent classification (Chapter 5.6) is employed on the full archive of Sentinel-1 SAR and optical Sentinel-2 data over six major ice shelves on the API and EAIS. In particular, fused supraglacial lake extent mappings are derived for the period 2015-2021 at bi-weekly temporal scale and 10 m spatial resolution. As described in Chapter 4.3.2, the combination of optical and SAR data is particularly beneficial in order to exploit and overcome sensor-specific advantages and limitations as well as to obtain more complete mapping records than with single-sensor data. In detail, this chapter aims to (1) analyze intra-annual and inter-annual supraglacial lake extent dynamics in 2015-2021, (2) investigate anomalous supraglacial meltwater ponding above or below average with respect to the observational period 2015-2021, (3) establish a link between 2015-2021 supraglacial meltwater ponding and environmental controls, including the local glaciological setting, the regional near-surface climate and large-scale atmospheric modes, through application of multi-temporal linear correlation analysis and (4) reveal first-order controls on supraglacial lake formation and highlight potential implications for other ice sheet regions and future ice shelf stability.

The investigated study sites, used datasets and employed methods are introduced in Chapters 6.1-6.3. Chapter 6.4 presents the obtained results and Chapter 6.5 provides a thorough discussion on environmental drivers of 2015-2021 supraglacial meltwater ponding. Finally, Chapter 6.6 summarizes the key findings and conclusions of Chapter 6.

## 6.1 Study Sites

The six investigated ice shelves are among the largest across the entire Antarctic continent and include George VI, Bach and Wilkins on the south-west API as well as Riiser-Larsen, Nivlisen and Amery on the EAIS (Figure 6.1). The choice of ice shelves was made in agreement with their spatial distribution around Antarctica where different climatic conditions and local glaciological settings prevail. This allows to investigate the agreement of drivers among different regions and thus their potential transferability to other ice sheet regions. In addition, study sites were selected to cover regions of frequent lake recurrence with lakes being most abundant on the API and EAIS, while showing only sporadic occurrence on the WAIS (Chapter 3.2) (Banwell et al., 2021; Dell et al., 2020; Kingslake et al., 2017; Moussavi et al., 2020; Reynolds, 1981; Spergel et al., 2021; Stokes et al., 2019; Wagner, 1972). Further, the ice shelves were selected on the basis of satellite data availability with respect to Sentinel-1 and Sentinel-2.

The three investigated API ice shelves cover an area of  $\sim 23,370 \text{ km}^2$ ,  $\sim 4,540 \text{ km}^2$  and  $11,144 \text{ km}^2$  representing the neighboring George VI, Bach and Wilkins ice shelves in the Bellingshausen Sea sector (Figure 6.1a-c) (Cook and Vaughan, 2010; Holt et al.,

2013). To start with, George VI Ice Shelf is located in a narrow channel between Alexander Island and Palmer Land. The latter provides most of its ice inflow, compressing laterally against the western grounding line (Hambrey et al., 2015; Holt et al., 2013; LaBarbera and MacAyeal, 2011; Reynolds and Hambrey, 1988). On the other hand, Bach and Wilkins receive most of their ice inflow from Alexander Island.

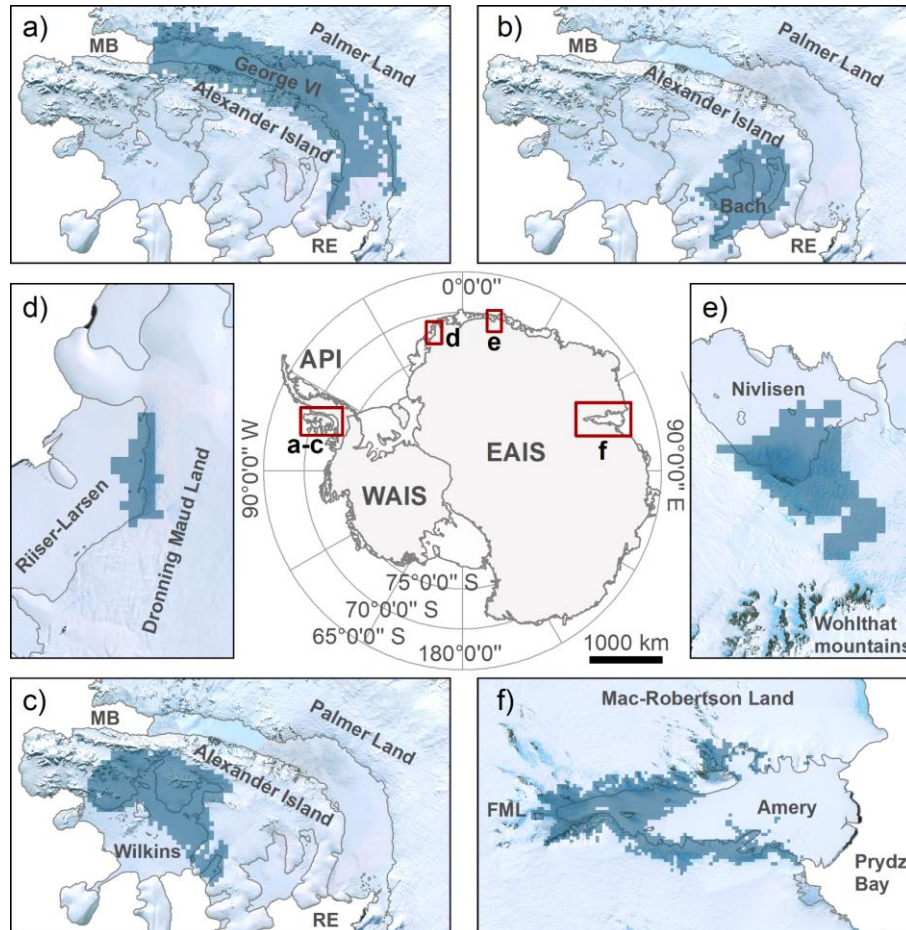


**Figure 6.1.** Overview map of Antarctica showing the locations of the six investigated ice shelves George VI (a), Bach (b), Wilkins (c), Riiser-Larsen (d), Nivlisen (e) and Amery (f). The area of interest for satellite data acquisition and lake extent mapping corresponds to the red outlines and the area of interest used for statistical analyses corresponds to the shaded blue area in (a-f). Over Amery, a permanent lake feature at the western grounding line (Beaver Lake) was excluded from analyses to avoid misclassifications in optical imagery. FML: Fisher, Mellor and Lambert glacier systems. MB: Marguerite Bay. RE; Ronne Entrance. Modified after Dirscherl et al. (2021b). Data: (Bindschadler et al., 2008; IMBIE, 2016; Mouginot et al., 2017b; Rignot et al., 2013).

On the other hand, the three investigated EAIS ice shelves include Riiser-Larsen, Nivlisen and Amery, each covering an area of  $\sim 48,180 \text{ km}^2$ ,  $7,600 \text{ km}^2$ ,  $62,620 \text{ km}^2$ , respectively (Figure 6.1d-f) (Dell et al., 2020; Foley et al., 2013). To start with, Riiser-Larsen Ice Shelf is located in western Dronning Maud Land with most of its ice inflow originating from the adjacent Plogbreen and Veststraumen ice streams. Nivlisen Ice Shelf is located several hundred kilometers to the east of Riiser-Larsen Ice Shelf, in

central Dronning Maud Land, and is nourished by ice draining through the Wholthat Mountains (Horwath et al., 2006). Finally, Amery Ice Shelf is located in Mac-Robertson Land and is the largest of all EAIS ice shelves. Amery is fed by Fisher, Mellor and Lambert glaciers (Figure 6.1f).

For each ice shelf, AOIs were drawn for both satellite data acquisition and classification as well as statistical analyses. For satellite data acquisition and classification, the red outlines in Figure 6.1 ensured a spatially complete data record over the full ice shelves. On the other hand, statistical analyses were performed on the basis of the shaded blue areas in Figure 6.1a-f. These areas were drawn in agreement with confirmed supraglacial lake occurrences during at least one time step within the period 2015-2021 as well as on the basis of resampled ERA5-Land pixel footprints (Chapter 6.2). For George VI, Bach, Wilkins, Riiser-Larsen, Nivlisen and Amery ice shelves, this resulted in AOI subsets of 27,324 km<sup>2</sup>, 9,504 km<sup>2</sup>, 15,660 km<sup>2</sup>, 1,512 km<sup>2</sup>, 5,292 km<sup>2</sup>, and 41,760 km<sup>2</sup>, respectively. Where lake coverage expanded onto the adjacent grounded ice, regions upstream of the grounding line were included explaining the partly larger AOI sizes compared to the ice shelf areas (Dirscherl et al., 2021b).

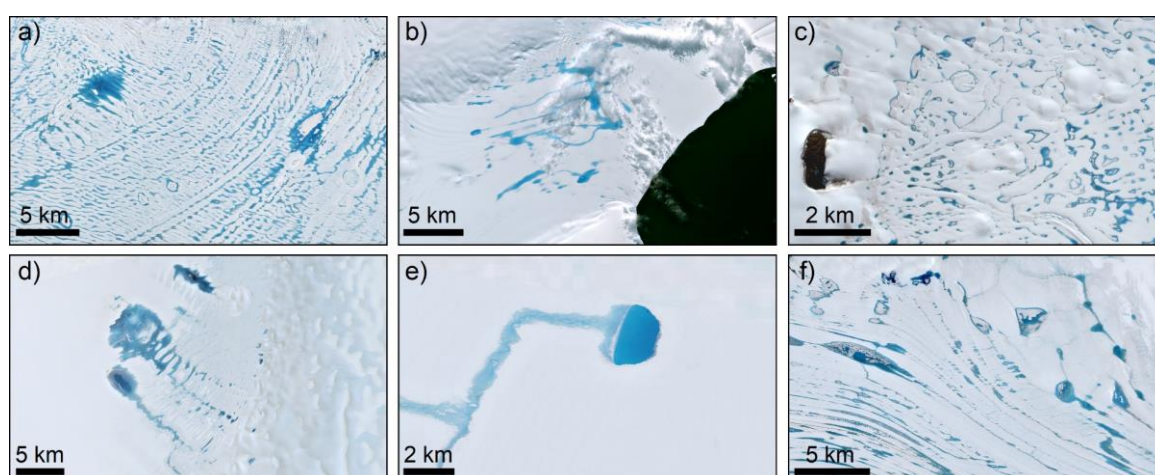


**Figure 6.2.** Sentinel-2 imagery showing supraglacial lakes on (a) George VI (19 January 2020), (b) Bach (29 January 2020), (c) Wilkins (23 January 2021), (d) Riiser-Larsen (2 February 2017), (e) Nivlisen (21 January 2019) and (f) Amery (2 January 2019) ice shelves. Modified after Dirscherl et al. (2021b). Data: (Copernicus Sentinel-2 data).

## 6.2 Datasets

### 6.2.1 Satellite Imagery

For automated supraglacial lake extent mapping, the full archive of Sentinel-1 and Sentinel-2 was exploited. Satellite data retrieval was performed automatically on IDA using the implemented workflow outlined in Figure 5.28. In detail, all available Sentinel-1 data in GRDH format, IW swath mode and horizontal transmit-and-receive polarization

(HH) were acquired for the AOI outlines considering the period 1 November to 31 March in 2015-2021. Over API ice shelves, data were available for the entire investigation period 2015-2021 (Figure 6.3, Figure 6.4). Yet, over Riiser-Larsen, Nivlisen and Amery ice shelves, no data were available during melting season 2015-2016. Considering the high revisit frequency of Sentinel-1 over polar regions (<6 days), this resulted in a total number of 3,075 Sentinel-1 acquisitions (Table 6.1).

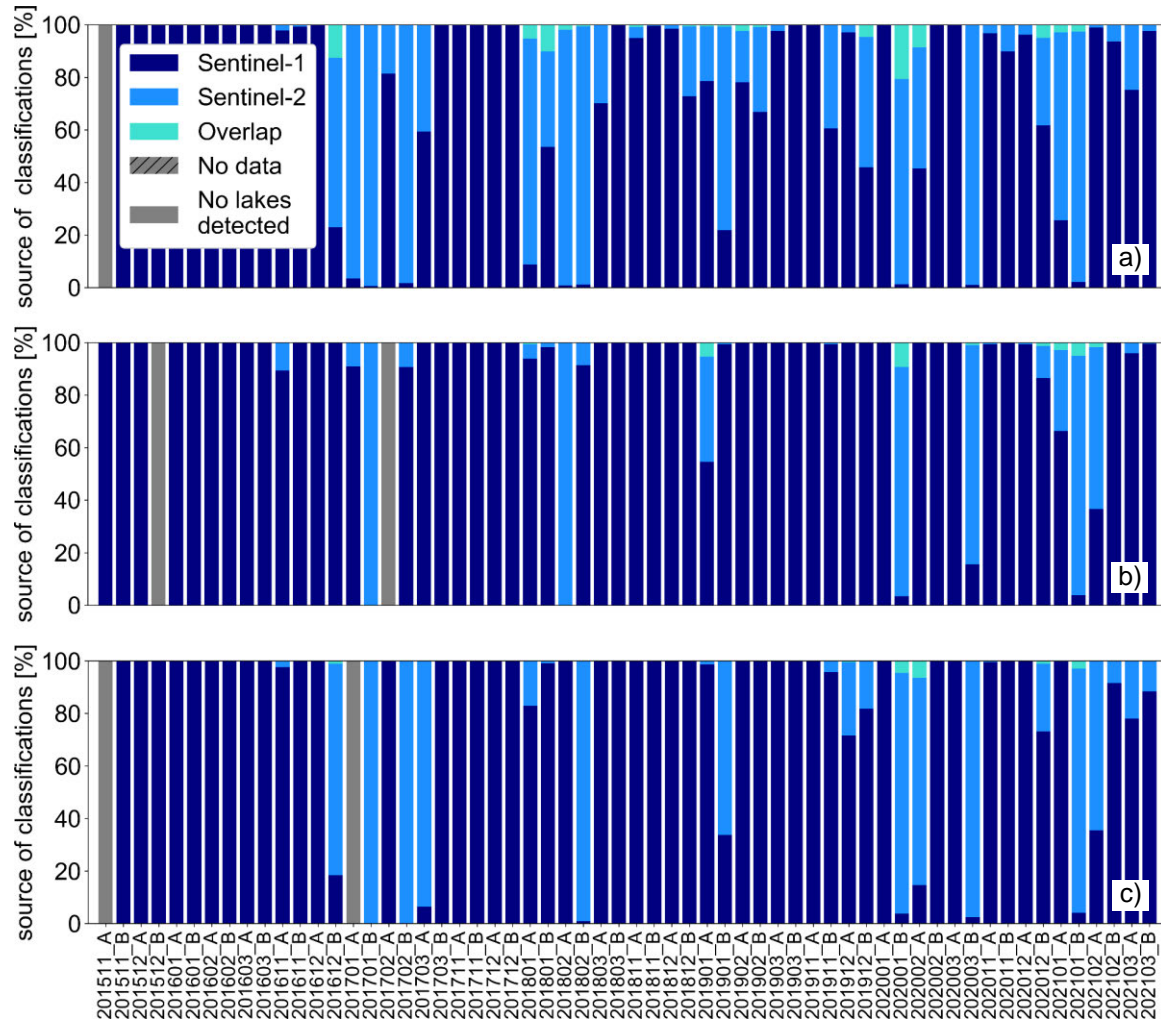


**Figure 6.3.** Data source of bi-weekly lake extent classifications over George VI (a), Bach (b) and Wilkins (c) ice shelves from Sentinel-1, Sentinel-2 or both. Modified after Dirscherl et al. (2021b).

The acquisition of Sentinel-2 data was performed on the basis of a cloud coverage <75%. This comparatively high cloud threshold was chosen to ensure a complete data record also for acquisitions where only parts of the image scenes were affected by cloud cover. In addition, the performance of cloud masking algorithms over ice sheets can be degraded due to the spectral similarity between clouds and snow/ice resulting in a higher specified cloud cover than is present in the actual satellite acquisition and thus an incomplete data record. Considering the high revisit frequency of Sentinel-2 over polar regions (<5 days), a total of 2,167 Sentinel-2 acquisitions was retrieved for the six



investigated ice shelves (Table 6.1). As no Sentinel-2 data were available during melting season 2015-2016, data retrieval was yet restricted to years 2016-2021.

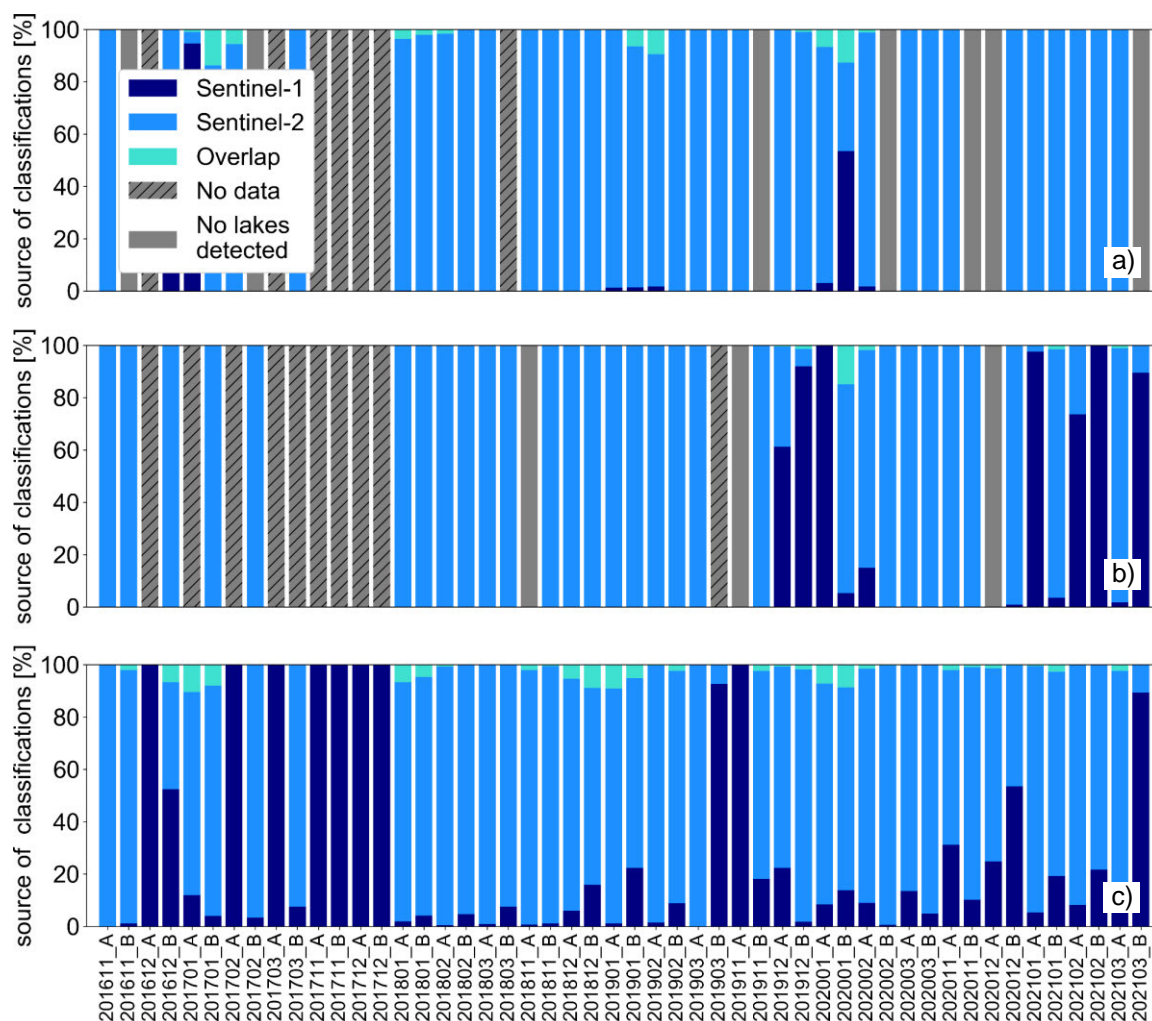


**Figure 6.4.** Data source of bi-weekly lake extents over Riiser-Larsen (a), Nivlisen (b) and Amery (c) ice shelves from Sentinel-1, Sentinel-2 or both. Modified after Dirscherl et al. (2021b).

**Table 6.1.** Sentinel-1 and Sentinel-2 data availability over the six investigated ice shelves.

Area of interest	Number of Sentinel-1 scenes	Number of Sentinel-2 scenes	Total number of scenes
George VI, Bach, Wilkins	1,048	623	1,671
Riiser-Larsen	160	380	540
Nivlisen	302	192	494
Amery	1,565	972	2,537
<b>Total</b>	<b>3,075</b>	<b>2,167</b>	<b>5,242</b>

## 6.2.2 ERA5-Land Climate Reanalysis Data

For analysis of environmental controls on Antarctic supraglacial lake formation in 2015-2021, hourly ERA5-Land climate reanalysis data were used (Munoz Sabater, 2019a). Replacing the former ERA-Interim reanalysis of the European Centre for

Medium-Range Weather Forecasts, ERA5-Land provides estimates for a range of land variables at a grid spacing of ~9 km (0.1°) and a temporal coverage dating back to 1950. Over Antarctica, the use of climate reanalysis data is of particular advantage as its vast size, harsh climate and remote geographical location complicate detailed ground-based monitoring efforts. Besides, data from weather stations are available only sparsely requiring extensive interpolation when used for large-scale analyses.

The ERA5-Land variables used for statistical analyses include surface net solar radiation, 2 m air temperature, 10 m wind components, total precipitation and modelled snowmelt. Hourly ERA5-Land estimates were retrieved for the period 1 October to 31 March in 2015-2021. In this context, October and November data were used for analysis of climate drivers at different time lags. In addition, estimates of ERA5-Land total precipitation were acquired for all remaining months in 2015-2020 enabling the investigation of links to previous-year precipitation. Data on previous-year precipitation provide important insight into the influence of the FAC where previous-year low precipitation leads to a reduced FAC facilitating ponding and previous-year high precipitation leads to an increased FAC allowing the infiltration of meltwater into the firn.

To provide more detail on the quality of used climate datasets, the following paragraph briefly outlines their main characteristics. To start with, ERA5-Land reanalysis data on surface net solar radiation represent the difference between downward shortwave radiation incident upon the Earth's surface and the amount of radiation reflected back to space. Even though data on surface net solar radiation have not been validated over Antarctica, investigations over China and Europe point towards an improved performance compared to the other reanalysis datasets (Jiang et al., 2020; Urraca et al., 2018). Next, ERA5-Land air temperature data are provided at 2 m above the surface and are the best estimate of the seasonal cycle of air temperature over coastal Antarctica and particularly the API (Gossart et al., 2019; Tetzner et al., 2019). The low bias and low mean absolute error of 2°C over Antarctica make ERA5-Land air temperature data superior to other reanalysis datasets (Gossart et al., 2019). On the other hand, ERA5-Land wind data reflect the horizontal speed of air at 10 m above the surface moving towards the north and east, respectively. Reanalysis of wind data captures the typical annual cycle of wind with a mean underestimation during katabatic wind forcing in winter and over coastal Antarctica during summer resulting in an overall mean absolute error of 2.8 m s<sup>-1</sup> (Gossart et al., 2019). Furthermore, estimates of total precipitation are provided in meters depth and include all liquid and frozen water accumulated on the Earth's surface. ERA5-Land total precipitation data perform well in detecting precipitation events over the API. At the same time, a bias may exist, e.g. due to the negligence of the redeposition of snow (Tetzner et al., 2019). Finally, the ERA5-Land modelled snowmelt product is available in meters of water equivalent. To date, no evaluation of ERA5-Land snowmelt data has been performed over Antarctica.



## 6.3 Methods

### 6.3.1 Pre-Processing of ERA5-Land Climate Reanalysis Data

Before statistical correlation analysis could be performed, the ERA5-Land climate reanalysis data required to be pre-processed. First, hourly estimates of surface net solar radiation were converted to daily energy fluxes in watts per square meter ( $W\ m^{-2}$ ). Similarly, hourly estimates of air temperature were converted from Kelvin (K) to degrees Celsius ( $^{\circ}C$ ) and aggregated to daily average air temperature. Hourly estimates of zonal ( $u$ ) and meridional ( $v$ ) wind stress components were first resampled to daily averages. Following aggregation to time series (Chapter 6.3.2), the data were converted to wind magnitude ( $w_m = \sqrt{u^2 + v^2}$ ) and wind direction ( $w_d = 180 + (\arctan(v, u) \times 180/\pi)$ ). Next, daily estimates of total precipitation and snowmelt were obtained from hourly ERA5-Land data through consideration of the total accumulated value of a day. Subsequently, daily estimates of total precipitation and snowmelt were converted to millimeters depth and millimeters water equivalent, respectively. Finally, all climate reanalysis data were reprojected to the Antarctic Polar Stereographic projection.

### 6.3.2 Time Series Generation

Since the acquired Sentinel-1 and Sentinel-2 satellite data were automatically pre-processed, classified and post-processed to fused supraglacial lake extent classification products at 10 m spatial resolution and bi-weekly temporal scale using the implemented processor for circum-Antarctic supraglacial lake extent mapping (Chapter 5.6), the only remaining processing step was to fill data gaps in the bi-weekly time series over Riiser-Larsen and Nivlisen ice shelves. For this purpose, the respective bi-weekly long-term mean of the period 2016-2021 was used for interpolation. Given that data gaps were mostly present during months of low lake coverage during the early or late melting season (Figure 6.4a-b), this interpolation strategy was considered acceptable. To support statistical analyses with previous-year precipitation and annual SAM (Marshall, 2018, 2003), an atmospheric index used for investigation of large-scale drivers, the bi-weekly time series covering January of each year in 2016-2021 were further aggregated to monthly supraglacial lake extent mappings. Monthly lake extent mapping products were also used for investigation of local controls and of inter-annual supraglacial lake recurrence times. In the following, the automatically derived bi-weekly and monthly supraglacial lake extent time series were converted to time series of fractional lake extent considering the ERA5-Land pixel footprints (Figure 6.1a-f).

Likewise, the daily ERA5-Land data were aggregated to average bi-weekly time series. In addition, bi-weekly maxima were calculated for air temperature in order to capture temperature extreme events and positive degree days. Overall, this resulted in

seven climate variables used for bi-weekly statistical analyses. To investigate whether above or below normal climatic conditions resulted in above or below normal meltwater ponding, the bi-weekly fractional lake extent and climate time series were also converted to time series of anomalies considering the 2015-2021 long-term mean of each bi-weekly interval. Furthermore, data on bi-weekly precipitation were converted to annual aggregates of previous-year precipitation considering the period March to October of each year in 2015-2020. As previously mentioned, previous-year precipitation was used as an indirect indicator of the FAC of snow.

### **6.3.3 Multi-Temporal Statistical Correlation Analysis**

For multi-temporal statistical correlation analysis between fractional lake extent and regional and large-scale climate variables, the Pearson correlation coefficient ( $r$ ) was used. The Pearson correlation measures the linear relationship between two variables returning values in the range of  $[-1, +1]$  where  $-1$  and  $+1$  represent a strong negative and strong positive linear relationship, respectively. Lower correlation values close to  $0$  represent the existence of a weak statistical link between two variables. Furthermore, the statistical significance of correlations can be measured with the  $p$ -value ( $p$ ). In the following, significance levels of  $p < 0.05$  (\*),  $p < 0.01$  (\*\*) and  $p < 0.001$  (\*\*\*) are used.

To obtain more robust correlation values, only bi-weekly data covering summer months (December, January and February) were considered for statistical correlation. During these months, lake extents are highest and data gaps and misclassifications are lowest. For the study regions on the API and EAIS, this resulted in a total of 36 and 30 observations for each bi-weekly time series in the period 2015-2021 and 2016-2021, respectively. Apart from correlating fractional lake extent and climate time series at identical time intervals (lag 0), cross-correlation with climate data at time lags 1-4 was performed. In this context, each lag represents a shift by half a month with respect to the previous lag resulting in the maximum cross-correlation at lag 4 to cover the period October to December of a year. Statistical correlation analysis was performed with spatial averages representing the full ice shelves, anomalies of spatial averages as well as at pixel level. For correlations between time series of January fractional lake extent and annual SAM as well as previous-year precipitation, six and five observations were available for the API and EAIS, respectively. At this point it has to be noted that the low number of observations used for correlation with previous-year precipitation and SAM may result in unreliable values of  $p$  and rather the  $r$ -value should be considered for interpretation. For completeness, links to local controls, including melt-albedo feedbacks and topographic factors, were investigated through visual comparison of lake density to topographic DEM data (Wessel et al., 2021), blue ice occurrence in optical imagery as well as the distribution of rock outcrop in Sentinel-2 classifications (Dirscherl et al.,

2020b). In the following, also previous-year precipitation is considered a local control factor due to the FAC being part of the local glaciological setting (Dirscherl et al., 2021b).

## 6.4 Results

The following chapters present the results for the Antarctic Peninsula (Chapter 6.4.1) and East Antarctic Ice Sheet (Chapter 6.4.2) separately. At first, supraglacial lake extent dynamics are described using time series of bi-weekly spatial averages and anomalies thereof (Chapter 6.4.1.1, Chapter 6.4.2.1). In the following, the results of the multi-temporal statistical correlation analysis are outlined. In detail, correlations with respect to spatial averages (Chapter 6.4.1.2, Chapter 6.4.2.2) and over individual pixels are shown (Chapter 6.4.1.3, Chapter 6.4.2.3).

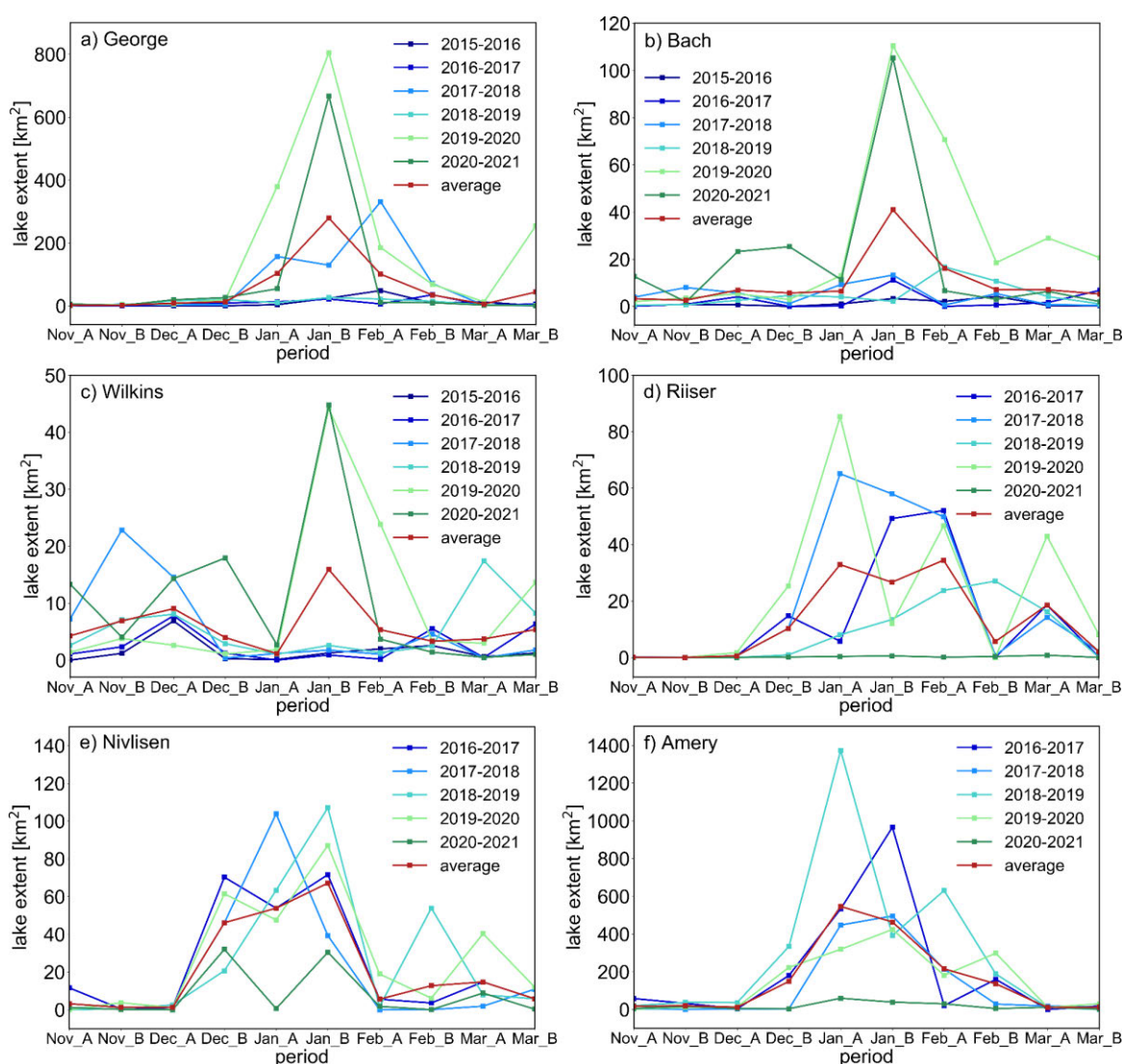


**Figure 6.5.** Supraglacial lake extent dynamics in 2015-2021 over George VI (a), Bach (b), Wilkins (c), Riiser-Larsen (d), Nivlisen (e) and Amery (f) ice shelves. The periods represent bi-weekly temporal intervals where “A” is the first half of a month and “B” the second half. Modified after Dirscherl et al. (2021b).

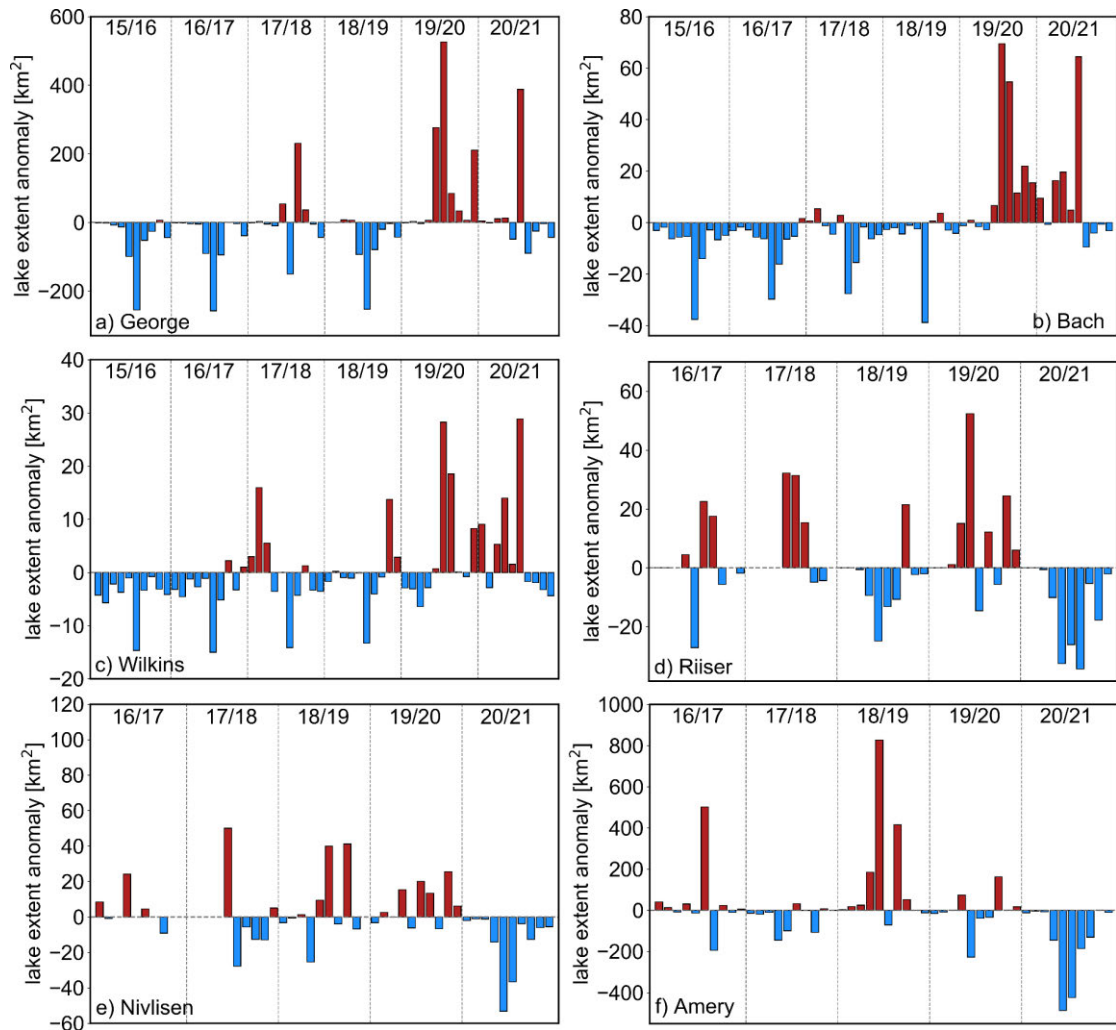


**Figure 6.6.** Anomalies of bi-weekly supraglacial lake extent time series during November to March of a melting season in the reference period 2015-2021 (a-c) and 2016-2021 (d-f) over George VI (a), Bach (b), Wilkins (c), Riiser-Larsen (d), Nivlisen (e) and Amery (f) ice shelves. For Riiser-Larsen and Nivlisen, data gaps are visible due to the interpolation with the bi-weekly long-term mean 2016-2021. Melting seasons are separated with dashed lines. Modified after Dirscherl et al. (2021b).

## 6.4.1 Antarctic Peninsula Ice Shelves

### 6.4.1.1 Supraglacial Lake Extent Dynamics in 2015-2021

As can be seen in Figure 6.5a-c, the bi-weekly supraglacial lake extent time series over George VI, Bach and Wilkins ice shelves on the API reveal strongly fluctuating supraglacial lake extents both intra-annually and inter-annually. During summer melting seasons 2015-2018, lake extents were generally low with the exception of melting season 2017-2018 over George VI Ice Shelf. On the other hand, melting seasons 2019-2020 and 2020-2021 were characterized by particularly strong surface melting and ponding over all three ice shelves. In this context, the highest supraglacial lake extents over George VI (~805 km<sup>2</sup>), Bach (~110 km<sup>2</sup>) and Wilkins (~45 km<sup>2</sup>) ice shelves were

observed during January 2020. Over all three ice shelves, late January marked the peak of a melting season and early or late February the end of a melting season. Moreover, Figure 6.6a-c shows anomalies of intra-annual supraglacial lake evolution with respect to the reference period 2015-2021. For melting season 2019-2020, API lake coverage was generally below average during the early melting season and above average during the peak of the melting season. Similarly, intra-annual anomalies of supraglacial lake extent time series reveal above-average meltwater ponding during the peak of the 2020-2021 melting season and below-average meltwater ponding during the late 2020-2021 melting season.

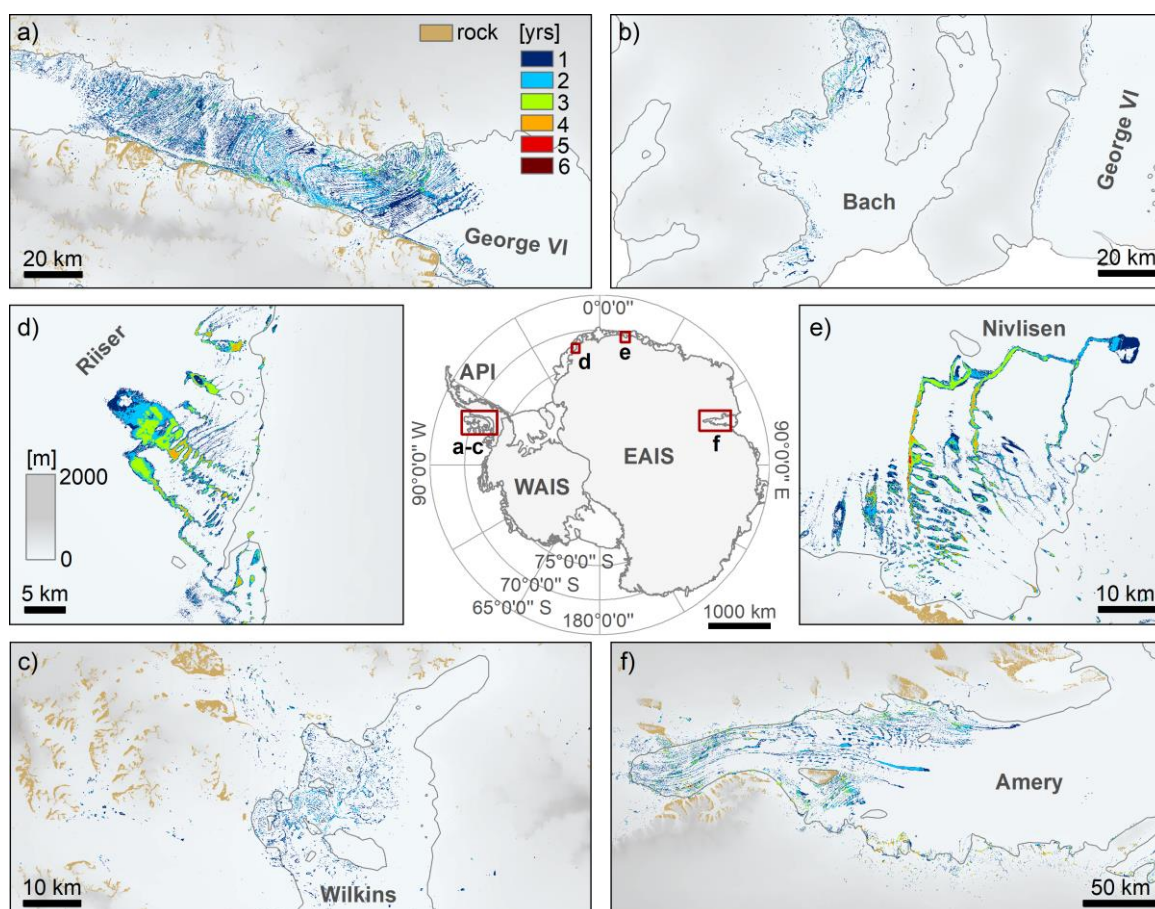


**Figure 6.7.** Inter-annual January recurrence of supraglacial lakes over George VI (a), Bach (b), Wilkins (c), Riiser-Larsen (d), Nivlisen (e) and Amery (f) ice shelves. The overview map in the middle shows the approximate location of the AOIs. In some regions, the movement of lakes with ice flow might have biased the calculation of annual lake recurrence times. API: Antarctic Peninsula. WAIS: West Antarctic Ice Sheet. EAIS: East Antarctic Ice Sheet. Modified after Dirscherl et al. (2021b). Data: (Dirscherl et al., 2020b; Howat et al., 2019; IMBIE, 2016; Mouginit et al., 2017b; Rignot et al., 2013).

Figure 6.7a-c shows the spatial pattern of the inter-annual recurrence of API lakes during January 2016-2021. Over all three ice shelves, supraglacial lakes tend to cluster at low elevations and low surface slopes downstream of the grounding line. Due to

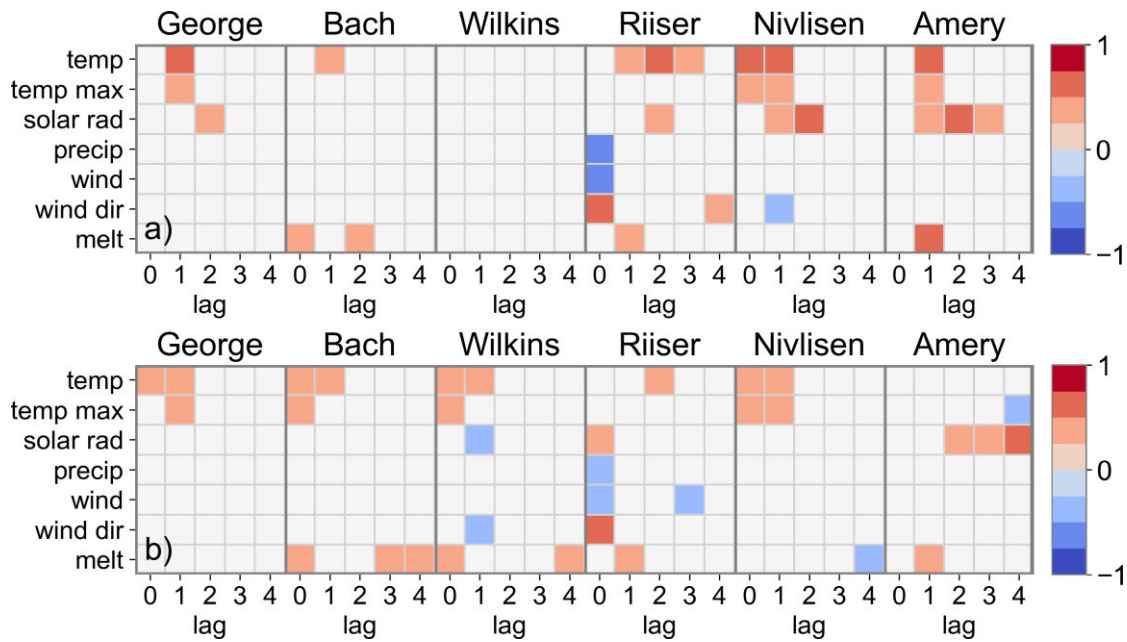
supraglacial lake coverage being comparatively low in 2015-2018, the inter-annual recurrence time of lakes was generally below three years with only few locations showing higher recurrence times. Over George VI Ice Shelf, lakes during low-melt years clustered closer to the grounding line and rock outcrop than during high-melt years, where they accumulated in flow stripes stretching over vast parts of the ice shelf (Figure 6.7a). Over Bach and Wilkins ice shelves, lakes generally clustered closer to the grounding line than on George VI Ice Shelf. For Wilkins Ice Shelf, lakes expanded farthest onto the adjacent grounded ice where rock outcrop is present (Figure 6.7c).

#### 6.4.1.2 Multi-Temporal Correlation Analysis with Spatial Averages

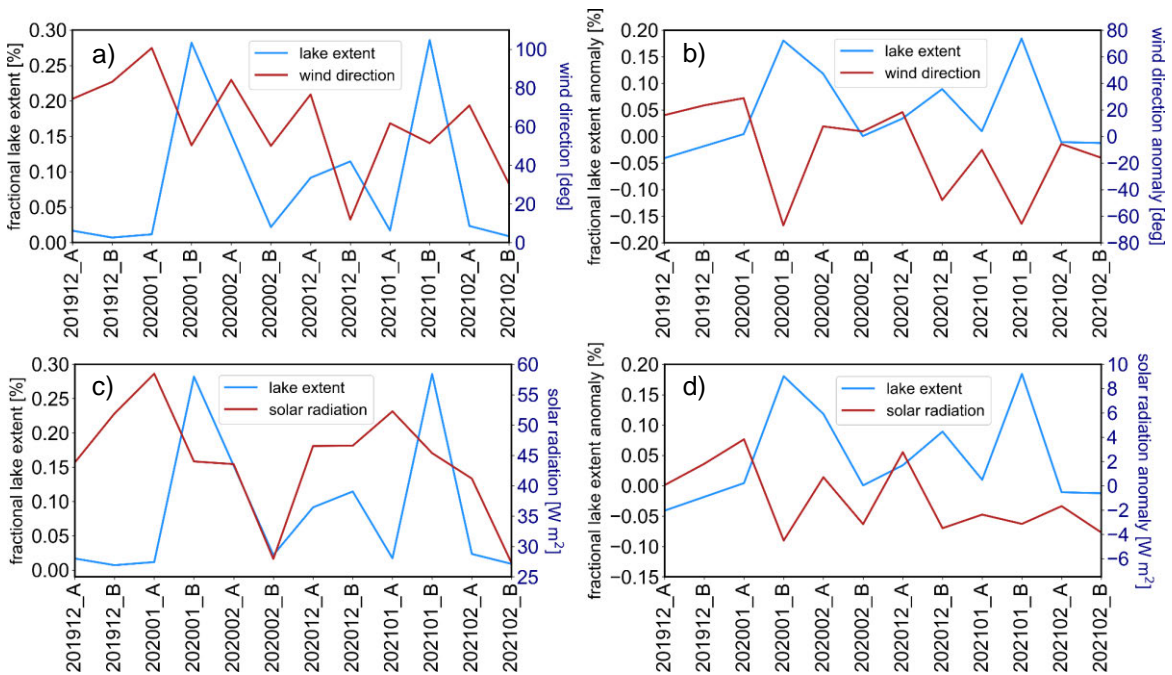
Figure 6.8 shows the results of the statistical correlation analysis between time series of bi-weekly fractional lake extent and climate variables considering spatial averages (Figure 6.8a) and anomalies of spatial averages (Figure 6.8b). Considering both quantities, all three API ice shelves show strong positive correlation with lag 0-1 average and maximum air temperature. Further, spatial averages of lag 2 solar radiation correlate positively with spatial averages of fractional lake extent over George VI Ice Shelf. Over Wilkins Ice Shelf, anomalies of lag 1 solar radiation and lag 1 wind direction correlate negatively with anomalies of fractional lake extent. In this context, correlation with solar radiation mostly reflects an anomalous low availability of incoming solar radiation during periods of high meltwater ponding in 2019-2020 and 2020-2021 (Figure 6.9c-d). On the other hand, negative lag 1 correlation with wind direction over Wilkins Ice Shelf reflects a shift to north(-easterly) winds (i.e., north-easterly winds that are inclined more towards northerly direction) preceding recent increased lake ponding (Figure 6.9a-b). Finally, correlations with snowmelt show a positive linear relationship over both Wilkins and Bach ice shelves (Figure 6.8a-b).

Table 6.2 presents the correlation results between monthly fractional lake extent and previous-year precipitation as well as annual SAM. For all three API ice shelves, correlations with previous-year precipitation and annual SAM returned a negative linear relationship even though correlations with annual SAM were more significant. Strongest correlation with annual SAM was found for George VI Ice Shelf (-0.82\*), closely followed by Bach (-0.78) and Wilkins (-0.74) ice shelves.





**Figure 6.8.** Results of the statistical correlation analysis for variables average air temperature (temp), maximum air temperature (temp max), solar radiation (solar rad), precipitation (precip), wind magnitude (wind) and direction (wind dir) as well as snowmelt (melt). Correlations are shown for spatial averages (a) and anomalies of spatial averages (b) of bi-weekly fractional lake extent and climate time series at lags 0-4. The correlation coefficient  $r$  is illustrated for significant correlations with  $p < 0.05$  only. Modified after Dirscherl et al. (2021b).



**Figure 6.9.** Spatially averaged fractional lake extents shown with lag 1 wind direction (a) and lag 1 solar radiation (c) as well as anomalies thereof (b,d) for melting seasons 2019-2020 and 2020-2021 over Wilkins Ice Shelf. Wind from north, east, south and west corresponds to  $0^\circ$ ,  $90^\circ$ ,  $180^\circ$  and  $270^\circ$  in degrees (deg). Modified after Dirscherl et al. (2021b).



### 6.4.1.3 Multi-Temporal Correlation Analysis at Pixel Level

Figure 6.10 shows selected results for pixel-based correlations between bi-weekly fractional lake extents and climate variables over George VI, Bach and Wilkins ice shelves. The selection of maps was made in agreement with Figure 6.8 and considering meaningful mapping results only. Similar as in Figure 6.8, only significant pixels with the highest correlations considering all performed cross-correlations as well as the corresponding lags are shown. Pixels below a significance level of  $p < 0.05$  are masked.

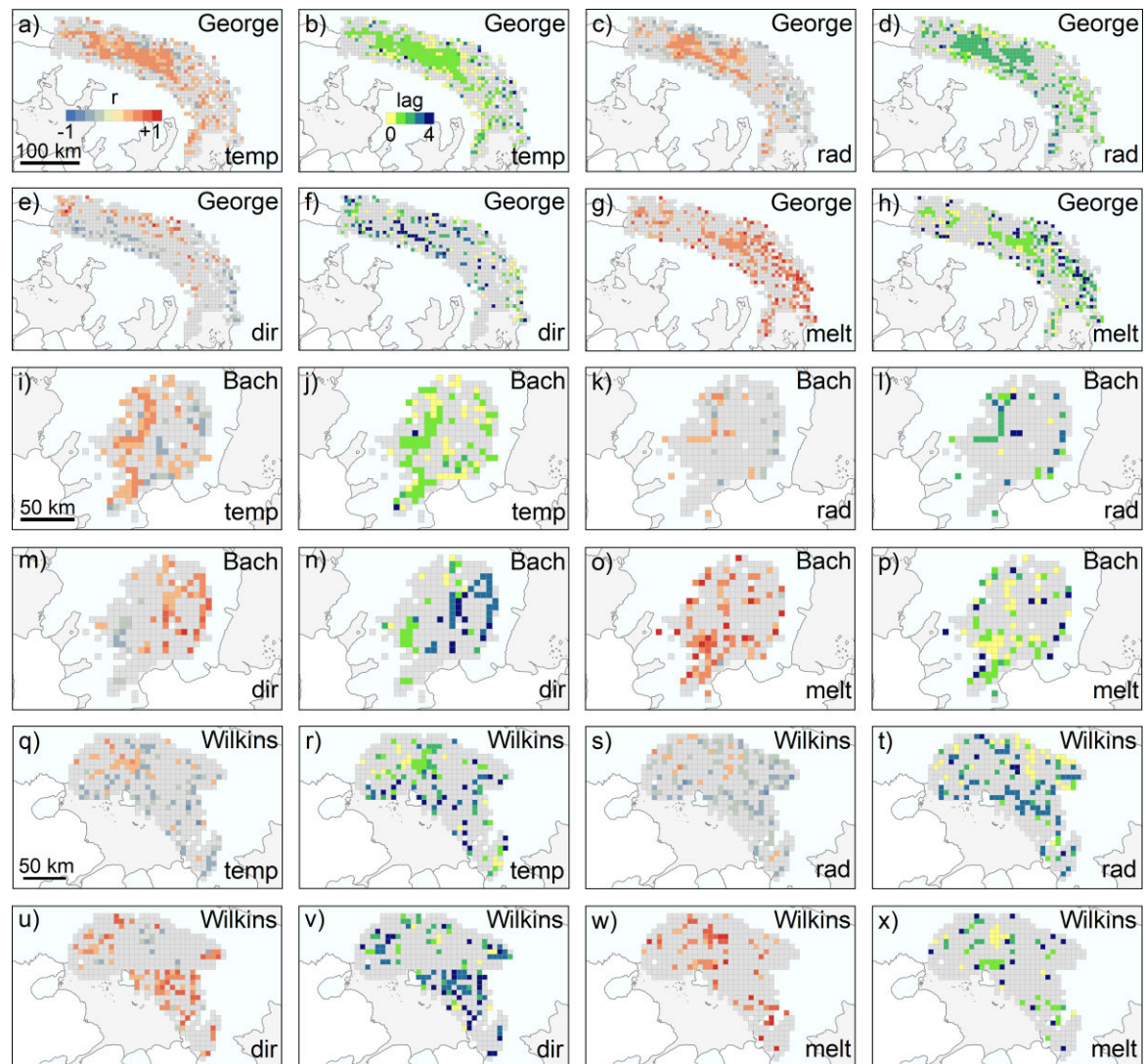


**Figure 6.10.** Pixel-based Pearson correlation (a,c,e,g,i,k,m,o,q,s,u,w) and corresponding temporal lags (b,d,f,h,j,l,n,p,r,t,v,x) between fractional lake extents and climate variables air temperature (temp), solar radiation (rad), wind direction (dir) and snowmelt (melt) over George VI (a-h), Bach (i-p), and Wilkins (q-x) ice shelves for pixels with  $p < 0.05$ . Modified after Dirscherl et al. (2021b). Data: (Mouginot et al., 2017b; Rignot et al., 2013).

Over George VI Ice Shelf, the pixel-based correlation analysis revealed a strong positive relationship between fractional lake extent and average air temperature as well as solar radiation. Both variables correlate at highest lags in the central ice shelf section

and at lower lags near the western and eastern grounding lines (Figure 6.10a-d). On the other hand, wind direction correlates positively in the east and negatively in the west and snowmelt correlates positively across large parts of the ice shelf (Figure 6.10e-h). Likewise, the statistical correlation analysis over Bach Ice Shelf (Figure 6.10i-p) revealed a strong positive linear relationship between fractional lake extent and air temperature, solar radiation and snowmelt, while wind direction revealed positive correlations in the east and negative correlations in the west. Even though the spatial correlation pattern over Wilkins Ice Shelf is rather heterogeneous (Figure 6.10q-x), regions of frequent lake recurrence (Figure 6.7) show positive correlations for climate variables air temperature and snowmelt and negative correlations for wind direction. At the same time, wind direction shows strong positive correlations in the surrounding area reflecting short-lived shifts to north-westerly winds preceding recent high lake coverage.

Finally, pixel-based correlation analysis between January fractional lake extents and previous-year precipitation revealed negative correlations to prevail in regions of frequent lake recurrence (Figure 6.7a-c) over all three API ice shelves (Figure 6.15a-c).

## **6.4.2 East Antarctic Ice Shelves**

### **6.4.2.1 Supraglacial Lake Extent Dynamics in 2016-2021**

Figure 6.5d-f and Figure 6.6d-f show temporal dynamics of supraglacial lake evolution over Riiser-Larsen, Nivlisen and Amery ice shelves. In contrast to API ice shelves, supraglacial lake extents were comparatively high during melting seasons 2016-2019 and at minimum during 2020-2021. Highest supraglacial lake coverage on Riiser-Larsen (~85 km<sup>2</sup>), Nivlisen (~107 km<sup>2</sup>) and Amery (~1,373 km<sup>2</sup>) ice shelves was detected during early January 2020, late January 2019 and early January 2019, respectively (Figure 6.5d-f). In general, the average onset of supraglacial meltwater ponding on the EAIS was during late December. At the same time, supraglacial lakes on the EAIS persisted considerably longer throughout the melting seasons than lakes on the API.

Likewise, the annual January recurrence time of lakes is higher on the EAIS than on the API (Figure 6.7). Over Riiser-Larsen, Nivlisen and Amery ice shelves, the January recurrence time of lakes reached up to 4-5 years over local surface depressions on grounded ice as well as in supraglacial meltwater channels on ice shelves (Figure 6.7d-f). In addition, Figure 6.7 reveals supraglacial lake clustering near a blue ice area (Figure 6.2) at the grounding line of Riiser-Larsen Ice Shelf, supraglacial lakes spreading across Nivlisen Ice Shelf with a progressive advance in north-easterly direction during January 2017-2020 (Figure 6.11) as well as supraglacial lake occurrence near the southern and eastern grounding zone of Amery Ice Shelf where rock outcrop and blue ice is widespread (Figure 6.1f). During years of high lake coverage, lakes expanded further onto the ice shelves than during years of low lake coverage where lakes accumulated

closer to the grounding line, rock outcrop or blue ice (Figure 6.7d-f, Figure 6.11). Over all three ice shelves, lakes are generally clustered at low elevations and low surface slopes.

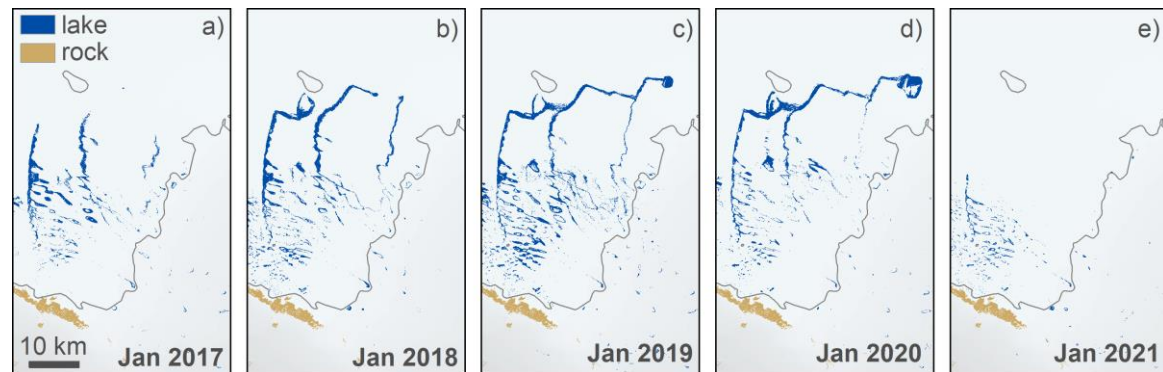


**Figure 6.11.** Supraglacial lake evolution during January 2017 (a), 2018 (b), 2019 (c), 2020 (d) and 2021 (e) over Nivlisen Ice Shelf. Modified after Dirscherl et al. (2021b). Data: (Dirscherl et al., 2020b; Mougnot et al., 2017b; Rignot et al., 2013).

#### 6.4.2.2 Multi-Temporal Correlation Analysis with Spatial Averages

The results of the statistical correlation analysis with time series of bi-weekly spatial averages and anomalies revealed EAIS supraglacial lake formation to be positively coupled to lag 0-3 average and maximum air temperature (Figure 6.8a-b). Similarly, correlations with surface net solar radiation revealed a positive linear relationship at varying time lags over all three ice shelves. Furthermore, statistical correlation analysis over Riiser-Larsen Ice Shelf revealed a negative linear relationship between fractional lake extent and lag 0 precipitation as well as lag 0 wind magnitude and a positive linear relationship between fractional lake extent and lag 0 wind direction. On the one hand, this indicates supraglacial lakes to be peaking during periods of low precipitation. On the other hand, this pattern reflects high lake coverage to be coincident with low speed winds from (south-)easterly direction following periods of anomalous high wind speeds from north-easterly direction (Figure 6.8a-b, Figure 6.12a-b, Figure 6.13a-b). Over Nivlisen Ice Shelf, lag 1 wind direction correlates negatively. Here, shifts in wind direction from south-easterly winds to (south-)easterly winds preceding high supraglacial lake coverage can be attributed to the observed correlations (Figure 6.12c-d). At the same time, lake formation followed minor peaks in wind magnitude (Figure 6.13c-d). Even though Figure 6.8 reveals no significant link between wind direction and fractional lake extent for Amery Ice Shelf, Figure 6.12e-f and Figure 6.13e-f highlight supraglacial lake coverage to be peaking following shifts from comparatively high-speed south-westerly winds to southerly winds at low and high wind speeds. Finally, lag 1 snowmelt correlates positively with fractional lake extent over Riiser-Larsen and Amery ice shelves (Figure 6.8a,b).

As can be seen in Table 6.2, the multi-temporal linear correlation analysis between January fractional lake extents and previous-year precipitation revealed a weak negative correlation over Riiser-Larsen Ice Shelf, a strong negative correlation over Amery Ice Shelf and a weak positive correlation over Nivlisen Ice Shelf. On the other hand, correlations between January fractional lake extents and annual SAM returned a negative linear relationship over Riiser-Larsen Ice Shelf and a weak positive linear relationship over Nivlisen and Amery ice shelves.

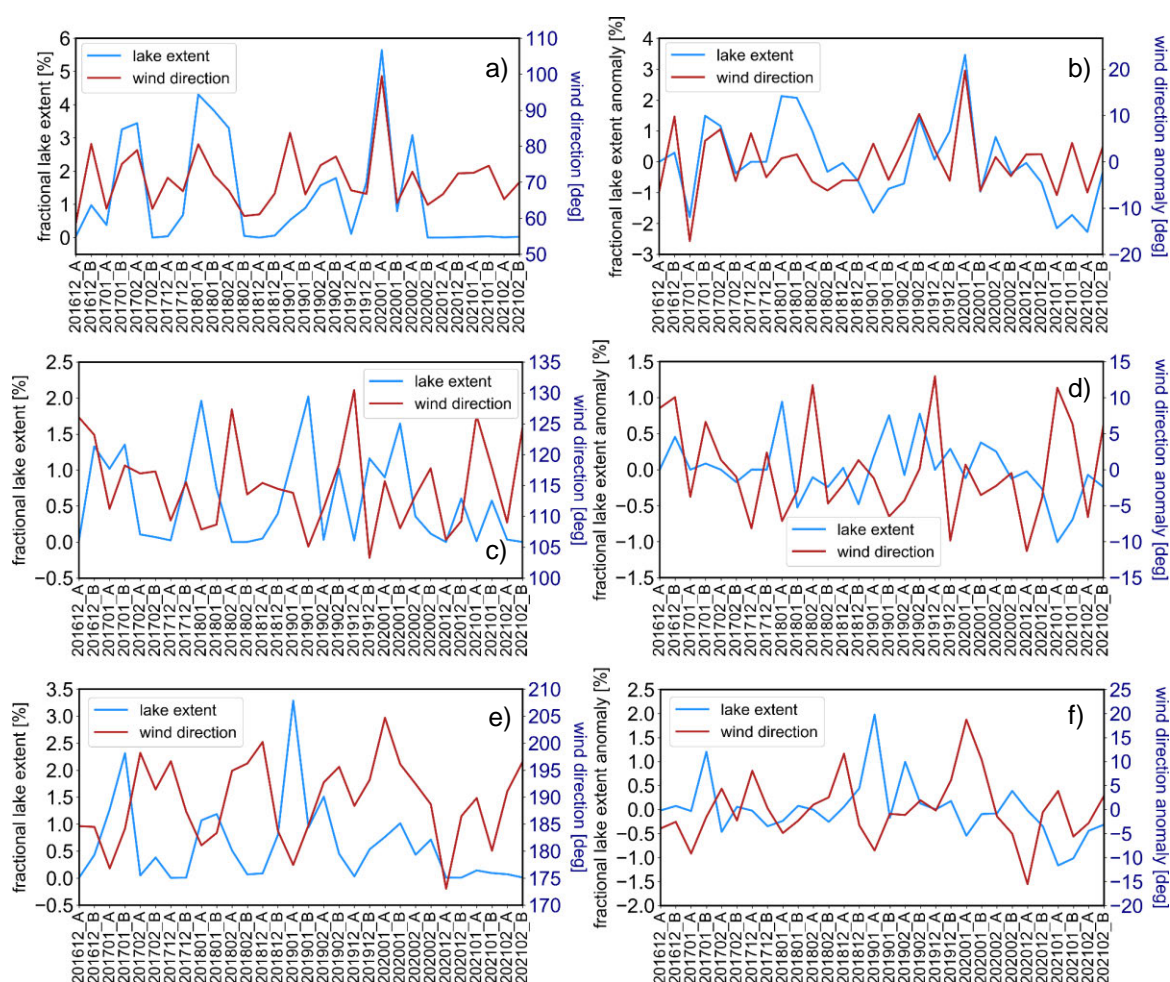


**Figure 6.12.** Spatially averaged fractional lake extents shown with wind direction (a,c,e) and anomalies (b,d,f) during 2016-2021 at lag 0 over Riiser Larsen Ice Shelf (a,b) at lag 1 over Nivlisen Ice Shelf (c,d) and at lag 1 over Amery Ice Shelf (e-f). Wind from north, east, south and west corresponds to 0°, 90°, 180° and 270° in degrees (deg). Modified after Dirscherl et al. (2021b).

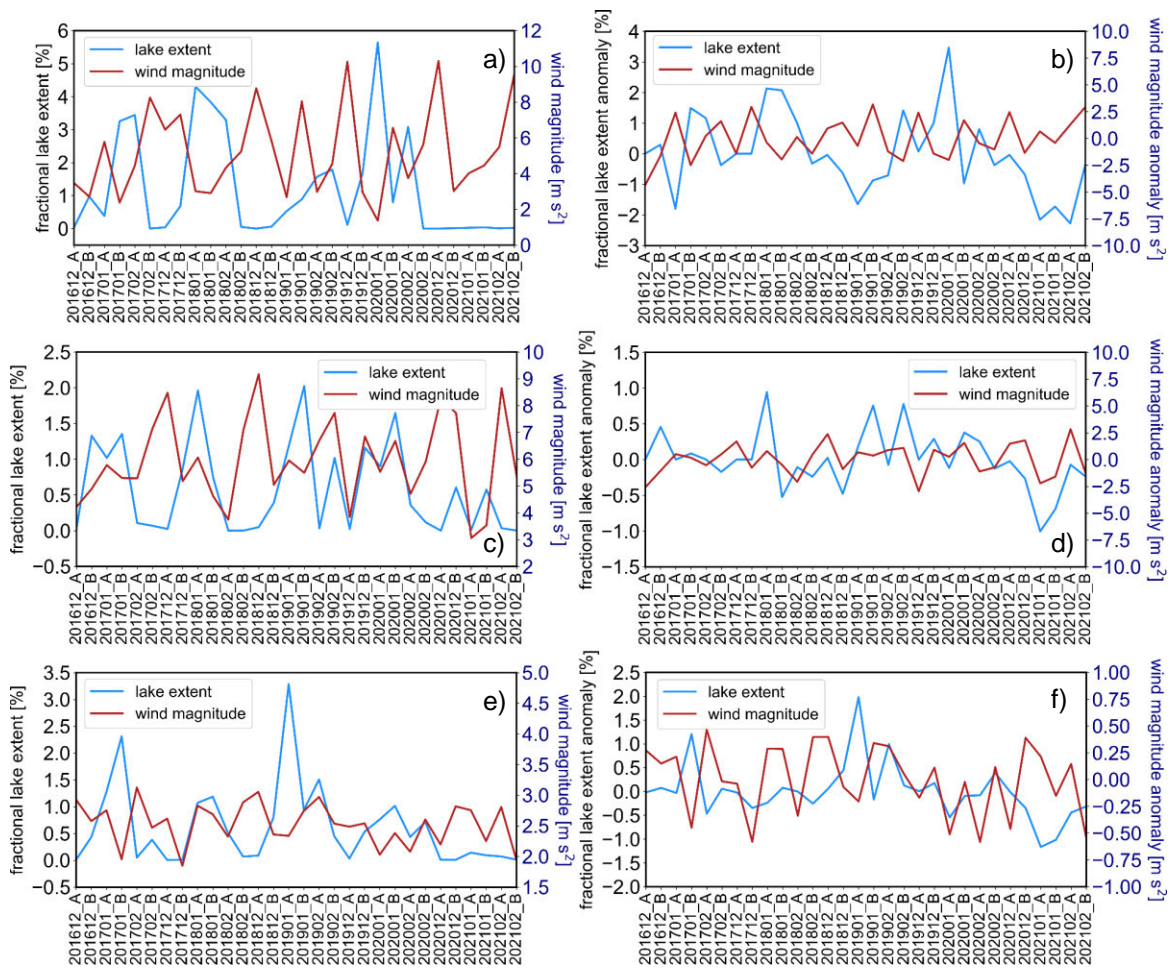
#### 6.4.2.3 Multi-Temporal Correlation Analysis at Pixel Level

Figure 6.14 shows the results of the pixel-based correlation analysis over Riiser-Larsen, Nivlisen and Amery ice shelves. Over all three ice shelves, pixel-based correlations revealed a strong positive link between bi-weekly fractional lake extent and average air temperature as well as solar radiation. For both climate variables, lags were



highest downstream of the grounding lines and lowest near and upstream of the grounding zones (Figure 6.14b,d,n,p,r,t). Over Riiser-Larsen Ice Shelf, lag 0 wind magnitude and precipitation correlate negatively (Figure 6.14e,f,i,j) and lag 0 wind direction correlates positively over the entire ice shelf (Figure 6.14g,h). Moreover, the pixel-based correlation analysis over Amery Ice Shelf revealed a negative link with wind magnitude over the south-eastern ice shelf and a positive link along the eastern grounding zone (Figure 6.14u,v). At the same time, wind direction showed mostly negative correlations over both regions (Figure 6.14w,x). Along the north-east grounding line, this correlation pattern reflects that supraglacial lakes peak shortly after occurrence of high-speed (south-)easterly winds. In the south of Amery Ice Shelf, the correlations reveal supraglacial lakes to peak during low-speed winds from south(-east) or south(-west) following high-speed southerly winds.

Furthermore, Figure 6.15d-f reveals a strong negative linear relationship between January fractional lake extents and previous-year precipitation over Riiser-Larsen and Amery ice shelves and mostly positive correlations over Nivlisen Ice Shelf.



**Figure 6.13.** Spatially averaged fractional lake extents shown with wind magnitude (a,c,e) and anomalies (b,d,f) during 2016-2021 at lag 0 over Riiser Larsen Ice Shelf (a,b) at lag 1 over Nivlisen Ice Shelf (c,d) and at lag 1 over Amery Ice Shelf (e-f).

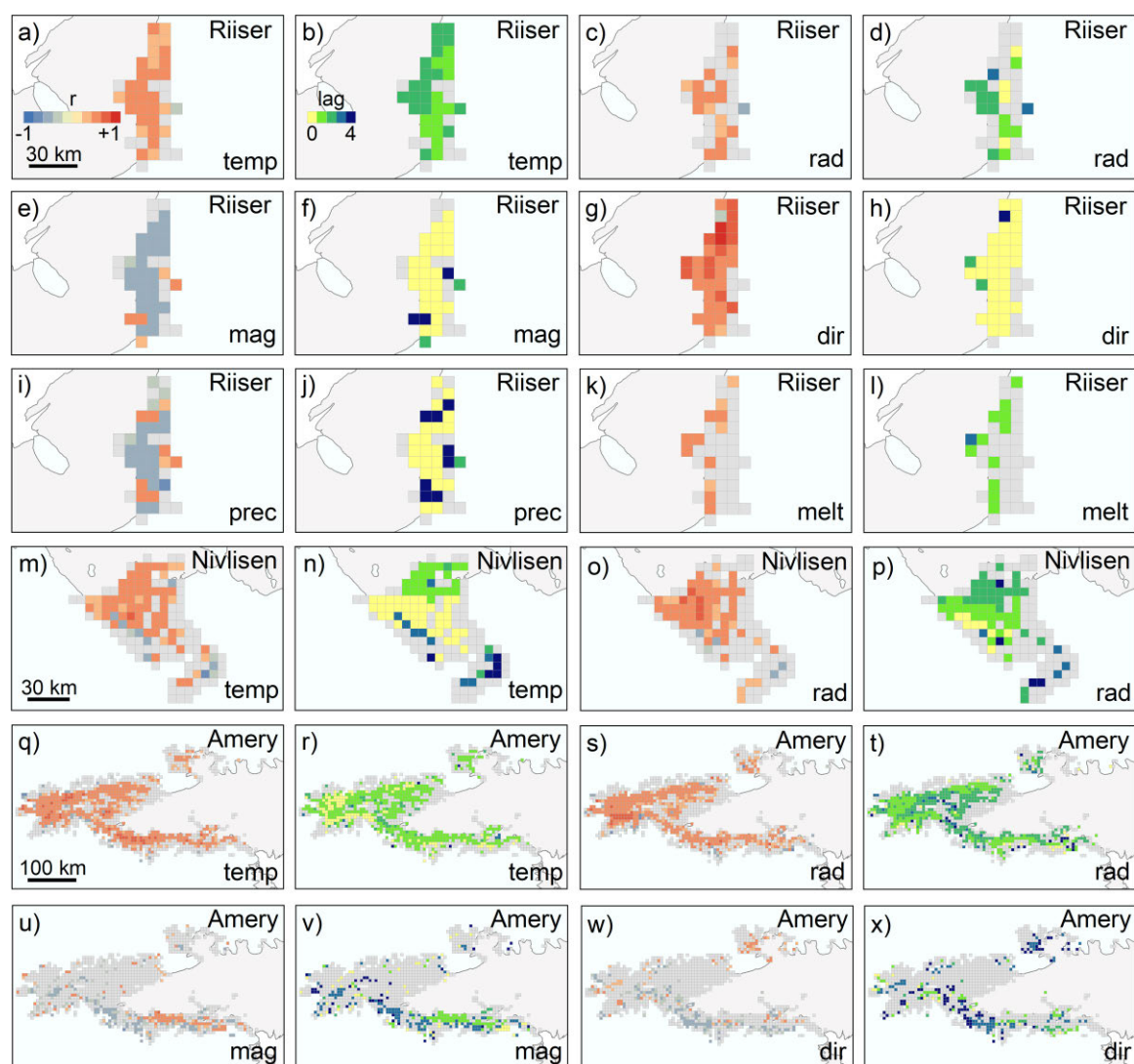


**Figure 6.14.** Pixel-based Pearson correlation (a,c,e,g,i,k,m,o,q,s,u,w) and corresponding temporal lags (b,d,f,h,j,l,n,p,r,t,v,x) between fractional lake extents and climate variables air temperature (temp), solar radiation (rad), wind magnitude (mag), wind direction (dir), precipitation (prec) and snowmelt (melt) over Riiser-Larsen (a-l), Nivlisen (m-p), and Amery (q-x) ice shelves for pixels with  $p < 0.05$ . Modified after Dirscherl et al. (2021b). Data: (Mouginot et al., 2017b; Rignot et al., 2013).

**Table 6.2.** Results of the statistical correlation analysis between January fractional lake extent and annual SAM as well as previous-year precipitation. Due to the low number of observations used for correlation, the p-value might not be representative and rather the Pearson correlation coefficient ( $r$ ) should be considered for interpretation. Modified after Dirscherl et al. (2021b).

Variable	Precipitation		SAM	
	r	p	r	p
George VI Ice Shelf	-0.35	0.50	<b>-0.82*</b>	0.04
Bach Ice Shelf	-0.22	0.68	-0.78	0.07
Wilkins Ice Shelf	-0.36	0.48	-0.74	0.09
Riiser-Larsen Ice Shelf	-0.40	0.51	-0.48	0.42
Nivlisen Ice Shelf	0.17	0.79	0.10	0.87
Amery Ice Shelf	<b>-0.87*</b>	0.05	0.44	0.46

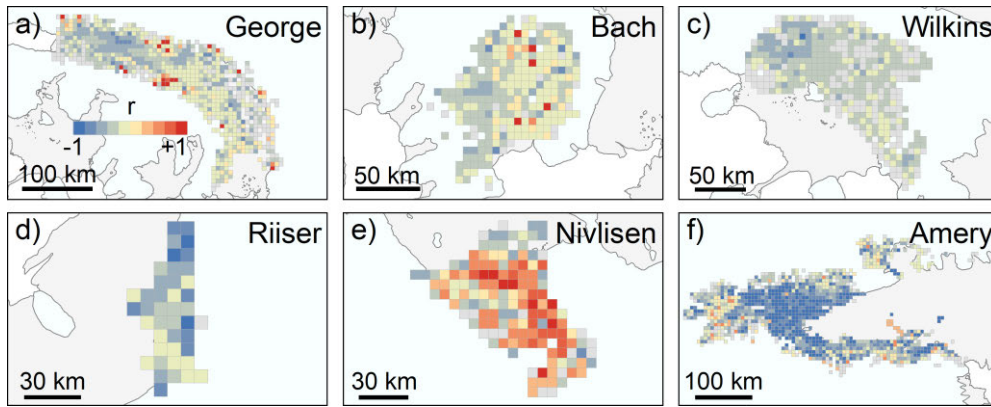


**Figure 6.15.** Pixel-based correlation between January fractional lake extents and previous-year precipitation over George VI (a), Bach (b), Wilkins (c), Riiser-Larsen (d), Nivlisen (e) and Amery (f) ice shelves. Due to the low number of observations, also correlations with  $p > 0.05$  are shown. Modified after Dirscherl et al. (2021b). Data: (Mouginot et al., 2017b; Rignot et al., 2013).

## 6.5 Discussion

### 6.5.1 Antarctic Peninsula Ice Shelves

#### 6.5.1.1 Local Controls

The investigation of local control factors revealed API supraglacial lake formation to be coupled to the distribution of low-albedo surface features, the local ice surface topography as well as the firn air content. To start with, supraglacial lake formation on George VI and Wilkins ice shelves was found to be enhanced near low-albedo rock. Over George VI Ice Shelf, low-melt years were characterized by lakes forming closer to the grounding line where rock outcrop is present (Figure 6.7a). Similarly, lakes on Wilkins Ice Shelf expanded upstream of the grounding line in regions where exposed rock is widespread (Figure 6.7c). The dependence on low-albedo surface features is also reflected in pixel-based correlations showing lower temporal lags near the grounding zone of George VI Ice Shelf (Figure 6.10b,d) and thus a faster response time to climate drivers where low-albedo surface features promote supraglacial melting and ponding. Next, supraglacial lakes were found to be clustered at low elevations and low surface slopes (Figure 6.7a-c) being favorable to surface ponding (Arthur et al., 2020a; Stokes et al., 2019). Over George VI Ice Shelf, meltwater accumulated in flow stripes forming as part of the prevailing compressive flow regime (Hambrey et al., 2015; LaBarbera and MacAyeal, 2011) which again highlights the influence of the local ice surface topography. In addition, also the refreezing of meltwater in firn pore space and channelized basal melting could have influenced meltwater ponding through a modified ice surface topography (Dow et al., 2018; McGrath et al., 2012; Spergel et al., 2021). Furthermore, supraglacial lake formation was dictated by the ice shelf geometry and grounding line location where lakes primarily clustered (Figure 6.7a-c). Another important control on



supraglacial lake formation is the FAC of snow, shown to influence lake formation over all three API ice shelves. In fact, correlation analysis with previous-year precipitation revealed supraglacial lake coverage to be peaking in regions that received comparatively low precipitation during the previous year (Table 6.2, Figure 6.15a-c). This highlights supraglacial lake formation to be facilitated over more compact, air-depleted firn (Arthur et al., 2020a; Leeson et al., 2020), while fresh snow dampens lake evolution allowing the percolation of meltwater into the low-density firn layer (Kuipers Munneke et al., 2014; Lenaerts et al., 2017; Stokes et al., 2019). Consequently, low precipitation in 2017, 2019 and 2020 likely contributed to increased firn air depletion and enhanced meltwater ponding during melting seasons 2017-2018, 2019-2020 and 2020-2021.

### 6.5.1.2 Regional Controls

Regional control factors include the near-surface climate with variables air temperature, solar radiation, wind and snowmelt. To start with, cross-correlation with average and maximum air temperature revealed a positive relationship over all three API ice shelves with lag 1 dominating on the central ice shelves where lakes form during high-melt years and lag 0 close to and upstream of the grounding zones where lakes form during low-melt years (Figure 6.8, Figure 6.10b,j,r). In agreement with Chapter 6.5.1.1, these findings point towards supraglacial formation to be initiated directly after temperature rises particularly in regions where melt-albedo feedbacks promote lake formation. Additionally, meltwater transport across the ice shelves later in the melting season (Figure 6.2) (Kingslake et al., 2017) likely contributed to the observed higher lags on the central ice shelves. In agreement with the observed positive correlations for air temperature, Banwell et al (2021) suggest that 2019-2020 meltwater ponding on George VI Ice Shelf was driven by sustained air temperatures  $\geq 0^{\circ}\text{C}$ . Likewise, the influence of air temperature was found to be coupled to lake formation over other Antarctic ice shelves (Dell et al., 2020; Kingslake et al., 2015; Langley et al., 2016).

Moreover, solar radiation was found to be positively coupled to supraglacial lake formation over George VI and Bach ice shelves (Figure 6.8a-b, Figure 6.10c,d,k,l). This particularly applies to regions where supraglacial lakes form during high-melt years. With Laffin et al. (2021) suggesting that solar radiation is a primary driver for foehn-induced melt on Bach and George VI ice shelves, foehn wind conditions likely contributed to the observed peaks in meltwater ponding during 2019-2020 and 2020-2021. Over Wilkins Ice Shelf, the correlation of anomalies of fractional lake extent and solar radiation revealed a negative relationship pointing towards the higher influence of effects such as sensible heat transport caused by cloud cover and enhanced longwave radiation (Banwell et al., 2021; Laffin et al., 2021). Even though the overall heterogeneous correlation pattern over Wilkins Ice Shelf could reflect spurious correlation, weak negative lag 0-1 correlation was also found for George VI and Bach ice shelves reflecting

an anomalous low availability of incoming shortwave radiation during melting seasons 2019-2020 and 2020-2021 (Figure 6.9c-d), thus supporting the assumption of sensible heat transfer to contribute to increased API meltwater ponding.

In agreement with these findings, an equally important driver for supraglacial melting and ponding are regional wind conditions. The detected negative link with anomalies of wind direction over regions of frequent lake recurrence on Wilkins Ice Shelf as well as positive correlations in the surrounding area (Figure 6.8, Figure 6.9a-b, Figure 6.10u) were revealed to be linked to shifts in wind direction towards north(-easterly) and north-westerly winds, respectively. Similar trends have been observed along the western and eastern grounding lines of George VI and Bach ice shelves (Figure 6.10e,m). This pattern is in good agreement with previous studies reporting of north-westerly and north-easterly winds to promote warm air temperatures over George VI Ice Shelf through sensible heat transport as well as a shift towards more frequent north-easterlies (Banwell et al., 2021). Similar to westerly foehn wind occurrence on the north-eastern API (Cape et al., 2015; Datta et al., 2019; Luckman et al., 2014; Turton et al., 2020), (north)-easterly foehn winds are known to influence surface melting on the western API (Laffin et al., 2021) and likely explain lake clustering near the grounding lines of the ice shelves where the influence of foehn wind is highest (Lenaerts et al., 2017). In addition, the detected positive link with lag 0-1 snowmelt (Figure 6.8, Figure 6.10) potentially reflects short-lived foehn-induced melt events (Cape et al., 2015; Turton et al., 2020). Overall, this suggests the occurrence of both foehn winds and sensible heat transport over the API.

### **6.5.1.3 Large-Scale Controls**

The investigation of large-scale atmospheric modes was performed on the basis of correlations between January fractional lake extents and annual SAM. Over API ice shelves, the correlation results in Table 6.2 revealed a strong negative relationship with annual SAM mostly due to a negative SAM year in 2019 (Figure 6.16) coincident with high lake coverage during 2019-2020 (Figure 6.6a-c). Even though negative SAM years usually lead to cold conditions and low melt on the API, the influence of teleconnections between the tropics and high latitudes in 2019 (Bevan et al., 2020) is suggested to have caused increased API melting during 2019-2020. In detail, teleconnections between the tropics and high latitudes caused unusual perturbations of Southern Hemisphere atmospheric flow, including sudden stratospheric warming (SSW) and a positive Indian Ocean Dipole (IOD) (BOM, 2021), to result in SAM to be negative and warm air to penetrate the API via northerly winds. The IOD can be represented via the Dipole Mode Index (DMI) (Figure 6.16), a measure of the east to west SST gradient across the tropical Indian Ocean. This large-scale atmospheric driver is well in line with the obtained correlations for air temperature and wind and could potentially explain high meltwater ponding in 2019-2020. With DMI being neutral in 2020, other overarching drivers,

including SAM returning to positive values (Figure 6.16) as well as modified pressure conditions in the Amundsen Sea Low (ASL) (NSIDC, 2021), likely contributed to high and low lake extents during the early and late 2020-2021 melting season, respectively.

To summarize the results for the API, the complex interplay between local, regional and large-scale environmental factors is suggested to influence supraglacial lake formation. In this context, the local glaciological and geomorphological setting, including the FAC, the ice surface topography, the ice shelf geometry and the surface albedo, were found to influence supraglacial lake distribution and evolution. Moreover, the regional near-surface climate, including air temperature, solar radiation, (foehn) wind conditions and sensible heat transport, is a primary driver for meltwater ponding in 2015-2021. Regional climatic conditions are mainly driven by large-scale atmospheric modes including SAM, IOD and ASL. Considering the good agreement between lake evolution and detected driving factors over all three API ice shelves (Table 6.3), a similar evolution of lakes over other API ice shelves, e.g. during 2019-2020 and 2020-2021, is suggested.

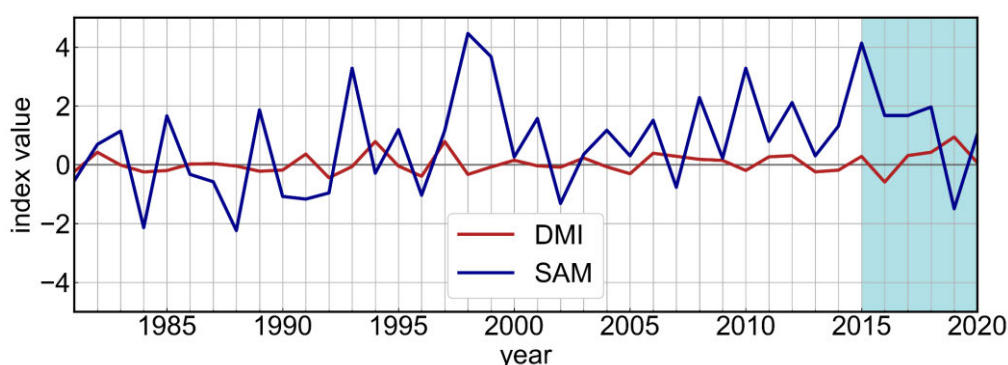


**Figure 6.16.** Annual observations of Southern Annular Mode (SAM) and Dipole Mode Index (DMI) between 1981 and 2020. The study period is highlighted in blue. Modified after Dirscherl et al. (2021b). Data: (Marshall (2018), <https://stateoftheocean.osmc.noaa.gov/sur/ind/dmi.php> (last accessed 28 October 2021)).

## 6.5.2 East Antarctic Ice Shelves

### 6.5.2.1 Local Controls

EAIS supraglacial lake formation is controlled by local factors including melt-albedo feedbacks, the ice surface topography and the FAC. To start with, the influence of a reduced FAC is reflected in the negative correlation between fractional lake extent and short-term precipitation over Riiser-Larsen Ice Shelf (Figure 6.8, Figure 6.14i). At the same time, correlation with previous-year precipitation raised a strong negative relationship over Riiser-Larsen and particularly Amery Ice Shelf (Table 6.2, Figure 6.15d,f). Over the latter, a strong link between 2016-2017 and 2018-2019 increased meltwater ponding and low precipitation during 2016 and 2018 was found. Over Nivlisen Ice Shelf, correlations with previous-year precipitation were mostly positive (Table 6.2,

Figure 6.15e) pointing towards the higher influence of other drivers. For example, the high recurrence time of lakes on the EAIS (Figure 6.7d-f) highlights that supraglacial lake formation is controlled by the ice surface topography (Arthur et al., 2020a; Echelmeyer et al., 1991; Langley et al., 2016) with lakes recurring in the same ice surface depressions each year. This particularly applies to meltwater ponding in elongated ice surface depressions on Nivlisen and Riiser-Larsen ice shelves but also to Amery Ice Shelf, where meltwater recurs in ice surface depressions on grounded ice and in longitudinal flow stripes migrating with ice flow (Figure 6.7d-f) (Glasser and Gudmundsson, 2012; Spergel et al., 2021). At the same time, lakes tend to cluster at low elevations and low surface slopes (Figure 6.7d-f) as well as near rock outcrop and blue ice (Figure 6.1d-f, Figure 6.2d, Figure 6.7e-f) reflecting a link to melt-albedo feedbacks. Other local control factors that could have contributed to facilitated meltwater ponding include the refreezing of meltwater in firn pore space potentially leading to a modification of the ice surface topography or firn air depletion (Kuipers Munneke et al., 2014; Spergel et al., 2021).

### 6.5.2.2 Regional Controls

Similarly, regional control factors, including air temperature, solar radiation and wind, were found to influence lake ponding on the investigated EAIS ice shelves. First, cross-correlation with air temperature revealed EAIS supraglacial lake formation to be controlled by lag 0-2 average and maximum air temperature (Figure 6.8, Figure 6.14a,b,m,n,q,r). As lags were higher on the floating ice shelves where lakes accumulate during high-melt years (Figure 6.14b,n,r), the temporal evolution of drainage systems later in the melting season is suggested to be responsible for the observed pattern (Figure 6.2d-f, Figure 6.7d-f, Figure 6.11) (Dell et al., 2020; Kingslake et al., 2017; Spergel et al., 2021). At the same time, a longer response time of lake evolution to increased air temperatures in regions where no albedo feedbacks promote supraglacial lake formation could potentially explain the higher temporal lags on the central ice shelves (Figure 6.14b,n,r).

Further, cross-correlation with solar radiation revealed EAIS supraglacial lake formation to be coupled to the amount of incoming shortwave radiation (Figure 6.8, Figure 6.14c,o,s). In detail, solar radiation correlated at lags 0-2 whereat highest lags were observed on the central ice shelf sections and lowest lags near and upstream of the grounding lines (Figure 6.14d,p,t). This likely reflects similar effects as found for air temperature, also considering the presence of rock outcrop and blue ice near all three ice shelves (Figure 6.1e-f, Figure 6.2d, Figure 6.7e-f). Similar links between supraglacial lake formation and solar radiation were observed over Roi Baudouin Ice Shelf, where katabatic-wind-driven blue ice exposure triggered enhanced surface melting through an increased absorption of solar radiation (Lenaerts et al., 2017).

Another important control factor on EAIS supraglacial lake formation in 2016-2021 was found to be the regional wind regime. Over Riiser-Larsen Ice Shelf, the observed correlation pattern revealed supraglacial lake formation to be coincident with low-speed (south-)easterly winds following periods of high-speed north-easterly winds (Chapter 6.4.2.2). This indicates supraglacial lake formation on Riiser-Larsen Ice Shelf to be linked to katabatic wind forcing. Similar results were found for Nivlisen Ice Shelf, where strong (south-)easterly winds preceding increased lake ponding likely reflect katabatic winds (see Chapter 6.4.2.2) that also influence supraglacial lake formation through wind-induced blue ice exposure near the Wohlthat Mountains (Figure 6.1e) (Horwath et al., 2006). Over Amery Ice Shelf, the detected correlation pattern was twofold revealing supraglacial lakes to be peaking after occurrence of high-speed (south-)easterly winds along the north-eastern grounding line and after high-speed southerly winds along the south-eastern grounding zone (see Chapter 6.4.2.3). The observed pattern along the north-east grounding line likely reflects katabatic winds flowing onto the ice shelf via the adjacent eastern ice plateau (Stokes et al., 2019). Along the south-east grounding line, katabatic wind inflow originates in the south highlighting that katabatic winds drive melting in agreement with the local topography determining the direction of wind inflow. In agreement with these results, lag 1 correlation with modelled snowmelt events over Riiser-Larsen and Amery ice shelves (Figure 6.8, Figure 6.14k-l) likely reflects localized katabatic wind-induced peaks in melting. In general, (easterly) katabatic winds warm adiabatically through vertical mixing (Arthur et al., 2020a) and often trigger melt-albedo feedbacks through wind-induced blue ice and firn exposure (Lenaerts et al., 2017).

### 6.5.2.3 Large-Scale Controls

Large-scale atmospheric modes including SAM revealed a varying correlation pattern over the three investigated ice shelves. For Riiser-Larsen Ice Shelf, a weak negative linear relationship was detected likely pointing towards SH atmospheric modes affecting western East Antarctica in a similar manner as revealed for the API. This likely results from the spatial proximity of both regions to the Weddell Sea. In particular, supraglacial lake extents on Riiser-Larsen Ice Shelf were above average during January 2020 considering years 2016-2021 as reference period. This is in line with observations on the API (Chapter 6.5.1.3) as well as a positive IOD/DMI and a negative SAM in 2019 (Figure 6.16). On the other hand, correlations with SAM over Nivlisen and Amery ice shelves were weak positive likely reflecting the opposite climate effects SAM can have on the API and EAIS (Kwok and Comiso, 2002). Likewise, also the influence of an atypical ASL driving below-average air temperature in 2020-2021 (NSIDC, 2021) has to be considered and can likely be attributed to the observed low lake extents over EAIS ice shelves during melting season 2020-2021.

In summary, controls on East Antarctic meltwater ponding in 2016-2021 result from the complex interplay of local, regional and large-scale environmental drivers. While local controls, including the FAC, the ice surface topography and melt-albedo feedbacks, primarily influence supraglacial lake distribution, regional climate variables are found to control above or below normal meltwater ponding. In this context, air temperature, solar radiation and (katabatic) wind forcing are first-order controls on supraglacial lake formation. Similar as found for the API, regional climate variability was found to be driven by large-scale atmospheric modes including SAM, IOD and ASL.

At this point it has to be noted, that the complex interplay of climate variables might have led to non-linear interactions that are not captured using the Pearson correlation. At the same time, the comparatively low number of observations might have led to statistically insignificant correlations despite the existence of causal links. Further, also the coarse resolution of climate reanalysis data might have affected correlation values particularly at small-scale. However, since ERA5-Land data are the only public reanalysis dataset at global coverage, they are of great value for scientific analyses on climate drivers.

### **6.5.3 Implications for the Antarctic Continent**

Table 6.3 summarizes environmental controls on 2015-2021 supraglacial meltwater ponding for the API and EAIS. Despite the existence of slightly different drivers for each ice shelf, local control factors, including melt-albedo feedbacks, the ice surface topography and the FAC, show an overall good agreement over all ice shelves. Likewise, regional climatic conditions, including air temperature and solar radiation, were found to influence all six ice shelves in a similar manner. The same applies to wind conditions, with foehn winds promoting supraglacial lake formation on the API and katabatic winds influencing supraglacial lake ponding on the EAIS. Furthermore, large-scale atmospheric modes were revealed to influence entire ice sheet sections. For example, the intense ASL in 2020-2021 was shown to influence all six ice shelves in a similar manner highlighting the potential influence of atmospheric modes at continent-wide scale (Table 6.3). Likewise, SAM and IOD showed similar effects on neighboring ice sheet regions of the API and EAIS (Table 6.3).

Overall, these findings point towards the transferability of detected drivers to other Antarctic regions as well as their role as first-order controls on lake formation. For instance, similar trends in lake evolution can be expected in terms of the intense ASL driving low lake coverage over other Antarctic regions during the 2020-2021 melting season. In addition, the observed relationship with SAM and IOD suggests high lake extents to prevail during the 2019-2020 melting season over other API regions and



adjacent ice sheet sections on the EAIS and WAIS. Further, high lake extents likely prevailed over other API regions during the peak of the 2020-2021 melting season.

**Table 6.3.** Summary of environmental controls on 2015-2021 meltwater ponding on six investigated Antarctic ice shelves. The table summarizes pixel-based and spatially averaged correlations, also considering weak correlations and neglecting spurious results. Positive and negative signs indicate positive and negative relationships, respectively. The signs '+/-' and '/' denote the coexistence of positive and negative links as well as no observed links, respectively. The strength or lag of correlations is not shown. Modified after Dirscherl et al. (2021b).

Scale	Driving variable	Antarctic Peninsula			East Antarctica		
		George	Bach	Wilkins	Riiser-Larsen	Nivlisen	Amery
Local	Melt-albedo feedbacks	+	/	+	+	+	+
	Elevation and slope	-	-	-	-	-	-
	Ice surface morphology*	+	+	+	+	+	+
	Firn air content	-	-	-	-	/	-
Regional	Air temperature	+	+	+	+	+	+
	Max. air temperature	+	+	+	/	+	+
	Solar radiation	+/-	+/-	-	+	+	+
	Short-term precipitation	/	/	/	-	-	-
	Wind speed	/	/	/	-	+	+/-
	Wind direction	+/-	+/-	+/-	+	-	-
	Snowmelt	+	+	+	+	+	+
Large-scale	SAM	-	-	-	-	+	+
	DMI and SSW	+	+	+	+	**	**
	Intense ASL	-	-	-	-	-	-

\*the positive sign refers to the existence of a link without directional component \*\*not investigated but likely weak negative

#### 6.5.4 Potential Implications for Future Ice Shelf Stability

With accelerating global climate change, Antarctic surface melting and ponding will intensify (Bell et al., 2018; Gilbert and Kittel, 2021; Kingslake et al., 2017; Trusel et al., 2015). This is also reflected in the correlation results with climate variables highlighting the high sensitivity of surface melting and lake ponding to climate variability and average and maximum air temperature in particular. In this context, ice shelves on the API as well as surrounding islands will be particularly susceptible to increasing air temperatures due to their maritime climate and the location in comparatively low latitudes (Hock et al., 2009). At the same time, atmospheric warming will also lead to enhanced surface melting over other Antarctic ice shelves, e.g. on the WAIS (Bromwich et al., 2013), where surface ponding is so far limited. With an increasing abundance of supraglacial lakes on Antarctic ice shelves, their stability is at risk. As previously mentioned, supraglacial lakes threaten ice shelf stability through stress causing flexure and ultimately hydrofracturing and ice shelf collapse (Banwell et al., 2019; Banwell and Macayeal, 2015; Fürst et al., 2016; Leeson et al., 2020; Rott et al., 2018; Scambos et al., 2004). Ice shelf regions that

are vulnerable to hydrofracture are widespread around Antarctica (Alley et al., 2018; Lai et al., 2020) particularly when they are pre-weakened by firn air depletion (Kuipers Munneke et al., 2014; Lenaerts et al., 2017; Spergel et al., 2021) or fractures and crevasses (Lhermitte et al., 2020). In addition, lateral meltwater transport across ice shelves delivers meltwater to regions that receive only little or no surface melt making them more susceptible to hydrofracture through a reduced FAC (Dell et al., 2020). This particularly applies to ice shelves with isolated drainage systems that do not deliver meltwater to the ocean (Bell et al., 2017).

Since lateral meltwater transport was observed across all six EAIS and API ice shelves (Figure 6.7), that are classified as potentially vulnerable to hydrofracture (Lai et al., 2020), ice shelf destabilization could be inevitable. Furthermore, recent increased meltwater ponding during 2019-2020 and 2020-2021 on the API likely contributed to a further reduction in the FAC making the ice shelves more susceptible to future meltwater ponding. Even though the enhanced moisture holding capacity of warmer air may partly compensate this through an increase in future precipitation (Bell et al., 2018; Bengtsson et al., 2011; Krinner et al., 2007; Lenaerts et al., 2016), additional research is required for an improved assessment of all contribution factors. For example, these include an increased risk for hydrofracture due to the development of firn aquifers under high-precipitation scenarios (Bell et al., 2018; van Wessem et al., 2021) as well as a faster response time of surface melt to increased air temperatures than atmospheric-driven gain through precipitation (Holland et al., 2020). On the other hand, a more frequent occurrence of positive IODs under high-emission scenarios may counteract API warming in the absence of SH atmospheric perturbations such as SSW (Bevan et al., 2020). At the same time, teleconnections with the tropics and increasingly positive SAM years in the future might cause additional atmospheric warming and AIS meltwater ponding.

## 6.6 Summary

This chapter provided new insight into the intra-annual and inter-annual evolution of present-day Antarctic surface hydrology applying the novel processor for automated supraglacial lake extent mapping (Chapter 5.6) on spaceborne observations from Sentinel-1 SAR and optical Sentinel-2. Through exploitation of the full data archives of both satellite sensors, fused supraglacial lake extent mapping products were derived at bi-weekly temporal scale and unprecedented 10 m spatial resolution covering six major API and EAIS ice shelves during November to March in 2015-2021. The supraglacial lake extent mapping results for API ice shelves revealed comparatively low lake coverage during 2015-2018 and high lake coverage during melting seasons 2019-2020 and 2020-2021. EAIS ice shelves were characterized by above-average lake coverage during most of the melting seasons 2016-2019 and below-average lake coverage during

2020-2021 with respect to the observational period 2016-2021. Over all six investigated ice shelves, the development of drainage systems was revealed highlighting an increased risk for ice shelf instability due to meltwater delivery to regions with only little or no surface melt. This particularly applies to API ice shelves, where recent increased meltwater ponding likely contributed to further firn air depletion.

Moreover, intra-annual supraglacial lake extent evolution in 2015-2021 was linked to climate drivers from ERA5-Land reanalysis data through application of multi-temporal linear correlation analysis at varying time lags using spatially averaged as well as pixel-based observations. In addition, inter-annual observations of January supraglacial lake extents were linked to large-scale atmospheric modes and previous-year precipitation, used as an indirect indicator of the FAC. The results of the analysis reveal API supraglacial lake distribution to be linked to the local glaciological setting including the ice surface topography, the ice shelf geometry, the presence of low-albedo features as well as a reduced firn air content. Furthermore, API lake coverage was shown to be coupled to the regional near-surface climate with variables air temperature, solar radiation and (foehn) wind showing highest correlations. In addition, sensible heat transport was found to be an important regional control on supraglacial lake formation on the API as well. In this context, large-scale atmospheric modes were found to exert strong control on the regional climate with SAM, IOD and SSW influencing recent increased API meltwater ponding during 2019-2020 and 2020-2021 and ASL causing low meltwater ponding during the late 2020-2021 melting season. For EAIS ice shelves, similar driving factors were found to influence lake ponding. To start with, the local geomorphological setting as well as melt-albedo feedbacks were found to control supraglacial lake distribution across all three ice shelves. Besides, a reduced FAC showed strong influence on lake ponding over Riiser-Larsen and Amery ice shelves. Further, the regional near-surface climate, including air temperature, solar radiation and (katabatic) winds, was shown to exert strong control on EAIS meltwater ponding. Similar as for API ice shelves, large-scale atmospheric modes were shown to influence the regional climatic setting with SAM, IOD, SSW and ASL influencing both above- and below-average meltwater ponding. On the one hand, these findings indicate that supraglacial lake formation is coupled to the complex interplay of local, regional and large-scale environmental controls. On the other hand, they highlight similar driving factors to control supraglacial lake formation on the API and EAIS pointing towards their transferability to other Antarctic regions.

## CHAPTER 7

### 7 Synthesis and Outlook

This chapter provides a synthesis of the conclusive findings of this dissertation. In particular, Chapter 7.1 discusses the results of this dissertation in consideration of the research questions defined in Chapter 1.3 and Chapter 7.2 addresses future challenges and opportunities of spaceborne remote sensing of Antarctic supraglacial lakes.

#### 7.1 Summary and Conclusive Findings

In the introductory chapter of this thesis, future climate scenarios were summarized suggesting atmospheric warming and melt intensification to become a dominant driver for future Antarctic ice mass loss. Despite the availability of estimations from climate scenarios, the future of Antarctica remains difficult to predict with its contribution to SLR representing the largest uncertainty in current projections. However, if GHG emissions continue undiminished, Antarctica's contribution to global SLR could exceed 15 m until 2500. Given that the Antarctic Ice Sheet has the potential to raise global mean sea level by 57.3 m and that a considerable share of Antarctic ice mass loss during recent decades resulted from supraglacial meltwater ponding, a detailed evaluation of Antarctic supraglacial lakes on ice shelves as well as of associated controls and impacts is of utmost importance. In this context, earth observation provides valuable data for a continuous, continent-wide monitoring of the Antarctic surface hydrological network.

This dissertation addressed the pressing need for an improved understanding and spatio-temporal monitoring of Antarctic surface hydrology. Apart from establishing a novel methodological framework for automated delineation of Antarctic supraglacial lake extents in large volumes of high-resolution Sentinel-1 SAR and optical Sentinel-2 data, the main research objectives of this thesis were to provide new insight into the intra-annual and inter-annual evolution of present-day Antarctic surface hydrology as well as to assess links to environmental drivers of supraglacial lake formation at local, regional and continental scale. These overarching research objectives were formulated as part of several research questions (Chapter 1.3). While detailed answering of the research

questions is provided in Chapters 3-6, the following paragraphs provide a short summary thereof.

#### Research Questions 1

- a. *Why are Antarctic supraglacial lakes of relevance?*
- b. *What are known controls on supraglacial lake formation and how widespread are supraglacial lakes around Antarctica?*
- c. *What are potential influences of supraglacial lakes on ice dynamics?*
- d. *How many studies address Antarctic supraglacial lake dynamics and what is their spatio-temporal coverage and resolution?*
- e. *What are the most frequently applied EO sensors and methods for supraglacial lake extent mapping?*
- f. *Which research gaps exist and how can they be addressed?*

A detailed literature review on fundamentals of Antarctic surface hydrology (Chapter 3) revealed that supraglacial lakes can have considerable impact on ice sheet mass balance and global SLR affecting the entire physical, biological and socioeconomic environment. Even though knowledge on the spatio-temporal distribution of Antarctic supraglacial lakes as well as their influence on ice mass loss is still restricted, Antarctic supraglacial lakes were revealed to be more widespread than previously assumed and linked to recent ice shelf disintegration events along the API. Considering that an expansion of the Antarctic surface hydrological network is expected in the future, supraglacial lakes will likely trigger further ice shelf destabilization and collapse leading to accelerated ice discharge and an increasing contribution of the AIS to global SLR. Since links to environmental controls and implications for global SLR remain poorly constrained, an improved understanding of Antarctic surface hydrology is of highest relevance. This is also required for models on SMB or supraglacial lake behavior enabling an improved investigation of their influence on ice shelf stability and global SLR.

To provide more detail on known controls on supraglacial lake formation, the literature review on fundamentals of Antarctic surface hydrology further revealed supraglacial lake evolution to be driven by local, regional and large-scale environmental factors. In this context, local control mechanisms were found to include the ice surface topography, the firn air content and melt-albedo feedbacks. Regional controls on Antarctic meltwater ponding were suggested to result from the near-surface climate including the amount of incoming solar radiation, air temperature, wind and precipitation. Finally, large-scale atmospheric modes and teleconnections were shown to exert control on meltwater ponding, e.g. in connection to positive SAM years.

Furthermore, it was shown that Antarctic supraglacial lakes occur across all three Antarctic regions even though most studies report of supraglacial lake occurrence over individual ice shelves and drainage basins on the API and EAIS. Regions of frequent lake coverage were shown to be George VI, Wilkins and the Larsen ice shelves on the API as well as Riiser-Larsen, Nivlisen, Roi Baudouin, Amery and Shackleton ice shelves on the EAIS. Observations of supraglacial lakes on the WAIS are so far scarce.

On the other hand, potential impacts of supraglacial lakes on Antarctic ice dynamics and mass balance were highlighted to result from melt-albedo feedbacks, direct surface runoff, hydrofracture and meltwater penetration to the glacier bed. First, melt-albedo feedbacks arise due to the low albedo of supraglacial lakes themselves triggering enhanced melting due to an increased absorption of solar radiation. On the other hand, direct surface runoff leads to enhanced ice thinning and a negative SMB. A more dramatic consequence of supraglacial lakes is their penetration into fractures and crevasses of ice shelves initiating hydrofracture and ice shelf collapse. Ice shelf collapse leads to a reduction in buttressing causing ice flow accelerations and increased ice discharge. Likewise, the penetration of supraglacial meltwater to the glacier bed can initiate basal sliding and transient glacier accelerations. At this point, it has to be noted that most knowledge on fundamentals of Antarctic surface hydrology resulted from theoretical considerations and from observations over individual ice shelves or the Greenland Ice Sheet.

Furthermore, a literature review on spaceborne remote sensing of Antarctic supraglacial lakes was conducted on the basis of all investigations that were published between January 1980 and June 2021. In agreement with the distribution of supraglacial lakes across the AIS, spaceborne remote sensing primarily revealed supraglacial lake occurrence on the API and EAIS, while only one study investigated lakes on the WAIS as part of a pan-Antarctic assessment. Overall, ~89% of all investigations were performed at local-scale and ~9% of all studies were performed at regional-scale. The only pan-Antarctic study covered all three Antarctic regions, yet at incomplete spatial coverage and limited temporal resolution. In particular, ~77% of all investigations were performed at inter-annual temporal resolution or using single satellite observations and ~23% of all studies investigated intra-annual supraglacial lake extent dynamics. However, recent studies marked a shift towards more frequent intra-annual analyses at regional-scale primarily due to the launch of Landsat 8 and the Sentinel satellites in the 2010s. Furthermore, the literature review revealed that ~77% of all studies relied on the use of optical imagery, while only ~11% of all studies were SAR-based. At the same time, ~12% of all studies on Antarctic supraglacial lakes employed a combination of optical and SAR data. In this context, optical data were most frequently from the Landsat, Sentinel-2 and the Aqua/Terra satellites and SAR data were most frequently from C-band SAR sensors aboard ERS-1/-2, Envisat and Sentinel-1. However, due to



the lack of automated mapping techniques for optical and SAR data, past studies on Antarctic supraglacial lakes relied on mainly visual, manual or semi-automated supraglacial lake identification.

In agreement with these findings, several research gaps were identified as part of the literature review. To start with, current research on Antarctic supraglacial lakes was found to be limited by the overall low number of investigations as well as their insufficient spatial and temporal coverage and resolution. In this context, the lack of automated mapping techniques with spatio-temporal transferability was found to be the main drawback hindering analyses of Antarctic supraglacial lake evolution using optical or SAR satellite data. Therefore, a main conclusion of the literature review was that future studies should exploit data from spaceborne remote sensing together with advanced image classification techniques, e.g. from artificial intelligence, to address historical, present-day and future supraglacial lake evolution using intra-annual and inter-annual supraglacial lake extent mappings at regional to circum-Antarctic spatial scale. This particularly applies to regions that remain understudied including most glaciers and ice shelves on the WAIS but also large coastal sections along the EAIS and API. To enable a more complete mapping record, also the combination of optical and SAR data was found to be of utmost importance, while being rarely performed. In this regard, the combination of mappings should be performed at a pre-defined pixel spacing and temporal coverage that is short enough to avoid misclassifications due to the movement of lakes with ice flow and long enough to capture the full picture of lake coverage.

### Research Questions 2

- a. *What are potentials and challenges for mapping Antarctic supraglacial lake extents in optical and SAR satellite imagery and how can they be addressed and overcome?*
- b. *How can recent advances in EO, including innovative Artificial Intelligence (AI) approaches, support an improved monitoring and understanding of Antarctic supraglacial meltwater features?*
- c. *How can ML and DL support a fully automated mapping of Antarctic supraglacial lakes in Sentinel-1 SAR and optical Sentinel-2 imagery?*
- d. *What opportunities exist for the implementation of a holistic framework for circum-Antarctic supraglacial lake extent mapping?*

Spaceborne remote sensing provides a valuable tool for the large-scale monitoring of the Antarctic Ice Sheet where ground-based mapping efforts are difficult to perform due to its vast size and remote location. In particular, recent progress in EO offers new opportunities for the monitoring of Antarctica enabling continuous mapping efforts at high spatial accuracy, coverage and repeat intervals. Over the Antarctic coastline, data of the

recently launched Sentinel-1 SAR and optical Sentinel-2 satellite missions provide a wealth of data at sub-weekly temporal resolution. However, due to the lack of automated mapping techniques, data of these missions remain underexploited.

In this context, a review on potentials and challenges of spaceborne remote sensing for Antarctic supraglacial lake extent delineation revealed sensor-specific advantages and limitations for optical and SAR satellite data. To start with, supraglacial lake extent delineation in optical satellite imagery was found to be particularly advantageous due to the high spatial accuracy and resolution of data from current satellite missions such as Sentinel-2 as well as the ability to map surface lakes that are subject to environmental effects such as severe wind roughening hindering supraglacial lake identification in SAR imagery. At the same time, limitations of optical satellite data include the similar appearance of supraglacial lakes and surface features such as shadow, blue ice or slush as well as the general lack of data during cloud cover and Antarctic polar night. On the other hand, SAR remote sensing provides continuous data coverage due to the independence of meteorological and illumination conditions and enables the delineation of buried and partly frozen lakes. However, SAR data are subject to speckle noise as well as the similar backscattering signature of supraglacial lakes, wet snow, dry snow, bare ice, radar shadow and open ocean. As previously mentioned, also strong wind roughening of lake surfaces complicates supraglacial lake extent mapping in SAR imagery. While some of these limitations, including the lack of optical data during cloud cover or the severe roughening of lake surfaces, can be overcome through combination of optical and SAR satellite imagery, other limitations, including difficulties in discriminating lakes from other ice sheet surface features as well as the general wealth of available satellite data, were found to complicate an automated mapping of Antarctic supraglacial lake extents with conventional image processing techniques. Therefore, the use of advanced image classification techniques is required. In this context, methods from artificial intelligence are frequently employed for big data processing and can greatly support an automated mapping of Antarctic supraglacial lakes in time series of optical and SAR satellite data at full ice sheet coverage. For example, the ability of machine learning algorithms to learn from a given training dataset allows to adjust the training process to the regional environmental setting enabling method developments with spatio-temporal transferability.

In agreement with these requirements, a novel framework for supraglacial lake extent delineation in high-resolution Sentinel-1 SAR and optical Sentinel-2 satellite imagery was developed through exploitation of state-of-the-art machine learning methods for image classification. In particular, two separate machine learning models were trained for Sentinel-1 and Sentinel-2 and combined by means of the fusion of classifications from both sensors at decision-level. In this context, the classification of Sentinel-1 SAR imagery was performed with a deep convolutional neural network based on residual U-

Net enabling the semantic segmentation of satellite scenes through consideration of the spatial image context. Being trained on 21,200 multi-temporal Sentinel-1 image patches covering 13 Antarctic regions, the final deep learning model reached a classification accuracy of ~93% (F-score) for supraglacial lakes in 10 independent test scenes. On the other hand, Sentinel-2 data were classified by means of a pixel-based Random Forest classifier that was trained on the basis of a range of spectral bands and indices as well as topographic data covering 14 Antarctic regions. The best performing classification model returned an average F-score of ~95% for supraglacial lakes in 14 independent test scenes. Finally, the fusion of optical and SAR classifications resulted in bi-weekly mapping products at 10 m spatial resolution. The overall workflow ranging from data acquisition and pre-processing over image classification to post-processing was implemented as part of DLR's internal HPC infrastructure enabling the automated processing of large amounts of satellite data over the entire Antarctic continent. Further, the application of the developed classification algorithm to study regions on the Greenland Ice Sheet highlighted the spatio-temporal transferability of the developed workflow to glaciated regions beyond Antarctica. With the planned launches of Sentinel-1C and Sentinel-1D as well as Sentinel-2C and Sentinel-2D, the presented framework will enable a continuous monitoring of Antarctic supraglacial lakes also in the future.

### Research Questions 3

- a. *What are intra-annual and inter-annual patterns and anomalies of supraglacial lake evolution?*
- b. *What are the properties of observed supraglacial lakes?*
- c. *Where do supraglacial lakes cluster on ice shelves and grounded ice and how often do they reoccur at the same locations?*
- d. *Are the observed ice shelf regions particularly vulnerable to ice shelf collapse and what are potential implications for future ice shelf stability?*
- e. *What are the dominant controls on supraglacial lake distribution and evolution? What are implications for other Antarctic regions?*

To demonstrate the functionality and potentials of the developed framework for automated supraglacial lake extent delineation in optical and SAR satellite imagery, it was applied on the full archive of Sentinel-1 and Sentinel-2 over six major Antarctic ice shelves on the API and EAIS. In detail, fused supraglacial lake extent mapping products were derived for the period November to March in 2015-2021. For the first time, the results provide insight into present-day Antarctic surface hydrology at bi-weekly temporal scale and unprecedented 10 m spatial resolution.

Over the API, the intra-annual supraglacial lake extent mapping results revealed comparatively low lake extents during 2015-2018 and particularly high lake coverage during melting seasons 2019-2020 and 2020-2021. Peak lake coverage was observed

during January 2020 reaching 805 km<sup>2</sup>, 110 km<sup>2</sup> and 45 km<sup>2</sup> over George VI, Bach and Wilkins ice shelves, respectively. Furthermore, the intra-annual time series revealed late January to mark the peak of a melting season with lake extents reducing significantly during early or late February. During the 2019-2020 and 2020-2021 melting seasons, anomalies of intra-annual lake extent time series additionally revealed below-average meltwater ponding during the early and late melting seasons, respectively. Lake evolution on the investigated EAIS ice shelves showed particularly high lake coverage during melting seasons 2016-2019 and extremely low lake coverage throughout 2020-2021. Here, peak lake extents reached areal coverages of 85 km<sup>2</sup>, 107 km<sup>2</sup> and 1,373 km<sup>2</sup> over Riiser-Larsen, Nivlisen and Amery ice shelves. In addition, the average onset of lake formation on the EAIS was found to be in late December with lakes persisting considerably longer throughout the melting seasons than on the API.

Furthermore, the analysis of inter-annual January recurrence times of lakes on the API showed lake clustering near the grounding lines of the ice shelves with the exception of George VI, where lakes covered vast parts of the central ice shelf during years of peak lake coverage. Over George VI and Wilkins ice shelves, years of low lake coverage were additionally characterized by lake clustering close to low-albedo rock outcrop near the grounding zones. At the same time, lakes predominantly formed at low elevations and low surface slopes with comparatively low recurrence times of mostly 2-3 years. Over EAIS ice shelves, the January recurrence time of lakes was considerably higher reaching 4-5 years in local surface depressions on grounded ice as well as in elongated supraglacial meltwater channels or in longitudinal flow stripes on ice shelves. Further, supraglacial lake distribution on the EAIS was found to be coupled to the location of low-albedo rock and blue ice, while they generally clustered at low elevations and low surface slopes. Over all six ice shelves, lateral meltwater transport across the ice shelves was observed. Since the development of drainage systems delivers meltwater to regions with only little or no surface melt, this points towards an increased risk for hydrofracture also considering the classification of corresponding API and EAIS ice shelf regions as potentially vulnerable to hydrofracture. Further, recent increased meltwater ponding during 2019-2020 and 2020-2021 on the API likely contributed to a further reduction in the FAC suggesting that ice shelf destabilization could be imminent.

Moreover, the multi-temporal statistical correlation analysis with climate variables uncovered drivers of intra-annual and inter-annual supraglacial lake evolution in 2015-2021. Over both ice sheet regions, the complex interplay of local, regional and large-scale environmental drivers was found to control supraglacial lake evolution. For ice shelves on the API, local controls on supraglacial lake distribution were found to include the ice surface topography, the ice shelf geometry, the presence of low-albedo features as well as a reduced FAC. On the other hand, regional controls on supraglacial lake evolution were revealed to be the amount of incoming solar radiation, air temperature,

(foehn) wind occurrence and sensible heat transport. In this context, the regional near-surface climate was driven by large-scale atmospheric modes including SAM, IOD, SSW and ASL. While SAM, IOD and SSW caused increased meltwater ponding during the peaks of the 2019-2020 and 2020-2021 melting seasons, ASL caused below-average meltwater ponding during the late 2020-2021 melting season. For the EAIS, similar local drivers were found to control supraglacial lake distribution despite some variations over each ice shelf. In addition, the regional climate setting, including solar radiation, air temperature and (katabatic) wind conditions, was revealed to drive supraglacial lake evolution over all three ice shelves. Similar as for the API, regional climatic drivers were influenced by large-scale atmospheric modes including SAM, IOD, SSW and ASL. Overall, the results highlight similar driving factors to control supraglacial lake formation on the API and EAIS pointing towards their transferability to other Antarctic regions. In agreement with this, high meltwater ponding is suggested to have prevailed over other API ice shelves and surrounding ice sheet regions during 2019-2020 and 2020-2021 and low meltwater ponding is suggested to have prevailed over large parts of the AIS during the 2020-2021 melting season.

## 7.2 Future Challenges and Opportunities

With accelerating global climate change, the Antarctic Ice Sheet will be exposed to increasing ice dynamic change in the future. Due to supraglacial lakes being important precursors of ice shelf collapse as well as their potential effects on Antarctic ice dynamics, the continuous monitoring of Antarctic surface hydrology is of utmost importance. This particularly applies as future climate scenarios suggest a dramatic expansion of the Antarctic surface hydrological network in the coming decades. In this regard, the novel framework for automated supraglacial lake extent mapping in Sentinel-1 SAR and optical Sentinel-2 imagery enables a fast and efficient processing of remote sensing imagery providing dense time series on intra-annual and inter-annual supraglacial lake evolution at unprecedented spatial and temporal resolution and coverage. Through the future integration of the developed framework into a near-real time web service such as DLR's GeoService, the data will be made publicly available for the entire Antarctic continent and provide the scientific community with high-resolution supraglacial lake extent mappings. These will be particularly valuable for an improved representation of meltwater transport across Antarctic ice shelves in modelling efforts, e.g. on ice shelf stability or SMB, and contribute to an improved understanding of Antarctica's present and future contribution to global SLR. With the future launch of additional satellites for the Sentinel-1 and Sentinel-2 constellations, the developed methodological framework presents a sustainable, long-term contribution to the field.

Before ingestion of the developed framework into a web service, further method improvements would be required in order to obtain reliable classification results for the entire Antarctic continent. For Sentinel-1, an integration of additional training data with focus on regions that are most distant from current training regions, including coastal sections along the EAIS and WAIS, would contribute to an enhanced model performance and improved spatio-temporal transferability. In this regard, additional training samples should be collected over particularly large lakes as well as surface features that are difficult to discriminate from lakes. Similarly, more training data should be collected for Sentinel-2 focusing on regions on the EAIS and WAIS. In detail, additional training data should cover slush, lake edges and lakes affected by cloud shadow. Another future opportunity would be the integration of additional training data covering the Greenland Ice Sheet. While the potential of the developed method for supraglacial lake extent delineation in south-west Greenland was already highlighted, an integration of additional training data covering the Greenland Ice Sheet would enable the application of the developed workflow over both ice sheets or even other glaciated regions. In this context, the development of an uncertainty layer providing extra detail on the quality of obtained classification results would be of particular advantage.

For an additional derivation of lake depths and volumes in optical data, another future requirement would be to accurately discriminate between open water and slightly frozen lakes. As this remains challenging with conventional machine learning classification techniques, including Random Forest or Support Vector Machines, additional deep learning method developments would be required. The derivation of lake depths and volumes would provide valuable information on temporal lake evolution and support numerical models in constraining volume-dependent drainage thresholds. In addition, method developments with data of the Landsat missions would allow to extend the observational period back in time even though data of the Landsat missions are restricted in terms of their lower spatial and temporal resolution compared to Sentinel-2.

In light of predictions of future enhanced precipitation conditions, e.g. over the API, another opportunity would be to establish a mapping method for englacial drainage structures including firn aquifers. Even though the literature review on fundamentals of Antarctic surface hydrology showed that observations of Antarctic firn aquifers are so far scarce, results from modelling suggest their widespread occurrence, e.g. along the API. As firn aquifers may have similar effects on ice shelf stability as meltwater ponding, their monitoring is overdue. In this context, future L-Band missions such as TanDEM-L or the NASA/ISRO SAR will be particularly suitable due to their increased penetration capabilities into snow and ice.

To summarize, this dissertation greatly contributed to an improved understanding of Antarctic surface hydrology. For the first time, time series on intra-annual and inter-

annual supraglacial lake evolution were derived over six major Antarctic ice shelves and linked to environmental drivers for investigation of the main control mechanisms influencing Antarctic supraglacial lake formation. In this context, a novel processing chain for the automated mapping of Antarctic supraglacial lake extents in Sentinel-1 SAR and optical Sentinel-2 satellite imagery was developed. The methodological framework exploits methods from artificial intelligence and forms the basis for the development of an ice sheet wide monitoring system delivering data on supraglacial lake evolution at unprecedented spatial and temporal resolution. Overall, the results of this dissertation are of particular importance for establishment of an improved understanding of Antarctica's future contribution to global sea-level-rise.



## Bibliography

- AAD, 2021. Australian Antarctic Data Centre: Data management and spatial data services: <https://data.aad.gov.au/>, last accessed: 12 March 2021.
- Abram, N.J., Mulvaney, R., Vimeux, F., Phipps, S.J., Turner, J., England, M.H., 2014. Evolution of the Southern Annular Mode during the past millennium. *Nature Clim Change* 4, 564–569. <https://doi.org/10.1038/nclimate2235>
- Alley, K.E., Scambos, T.A., Miller, J.Z., Long, D.G., MacFerrin, M., 2018. Quantifying vulnerability of Antarctic ice shelves to hydrofracture using microwave scattering properties. *Remote Sens. Environ.* 210, 297–306. <https://doi.org/10.1016/j.rse.2018.03.025>
- Arthur, J.F., Stokes, C.R., Jamieson, S.S.R., Carr, J.R., Leeson, A.A., 2020a. Recent understanding of Antarctic supraglacial lakes using satellite remote sensing. *Prog Phys Geogr* 44, 6, 837–869. <https://doi.org/10.1177/0309133320916114>
- Arthur, J.F., Stokes, C.R., Jamieson, S.S.R., Carr, J.R., Leeson, A.A., 2020b. Distribution and seasonal evolution of supraglacial lakes on Shackleton Ice Shelf, East Antarctica. *The Cryosphere* 14, 11, 4103–4120. <https://doi.org/10.5194/tc-14-4103-2020>
- Ashmore, D.W., Bingham, R.G., 2014. Antarctic subglacial hydrology: current knowledge and future challenges. *Antarct. Sci.* 26, 6, 758–773. <https://doi.org/10.1017/S0954102014000546>
- ATS, 2021. Secretariat of the Antarctic Treaty - The Antarctic Treaty: <https://www.ats.aq/e/antarctic treaty.html>, last accessed: 24 February 2021.
- Baheti, B., Innani, S., Gajre, S., Talbar, S., 2020. Semantic scene segmentation in unstructured environment with modified DeepLabV3+. *Pattern Recognit. Lett.* 138, 223–229. <https://doi.org/10.1016/j.patrec.2020.07.029>
- Bamber, J.L., Rignot, E., 2002. Unsteady flow inferred for Thwaites Glacier, and comparison with Pine Island Glacier, West Antarctica. *J. Glaciol.* 48, 161, 237–246. <https://doi.org/10.3189/172756502781831395>
- Bamber, J.L., Riva, R.E.M., Vermeersen, B.L.A., LeBrocq, A.M., 2009. Reassessment of the Potential Sea-Level Rise from a Collapse of the West Antarctic Ice Sheet. *Science* 324, 8929, 901–903. <https://doi.org/10.1126/science.1169335>
- Bamber, J.L., Westaway, R.M., Marzeion, B., Wouters, B., 2018. The land ice contribution to sea level during the satellite era. *Environ. Res. Lett.* 13, 6. <https://doi.org/10.1088/1748-9326/aac2f0>
- Banwell, A.F., Caballero, M., Arnold, N.S., Glasser, N.F., Mac Cathles, L., MacAyeal, D.R., 2014. Supraglacial lakes on the Larsen B ice shelf, Antarctica, and at Paakitsoq, West Greenland: a comparative study. *Ann. Glaciol.* 55, 66, 1–8. <https://doi.org/10.3189/2014AoG66A049>
- Banwell, A.F., Datta, R.T., Dell, R.L., Moussavi, M., Brucker, L., Picard, G., Shuman, C.A., Stevens, L.A., 2021. The 32-year record-high surface melt in 2019/2020 on the northern George VI Ice Shelf, Antarctic Peninsula. *The Cryosphere* 15, 2, 909–925. <https://doi.org/10.5194/tc-15-909-2021>
- Banwell, A.F., MacAyeal, D.R., 2015. Ice-shelf fracture due to viscoelastic flexure stress induced by fill/drain cycles of supraglacial lakes. *Antarct. Sci.* 27, 6, 587–597. <https://doi.org/10.1017/S0954102015000292>
- Banwell, A.F., MacAyeal, D.R., Sergienko, O.V., 2013. Breakup of the Larsen B Ice Shelf triggered by chain reaction drainage of supraglacial lakes. *Geophys. Res. Lett.* 40, 22, 5872–5876. <https://doi.org/10.1002/2013GL057694>
- Banwell, A.F., Willis, I.C., Macdonald, G.J., Goodsell, B., MacAyeal, D.R., 2019. Direct measurements of ice-shelf flexure caused by surface meltwater ponding and drainage. *Nat. Commun.* 10, 730. <https://doi.org/10.1038/s41467-019-08522-5>
- Bartholomew, I., Nienow, P., Mair, D., Hubbard, A., King, M.A., Sole, A., 2010. Seasonal evolution of subglacial drainage and acceleration in a Greenland outlet glacier. *Nat. Geosci.* 3, 408–411. <https://doi.org/10.1038/ngeo863>
- Baumhoer, C.A., Dietz, A.J., Kneisel, C., Kuenzer, C., 2019. Automated Extraction of Antarctic Glacier and Ice Shelf Fronts from Sentinel-1 Imagery Using Deep Learning. *Remote Sens.* 11, 21, 2529. <https://doi.org/10.3390/rs11212529>

- Baumhoer, C.A., Dietz, A.J., Kneisel, C., Paeth, H., Kuenzer, C., 2021. Environmental drivers of circum-Antarctic glacier and ice shelf front retreat over the last two decades. *The Cryosphere* 15, 5, 2357–2381. <https://doi.org/10.5194/tc-15-2357-2021>
- Beckley, B.D., Callahan, P.S., Hancock, D.W., Mitchum, G.T., Ray, R.D., 2017. On the “Cal-Mode” Correction to TOPEX Satellite Altimetry and Its Effect on the Global Mean Sea Level Time Series. *J. Geophys. Res.-Oceans* 122, 11, 8371–8384. <https://doi.org/10.1002/2017JC013090>
- Belgiu, M., Drăguț, L., 2016. Random forest in remote sensing: A review of applications and future directions. *ISPRS J. Photogramm. Remote Sens.* 114, 24–31. <https://doi.org/10.1016/j.isprsjprs.2016.01.011>
- Bell, R.E., Banwell, A.F., Trusel, L.D., Kingslake, J., 2018. Antarctic surface hydrology and impacts on ice-sheet mass balance. *Nat. Clim. Change* 8, 1044–1052. <https://doi.org/10.1038/s41558-018-0326-3>
- Bell, R.E., Chu, W., Kingslake, J., Das, I., Tedesco, M., Tinto, K.J., Zappa, C.J., Frezzotti, M., Boghosian, A., Lee, W.S., 2017. Antarctic ice shelf potentially stabilized by export of meltwater in surface river. *Nature* 544, 344–348. <https://doi.org/10.1038/nature22048>
- Bell, R.E., Seroussi, H., 2020. History, mass loss, structure, and dynamic behavior of the Antarctic Ice Sheet. *Science* 367, 6484, 1321–1325. <https://doi.org/10.1126/science.aaz5489>
- Bell, R.E., Studinger, M., Shuman, C.A., Fahnestock, M.A., Joughin, I., 2007. Large subglacial lakes in East Antarctica at the onset of fast-flowing ice streams. *Nature* 445, 904–907. <https://doi.org/10.1038/nature05554>
- Bengtsson, L., Koumoutsaris, S., Hodges, K., 2011. Large-Scale Surface Mass Balance of Ice Sheets from a Comprehensive Atmospheric Model. *Surv. Geophys.* 32, 459. <https://doi.org/10.1007/s10712-011-9120-8>
- Benson, C.S., 1960. Stratigraphic studies in the snow and firn of the Greenland ice sheet. California Institute of Technology.
- Berhane, T.M., Lane, C.R., Wu, Q., Autrey, B.C., Anenkhonov, O.A., Chepinoga, V.V., Liu, H., 2018. Decision-Tree, Rule-Based, and Random Forest Classification of High-Resolution Multispectral Imagery for Wetland Mapping and Inventory. *Remote Sens.* 10, 4, 580. <https://doi.org/10.3390/rs10040580>
- Bernier, P.Y., 1987. Microwave Remote Sensing of Snowpack Properties: Potential and Limitations. *Hydrol Res* 18, 1, 1–20. <https://doi.org/10.2166/nh.1987.0001>
- Berthier, E., Scambos, T.A., Shuman, C.A., 2012. Mass loss of Larsen B tributary glaciers (Antarctic Peninsula) unabated since 2002. *Geophys. Res. Lett.* 39, 13. <https://doi.org/10.1029/2012GL051755>
- Bevan, S., Luckman, A., Hendon, H., Wang, G., 2020. The 2020 Larsen C Ice Shelf surface melt is a 40-year record high. *The Cryosphere* 14, 10, 3551–3564. <https://doi.org/10.5194/tc-14-3551-2020>
- Bindschadler, R., Vornberger, P., Fleming, A., Fox, A., Mullins, J., Binnie, D., Paulsen, S.J., Granneman, B., Gorodetzky, D., 2008. The Landsat Image Mosaic of Antarctica. *Remote Sens. Environ.* 112, 12, 4214–4226. <https://doi.org/10.1016/j.rse.2008.07.006>
- Bindschadler, R.A., Vornberger, P.L., King, M.A., Padman, L., 2003. Tidally driven stick–slip motion in the mouth of Whillans Ice Stream, Antarctica. *Ann. Glaciol.* 36, 263–272. <https://doi.org/10.3189/172756403781816284>
- BOM, 2021. Climate Driver Update: <http://www.bom.gov.au/climate/enso/>, last accessed: 22 June 2021.
- Box, J.E., Ski, K., 2007. Remote sounding of Greenland supraglacial melt lakes: implications for subglacial hydraulics. *J. Glaciol.* 53, 181, 257–265. <https://doi.org/10.3189/172756507782202883>
- Bozkurt, D., Bromwich, D.H., Carrasco, J., Hines, K.M., Maureira, J.C., Rondanelli, R., 2020. Recent Near-surface Temperature Trends in the Antarctic Peninsula from Observed, Reanalysis and Regional Climate Model Data. *Adv. Atmos. Sci.* 37, 477–493. <https://doi.org/10.1007/s00376-020-9183-x>
- Braun, M., Humbert, A., 2009. Recent Retreat of Wilkins Ice Shelf Reveals New Insights in Ice Shelf Breakup Mechanisms. *IEEE Geosci. Remote Sens. Lett.* 6, 2, 263–267. <https://doi.org/10.1109/LGRS.2008.2011925>

- Braun, M., Humbert, A., Moll, A., 2009. Changes of Wilkins Ice Shelf over the past 15 years and inferences on its stability. *The Cryosphere* 3, 1, 41–56. <https://doi.org/10.5194/tc-3-41-2009>
- Braun, M., Rau, F., Saurer, H., Gobmann, H., 2000. Development of radar glacier zones on the King George Island ice cap, Antarctica, during austral summer 1996/97 as observed in ERS-2 SAR data. *Ann. Glaciol.* 31, 357–363. <https://doi.org/10.3189/172756400781819950>
- Breiman, L., 2001. Random Forests. *Machine Learning* 45, 5–32. <https://doi.org/10.1023/A:1010933404324>
- Broecker, W.S., Peng, T.-H., 1987. The oceanic salt pump: Does it contribute to the glacial-interglacial difference in atmospheric CO<sub>2</sub> content? *Global Biogeochem Cycles* 1, 3, 251–259. <https://doi.org/10.1029/GB001i003p00251>
- Bromwich, D.H., Nicolas, J.P., Monaghan, A.J., Lazzara, M.A., Keller, L.M., Weidner, G.A., Wilson, A.B., 2013. Central West Antarctica among the most rapidly warming regions on Earth. *Nat. Geosci.* 6, 139–145. <https://doi.org/10.1038/ngeo1671>
- Buzzard, S., Feltham, D.L., Flocco, D., 2018a. Modelling the fate of surface melt on the Larsen C Ice Shelf. *The Cryosphere* 12, 11, 3565–3575. <https://doi.org/10.5194/tc-12-3565-2018>
- Buzzard, S., Feltham, D.L., Flocco, D., 2018b. A Mathematical Model of Melt Lake Development on an Ice Shelf. *J. Adv. Model. Earth Syst.* 10, 2, 262–283. <https://doi.org/10.1002/2017MS001155>
- Cape, M.R., Vernet, M., Skvarca, P., Marinsek, S., Scambos, T., Domack, E., 2015. Foehn winds link climate-driven warming to ice shelf evolution in Antarctica. *J. Geophys. Res.-Atmos.* 120, 21, 11,037-11,057. <https://doi.org/10.1002/2015JD023465>
- Carrasco, J.F., Bozkurt, D., Cordero, R.R., 2021. A review of the observed air temperature in the Antarctic Peninsula. Did the warming trend come back after the early 21st hiatus? *Polar Sci.* 28, 100653. <https://doi.org/10.1016/j.polar.2021.100653>
- Carter, L., McCave, I.N., Williams, M.J.M., 2008. Chapter 4 Circulation and Water Masses of the Southern Ocean: A Review, in: Florindo, F., Siebert, M. (Eds.), *Developments in Earth and Environmental Sciences, Antarctic Climate Evolution*. Elsevier, pp. 85–114. [https://doi.org/10.1016/S1571-9197\(08\)00004-9](https://doi.org/10.1016/S1571-9197(08)00004-9)
- Carter, S.P., Fricker, H.A., Siegfried, M.R., 2013. Evidence of rapid subglacial water piracy under Whillans Ice Stream, West Antarctica. *J. Glaciol.* 59, 218, 1147–1162. <https://doi.org/10.3189/2013JoG13J085>
- Chen, L.-C., Papandreou, G., Kokkinos, I., Murphy, K., Yuille, A.L., 2018a. DeepLab: Semantic Image Segmentation with Deep Convolutional Nets, Atrous Convolution, and Fully Connected CRFs. *IEEE Trans. Pattern Anal. Mach. Intell.* 40, 4, 834–848. <https://doi.org/10.1109/TPAMI.2017.2699184>
- Chen, L.-C., Papandreou, G., Kokkinos, I., Murphy, K., Yuille, A.L., 2016. Semantic Image Segmentation with Deep Convolutional Nets and Fully Connected CRFs. *arXiv:1412.7062*.
- Chen, L.-C., Papandreou, G., Schroff, F., Adam, H., 2017. Rethinking Atrous Convolution for Semantic Image Segmentation. *arXiv arXiv:1706.05587*.
- Chen, L.-C., Zhu, Y., Papandreou, G., Schroff, F., Adam, H., 2018b. Encoder-Decoder with Atrous Separable Convolution for Semantic Image Segmentation. *arXiv:1802.02611*.
- Christianson, K., Bushuk, M., P., P., Parizek, B.R., Joughin, I.R., Alley, R.B., Shean, D.E., Abrahamsen, E.P., Anandakrishnan, S., Heywood, K.J., Kim, T.-W., Lee, S.H., Nicholls, K., Stanton, T., Truffer, M., Webber, B.G.M., Jenkins, A., Jacobs, S., Bindschadler, R., Holland, D.M., 2016. Sensitivity of Pine Island Glacier to observed ocean forcing. *Geophys. Res. Lett.* 43, 20, 10,817-10,825. <https://doi.org/10.1002/2016GL070500>
- Chu, V.W., 2014. Greenland ice sheet hydrology: A review. *Prog Phys Geogr* 38, 1, 19–54. <https://doi.org/10.1177/0309133313507075>
- Chu, Z., Tian, T., Feng, R., Wang, L., 2019. Sea-Land Segmentation With Res-UNet And Fully Connected CRF. Presented at the IGARSS 2019 - 2019 IEEE International Geoscience and Remote Sensing Symposium, Yokohama, Japan, pp. 3840–3843. <https://doi.org/10.1109/IGARSS.2019.8900625>
- CIA, 2021. The World Factbook - Antarctica: <https://www.cia.gov/the-world-factbook/countries/antarctica/>, last accessed: 24 February 2021.

- Clem, K.R., Fogt, R.L., 2013. Varying roles of ENSO and SAM on the Antarctic Peninsula climate in austral spring. *J. Geophys. Res.-Atmos.* 118, 20, 11,481-11,492. <https://doi.org/10.1002/jgrd.50860>
- Clem, K.R., Fogt, R.L., Turner, J., Lintner, B.R., Marshall, G.J., Miller, J.R., Renwick, J.A., 2020. Record warming at the South Pole during the past three decades. *Nat. Clim. Chang.* 10, 762–770. <https://doi.org/10.1038/s41558-020-0815-z>
- Cohen, J., 1960. A Coefficient of Agreement for Nominal Scales. *Educ Psychol Meas* 20, 1, 37–46. <https://doi.org/10.1177/001316446002000104>
- Collins, M., Knutti, R., Arblaster, J., Dufresne, J.-L., Fichet, T., Friedlingstein, P., Gao, X., Gutowski, W.J., Johns, T., Krinner, G., Shongwe, M., Tebaldi, C., Weaver, A.J., Wehner, M., 2013. Long-term Climate Change: Projections, Commitments and Irreversibility. In: *Climate Change 2013: The Physical Science Basis. Contribution of Working Group I to the Fifth Assessment Report of the Intergovernmental Panel on Climate Change* [Stocker, T.F., D. Qin, G.-K. Plattner, M. Tignor, S.K. Allen, J. Boschung, A. Nauels, Y. Xia, V. Bex and P.M. Midgley (eds.)]. Cambridge University Press, Cambridge, United Kingdom and New York, NY, USA.
- Comiso, J.C., 2000. Variability and Trends in Antarctic Surface Temperatures from In Situ and Satellite Infrared Measurements. *J. Climate* 13, 10, 1674–1696. [https://doi.org/10.1175/1520-0442\(2000\)013<1674:VATIAS>2.0.CO;2](https://doi.org/10.1175/1520-0442(2000)013<1674:VATIAS>2.0.CO;2)
- CONMAP, 2021. Council of Managers of National Antarctic Program (CONMAP) Antarctic Information: <https://www.comnap.aq/antarctic-information/>, last accessed: 24 February 2021.
- Cook, A.J., Holland, P.R., Meredith, M.P., Murray, T., Luckman, A., Vaughan, D.G., 2016. Ocean forcing of glacier retreat in the western Antarctic Peninsula. *Science* 353, 6296, 283–286. <https://doi.org/10.1126/science.aae0017>
- Cook, A.J., Vaughan, D.G., 2010. Overview of areal changes of the ice shelves on the Antarctic Peninsula over the past 50 years. *The Cryosphere* 4, 1, 77–98. <https://doi.org/10.5194/tc-4-77-2010>
- Cuffey, K.M., Paterson, W.S.B., 2010. *The Physics of Glaciers*, Fourth Edition. ed. Butterworth-Heinemann.
- Das, I., Bell, R.E., Scambos, T.A., Wolovick, M., Creyts, T.T., Studinger, M., Frearson, N., Nicolas, J.P., Lenaerts, J.T.M., van den Broeke, M.R., 2013. Influence of persistent wind scour on the surface mass balance of Antarctica. *Nat. Geosci.* 6, 367–371. <https://doi.org/10.1038/ngeo1766>
- Das, S.B., Joughin, I., Behn, M.D., Howat, I.M., King, M.A., Lizarralde, D., Bhatia, M.P., 2008. Fracture Propagation to the Base of the Greenland Ice Sheet During Supraglacial Lake Drainage. *Science* 320, 5877, 778–781. <https://doi.org/10.1126/science.1153360>
- Datta, R.T., Tedesco, M., Fettweis, X., Agosta, C., Lhermitte, S., Lenaerts, J.T.M., Wever, N., 2019. The Effect of Foehn-Induced Surface Melt on Firn Evolution Over the Northeast Antarctic Peninsula. *Geophys. Res. Lett.* 46, 7, 3822–3831. <https://doi.org/10.1029/2018GL080845>
- DeConto, R.M., Pollard, D., 2016. Contribution of Antarctica to past and future sea-level rise. *Nature* 531, 591–597. <https://doi.org/10.1038/nature17145>
- Dell, R., Arnold, N., Willis, I., Banwell, A., Williamson, A., Pritchard, H., Orr, A., 2020. Lateral meltwater transfer across an Antarctic ice shelf. *The Cryosphere* 14, 7, 2313–2330. <https://doi.org/10.5194/tc-14-2313-2020>
- Depoorter, M.A., Bamber, J.L., Griggs, J.A., Lenaerts, J.T.M., Ligtenberg, S.R.M., Broeke, M.R. van den, Moholdt, G., 2013. Calving fluxes and basal melt rates of Antarctic ice shelves. *Nature* 502, 89–92. <https://doi.org/10.1038/nature12567>
- Diakogiannis, F.I., Waldner, F., Caccetta, P., Wu, C., 2020. ResUNet-a: A deep learning framework for semantic segmentation of remotely sensed data. *ISPRS J. Photogramm. Remote Sens.* 162, 94–114. <https://doi.org/10.1016/j.isprsjprs.2020.01.013>
- Dietz, A.J., Kuenzer, C., Gessner, U., Dech, S., 2012. Remote sensing of snow – a review of available methods. *Int. J. Remote Sens.* 33, 13, 4094–4134. <https://doi.org/10.1080/01431161.2011.640964>
- Ding, F., 2009. Study on information extraction of water body with a new water index (NWI). *Sci. Surv. Mapp.* 155–157.

- Ding, Q., Steig, E.J., Battisti, D.S., Küttel, M., 2011. Winter warming in West Antarctica caused by central tropical Pacific warming. *Nat. Geosci.* 4, 398–403. <https://doi.org/10.1038/ngeo1129>
- Dirscherl, M., Dietz, A.J., Dech, S., Kuenzer, C., 2020a. Remote sensing of ice motion in Antarctica – A review. *Remote Sens. Environ.* 237, 111595. <https://doi.org/10.1016/j.rse.2019.111595>
- Dirscherl, M., Dietz, A.J., Kneisel, C., Kuenzer, C., 2021a. A Novel Method for Automated Supraglacial Lake Mapping in Antarctica Using Sentinel-1 SAR Imagery and Deep Learning. *Remote Sens.* 13, 2, 197. <https://doi.org/10.3390/rs13020197>
- Dirscherl, M., Dietz, A.J., Kneisel, C., Kuenzer, C., 2020b. Automated Mapping of Antarctic Supraglacial Lakes Using a Machine Learning Approach. *Remote Sens.* 12, 7, 1203. <https://doi.org/10.3390/rs12071203>
- Dirscherl, M., Dietz, A.J., Kuenzer, C., 2021b. Seasonal evolution of Antarctic supraglacial lakes in 2015–2021 and links to environmental controls. *The Cryosphere*, 15, 11, 5205–5226. <https://doi.org/10.5194/tc-15-5205-2021>
- Doake, C.S.M., Vaughan, D.G., 1991. Rapid disintegration of the Wordie Ice Shelf in response to atmospheric warming. *Nature* 350, 328–330. <https://doi.org/10.1038/350328a0>
- Dodds, K., 2010. Governing Antarctica: Contemporary Challenges and the Enduring Legacy of the 1959 Antarctic Treaty. *Glob Policy* 1, 1, 108–115. <https://doi.org/10.1111/j.1758-5899.2009.00006.x>
- Dow, C.F., Lee, W.S., Greenbaum, J.S., Greene, C.A., Blankenship, D.D., Poinar, K., Forrest, A.L., Young, D.A., Zappa, C.J., 2018. Basal channels drive active surface hydrology and transverse ice shelf fracture. *Sci. Adv.* 4, 6. <https://doi.org/10.1126/sciadv.aao7212>
- Dunmire, D., Lenaerts, J.T.M., Banwell, A.F., Wever, N., Shragge, J., Lhermitte, S., Drews, R., Pattyn, F., Hansen, J.S.S., Willis, I.C., Miller, J., Keenan, E., 2020. Observations of Buried Lake Drainage on the Antarctic Ice Sheet. *Geophys. Res. Lett.* 47, 15. <https://doi.org/10.1029/2020GL087970>
- Dutrieux, P., De Rydt, J., Jenkins, A., Holland, P.R., Ha, H.K., Lee, S.H., Steig, E.J., Ding, Q., Abrahamsen, E.P., Schröder, M., 2014. Strong Sensitivity of Pine Island Ice-Shelf Melting to Climatic Variability. *Science* 343, 6167, 174–178. <https://doi.org/10.1126/science.1244341>
- DWD, 2021. Deutscher Wetterdienst. Klimadaten weltweit - Monatswerte Antarktis: <https://www.dwd.de/DE/leistungen/klimadatenweltweit/klimadatenweltweit.html#buehneTop>, last accessed: 14 March 2021.
- Echelmeyer, K., Clarke, T.S., Harrison, W.D., 1991. Surficial glaciology of Jakobshavns Isbræ, West Greenland: Part I. Surface morphology. *J. Glaciol.* 37, 127, 368–382. <https://doi.org/10.3189/S0022143000005803>
- Enderlin, E.M., Howat, I.M., Jeong, S., Noh, M.-J., Angelen, J.H. van, Broeke, M.R. van den, 2014. An improved mass budget for the Greenland ice sheet. *Geophys. Res. Lett.* 41, 3, 866–872. <https://doi.org/10.1002/2013GL059010>
- ESA, 2021a. Sentinel-1 SAR User Guide: <https://sentinel.esa.int/web/sentinel/user-guides/sentinel-1-sar/>, last accessed: 13 September 2021.
- ESA, 2021b. Sentinel online: <https://sentinels.copernicus.eu/web/sentinel/missions/>, last accessed: 13 September 2021.
- ESA, 2019. Sentinel-2 MSI Level-2A Algorithm Overview: <https://earth.esa.int/web/sentinel/technical-guides/sentinel-2-msi/level-2a/algorithm/>, last accessed: 19 September 2021.
- ESA, 2016. ESA Sentinel-1 Product Definition: <https://sentinel.esa.int/web/sentinel/user-guides/sentinel-1-sar/document-library>, last accessed: 13 September 2021.
- ESA, 2015. Sentinel-2 User Handbook: [https://sentinel.esa.int/documents/247904/685211/Sentinel-2\\_User\\_Handbook](https://sentinel.esa.int/documents/247904/685211/Sentinel-2_User_Handbook), last accessed: 13 September 2021.
- Fahnestock, M., Bindschadler, R., Kwok, R., Jezek, K., 1993. Greenland Ice Sheet Surface Properties and Ice Dynamics from ERS-1 SAR Imagery. *Science* 262, 5139, 1530–1534. <https://doi.org/10.1126/science.262.5139.1530>

- Fahnestock, M., Scambos, T., Moon, T., Gardner, A., Haran, T., Klinger, M., 2016. Rapid large-area mapping of ice flow using Landsat 8. *Remote Sens. Environ.* 185, 84–94. <https://doi.org/10.1016/j.rse.2015.11.023>
- Fetterer, F., Knowles, K., Meier, W.N., Savoie, M., Windnagel, A.K., 2017. Updated daily. Sea Ice Index, Version 3. [Median sea ice extent March and September 1981-2010]. Boulder, Colorado USA. NSIDC: National Snow and Ice Data Center. doi: <https://doi.org/10.7265/N5K072F8>. [Last accessed 13 March 2021].
- Fettweis, X., Hanna, E., Lang, C., Belleflamme, A., Erpicum, M., Gallée, H., 2013. Brief communication “Important role of the mid-tropospheric atmospheric circulation in the recent surface melt increase over the Greenland ice sheet.” *The Cryosphere* 7, 1, 241–248. <https://doi.org/10.5194/tc-7-241-2013>
- Feyisa, G.L., Meilby, H., Fensholt, R., Proud, S.R., 2014. Automated Water Extraction Index: A new technique for surface water mapping using Landsat imagery. *Remote Sens. Environ.* 140, 23–35. <https://doi.org/10.1016/j.rse.2013.08.029>
- Foley, K.M., Ferrigno, J.G., Swithinbank, C., Williams, R.S.Jr., Orndorff, A.L., 2013. Coastal-Change and Glaciological Map of the Amery Ice Shelf Area, Antarctica: 1961—2004. U.S. Geological Survey Geologic Investigations Series Map I-2600-Q, 1 map sheet, 8-p. text, also available at <https://pubs.usgs.gov/imap/2600/Q>. <https://doi.org/10.1016/j.jag.2019.01.008>
- Fountain, A.G., Walder, J.S., 1998. Water flow through temperate glaciers. *Rev. Geophys.* 36, 3, 299–328. <https://doi.org/10.1029/97RG03579>
- Fraser, A.D., Massom, R.A., Ohshima, K.I., Willmes, S., Kappes, P.J., Cartwright, J., Porter-Smith, R., 2020. High-resolution mapping of circum-Antarctic landfast sea ice distribution, 2000–2018. *Earth Syst. Sci. Data* 12, 4, 2987–2999. <https://doi.org/10.5194/essd-12-2987-2020>
- Fretwell, P., Pritchard, H.D., Vaughan, D.G., Bamber, J.L., Barrand, N.E., Bell, R., Bianchi, C., Bingham, R.G., Blankenship, D.D., Casassa, G., Catania, G., Callens, D., Conway, H., Cook, A.J., Corr, H.F.J., Damaske, D., Damm, V., Ferraccioli, F., Forsberg, R., Fujita, S., Gim, Y., Gogineni, P., Griggs, J.A., Hindmarsh, R.C.A., Holmlund, P., Holt, J.W., Jacobel, R.W., Jenkins, A., Jokat, W., Jordan, T., King, E.C., Kohler, J., Krabill, W., Riger-Kusk, M., Langley, K.A., Leitchenkov, G., Leuschen, C., Luyendyk, B.P., Matsuoka, K., Mouginot, J., Nitsche, F.O., Nogi, Y., Nost, O.A., Popov, S.V., Rignot, E., Ripplin, D.M., Rivera, A., Roberts, J., Ross, N., Siegert, M.J., Smith, A.M., Steinhage, D., Studinger, M., Sun, B., Tinto, B.K., Welch, B.C., Wilson, D., Young, D.A., Xiangbin, C., Zirizzotti, A., 2013. Bedmap2: improved ice bed, surface and thickness datasets for Antarctica. *The Cryosphere* 7, 1, 375–393. <https://doi.org/10.5194/tc-7-375-2013>
- Fricker, H.A., Allison, I., Craven, M., Hyland, G., Ruddell, A., Young, N., Coleman, R., King, M., Krebs, K., Popov, S., 2002. Redefinition of the Amery Ice Shelf, East Antarctica, grounding zone. *J. Geophys. Res.-Solid Earth* 107, B5, ECV 1-1-ECV 1-9. <https://doi.org/10.1029/2001JB000383>
- Fricker, H.A., Coleman, R., Padman, L., Scambos, T.A., Bohlander, J., Brunt, K.M., 2009. Mapping the grounding zone of the Amery Ice Shelf, East Antarctica using InSAR, MODIS and ICESat. *Antarct. Sci.* 21, 5, 515–532. <https://doi.org/10.1017/S095410200999023X>
- Friedl, P., Seehaus, T.C., Wendt, A., Braun, M.H., Höppner, K., 2018. Recent dynamic changes on Fleming Glacier after the disintegration of Wordie Ice Shelf, Antarctic Peninsula. *The Cryosphere* 12, 4, 1347–1365. <https://doi.org/10.5194/tc-12-1347-2018>
- Friedl, P., Weiser, F., Fluhrer, A., Braun, M.H., 2020. Remote sensing of glacier and ice sheet grounding lines: A review. *Earth Sci Rev* 201, 102948. <https://doi.org/10.1016/j.earscirev.2019.102948>
- Fukuda, T., Sugiyama, S., Sawagaki, T., Nakamura, K., 2014. Recent variations in the terminus position, ice velocity and surface elevation of Langhovde Glacier, East Antarctica. *Antarct. Sci.* 26, 6, 636–645. <https://doi.org/10.1017/S0954102014000364>
- Fürst, J.J., Durand, G., Gillet-Chaulet, F., Tavard, L., Rankl, M., Braun, M., Gagliardini, O., 2016. The safety band of Antarctic ice shelves. *Nat. Clim. Change* 6, 479–482. <https://doi.org/10.1038/nclimate2912>

- Gardner, A.S., Moholdt, G., Scambos, T., Fahnestock, M., Ligtenberg, S., Van den Broeke, M., Nilsson, J., 2018. Increased West Antarctic and unchanged East Antarctic ice discharge over the last 7 years. *The Cryosphere* 12, 2, 521–547. <https://doi.org/10.5194/tc-12-521-2018>
- GEBCO Compilation Group, 2020. The GEBCO\_2020 Grid - a continuous terrain model of the global oceans and land. British Oceanographic Data Centre, National Oceanography Centre, NERC, UK. <https://doi.org/10.5285/a29c5465-b138-234d-e053-6c86abc040b9>
- GEUS, 2020. Geological Survey of Denmark and Greenland: <http://frisbee.geus.dk/frisbee/>, last accessed: 13 November 2020.
- Gilbert, E., Kittel, C., 2021. Surface Melt and Runoff on Antarctic Ice Shelves at 1.5°C, 2°C, and 4°C of Future Warming. *Geophys. Res. Lett.* 48, 8. <https://doi.org/10.1029/2020GL091733>
- Glasser, N.F., Gudmundsson, G.H., 2012. Longitudinal surface structures (flowstripes) on Antarctic glaciers. *The Cryosphere* 6, 2, 383–391. <https://doi.org/10.5194/tc-6-383-2012>
- Glasser, N.F., Scambos, T.A., 2008. A structural glaciological analysis of the 2002 Larsen B ice-shelf collapse. *J. Glaciol.* 54, 184, 3–16. <https://doi.org/10.3189/002214308784409017>
- Glasser, N.F., Scambos, T.A., Bohlander, J., Truffer, M., Pettit, E., Davies, B.J., 2011. From ice-shelf tributary to tidewater glacier: continued rapid recession, acceleration and thinning of Röhss Glacier following the 1995 collapse of the Prince Gustav Ice Shelf, Antarctic Peninsula. *J. Glaciol.* 57, 203, 397–406. <https://doi.org/10.3189/002214311796905578>
- Gordon, A.L., 2001. Bottom Water Formation, in: Steele, J.H. (Ed.), *Encyclopedia of Ocean Sciences*. Academic Press, Oxford, pp. 334–340. <https://doi.org/10.1006/rwos.2001.0006>
- Gossart, A., Helsen, S., Lenaerts, J.T.M., Broucke, S.V., Lipzig, N.P.M. van, Souverijns, N., 2019. An Evaluation of Surface Climatology in State-of-the-Art Reanalyses over the Antarctic Ice Sheet. *J. Climate* 32, 20, 6899–6915. <https://doi.org/10.1175/JCLI-D-19-0030.1>
- Grazioli, J., Madeleine, J.-B., Gallée, H., Forbes, R.M., Genthon, C., Krinner, G., Berne, A., 2017. Katabatic winds diminish precipitation contribution to the Antarctic ice mass balance. *PNAS* 114, 41, 10858–10863. <https://doi.org/10.1073/pnas.1707633114>
- Greene, C.A., Blankenship, D.D., Gwyther, D.E., Silvano, A., Van Wijk, E., 2017. Wind causes Totten Ice Shelf melt and acceleration. *Sci. Adv.* 3, 11, e1701681. <https://doi.org/10.1126/sciadv.1701681>
- Greene, C.A., Young, D.A., Gwyther, D.E., Galton-Fenzi, B.K., Blankenship, D.D., 2018. Seasonal dynamics of Totten Ice Shelf controlled by sea ice buttressing. *The Cryosphere* 12, 9, 2869–2882. <https://doi.org/10.5194/tc-12-2869-2018>
- Groh, A., Ewert, H., Rosenau, R., Fagiolini, E., Gruber, C., Floricioiu, D., Abdel Jaber, W., Linow, S., Flechtner, F., Eineder, M., Dierking, W., Dietrich, R., 2014. Mass, Volume and Velocity of the Antarctic Ice Sheet: Present-Day Changes and Error Effects. *Surv. Geophys.* 35, 1481–1505. <https://doi.org/10.1007/s10712-014-9286-y>
- Gudmundsson, G.H., 2003. Transmission of basal variability to a glacier surface. *J. Geophys. Res.-Solid Earth* 108, B5. <https://doi.org/10.1029/2002JB002107>
- Halberstadt, A.R.W., Gleason, C.J., Moussavi, M.S., Pope, A., Trusel, L.D., DeConto, R.M., 2020. Antarctic Supraglacial Lake Identification Using Landsat-8 Image Classification. *Remote Sens.* 12, 8, 1327. <https://doi.org/10.3390/rs12081327>
- Hall, D.K., Riggs, G.A., Salomonson, V.V., 1995. Development of methods for mapping global snow cover using moderate resolution imaging spectroradiometer data. *Remote Sens. Environ.* 54, 2, 127–140. [https://doi.org/10.1016/0034-4257\(95\)00137-P](https://doi.org/10.1016/0034-4257(95)00137-P)
- Hambrey, M.J., Davies, B.J., Glasser, N.F., Holt, T.O., Smellie, J.L., Carrivick, J.L., 2015. Structure and sedimentology of George VI Ice Shelf, Antarctic Peninsula: implications for ice-sheet dynamics and landform development. *J. Geol. Soc.* 172, 5, 599–613. <https://doi.org/10.1144/jgs2014-134>
- Hambrey, M.J., Dowdeswell, J.A., 1994. Flow regime of the Lambert Glacier-Amery Ice Shelf system, Antarctica: structural evidence from Landsat imagery. *Ann. Glaciol.* 20, 401–406. <https://doi.org/10.3189/1994AoG20-1-401-406>
- Han, H., Im, J., Kim, H.-C., 2016. Variations in ice velocities of Pine Island Glacier Ice Shelf evaluated using multispectral image matching of Landsat time series data. *Remote Sens. Environ.* 186, 358–371. <https://doi.org/10.1016/j.rse.2016.09.001>



- Hanna, E., Navarro, F.J., Pattyn, F., Domingues, C.M., Fettweis, X., Ivins, E.R., Nicholls, R.J., Ritz, C., Smith, B., Tulaczyk, S., Whitehouse, P.L., Zwally, H.J., 2013. Ice-sheet mass balance and climate change. *Nature* 498, 51–59. <https://doi.org/10.1038/nature12238>
- Hay, W.W., 2016. *Experimenting on a Small Planet: A History of Scientific Discoveries, a Future of Climate Change and Global Warming*. Springer International Publishing, Switzerland.
- He, H., Yang, D., Wang, Shicheng, Wang, Shuyang, Li, Y., 2019. Road Extraction by Using Atrous Spatial Pyramid Pooling Integrated Encoder-Decoder Network and Structural Similarity Loss. *Remote Sens.* 11, 9, 1015. <https://doi.org/10.3390/rs11091015>
- He, K., Zhang, X., Ren, S., Sun, J., 2016. Deep Residual Learning for Image Recognition, in: 2016 IEEE Conference on Computer Vision and Pattern Recognition (CVPR). Presented at the 2016 IEEE Conference on Computer Vision and Pattern Recognition (CVPR), pp. 770–778. <https://doi.org/10.1109/CVPR.2016.90>
- Hersbach, H., Bell, B., Berrisford, P., Biavati, G., Horányi, A., Muñoz Sabater, J., Nicolas, J., Peubey, C., Radu, R., Rozum, I., Schepers, D., Simmons, A., Soci, C., Dee, D., Thépaut, J.-N., 2019. ERA5 monthly averaged data on single levels from 1979 to present. Copernicus Climate Change Service (C3S) Climate Data Store (CDS). [Last accessed 16 March 2021]. <https://doi.org/10.24381/cds.f17050d7>
- Hock, R., De Woul, M., Radić, V., Dyrgerov, M., 2009. Mountain glaciers and ice caps around Antarctica make a large sea-level rise contribution. *Geophys. Res. Lett.* 36, 7. <https://doi.org/10.1029/2008GL037020>
- Hoeser, T., Bachofer, F., Kuenzer, C., 2020. Object Detection and Image Segmentation with Deep Learning on Earth Observation Data: A Review—Part II: Applications. *Remote Sens.* 12, 18, 3053. <https://doi.org/10.3390/rs12183053>
- Hoeser, T., Kuenzer, C., 2020. Object Detection and Image Segmentation with Deep Learning on Earth Observation Data: A Review-Part I: Evolution and Recent Trends. *Remote Sens.* 12, 10, 1667. <https://doi.org/10.3390/rs12101667>
- Hoffman, M.J., Catania, G.A., Neumann, T.A., Andrews, L.C., Rumrill, J.A., 2011. Links between acceleration, melting, and supraglacial lake drainage of the western Greenland Ice Sheet. *J. Geophys. Res.-Earth Surface* 116, F4. <https://doi.org/10.1029/2010JF001934>
- Hogg, A.E., Shepherd, A., Cornford, S.L., Briggs, K.H., Gourmelen, N., Graham, J.A., Joughin, I., Mouginot, J., Nagler, T., Payne, A.J., Rignot, E., Wuite, J., 2017. Increased ice flow in Western Palmer Land linked to ocean melting. *Geophys. Res. Lett.* 44, 9, 4159–4167. <https://doi.org/10.1002/2016GL072110>
- Holland, D.M., Nicholls, K.W., Basinski, A., 2020. The Southern Ocean and its interaction with the Antarctic Ice Sheet. *Science* 367, 6484, 1326–1330. <https://doi.org/10.1126/science.aaz5491>
- Holland, D.M., Thomas, R.H., Young, B. de, Ribergaard, M.H., Lyberth, B., 2008. Acceleration of Jakobshavn Isbræ triggered by warm subsurface ocean waters. *Nat. Geosci.* 1, 659–664. <https://doi.org/10.1038/ngeo316>
- Holland, P.R., 2014. The seasonality of Antarctic sea ice trends. *Geophys. Res. Lett.* 41, 12, 4230–4237. <https://doi.org/10.1002/2014GL060172>
- Holland, P.R., Corr, H.F.J., Pritchard, H.D., Vaughan, D.G., Arthern, R.J., Jenkins, A., Tedesco, M., 2011. The air content of Larsen Ice Shelf. *Geophys. Res. Lett.* 38, 10. <https://doi.org/10.1029/2011GL047245>
- Holland, P.R., Kwok, R., 2012. Wind-driven trends in Antarctic sea-ice drift. *Nat. Geosci.* 5, 872–875. <https://doi.org/10.1038/ngeo1627>
- Holt, T., Glasser, N., Quincey, D., 2013. The structural glaciology of southwest Antarctic Peninsula Ice Shelves (ca. 2010). *J. Maps* 9, 4, 523–531. <https://doi.org/10.1080/17445647.2013.822836>
- Horwath, M., Dietrich, R., Baessler, M., Nixdorf, U., Steinhage, D., Fritzsche, D., Damm, V., Reitmayr, G., 2006. Nivlisen, an Antarctic ice shelf in Dronning Maud Land: geodetic–glaciological results from a combined analysis of ice thickness, ice surface height and ice-flow observations. *J. Glaciol.* 52, 176, 17–30. <https://doi.org/10.3189/172756506781828953>
- Howat, I.M., Peña, S. de la, Angelen, J.H. van, Lenaerts, J.T.M., Broeke, M.R. van den, 2013. Brief Communication: “Expansion of meltwater lakes on the Greenland Ice Sheet.” *The Cryosphere* 7, 1, 201–204. <https://doi.org/10.5194/tc-7-201-2013>

- Howat, I.M., Porter, C., Smith, B.E., Noh, M.-J., Morin, P., 2019. The Reference Elevation Model of Antarctica. *The Cryosphere* 13, 2, 665–674. <https://doi.org/10.5194/tc-13-665-2019>
- Hubbard, B., Luckman, A., Ashmore, D.W., Bevan, S., Kulesa, B., Munneke, P.K., Philippe, M., Jansen, D., Booth, A., Sevestre, H., Tison, J.-L., O’Leary, M., Rutt, I., 2016. Massive subsurface ice formed by refreezing of ice-shelf melt ponds. *Nat. Commun.* 7, 11897, 1–6. <https://doi.org/10.1038/ncomms11897>
- Huete, A.R., 1988. A soil-adjusted vegetation index (SAVI). *Remote Sens. Environ.* 25, 3, 295–309. [https://doi.org/10.1016/0034-4257\(88\)90106-X](https://doi.org/10.1016/0034-4257(88)90106-X)
- Hughes, T.J., 1981. The Weak Underbelly of the West Antarctic Ice-Sheet. *J. Glaciol.* 27, 97, 518–525. <https://doi.org/10.3189/S002214300001159X>
- Hui, F., Ci, T., Cheng, X., Scambo, T.A., Liu, Y., Zhang, Y., Chi, Z., Huang, H., Wang, X., Wang, F., Zhao, C., Jin, Z., Wang, K., 2014. Mapping blue-ice areas in Antarctica using ETM+ and MODIS data. *Ann. Glaciol.* 55, 66, 129–137. <https://doi.org/10.3189/2014AoG66A069>
- Hulbe, C.L., Scambos, T.A., Klinger, M., Fahnestock, M.A., 2016. Flow variability and ongoing margin shifts on Bindschadler and MacAyeal Ice Streams, West Antarctica. *J. Geophys. Res.-Earth Surface* 121, 2, 283–293. <https://doi.org/10.1002/2015JF003670>
- Hulbe, C.L., Scambos, T.A., Lee, C.-K., Bohlander, J., Haran, T., 2013. Recent changes in the flow of the Ross Ice Shelf, West Antarctica. *Earth Planet. Sci. Lett.* 376, 54–62. <https://doi.org/10.1016/j.epsl.2013.06.013>
- Ignéczi, Á., Sole, A.J., Livingstone, S.J., Ng, F.S.L., Yang, K., 2018. Greenland Ice Sheet Surface Topography and Drainage Structure Controlled by the Transfer of Basal Variability. *Front. Earth Sci.* 6, 101. <https://doi.org/10.3389/feart.2018.00101>
- IMBIE, 2016. Antarctica and Greenland Ice Sheet Drainage Basins: <http://imbie.org/imbie-2016/drainage-basins/>, last accessed: 15 June 2021.
- Immitzer, M., Atzberger, C., Koukal, T., 2012. Tree Species Classification with Random Forest Using Very High Spatial Resolution 8-Band WorldView-2 Satellite Data. *Remote Sens.* 4, 9, 2661–2693. <https://doi.org/10.3390/rs4092661>
- IPCC, 2019a. Technical Summary [H.-O. Pörtner, D.C. Roberts, V. Masson-Delmotte, P. Zhai, E. Poloczanska, K. Mintenbeck, M. Tignor, A. Alegría, M. Nicolai, A. Okem, J. Petzold, B. Rama, N.M. Weyer (eds.)]. In: IPCC Special Report on the Ocean and Cryosphere in a Changing Climate [H.-O. Pörtner, D.C. Roberts, V. Masson-Delmotte, P. Zhai, M. Tignor, E. Poloczanska, K. Mintenbeck, A. Alegría, M. Nicolai, A. Okem, J. Petzold, B. Rama, N.M. Weyer (eds.)]. In press.
- IPCC, 2019b. Summary for Policymakers. In: IPCC Special Report on the Ocean and Cryosphere in a Changing Climate [H.-O. Pörtner, D.C. Roberts, V. Masson-Delmotte, P. Zhai, M. Tignor, E. Poloczanska, K. Mintenbeck, A. Alegría, M. Nicolai, A. Okem, J. Petzold, B. Rama, N.M. Weyer (eds.)]. In press.
- Jacobs, S.S., Jenkins, A., Giulivi, C.F., Dutrieux, P., 2011. Stronger ocean circulation and increased melting under Pine Island Glacier ice shelf. *Nat. Geosci.* 4, 519–523. <https://doi.org/10.1038/ngeo1188>
- Jawak, S.D., Luis, A.J., 2014. A semiautomatic extraction of Antarctic lake features using Worldview-2 imagery. *Photogramm Eng Remote Sensing* 10, 939–952. <https://doi.org/10.14358/PERS.80.10.939>
- Jenkins, A., Dutrieux, P., Jacobs, S.S., McPhail, S.D., Perrett, J.R., Webb, A.T., White, D., 2010. Observations beneath Pine Island Glacier in West Antarctica and implications for its retreat. *Nat. Geosci.* 3, 468–472. <https://doi.org/10.1038/ngeo890>
- Jenkins, A., Jacobs, S., 2008. Circulation and melting beneath George VI Ice Shelf, Antarctica. *J. Geophys. Res.-Oceans* 113, C4. <https://doi.org/10.1029/2007JC004449>
- Jenkins, A., Shoosmith, D., Dutrieux, P., Jacobs, S., Kim, T.W., Lee, S.H., Ha, H.K., Stammerjohn, S., 2018. West Antarctic Ice Sheet retreat in the Amundsen Sea driven by decadal oceanic variability. *Nat. Geosci.* 11, 733–738. <https://doi.org/10.1038/s41561-018-0207-4>
- Ji, S., Wei, S., Lu, M., 2019. Fully Convolutional Networks for Multisource Building Extraction From an Open Aerial and Satellite Imagery Data Set. *IEEE Trans. Geosci. Remote Sens.* 57, 1, 574–586. <https://doi.org/10.1109/TGRS.2018.2858817>

- Jiang, H., Yang, Y., Bai, Y., Wang, H., 2020. Evaluation of the Total, Direct, and Diffuse Solar Radiations From the ERA5 Reanalysis Data in China. *IEEE Geosci. Remote Sens. Lett.* 17, 1, 47–51. <https://doi.org/10.1109/LGRS.2019.2916410>
- Johansson, A.M., Brown, I.A., 2013. Adaptive Classification of Supra-Glacial Lakes on the West Greenland Ice Sheet. *IEEE J Sel Top Appl Earth Obs Remote Sens* 6, 4, 1998–2007. <https://doi.org/10.1109/JSTARS.2012.2233722>
- Jolly, K., 2018. *Machine Learning with scikit-learn Quick Start Guide*. Packt Publishing Ltd., Birmingham, UK.
- Jones, J.M., Gille, S.T., Goosse, H., Abram, N.J., Canziani, P.O., Charman, D.J., Clem, K.R., Crosta, X., Lavergne, C. de, Eisenman, I., England, M.H., Fogt, R.L., Frankcombe, L.M., Marshall, G.J., Masson-Delmotte, V., Morrison, A.K., Orsi, A.J., Raphael, M.N., Renwick, J.A., Schneider, D.P., Simpkins, G.R., Steig, E.J., Stenni, B., Swingedouw, D., Vance, T.R., 2016. Assessing recent trends in high-latitude Southern Hemisphere surface climate. *Nature Clim Change* 6, 917–926. <https://doi.org/10.1038/nclimate3103>
- Joughin, I., Bindschadler, R.A., King, M.A., Voigt, D., Alley, R.B., Anandakrishnan, S., Horgan, H., Peters, L., Winberry, P., Das, S.B., Catania, G., 2005. Continued deceleration of Whillans Ice Stream, West Antarctica. *Geophys. Res. Lett.* 32, 22. <https://doi.org/10.1029/2005GL024319>
- Joughin, I., Rignot, E., Rosanova, C.E., Lucchitta, C.K., Bohlander, J., 2003. Timing of Recent Accelerations of Pine Island Glacier, Antarctica. *Geophys. Res. Lett.* 30, 13. <https://doi.org/10.1029/2003GL017609>
- Joughin, I., Smith, B.E., Abdalati, W., 2010. Glaciological advances made with interferometric synthetic aperture radar. *J. Glaciol.* 56, 200, 1026–1042. <https://doi.org/10.3189/002214311796406158>
- Joughin, I., Smith, B.E., Medley, B., 2014. Marine Ice Sheet Collapse Potentially Under Way for the Thwaites Glacier Basin, West Antarctica. *Science* 344, 6185, 735–738. <https://doi.org/10.1126/science.1249055>
- Joughin, I., Tulaczyk, S., Bamber, J.L., Blankenship, D., Holt, J.W., Scambos, T., Vaughan, D.G., 2009. Basal conditions for Pine Island and Thwaites Glaciers, West Antarctica, determined using satellite and airborne data. *J. Glaciol.* 55, 190, 245–257. <https://doi.org/10.3189/002214309788608705>
- Joughin, I., Tulaczyk, S., Bindschadler, R., Price, S.F., 2002. Changes in west Antarctic ice stream velocities: Observation and analysis. *J. Geophys. Res.-Solid Earth* 107, B11, EPM 3-1-EPM 3-22. <https://doi.org/10.1029/2001JB001029>
- Kang, J., Cheng, X., Hui, F., Ci, T., 2018. An Accurate and Automated Method for Identifying and Mapping Exposed Rock Outcrop in Antarctica Using Landsat 8 Images. *IEEE J Sel Top Appl Earth Obs Remote Sens* 11, 1, 57–67. <https://doi.org/10.1109/JSTARS.2017.2755502>
- Kauth, R.J., Thomas, G.S., 1976. The tasselled cap - A graphic description of the spectral-temporal development of agricultural crops as seen by Landsat, in: *Proceedings of the Symposium on Machine Processing of Remotely Sensed Data*. West Lafayette, IN, USA, pp. 41–51.
- Kennicutt, M.C., Chown, S.L., Cassano, J.J., Liggett, D., Peck, L.S., Massom, R., Rintoul, S.R., Storey, J., Vaughan, D.G., Wilson, T.J., Allison, I., Ayton, J., Badhe, R., Baeseman, J., Barrett, P.J., Bell, R.E., Bertler, N., Bo, S., Brandt, A., Bromwich, D., Cary, S.C., Clark, M.S., Convey, P., Costa, E.S., Cowan, D., Deconto, R., Dunbar, R., Elfring, C., Escutia, C., Francis, J., Fricker, H.A., Fukuchi, M., Gilbert, N., Gutt, J., Havermans, C., Hik, D., Hosie, G., Jones, C., Kim, Y.D., Maho, Y.L., Lee, S.H., Leppe, M., Leitchenkov, G., Li, X., Lipenkov, V., Lochte, K., López-Martínez, J., Lüdecke, C., Lyons, W., Marensi, S., Miller, H., Morozova, P., Naish, T., Nayak, S., Ravindra, R., Retamales, J., Ricci, C.A., Rogan-Finnemore, M., Ropert-Coudert, Y., Samah, A.A., Sanson, L., Scambos, T., Schloss, I.R., Shiraiishi, K., Siegert, M.J., Simões, J.C., Storey, B., Sparrow, M.D., Wall, D.H., Walsh, J.C., Wilson, G., Winther, J.G., Xavier, J.C., Yang, H., Sutherland, W.J., 2015. A roadmap for Antarctic and Southern Ocean science for the next two decades and beyond. *Antarct. Sci.* 27, 1, 3–18. <https://doi.org/10.1017/S0954102014000674>
- Keshri, A.K., Shukla, A., Gupta, R.P., 2009. ASTER ratio indices for supraglacial terrain mapping. *Int. J. Remote Sens.* 30, 2, 519–524. <https://doi.org/10.1080/01431160802385459>

- Khan, S.A., Aschwanden, A., Bjørk, A.A., Wahr, J., Kjeldsen, K.K., Kjær, K.H., 2015. Greenland ice sheet mass balance: a review. *Rep. Prog. Phys.* 78, 4. <https://doi.org/10.1088/0034-4885/78/4/046801>
- Khazendar, A., Rignot, E., Larour, E., 2009. Roles of marine ice, rheology, and fracture in the flow and stability of the Brunt/Stancomb-Wills Ice Shelf. *J. Geophys. Res.-Earth Surface* 114, F4. <https://doi.org/10.1029/2008JF001124>
- Kimura, S., Jenkins, A., Regan, H., Holland, P.R., Assmann, K.M., Whitt, D.B., Wessem, M.V., Berg, W.J. van de, Reijmer, C.H., Dutrieux, P., 2017. Oceanographic Controls on the Variability of Ice-Shelf Basal Melting and Circulation of Glacial Meltwater in the Amundsen Sea Embayment, Antarctica. *J. Geophys. Res.-Oceans* 122, 10, 131–10,155. <https://doi.org/10.1002/2017JC012926>
- Kingslake, Ely, J.C., Das, I., Bell, R.E., 2017. Widespread movement of meltwater onto and across Antarctic ice shelves. *Nature* 544, 349–352. <https://doi.org/10.1038/nature22049>
- Kingslake, J., Ng, F., Sole, A., 2015. Modelling channelized surface drainage of supraglacial lakes. *J. Glaciol.* 61, 225, 185–199. <https://doi.org/10.3189/2015JoG14J158>
- Konrad, H., Shepherd, A., Gilbert, L., Hogg, A.E., McMillan, M., Muir, A., Slater, T., 2018. Net retreat of Antarctic glacier grounding lines. *Nat. Geosci.* 11, 258–262. <https://doi.org/10.1038/s41561-018-0082-z>
- Krinner, G., Magand, O., Simmonds, I., Genthon, C., Dufresne, J.-L., 2007. Simulated Antarctic precipitation and surface mass balance at the end of the twentieth and twenty-first centuries. *Clim. Dyn.* 28, 215–230. <https://doi.org/10.1007/s00382-006-0177-x>
- Krizhevsky, A., Sutskever, I., Hinton, G.E., 2012. ImageNet classification with deep convolutional neural networks. *Communications of the ACM* 60, 6, 84–90. <https://doi.org/10.1145/3065386>
- Kuipers Munneke, P., Ligtenberg, S.R.M., Broeke, M.R.V.D., Vaughan, D.G., 2014. Firn air depletion as a precursor of Antarctic ice-shelf collapse. *J. Glaciol.* 60, 220, 205–214. <https://doi.org/10.3189/2014JoG13J183>
- Kuipers Munneke, P., Luckman, A.J., Bevan, S.L., Smeets, C.J.P.P., Gilbert, E., Broeke, M.R. van den, Wang, W., Zender, C., Hubbard, B., Ashmore, D., Orr, A., King, J.C., Kulesa, B., 2018. Intense Winter Surface Melt on an Antarctic Ice Shelf. *Geophys. Res. Lett.* 45, 15, 7615–7623. <https://doi.org/10.1029/2018GL077899>
- Kwok, R., Comiso, J.C., 2002. Spatial patterns of variability in Antarctic surface temperature: Connections to the Southern Hemisphere Annular Mode and the Southern Oscillation. *Geophys. Res. Lett.* 29, 14, 50-1-50-4. <https://doi.org/10.1029/2002GL015415>
- Kwok, R., Rignot, E., Holt, B., Onstott, R., 1992. Identification of sea ice types in spaceborne synthetic aperture radar data. *J. Geophys. Res.* 97, C2, 2391–2402. <https://doi.org/10.1029/91JC02652>
- LaBarbera, C.H., MacAyeal, D.R., 2011. Traveling supraglacial lakes on George VI Ice Shelf, Antarctica. *Geophys. Res. Lett.* 38, 24. <https://doi.org/10.1029/2011GL049970>
- Laffin, M.K., Zender, C.S., Singh, S., Wessem, J.M.V., Smeets, C.J.P.P., Reijmer, C.H., 2021. Climatology and Evolution of the Antarctic Peninsula Föhn Wind-Induced Melt Regime From 1979–2018. *Geophys. Res. Lett.* 126, 4. <https://doi.org/10.1029/2020JD033682>
- Lai, C.-Y., Kingslake, J., Wearing, M.G., Chen, P.-H.C., Gentine, P., Li, H., Spergel, J.J., Wessem, J.M. van, 2020. Vulnerability of Antarctica's ice shelves to meltwater-driven fracture. *Nature* 584, 574–578. <https://doi.org/10.1038/s41586-020-2627-8>
- Lampkin, D.J., VanderBerg, J., 2011. A preliminary investigation of the influence of basal and surface topography on supraglacial lake distribution near Jakobshavn Isbrae, western Greenland. *Hydrol Process* 25, 21, 3347–3355. <https://doi.org/10.1002/hyp.8170>
- Landis, J.R., Koch, G.G., 1977. The Measurement of Observer Agreement for Categorical Data. *Biometrics* 33, 1, 159-174. <https://doi.org/10.2307/2529310>
- Langley, E.S., Leeson, A.A., Stokes, C.R., Jamieson, S.S.R., 2016. Seasonal evolution of supraglacial lakes on an East Antarctic outlet glacier. *Geophys. Res. Lett.* 43, 16, 8563–8571. <https://doi.org/10.1002/2016GL069511>

- Larsen, J.N., Anisimov, O.A., Constable, A., Hollowed, A.B., Maynard, N., Prestrud, P., Prowse, T.D., Stone, J.M.R., 2014. Polar regions. In: *Climate Change 2014: Impacts, Adaptation, and Vulnerability. Part B: Regional Aspects. Contribution of Working Group II to the Fifth Assessment Report of the Intergovernmental Panel on Climate Change* [Barros, V.R., C.B. Field, D.J. Dokken, M.D. Mastrandrea, K.J. Mach, T.E. Bilir, M. Chatterjee, K.L. Ebi, Y.O. Estrada, R.C. Genova, B. Girma, E.S. Kissel, A.N. Levy, S. MacCracken, P.R. Mastrandrea, and L.L. White (eds.)]. Cambridge University Press, Cambridge, United Kingdom and New York, NY, USA, pp. 1567–1612.
- Law, R., Arnold, N., Benedek, C., Tedesco, M., Banwell, A., Willis, I., 2020. Over-winter persistence of supraglacial lakes on the Greenland Ice Sheet: results and insights from a new model. *J. Glaciol.* 66, 257, 362–372. <https://doi.org/10.1017/jog.2020.7>
- Leeson, A.A., Forster, E., Rice, A., Gourmelen, N., Van Wessem, J.M., 2020. Evolution of supraglacial lakes on the Larsen B ice shelf in the decades before it collapsed. *Geophys. Res. Lett.* 47, 4. <https://doi.org/10.1029/2019GL085591>
- Leeson, A.A., Shepherd, A., Sundal, A.V., Johansson, A.M., Selmes, N., Briggs, K., Hogg, A.E., Fettweis, X., 2013. A comparison of supraglacial lake observations derived from MODIS imagery at the western margin of the Greenland ice sheet. *J. Glaciol.* 59, 218, 1179–1188. <https://doi.org/10.3189/2013JoG13J064>
- Lenaerts, J.T.M., Lhermitte, S., Drews, R., Ligtenberg, S.R.M., Berger, S., Helm, V., Smeets, C.J.P.P., Broeke, M.R. van den, van de Berg, W.J., van Meijgaard, E., Eijkelboom, M., Eisen, O., Pattyn, F., 2017. Meltwater produced by wind–albedo interaction stored in an East Antarctic ice shelf. *Nat. Clim. Change* 7, 58–62. <https://doi.org/10.1038/nclimate3180>
- Lenaerts, J.T.M., Ligtenberg, S.R.M., Medley, B., Berg, W.J.V. de, Konrad, H., Nicolas, J.P., Wessem, J.M.V., Trusel, L.D., Mulvaney, R., Tuckwell, R.J., Hogg, A.E., Thomas, E.R., 2018. Climate and surface mass balance of coastal West Antarctica resolved by regional climate modelling. *Ann. Glaciol.* 59, 76pt1, 29–41. <https://doi.org/10.1017/aog.2017.42>
- Lenaerts, J.T.M., Vizcaino, M., Fyke, J., van Kampenhout, L., van den Broeke, M.R., 2016. Present-day and future Antarctic ice sheet climate and surface mass balance in the Community Earth System Model. *Clim. Dyn.* 47, 1367–1381. <https://doi.org/10.1007/s00382-015-2907-4>
- Leppäranta, M., Järvinen, O., Mattila, O.-P., 2013. Structure and life cycle of supraglacial lakes in Dronning Maud Land. *Antarct. Sci.* 25, 3, 457–467. <https://doi.org/10.1017/S0954102012001009>
- Leppäranta, M., Lindgren, E., Arvola, L., 2016. Heat balance of supraglacial lakes in the western Dronning Maud Land. *Ann. Glaciol.* 57, 72, 39–46. <https://doi.org/10.1017/aog.2016.12>
- Lhermitte, S., Sun, S., Shuman, C., Wouters, B., Pattyn, F., Wuite, J., Berthier, E., Nagler, T., 2020. Damage accelerates ice shelf instability and mass loss in Amundsen Sea Embayment. *PNAS* 117, 40, 24,735–24,741. <https://doi.org/10.1073/pnas.1912890117>
- Li, H., Xu, L., Shen, H., Zhang, L., 2016. A general variational framework considering cast shadows for the topographic correction of remote sensing imagery. *ISPRS J. Photogramm. Remote Sens.* 117, 161–171. <https://doi.org/10.1016/j.isprsjprs.2016.03.021>
- Liang, Q., Zhou, C., Howat, I.M., Jeong, S., Liu, R., Chen, Y., 2019. Ice flow variations at Polar Record Glacier, East Antarctica. *J. Glaciol.* 65, 250, 279–287. <https://doi.org/10.1017/jog.2019.6>
- Liang, Y.-L., Colgan, W., Lv, Q., Steffen, K., Abdalati, W., Stroeve, J., Gallaher, D., Bayou, N., 2012. A decadal investigation of supraglacial lakes in West Greenland using a fully automatic detection and tracking algorithm. *Remote Sens. Environ.* 123, 127–138. <https://doi.org/10.1016/j.rse.2012.03.020>
- Lilien, D.A., Joughin, I., Smith, B., Shean, D.E., 2018. Changes in flow of Crosson and Dotson ice shelves, West Antarctica, in response to elevated melt. *The Cryosphere* 12, 4, 1415–1431. <https://doi.org/10.5194/tc-12-1415-2018>
- Liston, G.E., Winther, J.-G., Bruland, O., Elvehøy, H., Sand, K., 1999. Below-surface ice melt on the coastal Antarctic ice sheet. *J. Glaciol.* 45, 150, 273–285. <https://doi.org/10.3189/S0022143000001775>
- Liu, H., Jezek, K., 2004. A Complete High-Resolution Coastline of Antarctica Extracted from Orthorectified Radarsat SAR Imagery. *Photogramm Eng Remote Sensing* 5, 605–616. <https://doi.org/10.14358/PERS.70.5.605>

- Liu, H., Wang, L., Jezek, K.C., 2006. Automated delineation of dry and melt snow zones in Antarctica using active and passive microwave observations from space. *IEEE Trans. Geosci. Remote Sens.* 44, 8, 2152–2163. <https://doi.org/10.1109/TGRS.2006.872132>
- Liu, Y., Gross, L., Li, Z., Li, X., Fan, X., Qi, W., 2019. Automatic Building Extraction on High-Resolution Remote Sensing Imagery Using Deep Convolutional Encoder-Decoder With Spatial Pyramid Pooling. *IEEE Access* 7, 128774–128786. <https://doi.org/10.1109/ACCESS.2019.2940527>
- Louis, J., Debaecker, V., Pflug, B., Main-Knorn, M., Bieniarz, J., Mueller-Wilm, U., Cadau, E., Gascon, F., 2016. Sentinel-2 Sen2Cor: L2A Processor For Users, in: *Proc. Living Planet Symposium 2016*. Prague, Czech Republic.
- Lu, X., Zhong, Y., Zheng, Z., Liu, Y., Zhao, J., Ma, A., Yang, J., 2019. Multi-Scale and Multi-Task Deep Learning Framework for Automatic Road Extraction. *IEEE Trans. Geosci. Remote Sens.* 57, 11, 9362–9377. <https://doi.org/10.1109/TGRS.2019.2926397>
- Lucchitta, B.K., Mullins, K.F., Smith, C.E., Ferrigno, J.G., 1994. Velocities of the Smith Glacier ice tongue and Dotson Ice Shelf, Walgreen Coast, Marie Byrd Land, West Antarctica. *Ann. Glaciol.* 20, 101–109. <https://doi.org/10.3189/172756494794587573>
- Lucchitta, B.K., Rosanova, C.E., 1998. Retreat of northern margins of George VI and Wilkins Ice Shelves, Antarctic Peninsula. *Ann. Glaciol.* 27, 41–46. <https://doi.org/10.3189/1998AoG27-1-41-46>
- Luckman, A., Elvidge, A., Jansen, D., Kulesa, B., Munneke, P.K., King, J., Barrand, N.E., 2014. Surface melt and ponding on Larsen C Ice Shelf and the impact of föhn winds. *Antarct. Sci.* 26, 6, 625–635. <https://doi.org/10.1017/S0954102014000339>
- Luckman, A., Jansen, D., Kulesa, B., King, E.C., Sammonds, P., Benn, D.I., 2012. Basal crevasses in Larsen C Ice Shelf and implications for their global abundance. *The Cryosphere* 6, 1, 113–123. <https://doi.org/10.5194/tc-6-113-2012>
- Ludescher, J., Yuan, N., Bunde, A., 2019. Detecting the statistical significance of the trends in the Antarctic sea ice extent: an indication for a turning point. *Clim. Dyn.* 53, 237–244. <https://doi.org/10.1007/s00382-018-4579-3>
- Lüthje, M., Pedersen, L.T., Reeh, N., Greuell, W., 2006. Modelling the evolution of supraglacial lakes on the West Greenland ice-sheet margin. *J. Glaciol.* 52, 179, 608–618. <https://doi.org/10.3189/172756506781828386>
- MacAyeal, D.R., Sergienko, O.V., 2013. The flexural dynamics of melting ice shelves. *Ann. Glaciol.* 54, 63, 1–10. <https://doi.org/10.3189/2013AoG63A256>
- Macdonald, G.J., Banwell, A.F., MacAyeal, D.R., 2018. Seasonal evolution of supraglacial lakes on a floating ice tongue, Petermann Glacier, Greenland. *Ann. Glaciol.* 59, 76pt1, 56–65. <https://doi.org/10.1017/aog.2018.9>
- MacDonell, S., Valois, R., Fernandoy, F., Villar, P., Casassa, G., Hammann, A., Marambio, M., 2020. Exploring firn aquifers on the Muller Ice Shelf, Antarctica. Presented at the EGU General Assembly, Vienna, Austria, p. 11695. <https://doi.org/10.5194/egusphere-egu2020-11695>
- Malinka, A., Zege, E., Istomina, L., Heygster, G., Spreen, G., Perovich, D., Polashenski, C., 2018. Reflective properties of melt ponds on sea ice. *The Cryosphere* 12, 6, 1921–1937. <https://doi.org/10.5194/tc-12-1921-2018>
- Marsh, O.J., Price, D., Courville, Z.R., Floricioiu, D., 2021. Crevasse and rift detection in Antarctica from TerraSAR-X satellite imagery. *Cold Reg Sci Technol* 187, 103284. <https://doi.org/10.1016/j.coldregions.2021.103284>
- Marshall, G.J., 2018. The Climate Data Guide: Marshall Southern Annular Mode (SAM) Index (Station-based): <https://climatedataguide.ucar.edu/climate-data/marshall-southern-annular-mode-sam-index-station-based>, last accessed: 20 June 2021.
- Marshall, G.J., 2003. Trends in the Southern Annular Mode from Observations and Reanalyses. *J. Climate* 16, 24, 4134–4143. [https://doi.org/10.1175/1520-0442\(2003\)016<4134:TITSAM>2.0.CO;2](https://doi.org/10.1175/1520-0442(2003)016<4134:TITSAM>2.0.CO;2)
- Marshall, G.J., Orr, A., Lipzig, N.P.M. van, King, J.C., 2006. The Impact of a Changing Southern Hemisphere Annular Mode on Antarctic Peninsula Summer Temperatures. *J. Climate* 19, 20, 5388–5404. <https://doi.org/10.1175/JCLI3844.1>

- Marshall, G.J., Stott, P.A., Turner, J., Connolley, W.M., King, J.C., Lachlan-Cope, T.A., 2004. Causes of exceptional atmospheric circulation changes in the Southern Hemisphere. *Geophys. Res. Lett.* 31, 14. <https://doi.org/10.1029/2004GL019952>
- Marshall, G.J., Thompson, D.W.J., Broeke, M.R. van den, 2017. The Signature of Southern Hemisphere Atmospheric Circulation Patterns in Antarctic Precipitation. *Geophys. Res. Lett.* 44, 22, 11,580–11,589. <https://doi.org/10.1002/2017GL075998>
- Martín-Español, A., Bamber, J.L., Zammit-Mangion, A., 2017. Constraining the mass balance of East Antarctica. *Geophys. Res. Lett.* 44, 9, 4,168–4,175. <https://doi.org/10.1002/2017GL072937>
- Martín-Español, A., Zammit-Mangion, A., Clarke, P.J., Flament, T., Helm, V., King, M.A., Luthcke, S.B., Petrie, E., Rémy, F., Schön, N., Wouters, B., Bamber, J.L., 2016. Spatial and temporal Antarctic Ice Sheet mass trends, glacio-isostatic adjustment, and surface processes from a joint inversion of satellite altimeter, gravity, and GPS data. *J. Geophys. Res.-Earth Surface* 121, 2, 182–200. <https://doi.org/10.1002/2015JF003550>
- Mätzler, C., 1987. Applications of the interaction of microwaves with the natural snow cover. *Remote Sensing Reviews* 2, 2, 259–387. <https://doi.org/10.1080/02757258709532086>
- Mayewski, P.A., Meredith, M.P., Summerhayes, C.P., Turner, J., Worby, A., Barrett, P.J., Casassa, G., Bertler, N. a. N., Bracegirdle, T., Garabato, A.C.N., Bromwich, D., Campbell, H., Hamilton, G.S., Lyons, W.B., Maasch, K.A., Aoki, S., Xiao, C., Ommen, T. van, 2009. State of the Antarctic and Southern Ocean climate system. *Rev. Geophys.* 47, 1. <https://doi.org/10.1029/2007RG000231>
- McFeeters, S.K., 1996. The use of the Normalized Difference Water Index (NDWI) in the delineation of open water features. *Int. J. Remote Sens.* 17, 7, 1425–1432. <https://doi.org/10.1080/01431169608948714>
- McGrath, D., Steffen, K., Rajaram, H., Scambos, T., Abdalati, W., Rignot, E., 2012. Basal crevasses on the Larsen C Ice Shelf, Antarctica: Implications for meltwater ponding and hydrofracture. *Geophys. Res. Lett.* 39, 16. <https://doi.org/10.1029/2012GL052413>
- Medley, B., Thomas, E.R., 2019. Increased snowfall over the Antarctic Ice Sheet mitigated twentieth-century sea-level rise. *Nat. Clim. Change* 9, 34–39. <https://doi.org/10.1038/s41558-018-0356-x>
- Mellor, M., McKinnon, G., 1960. The Amery Ice Shelf and its hinterland. *Polar Rec.* 10, 64, 30–34. <https://doi.org/10.1017/S0032247400050579>
- Meredith, M., Sommerkorn, M., Cassotta, S., Derksen, C., Ekaykin, A., Hollowed, A., Kofinas, G., Mackintosh, A., Melbourne-Thomas, J., Muelbert, M.M.C., Ottersen, G., Pritchard, H., Schuur, E.A.G., 2019. Polar Regions. In: IPCC Special Report on the Ocean and Cryosphere in a Changing Climate [H.-O. Pörtner, D.C. Roberts, V. Masson-Delmotte, P. Zhai, M. Tignor, E. Poloczanska, K. Mintenbeck, A. Alegría, M. Nicolai, A. Okem, J. Petzold, B. Rama, N.M. Weyer (eds.)]. In press.
- Meredith, M.P., Hogg, A.M., 2006. Circumpolar response of Southern Ocean eddy activity to a change in the Southern Annular Mode. *Geophys. Res. Lett.* 33, 16. <https://doi.org/10.1029/2006GL026499>
- Miao, Z., Fu, K., Sun, H., Sun, X., Yan, M., 2018. Automatic Water-Body Segmentation From High-Resolution Satellite Images via Deep Networks. *IEEE Geosci. Remote. Sens. Lett.* 15, 4, 602–606. <https://doi.org/10.1109/LGRS.2018.2794545>
- Miles, B.W.J., Stokes, C.R., Jamieson, S.S.R., 2018. Velocity increases at Cook Glacier, East Antarctica, linked to ice shelf loss and a subglacial flood event. *The Cryosphere* 12, 10, 3,123–3,136. <https://doi.org/10.5194/tc-12-3123-2018>
- Miles, K.E., Willis, I.C., Benedek, C.L., Williamson, A.G., Tedesco, M., 2017. Toward Monitoring Surface and Subsurface Lakes on the Greenland Ice Sheet Using Sentinel-1 SAR and Landsat-8 OLI Imagery. *Front. Earth Sci.* 5, 58. <https://doi.org/10.3389/feart.2017.00058>
- Milillo, P., Rignot, E., Mouginot, J., Scheuchl, B., Morlighem, M., Li, X., Salzer, J.T., 2017. On the Short-term Grounding Zone Dynamics of Pine Island Glacier, West Antarctica, Observed With COSMO-SkyMed Interferometric Data. *Geophys. Res. Lett.* 44, 20, 10,436–10,444. <https://doi.org/10.1002/2017GL074320>
- Milillo, P., Rignot, E., Rizzoli, P., Scheuchl, B., Mouginot, J., Bueso-Bello, J., Prats-Iraola, P., 2019. Heterogeneous retreat and ice melt of Thwaites Glacier, West Antarctica. *Sci. Adv.* 5, 1. <https://doi.org/10.1126/sciadv.aau3433>



- Minchew, B.M., Gudmundsson, G.H., Gardner, A.S., Paolo, F.S., Fricker, H.A., 2018. Modeling the dynamic response of outlet glaciers to observed ice-shelf thinning in the Bellingshausen Sea Sector, West Antarctica. *J. Glaciol.* 64, 244, 333–342. <https://doi.org/10.1017/jog.2018.24>
- Mohajerani, Y., Wood, M., Velicogna, I., Rignot, E., 2019. Detection of Glacier Calving Margins with Convolutional Neural Networks: A Case Study. *Remote Sens.* 11, 1, 74. <https://doi.org/10.3390/rs11010074>
- Montgomery, L., Miège, C., Miller, J., Scambos, T.A., Wallin, B., Miller, O., Solomon, D.K., Forster, R., Koenig, L., 2020. Hydrologic Properties of a Highly Permeable Firn Aquifer in the Wilkins Ice Shelf, Antarctica. *Geophys. Res. Lett.* 47, 22. <https://doi.org/10.1029/2020GL089552>
- Moreno, P.I., Vilanova, I., Villa-Martínez, R., Dunbar, R.B., Mucciarone, D.A., Kaplan, M.R., Garreaud, R.D., Rojas, M., Moy, C.M., Pol-Holz, R.D., Lambert, F., 2018. Onset and Evolution of Southern Annular Mode-Like Changes at Centennial Timescale. *Sci. Rep.* 8, 3458. <https://doi.org/10.1038/s41598-018-21836-6>
- Morlighem, M., 2020. MEaSURES BedMachine Antarctica, Version 2. [bed topography]. Boulder, Colorado USA. NASA National Snow and Ice Data Center Distributed Active Archive Center. [Last accessed 10 November 2021]. <https://doi.org/10.5067/E1QL9HFQ7A8M>
- Morlighem, M., Rignot, E., Binder, T., Blankenship, D., Drews, R., Eagles, G., Eisen, O., Ferraccioli, F., Forsberg, R., Fretwell, P., Goel, V., Greenbaum, J.S., Gudmundsson, H., Guo, J., Helm, V., Hofstede, C., Howat, I., Humbert, A., Jokat, W., Karlsson, N.B., Lee, W.S., Matsuoka, K., Millan, R., Mouginot, J., Paden, J., Pattyn, F., Roberts, J., Rosier, S., Ruppel, A., Seroussi, H., Smith, E.C., Steinhage, D., Sun, B., Broeke, M.R. van den, Ommen, T.D. van, Wessm, M. van, Young, D.A., 2020. Deep glacial troughs and stabilizing ridges unveiled beneath the margins of the Antarctic ice sheet. *Nat. Geosci.* 13, 132–137. <https://doi.org/10.1038/s41561-019-0510-8>
- Mouginot, J., Rignot, E., Scheuchl, B., 2014. Sustained increase in ice discharge from the Amundsen Sea Embayment, West Antarctica, from 1973 to 2013. *Geophys. Res. Lett.* 41, 5, 1576–1584. <https://doi.org/10.1002/2013GL059069>
- Mouginot, J., Rignot, E., Scheuchl, B., Millan, R., 2017a. Comprehensive Annual Ice Sheet Velocity Mapping Using Landsat-8, Sentinel-1, and RADARSAT-2 Data. *Remote Sens.* 9, 4, 364. <https://doi.org/10.3390/rs9040364>
- Mouginot, J., Scheuchl, B., Rignot, E., 2017b. MEaSURES Antarctic Boundaries for IPY 2007-2009 from Satellite Radar, Version 2. [Coastline, grounding line data]. Boulder, Colorado USA. NASA National Snow and Ice Data Center Distributed Active Archive Center. [Last accessed 27 May 2021]. <https://doi.org/10.5067/AXE4121732AD>
- Moussavi, M., Pope, A., Halberstadt, A.R.W., Trusel, L.D., Cioffi, L., Abdalati, W., 2020. Antarctic Supraglacial Lake Detection Using Landsat 8 and Sentinel-2 Imagery: Towards Continental Generation of Lake Volumes. *Remote Sens.* 12, 1, 134. <https://doi.org/10.3390/rs12010134>
- Moussavi, M.S., Abdalati, W., Pope, A., Scambos, T., Tedesco, M., MacFerrin, M., Grigsby, S., 2016. Derivation and validation of supraglacial lake volumes on the Greenland Ice Sheet from high-resolution satellite imagery. *Remote Sens. Environ.* 183, 294–303. <https://doi.org/10.1016/j.rse.2016.05.024>
- Müller, C., Guido, S., 2016. Introduction to Machine Learning with Python: A Guide for Data Scientists. O'Reilly Media, Inc., Sebastopol, USA.
- Munoz Sabater, J., 2019a. ERA5-Land hourly data from 1981 to present. Copernicus Climate Change Service (C3S) Climate Data Store (CDS). [Last accessed 14 March 2021]. <https://doi.org/10.24381/cds.e2161bac>
- Munoz Sabater, J., 2019b. ERA5-Land monthly averaged data from 1981 to present. Copernicus Climate Change Service (C3S) Climate Data Store (CDS). [Last accessed 16 March 2021]. <https://doi.org/10.24381/cds.68d2bb3>
- Nicolas, J.P., Bromwich, D.H., 2011. Climate of West Antarctica and Influence of Marine Air Intrusions. *J. Climate* 24, 1, 49–67. <https://doi.org/10.1175/2010JCLI3522.1>
- Nicolas, J.P., Vogelmann, A.M., Scott, R.C., Wilson, A.B., Cadetdu, M.P., Bromwich, D.H., Verlinde, J., Lubin, D., Russell, L.M., Jenkinson, C., Powers, H.H., Ryczek, M., Stone, G., Wille, J.D., 2017. January 2016 extensive summer melt in West Antarctica favoured by strong El Niño. *Nat. Commun.* 8, 15799. <https://doi.org/10.1038/ncomms15799>

- NSIDC, 2021. The Antarctic 2020 to 2021 melt season in review: <http://nsidc.org/greenland-today/2021/04/the-antarctic-2020-to-2021-melt-season-in-review/>, last accessed: 23 June 2021.
- Orheim, O., Lucchitta, B.K., 1987. Snow and Ice Studies By Thematic Mapper and Multispectral Scanner Landsat Images. *Ann. Glaciol.* 9, 109–118. <https://doi.org/10.3189/S0260305500000483>
- Pal, M., 2005. Random forest classifier for remote sensing classification. *Int. J. Remote Sens.* 26, 1, 217–222. <https://doi.org/10.1080/01431160412331269698>
- Paolo, F.S., Fricker, H.A., Padman, L., 2015. Volume loss from Antarctic ice shelves is accelerating. *Science* 348, 6232, 327–331. <https://doi.org/10.1126/science.aaa0940>
- Parish, T.R., Bromwich, D.H., 2007. Reexamination of the Near-Surface Airflow over the Antarctic Continent and Implications on Atmospheric Circulations at High Southern Latitudes. *Mon. Weather Rev.* 135, 5, 1961–1973. <https://doi.org/10.1175/MWR3374.1>
- Parish, T.R., Cassano, J.J., 2003. The Role of Katabatic Winds on the Antarctic Surface Wind Regime. *Mon. Weather Rev.* 131, 2, 317–333. [https://doi.org/10.1175/1520-0493\(2003\)131<0317:TROKWO>2.0.CO;2](https://doi.org/10.1175/1520-0493(2003)131<0317:TROKWO>2.0.CO;2)
- Pedregosa, F., Varoquaux, G., Gramfort, A., Michel, V., Thirion, B., Grisel, O., Blondel, M., Müller, A., Nothman, J., Louppe, G., Prettenhofer, P., Weiss, R., Dubourg, V., Vanderplas, J., Passos, A., Cournapeau, D., Brucher, M., Perrot, M., Duchesnay, E., 2011. Scikit-learn: Machine Learning in Python. *J Mach Learn Res* 12, 2825–2830.
- Phillips, H.A., 1998. Surface meltstreams on the Amery Ice Shelf, East Antarctica. *Ann. Glaciol.* 27, 177–181. <https://doi.org/10.3189/1998AoG27-1-177-181>
- Poinar, K., Joughin, I., Lilien, D., Brucker, L., Kehrl, L., Nowicki, S., 2017. Drainage of Southeast Greenland Firn Aquifer Water through Crevasses to the Bed. *Front. Earth Sci.* 5, 5. <https://doi.org/10.3389/feart.2017.00005>
- Pope, A., Scambos, T.A., Moussavi, M., Tedesco, M., Willis, M., Shean, D., Grigsby, S., 2016. Estimating supraglacial lake depth in West Greenland using Landsat 8 and comparison with other multispectral methods. *The Cryosphere* 10, 1, 15–27. <https://doi.org/10.5194/tc-10-15-2016>
- Pritchard, H.D., Ligtenberg, S.R.M., Fricker, H.A., Vaughan, D.G., Van den Broeke, M.R., Padman, L., 2012. Antarctic ice-sheet loss driven by basal melting of ice shelves. *Nature* 484, 502–505. <https://doi.org/10.1038/nature10968>
- Pritchard, H.D., Vaughan, D.G., 2007. Widespread acceleration of tidewater glaciers on the Antarctic Peninsula. *J. Geophys. Res.-Earth Surface* 112, F3. <https://doi.org/10.1029/2006JF000597>
- Purkey, S.G., Johnson, G.C., 2013. Antarctic Bottom Water Warming and Freshening: Contributions to Sea Level Rise, Ocean Freshwater Budgets, and Global Heat Gain. *J. Climate* 26, 16, 6,105–6,122. <https://doi.org/10.1175/JCLI-D-12-00834.1>
- Quéré, C.L., Rödenbeck, C., Buitenhuis, E.T., Conway, T.J., Langenfelds, R., Gomez, A., Labuschagne, C., Ramonet, M., Nakazawa, T., Metzl, N., Gillett, N., Heimann, M., 2007. Saturation of the Southern Ocean CO<sub>2</sub> Sink Due to Recent Climate Change. *Science* 316, 5832, 1,735–1,738. <https://doi.org/10.1126/science.1136188>
- Rabus, B.T., Lang, O., Adolphs, U., 2003. Interannual velocity variations and recent calving of Thwaites Glacier Tongue, West Antarctica. *Ann. Glaciol.* 36, 215–224. <https://doi.org/10.3189/172756403781816176>
- Rack, W., Doake, C.S.M., Rott, H., Siegel, A., Skvarca, P., 2000. Interferometric analysis of the deformation pattern of the northern Larsen Ice Shelf, Antarctic Peninsula, compared to field measurements and numerical modeling. *Ann. Glaciol.* 31, 205–210. <https://doi.org/10.3189/172756400781819851>
- Rack, W., Rott, H., Siegel, A., Skvarca, P., 1999. The motion field of northern Larsen Ice Shelf, Antarctic Peninsula, derived from satellite imagery. *Ann. Glaciol.* 29, 261–266. <https://doi.org/10.3189/172756499781821120>
- Rau, F., Braun, H.M., Saurer, H., Goßmann, H., Kothe, G., Weber, F., Ebel, M., Beppler, D., 2000. Monitoring multi-year snow cover dynamics on the Antarctic Peninsula using SAR imagery. *Polarforschung* 67, 27–40.

- Rau, F., Mauz, F., Vogt, S., Khalsa, S.J.S., Raup, B., 2005. Illustrated GLIMS Glacier Classification Manual, Version 1. GLIMS Regional Centre, 'Antarctic Peninsula': GLIMS (Global Land Ice Measurement from Space), NSIDC.
- Remy, F., Legresy, B., 2004. Subglacial hydrological networks in Antarctica and their impact on ice flow. *Ann. Glaciol.* 39, 67–72. <https://doi.org/10.3189/172756404781814401>
- Reynolds, J.M., 1981. Lakes on George VI Ice Shelf, Antarctica. *Polar Rec.* 20, 128, 425–432. <https://doi.org/10.1017/S0032247400003636>
- Reynolds, J.M., Hambrey, M.J., 1988. The structural glaciology of George VI Ice Shelf, Antarctic Peninsula. *Brit. Antarct. Surv. B.* 79, 79–95.
- Rignot, E., 2008. Changes in West Antarctic ice stream dynamics observed with ALOS PALSAR data. *Geophys. Res. Lett.* 35, 12. <https://doi.org/10.1029/2008GL033365>
- Rignot, E., 2006. Changes in ice dynamics and mass balance of the Antarctic ice sheet. *Phil. Trans. R. Soc.* 364, 1844, 1,637–1,655. <https://doi.org/10.1098/rsta.2006.1793>
- Rignot, E., Bamber, J.L., Van den Broeke, M.R., Davis, C., Li, Y., van de Berg, W.J., van Meijgaard, E., 2008. Recent Antarctic ice mass loss from radar interferometry and regional climate modelling. *Nat. Geosci.* 1, 106–110. <https://doi.org/10.1038/ngeo102>
- Rignot, E., Casassa, G., Gogineni, P., Krabill, W., Rivera, A., Thomas, R., 2004. Accelerated ice discharge from the Antarctic Peninsula following the collapse of Larsen B ice shelf. *Geophys. Res. Lett.* 31, 18. <https://doi.org/10.1029/2004GL020697>
- Rignot, E., Jacobs, S., Mouginot, J., Scheuchl, B., 2013. Ice-Shelf Melting Around Antarctica. *Science* 341, 6143, 266–270. <https://doi.org/10.1126/science.1235798>
- Rignot, E., Mouginot, J., Scheuchl, B., 2011. Ice Flow of the Antarctic Ice Sheet. *Science* 333, 6048, 1,427–1,430. <https://doi.org/10.1126/science.1208336>
- Rignot, E., Mouginot, J., Scheuchl, B., Van den Broeke, M., Van Wessel, M., Morlighem, M., 2019. Four decades of Antarctic Ice Sheet mass balance from 1979–2017. *PNAS* 116, 4, 1,095–1,103. <https://doi.org/10.1073/pnas.1812883116>
- Rignot, E., Vaughan, D.G., Schmelz, M., Dupont, T., Macayeal, D., 2002. Acceleration of Pine Island and Thwaites Glaciers, West Antarctica. *Ann. Glaciol.* 34, 189–194. <https://doi.org/10.3189/172756402781817950>
- Rintoul, S.R., Chown, S.L., DeConto, R.M., England, M.H., Fricker, H.A., Masson-Delmotte, V., Naish, T.R., Siegert, M.J., Xavier, J.C., 2018. Choosing the future of Antarctica. *Nature* 558, 233. <https://doi.org/10.1038/s41586-018-0173-4>
- Rintoul, S.R., Silvano, A., Pena-Molino, B., Van Wijk, E., Rosenberg, M., Greenbaum, J.S., Blankenship, D.D., 2016. Ocean heat drives rapid basal melt of the Totten Ice Shelf. *Sci. Adv.* 2, 12. <https://doi.org/10.1126/sciadv.1601610>
- Rivera, A., Cawkwell, F., Wendt, A., Zamora, R., 2014. Mapping Blue-Ice Areas and Crevasses in West Antarctica Using ASTER Images, GPS, and Radar Measurements, in: Kargel, J.S., Leonard, G.J., Bishop, M.P., Käb, A., Raup, B.H. (Eds.), *Global Land Ice Measurements from Space*, Springer Praxis Books. Springer, Berlin, Heidelberg, pp. 743–757. [https://doi.org/10.1007/978-3-540-79818-7\\_31](https://doi.org/10.1007/978-3-540-79818-7_31)
- Roberts, J., Galton-Fenzi, B.K., Paolo, F.S., Donnelly, C., Gwyther, D.E., Padman, L., Young, D., Warner, R., Greenbaum, J., Fricker, H.A., Payne, A.J., Cornford, S., Le Brocq, A., Van Ommen, T., Blankenship, D., Siegert, M.J., 2018. Ocean forced variability of Totten Glacier mass loss. *Geological Society, London, Special Publications* 461, 1, 175–186. <https://doi.org/10.1144/SP461.6>
- Ronneberger, O., Fischer, P., Brox, T., 2015. U-Net: Convolutional Networks for Biomedical Image Segmentation, in: *Medical Image Computing and Computer-Assisted Intervention – MICCAI 2015*; Navab, N., Hornegger, J., Wells, W.M., Frangi, A.F., Eds.; Springer International Publishing: Cham. pp. 234–241.
- Rott, H., Abdel Jaber, W., Wuite, J., Scheiblauer, S., Floricioiu, D., Van Wessel, J.M., Nagler, T., Miranda, N., Van den Broeke, M.R., 2018. Changing pattern of ice flow and mass balance for glaciers discharging into the Larsen A and B embayments, Antarctic Peninsula, 2011 to 2016. *The Cryosphere* 12, 4, 1,273–1,291. <https://doi.org/10.5194/tc-12-1273-2018>
- Rott, H., Eineder, M., Nagler, T., Floricioiu, D., 2008. New Results on Dynamic Instability of Antarctic Peninsula Glaciers detected by TerraSAR-X Ice Motion Analysis, in: 7th European Conference on Synthetic Aperture Radar. VDE, Friedrichshafen, Germany.

- Rott, H., Floricioiu, D., Wuite, J., Scheiblauer, S., Nagler, T., Kern, M., 2014. Mass changes of outlet glaciers along the Nordensjøkøld Coast, northern Antarctic Peninsula, based on TanDEM-X satellite measurements. *Geophys. Res. Lett.* 41, 22, 8,123–8,129. <https://doi.org/10.1002/2014GL061613>
- Rott, H., Müller, F., Nagler, T., Floricioiu, D., 2011. The imbalance of glaciers after disintegration of Larsen-B ice shelf, Antarctic Peninsula. *The Cryosphere* 5, 1, 125–134. <https://doi.org/10.5194/tc-5-125-2011>
- Rott, H., Rack, W., Nagler, T., 2007. Increased export of grounded ice after the collapse of northern Larsen ice shelf, Antarctic Peninsula, observed by Envisat ASAR, in: 2007 IEEE International Geoscience and Remote Sensing Symposium. IEEE, Barcelona, Spain, pp. 1174–1176. <https://doi.org/10.1109/IGARSS.2007.4423013>
- Rott, H., Rack, W., Skvarca, P., De Angelis, H., 2002. Northern Larsen Ice Shelf, Antarctica: further retreat after collapse. *Ann. Glaciol.* 34, 277–282. <https://doi.org/10.3189/172756402781817716>
- Rott, H., Skvarca, P., Nagler, T., 1996. Rapid Collapse of Northern Larsen Ice Shelf, Antarctica. *Science* 271, 5250, 788–792. <https://doi.org/10.1126/science.271.5250.788>
- Rott, H., Wuite, J., Floricioiu, D., Nagler, T., Scheiblauer, S., 2015. Synergy of TanDEM-X DEM differencing and input-output method for glacier monitoring. Presented at the 2015 IEEE International Geoscience and Remote Sensing Symposium (IGARSS), IEEE, Milan, Italy, pp. 5216–5219. <https://doi.org/10.1109/IGARSS.2015.7327010>
- Rowley, N.A., Carleton, A.M., Fegyveresi, J., 2020. Relationships of West Greenland supraglacial melt-lakes with local climate and regional atmospheric circulation. *Int J Climatol* 40, 2, 1,164–1,177. <https://doi.org/10.1002/joc.6262>
- Sazonau, V., 2012. Implementation and Evaluation of a Random Forest Machine Learning Algorithm. University of Manchester, Manchester, UK.
- Scambos, T., Fahnestock, M., Moon, T., Gardner, A., Klinger, M., 2019. Landsat 8 Ice Speed of Antarctica (LISA). <https://doi.org/10.7265/nxpc-e997>
- Scambos, T., Fricker, H.A., Liu, C.-C., Bohlander, J., Fastook, J., Sargent, A., Massom, R., Wu, A.-M., 2009. Ice shelf disintegration by plate bending and hydro-fracture: Satellite observations and model results of the 2008 Wilkins ice shelf break-ups. *Earth Planet. Sci. Lett.* 280, 1-4, 51–60. <https://doi.org/10.1016/j.epsl.2008.12.027>
- Scambos, T., Hulbe, C., Fahnestock, M., 2003. Climate-Induced Ice Shelf Disintegration in the Antarctic Peninsula, in: *Antarctic Peninsula Climate Variability: Historical and Paleoenvironmental Perspectives*, Antarctic Research Series. American Geophysical Union (AGU), pp. 79–92.
- Scambos, T.A., 2017. How much, how fast?: A science review and outlook for research on the instability of Antarctica's Thwaites Glacier in the 21st century. *Glob Planet Change* 153, 16–34. <https://doi.org/10.1016/j.gloplacha.2017.04.008>
- Scambos, T.A., Bohlander, J.A., Shuman, C.A., Skvarca, P., 2004. Glacier acceleration and thinning after ice shelf collapse in the Larsen B embayment, Antarctica. *Geophys. Res. Lett.* 31, 18. <https://doi.org/10.1029/2004GL020670>
- Scambos, T.A., Campbell, G.G., Pope, A., Haran, T., Muto, A., Lazzara, M., Reijmer, C.H., Broeke, M.R. van den, 2018. Ultralow Surface Temperatures in East Antarctica From Satellite Thermal Infrared Mapping: The Coldest Places on Earth. *Geophys. Res. Lett.* 45, 12, 6,124–6,133. <https://doi.org/10.1029/2018GL078133>
- Scambos, T.A., Hulbe, C., Fahnestock, M., Bohlander, J., 2000. The link between climate warming and break-up of ice shelves in the Antarctic Peninsula. *J. Glaciol.* 46, 154, 516–530. <https://doi.org/10.3189/172756500781833043>
- SCAR, 2019. SCAR Antarctic Digital Database (ADD): <https://www.add.scar.org/>, last accessed: 09 July 2021.
- Schneider, D.P., Deser, C., Okumura, Y., 2012. An assessment and interpretation of the observed warming of West Antarctica in the austral spring. *Clim Dyn* 38, 323–347. <https://doi.org/10.1007/s00382-010-0985-x>
- Schoof, C., 2010. Ice-sheet acceleration driven by melt supply variability. *Nature* 468, 803–806. <https://doi.org/10.1038/nature09618>
- Schoof, C., 2007. Ice sheet grounding line dynamics: Steady states, stability, and hysteresis. *J. Geophys. Res.-Earth Surface* 112, F3. <https://doi.org/10.1029/2006JF000664>

- Schröder, L., Neckel, N., Zindler, R., Humbert, A., 2020. Perennial Supraglacial Lakes in Northeast Greenland Observed by Polarimetric SAR. *Remote Sens.* 12, 7, 2798. <https://doi.org/10.3390/rs12172798>
- Schwatke, C., Scherer, D., Dettmering, D., 2019. Automated Extraction of Consistent Time-Variable Water Surfaces of Lakes and Reservoirs Based on Landsat and Sentinel-2. *Remote Sens.* 11, 9, 1010. <https://doi.org/10.3390/rs11091010>
- Seale, A., Christoffersen, P., Mugford, R.I., O'Leary, M., 2011. Ocean forcing of the Greenland Ice Sheet: Calving fronts and patterns of retreat identified by automatic satellite monitoring of eastern outlet glaciers. *J. Geophys. Res.-Earth Surface* 116, F3. <https://doi.org/10.1029/2010JF001847>
- Seehaus, T., Cook, A.J., Silva, A.B., Braun, M., 2018. Changes in glacier dynamics in the northern Antarctic Peninsula since 1985. *The Cryosphere* 12, 2, 577–594. <https://doi.org/10.5194/tc-12-577-2018>
- Seehaus, T., Marinsek, S., Helm, V., Skvarca, P., Braun, M., 2015. Changes in ice dynamics, elevation and mass discharge of Dinsmoor–Bombardier–Edgeworth glacier system, Antarctic Peninsula. *Earth Planet. Sci. Lett.* 427, 125–135. <https://doi.org/10.1016/j.epsl.2015.06.047>
- Seehaus, T.C., Marinsek, S., Skvarca, P., Van Wessem, J.M., Reijmer, C.H., Seco, J.L., Braun, M.H., 2016. Dynamic Response of Sjøgren Inlet Glaciers, Antarctic Peninsula, to Ice Shelf Breakup Derived from Multi-Mission Remote Sensing Time Series. *Front. Earth Sci.* 4, 66. <https://doi.org/10.3389/feart.2016.00066>
- Selmes, N., Murray, T., James, T.D., 2011. Fast draining lakes on the Greenland Ice Sheet. *Geophys. Res. Lett.* 38, 15. <https://doi.org/10.1029/2011GL047872>
- Sergienko, O.V., Hulbe, C.L., 2011. 'Sticky spots' and subglacial lakes under ice streams of the Siple Coast, Antarctica. *Ann. Glaciol.* 52, 58, 18–22. <https://doi.org/10.3189/172756411797252176>
- Shen, Q., Wang, H., Shum, C.K., Jiang, L., Hsu, H.T., Dong, J., 2018. Recent high-resolution Antarctic ice velocity maps reveal increased mass loss in Wilkes Land, East Antarctica. *Sci. Rep.* 8, 4477. <https://doi.org/10.1038/s41598-018-22765-0>
- Shepherd, A., Gilbert, L., Muir, A.S., Konrad, H., McMillan, M., Slater, T., Briggs, K.H., Sundal, A.V., Hogg, A.E., Engdahl, M.E., 2019. Trends in Antarctic Ice Sheet Elevation and Mass. *Geophys. Res. Lett.* 46, 14, 8,174–8,183. <https://doi.org/10.1029/2019GL082182>
- Shepherd, A., Hubbard, A., Nienow, P., King, M., McMillan, M., Joughin, I., 2009. Greenland ice sheet motion coupled with daily melting in late summer. *Geophys. Res. Lett.* 36, 1. <https://doi.org/10.1029/2008GL035758>
- Shepherd, A., Wingham, D., Rignot, E., 2004. Warm ocean is eroding West Antarctic Ice Sheet. *Geophys. Res. Lett.* 31, 23. <https://doi.org/10.1029/2004GL021106>
- Siegert, M.J., Dowdeswell, J.A., 1996. Spatial variations in heat at the base of the Antarctic ice sheet from analysis of the thermal regime above subglacial lakes. *J. Glaciol.* 42, 142, 501–509. <https://doi.org/10.3189/S0022143000003488>
- Siegert, M.J., Ellis-Evans, J.C., Tranter, M., Mayer, C., Petit, J.-R., Salamatin, A., Priscu, J.C., 2001. Physical, chemical and biological processes in Lake Vostok and other Antarctic subglacial lakes. *Nature* 414, 603–609. <https://doi.org/10.1038/414603a>
- Siegert, M.J., Kulesa, B., Bougamont, M., Christoffersen, P., Key, K., Andersen, K.R., Booth, A.D., Smith, A.M., 2018. Antarctic subglacial groundwater: a concept paper on its measurement and potential influence on ice flow. *Geol. Soc.* 461, 1, 197–213. <https://doi.org/10.1144/SP461.8>
- Siegert, M.J., Ross, N., Li, J., Schroeder, D.M., Rippin, D., Ashmore, D., Bingham, R., Gogineni, P., 2016. Subglacial controls on the flow of Institute Ice Stream, West Antarctica. *Ann. Glaciol.* 57, 73, 19–24. <https://doi.org/10.1017/aog.2016.17>
- Silvano, A., Rintoul, S.R., Peña-Molino, B., Hobbs, W.R., Wijk, E. van, Aoki, S., Tamura, T., Williams, G.D., 2018. Freshening by glacial meltwater enhances melting of ice shelves and reduces formation of Antarctic Bottom Water. *Sci. Adv.* 4, 4. <https://doi.org/10.1126/sciadv.aap9467>

- Smith, L.C., Chu, V.W., Yang, K., Gleason, C.J., Pitcher, L.H., Rennermalm, A.K., Legleiter, C.J., Behar, A.E., Overstreet, B.T., Moustafa, S.E., Tedesco, M., Forster, R.R., LeWinter, A.L., Finnegan, D.C., Sheng, Y., Balog, J., 2015. Efficient meltwater drainage through supraglacial streams and rivers on the southwest Greenland ice sheet. *PNAS* 112, 4, 1,001–1,006. <https://doi.org/10.1073/pnas.1413024112>
- Sneed, W.A., Hamilton, G.S., 2007. Evolution of melt pond volume on the surface of the Greenland Ice Sheet. *Geophys. Res. Lett.* 34, 3. <https://doi.org/10.1029/2006GL028697>
- Son, N.-T., Chen, C.-F., Chen, C.-R., Minh, V.-Q., 2018. Assessment of Sentinel-1A data for rice crop classification using random forests and support vector machines. *Geocarto International* 33, 6, 587–601. <https://doi.org/10.1080/10106049.2017.1289555>
- Speirs, J.C., Steinhoff, D.F., McGowan, H.A., Bromwich, D.H., Monaghan, A.J., 2010. Foehn Winds in the McMurdo Dry Valleys, Antarctica: The Origin of Extreme Warming Events. *J. Climate* 23, 13, 3,577–3,598. <https://doi.org/10.1175/2010JCLI3382.1>
- Spergel, J.J., Kingslake, J., Creyts, T., Wessem, M. van, Fricker, H.A., 2021. Surface meltwater drainage and ponding on Amery Ice Shelf, East Antarctica, 1973–2019. *J. Glaciol.* 67, 266, 985–998. <https://doi.org/10.1017/jog.2021.46>
- Stearns, L.A., Jezek, K.C., Van Der Veen, C.J., 2005. Decadal-scale variations in ice flow along Whillans Ice Stream and its tributaries, West Antarctica. *J. Glaciol.* 51, 172, 147–157. <https://doi.org/10.3189/172756505781829610>
- Stearns, L.A., Smith, B.E., Hamilton, G.S., 2008. Increased flow speed on a large East Antarctic outlet glacier caused by subglacial floods. *Nat. Geosci.* 1, 827–831. <https://doi.org/10.1038/ngeo356>
- Steig, E.J., Ding, Q., White, J.W.C., Küttel, M., Rupper, S.B., Neumann, T.A., Neff, P.D., Gallant, A.J.E., Mayewski, P.A., Taylor, K.C., Hoffmann, G., Dixon, D.A., Schoenemann, S.W., Markle, B.R., Fudge, T.J., Schneider, D.P., Schauer, A.J., Teel, R.P., Vaughn, B.H., Burgener, L., Williams, J., Korotkikh, E., 2013. Recent climate and ice-sheet changes in West Antarctica compared with the past 2,000 years. *Nat. Geosci.* 6, 372–375. <https://doi.org/10.1038/ngeo1778>
- Steig, E.J., Schneider, D.P., Rutherford, S.D., Mann, M.E., Comiso, J.C., Shindell, D.T., 2009. Warming of the Antarctic ice-sheet surface since the 1957 International Geophysical Year. *Nature* 457, 459–462. <https://doi.org/10.1038/nature07669>
- Stewart, A.L., Thompson, A.F., 2012. Sensitivity of the ocean's deep overturning circulation to easterly Antarctic winds. *Geophys. Res. Lett.* 39, 18. <https://doi.org/10.1029/2012GL053099>
- Stiles, W.H., Ulaby, F.T., 1980. The active and passive microwave response to snow parameters: 1. Wetness. *J. Geophys. Res.-Oceans* 85, C2, 1,037–1,044. <https://doi.org/10.1029/JC085iC02p01037>
- Stokes, C.R., Sanderson, J.E., Miles, B.W.J., Jamieson, S.S.R., Leeson, A.A., 2019. Widespread distribution of supraglacial lakes around the margin of the East Antarctic Ice Sheet. *Sci. Rep.* 9, 13823. <https://doi.org/10.1038/s41598-019-50343-5>
- Straneo, F., Heimbach, P., 2013. North Atlantic warming and the retreat of Greenland's outlet glaciers. *Nature* 504, 36–43. <https://doi.org/10.1038/nature12854>
- Sun, S., Lu, Z., Liu, W., Hu, W., Li, R., 2018. Shipnet for Semantic Segmentation on VHR Maritime Imagery, in: *IGARSS 2018 - 2018 IEEE International Geoscience and Remote Sensing Symposium*. Presented at the *IGARSS 2018 - 2018 IEEE International Geoscience and Remote Sensing Symposium*, pp. 6911–6914. <https://doi.org/10.1109/IGARSS.2018.8517337>
- Sundal, A.V., Shepherd, A., Nienow, P., Hanna, E., Palmer, S., Huybrechts, P., 2009. Evolution of supra-glacial lakes across the Greenland Ice Sheet. *Remote Sens. Environ.* 113, 10, 2,164–2,171. <https://doi.org/10.1016/j.rse.2009.05.018>
- Swithinbank, C., 1988. *Satellite Image Atlas of Glaciers of the World: Antarctica*, U.S. Geological Survey Professional Paper 1386B. United States Government Printing Office, Washington.
- Tedesco, M., 2015. Electromagnetic properties of components of the cryosphere. In: *Remote Sensing of the Cryosphere*, First Edition. ed. John Wiley & Sons, Ltd., Chichester, West Sussex.

- Tedesco, M., Lüthje, M., Steffen, K., Steiner, N., Fettweis, X., Willis, I., Bayou, N., Banwell, A., 2012. Measurement and modeling of ablation of the bottom of supraglacial lakes in western Greenland. *Geophys. Res. Lett.* 39, 2. <https://doi.org/10.1029/2011GL049882>
- Tedesco, M., Monaghan, A.J., 2009. An updated Antarctic melt record through 2009 and its linkages to high-latitude and tropical climate variability. *Geophys. Res. Lett.* 36, 18. <https://doi.org/10.1029/2009GL039186>
- Tedesco, M., Willis, I.C., Hoffman, M.J., Banwell, A.F., Alexander, P., Arnold, N.S., 2013. Ice dynamic response to two modes of surface lake drainage on the Greenland ice sheet. *Environ. Res. Lett.* 8, 034007. <https://doi.org/10.1088/1748-9326/8/3/034007>
- Tetzner, D., Thomas, E., Allen, C., 2019. A Validation of ERA5 Reanalysis Data in the Southern Antarctic Peninsula—Ellsworth Land Region, and Its Implications for Ice Core Studies. *Geosciences* 9, 7, 289. <https://doi.org/10.3390/geosciences9070289>
- The IMBIE Team, 2020. Mass balance of the Greenland Ice Sheet from 1992 to 2018. *Nature* 579, 233–239. <https://doi.org/10.1038/s41586-019-1855-2>
- The IMBIE Team, 2018. Mass balance of the Antarctic Ice Sheet from 1992 to 2017. *Nature* 558, 219–222. <https://doi.org/10.1038/s41586-018-0179-y>
- Thomas, E.R., van Wesseem, J.M., Roberts, J., Isaksson, E., Schlosser, E., Fudge, T.J., Vallelonga, P., Medley, B., Lenaerts, J., Bertler, N., van den Broeke, M.R., Dixon, D.A., Frezzotti, M., Stenni, B., Curran, M., Ekaykin, A.A., 2017. Regional Antarctic snow accumulation over the past 1000 years. *Clim. Past* 13, 11, 1,491–1,513. <https://doi.org/10.5194/cp-13-1491-2017>
- Thomas, R., Rignot, E., Kanagaratnam, P., Krabill, W., Casassa, G., 2004. Force-perturbation analysis of Pine Island Glacier, Antarctica, suggests cause for recent acceleration. *Ann. Glaciol.* 39, 133–138. <https://doi.org/10.3189/172756404781814429>
- Thompson, D.W.J., Solomon, S., 2002. Interpretation of Recent Southern Hemisphere Climate Change. *Science* 296, 5569, 895–899. <https://doi.org/10.1126/science.1069270>
- Thompson, D.W.J., Solomon, S., Kushner, P.J., England, M.H., Grise, K.M., Karoly, D.J., 2011. Signatures of the Antarctic ozone hole in Southern Hemisphere surface climate change. *Nat. Geosci.* 4, 741–749. <https://doi.org/10.1038/ngeo1296>
- Trusel, L.D., Frey, K.E., Das, S.B., Karnauskas, K.B., Kuipers Munneke, P., van Meijgaard, E., van den Broeke, M.R., 2015. Divergent trajectories of Antarctic surface melt under two twenty-first-century climate scenarios. *Nat. Geosci.* 8, 927–932. <https://doi.org/10.1038/ngeo2563>
- Tsai, Y.-L.S., Dietz, A., Oppelt, N., Kuenzer, C., 2019. Wet and Dry Snow Detection Using Sentinel-1 SAR Data for Mountainous Areas with a Machine Learning Technique. *Remote Sens.* 11, 8, 895. <https://doi.org/10.3390/rs11080895>
- Tuckett, P.A., Ely, J.C., Sole, A.J., Livingstone, S.J., Davison, B.J., Wesseem, J.M. van, Howard, J., 2019. Rapid accelerations of Antarctic Peninsula outlet glaciers driven by surface melt. *Nat. Commun.* 10, 4311. <https://doi.org/10.1038/s41467-019-12039-2>
- Turner, J., Anderson, P., Lachlan-Cope, T., Colwell, S., Phillips, T., Kirchgassner, A., Marshall, G.J., King, J.C., Bracegirdle, T., Vaughan, D.G., Lagun, V., Orr, A., 2009. Record low surface air temperature at Vostok station, Antarctica. *J. Geophys. Res.-Atmos.* 114, D24. <https://doi.org/10.1029/2009JD012104>
- Turner, J., Colwell, S.R., Marshall, G.J., Lachlan-Cope, T.A., Carleton, A.M., Jones, P.D., Lagun, V., Reid, P.A., Iagovkina, S., 2005. Antarctic climate change during the last 50 years. *Int J Climatol* 25, 3, 279–294. <https://doi.org/10.1002/joc.1130>
- Turner, J., Lachlan-Cope, T.A., Colwell, S., Marshall, G.J., Connolley, W.M., 2006. Significant Warming of the Antarctic Winter Troposphere. *Science* 311, 5769, 1,914–1,917. <https://doi.org/10.1126/science.1121652>
- Turner, J., Lu, H., White, I., King, J.C., Phillips, T., Hosking, J.S., Bracegirdle, T.J., Marshall, G.J., Mulvaney, R., Deb, P., 2016. Absence of 21st century warming on Antarctic Peninsula consistent with natural variability. *Nature* 535, 411–415. <https://doi.org/10.1038/nature18645>
- Turner, J., Maksym, T., Phillips, T., Marshall, G.J., Meredith, M.P., 2013. The impact of changes in sea ice advance on the large winter warming on the western Antarctic Peninsula. *Int J Climatol* 33, 4, 852–861. <https://doi.org/10.1002/joc.3474>



- Turner, J., Marshall, G.J., Clem, K., Colwell, S., Phillips, T., Lu, H., 2020. Antarctic temperature variability and change from station data. *Int J Climatol* 40, 6, 2,986–3,007. <https://doi.org/10.1002/joc.6378>
- Turton, J.V., Kirchgassner, A., Ross, A.N., King, J.C., Kuipers Munneke, P., 2020. The influence of föhn winds on annual and seasonal surface melt on the Larsen C Ice Shelf, Antarctica. *The Cryosphere* 14, 11, 4,165–4,180. <https://doi.org/10.5194/tc-14-4165-2020>
- Urraca, R., Huld, T., Gracia-Amillo, A., Martinez-de-Pison, F.J., Kaspar, F., Sanz-Garcia, A., 2018. Evaluation of global horizontal irradiance estimates from ERA5 and COSMO-REA6 reanalyses using ground and satellite-based data. *Sol Energy* 164, 339–354. <https://doi.org/10.1016/j.solener.2018.02.059>
- van Wessem, J.M., Ligtenberg, S.R.M., Reijmer, C.H., van de Berg, W.J., van den Broeke, M.R., Barrand, N.E., Thomas, E.R., Turner, J., Wuite, J., Scambos, T.A., van Meijgaard, E., 2016. The modelled surface mass balance of the Antarctic Peninsula at 5.5 km horizontal resolution. *The Cryosphere* 10, 1, 271–285. <https://doi.org/10.5194/tc-10-271-2016>
- van Wessem, J.M., Steger, C.R., Wever, N., van den Broeke, M.R., 2021. An exploratory modelling study of perennial firn aquifers in the Antarctic Peninsula for the period 1979–2016. *The Cryosphere* 15, 2, 695–714. <https://doi.org/10.5194/tc-15-695-2021>
- van Wessem, J.M., van de Berg, W.J., Noël, B.P.Y., van Meijgaard, E., Amory, C., Birnbaum, G., Jakobs, C.L., Krüger, K., Lenaerts, J.T.M., Lhermitte, S., Ligtenberg, S.R.M., Medley, B., Reijmer, C.H., van Tricht, K., Trusel, L.D., van Ulf, L.H., Wouters, B., Wuite, J., van den Broeke, M.R., 2018. Modelling the climate and surface mass balance of polar ice sheets using RACMO2 – Part 2: Antarctica (1979–2016). *The Cryosphere* 12, 4, 1,479–1,498. <https://doi.org/10.5194/tc-12-1479-2018>
- Vaughan, D.G., Comiso, J.C., Allison, I., Carrasco, J., Kaser, G., Kwok, R., Mote, P., Murray, T., Paul, F., Ren, J., Rignot, E., Solomina, O., Steffen, K., Zhang, T., 2013. Observations: Cryosphere. In: *Climate Change 2013: The Physical Science Basis. Contribution of Working Group I to the Fifth Assessment Report of the Intergovernmental Panel on Climate Change* [Stocker, T.F., D. Qin, G.-K. Plattner, M. Tignor, S.K. Allen, J. Boschung, A. Nauels, Y. Xia, V. Bex and P.M. Midgley (eds.)]. Cambridge University Press, Cambridge, United Kingdom and New York, NY, USA.
- Vaughan, D.G., Doake, C.S.M., 1996. Recent atmospheric warming and retreat of ice shelves on the Antarctic Peninsula. *Nature* 379, 328–331. <https://doi.org/10.1038/379328a0>
- Vaughan, D.G., Mantripp, D.R., Sievers, J., Doake, C.S.M., 1993. A synthesis of remote sensing data on Wilkins Ice Shelf, Antarctica. *Ann. Glaciol.* 17, 211–218. <https://doi.org/10.3189/S0260305500012866>
- Wagner, A.C., 1972. Flooding of the ice shelf in George VI Sound. *Brit. Antarct. Surv. B.* 28, 71–74.
- Walker, C.C., Gardner, A.S., 2017. Rapid drawdown of Antarctica's Wordie Ice Shelf glaciers in response to ENSO/Southern Annular Mode-driven warming in the Southern Ocean. *Earth Planet. Sci. Lett.* 476, 100–110. <https://doi.org/10.1016/j.epsl.2017.08.005>
- Wang, L., Scott, K.A., Xu, L., Clausi, D.A., 2016. Sea Ice Concentration Estimation During Melt From Dual-Pol SAR Scenes Using Deep Convolutional Neural Networks: A Case Study. *IEEE Trans. Geosci. Remote Sens.* 54, 8, 4,524–4,533. <https://doi.org/10.1109/TGRS.2016.2543660>
- Wesche, C., Dierking, W., 2014. From ice shelves to icebergs: Classification of calving fronts, iceberg monitoring and drift simulation, in: *IEEE Geoscience and Remote Sensing Symposium*. Presented at the IEEE Geoscience and Remote Sensing Symposium, pp. 274–277. <https://doi.org/10.1109/IGARSS.2014.6946410>
- Wessel, B., Huber, M., Wohlfart, C., Bertram, A., Osterkamp, N., Marschalk, U., Gruber, A., Reuß, F., Abdullahi, S., Georg, I., Roth, A., 2021. TanDEM-X PolarDEM 90 m of Antarctica: Generation and error characterization. *The Cryosphere*, 15, 11, 5241–5260. <https://doi.org/10.5194/tc-15-5241-2021>
- Whillans, I.M., Van Der Veen, C.J., 1993. New and improved determinations of velocity of Ice Streams B and C, West Antarctica. *J. Glaciol.* 39, 133, 483–590. <https://doi.org/10.3189/S0022143000016373>

- Williamson, A.G., Arnold, N.S., Banwell, A.F., Willis, I.C., 2017. A Fully Automated Supraglacial lake area and volume Tracking (“FAST”) algorithm: Development and application using MODIS imagery of West Greenland. *Remote Sens. Environ.* 196, 113–133. <https://doi.org/10.1016/j.rse.2017.04.032>
- Willis, M.J., Herried, B.G., Bevis, M.G., Bell, R.E., 2015. Recharge of a subglacial lake by surface meltwater in northeast Greenland. *Nature* 518, 223–227. <https://doi.org/10.1038/nature14116>
- Winther, J.-G., Elvehøy, H., Bøggild, C.E., Sand, K., Liston, G., 1996. Melting, runoff and the formation of frozen lakes in a mixed snow and blue-ice field in Dronning Maud Land, Antarctica. *J. Glaciol.* 42, 141, 271–278. <https://doi.org/10.3189/S0022143000004135>
- Winther, J.-G., Jespersen, M.N., Liston, G.E., 2001. Blue-ice areas in Antarctica derived from NOAA AVHRR satellite data. *J. Glaciol.* 47, 157, 325–334. <https://doi.org/10.3189/172756501781832386>
- Wood, M., Rignot, E., Fenty, I., An, L., Bjørk, A., Broeke, M. van den, Cai, C., Kane, E., Menemenlis, D., Millan, R., Morlighem, M., Mouginot, J., Noël, B., Scheuchl, B., Velicogna, I., Willis, J.K., Zhang, H., 2021. Ocean forcing drives glacier retreat in Greenland. *Sci. Adv.* 7, 1. <https://doi.org/10.1126/sciadv.aba7282>
- Wouters, B., Martin-Español, A., Helm, V., Flament, T., Wessem, J.M. van, Ligtenberg, S.R.M., Broeke, M.R. van den, Bamber, J.L., 2015. Dynamic thinning of glaciers on the Southern Antarctic Peninsula. *Science* 348, 6237, 899–903. <https://doi.org/10.1126/science.aaa5727>
- Wuite, J., Rott, H., Hetzenecker, M., Floricioiu, D., De Rydt, J., Gudmundsson, G.H., Nagler, T., Kern, M., 2015. Evolution of surface velocities and ice discharge of Larsen B outlet glaciers from 1995 to 2013. *The Cryosphere* 9, 3, 957–969. <https://doi.org/10.5194/tc-9-957-2015>
- Xu, H., 2006. Modification of normalised difference water index (NDWI) to enhance open water features in remotely sensed imagery. *Int. J. Remote Sens.* 27, 14, 3,025–3,033. <https://doi.org/10.1080/01431160600589179>
- Yang, K., Smith, L.C., 2013. Supraglacial Streams on the Greenland Ice Sheet Delineated From Combined Spectral–Shape Information in High-Resolution Satellite Imagery. *IEEE Geosci. Remote. Sens. Lett.* 10, 4, 801–805. <https://doi.org/10.1109/LGRS.2012.2224316>
- Young, N.W., Hyland, G., 2002. Velocity and strain rates derived from InSAR analysis over the Amery Ice Shelf, East Antarctica. *Ann. Glaciol.* 34, 228–234. <https://doi.org/10.3189/172756402781817842>
- Zhang, E., Liu, L., Huang, L., 2019. Automatically delineating the calving front of Jakobshavn Isbræ from multitemporal TerraSAR-X images: a deep learning approach. *The Cryosphere* 13, 6, 1,729–1,741. <https://doi.org/10.5194/tc-13-1729-2019>
- Zhang, P., Ke, Y., Zhang, Z., Wang, M., Li, P., Zhang, S., 2018. Urban Land Use and Land Cover Classification Using Novel Deep Learning Models Based on High Spatial Resolution Satellite Imagery. *Sensors* 18,11, 3717. <https://doi.org/10.3390/s18113717>
- Zhang, Z., Liu, Q., Wang, Y., 2018. Road Extraction by Deep Residual U-Net. *IEEE Geosci. Remote. Sens. Lett.* 15, 5, 749–753. <https://doi.org/10.1109/LGRS.2018.2802944>
- Zheng, L., Zhou, C., 2019. Comparisons of snowmelt detected by microwave sensors on the Shackleton Ice Shelf, East Antarctica. *Int. J. Remote Sens.* 41, 4, 1,338–1,348. <https://doi.org/10.1080/01431161.2019.1666316>
- Zhong, L., Hu, L., Zhou, H., 2019. Deep learning based multi-temporal crop classification. *Remote Sens. Environ.* 221, 430–443. <https://doi.org/10.1016/j.rse.2018.11.032>
- Zibordi, G., Van Woert, M.L., 1993. Antarctic sea ice mapping using the AVHRR. *Remote Sens. Environ.* 45, 2, 155–163. [https://doi.org/10.1016/0034-4257\(93\)90039-Z](https://doi.org/10.1016/0034-4257(93)90039-Z)
- Zwally, H.J., Abdalati, W., Herring, T., Larson, K., Saba, J., Steffen, K., 2002. Surface Melt-Induced Acceleration of Greenland Ice-Sheet Flow. *Science* 297, 5579, 218–222. <https://doi.org/10.1126/science.1072708>



## Eidesstattliche Erklärung

### Versicherung an Eides Statt

Ich, Mariel Dirscherl, wohnhaft in der Hammersbacher Str. 23a, 81377 München, mit der Matrikel-Nr. 2561552 versichere an Eides Statt durch meine Unterschrift, dass ich die Dissertation „Remote Sensing of Supraglacial Lake Dynamics in Antarctica - Exploiting Methods from Artificial Intelligence for Derivation of Antarctic Supraglacial Lake Extents in Multi-Sensor Remote Sensing Data“ selbständig und ohne fremde Hilfe angefertigt, alle Stellen, die ich wörtlich oder dem Sinne nach aus Veröffentlichungen entnommen habe, als solche kenntlich gemacht und ich auch keine anderen als die von mir angegebenen Quellen und Hilfsmittel benutzt habe.

Ich versichere an Eides Statt durch meine Unterschrift, dass ich die Regeln der Universität Würzburg über gute wissenschaftliche Praxis eingehalten habe, insbesondere, dass ich die Gelegenheit zum Promotionsvorhaben nicht kommerziell vermittelt bekommen und insbesondere nicht eine Person oder Organisation eingeschaltet habe, die gegen Entgelt Betreuer bzw. Betreuerinnen für die Anfertigung von Dissertationen sucht.

Ich versichere an Eides Statt, dass ich die vorgenannten Angaben nach bestem Wissen und Gewissen gemacht habe und dass die Angaben der Wahrheit entsprechen und ich nichts verschwiegen habe.

Die Strafbarkeit einer falschen eidesstattlichen Versicherung ist mir bekannt, namentlich die Strafandrohung gemäß § 156 StGB bis zu drei Jahren Freiheitsstrafe oder Geldstrafe bei vorsätzlicher Begehung der Tat bzw. gemäß § 161 Abs. 1 StGB bis zu einem Jahr Freiheitsstrafe oder Geldstrafe bei fahrlässiger Begehung.

München, 02.12.2021

Ort, Datum

Unterschrift



## Curriculum Vitae

### ————— Persönliche Daten

**Name** Mariel Christina Dirscherl  
**Geburtsdatum/-ort**  
**Anschrift**  
**Telefon**  
**E-Mail** mariel.dirscherl@dlr.de

### ————— Beruflicher Werdegang

**Seit 01/2022** **Wissenschaftliche Mitarbeiterin**  
 Deutsches Zentrum für Luft- und Raumfahrt (DLR), Deutsches Fernerkundungsdatenzentrum (DFD), Dynamik der Landoberfläche Fernerkundung supraglazialer Seen auf den globalen Eisschilden

**06/2018 – 12/2021** **Doktorandin / Wissenschaftliche Mitarbeiterin**  
 DLR, DFD, Dynamik der Landoberfläche  
 Automatisierte Ableitung von supraglazialen Seen in der Antarktis aus Fernerkundungsdaten

**02/2018 – 05/2018** **Gastwissenschaftlerin**  
 DLR, Methodik der Fernerkundung (IMF), SAR Signalverarbeitung  
 Ableitung von digitalen Höhenmodellen aus TanDEM-X Daten

**09/2017 – 05/2018** **Wissenschaftliche Mitarbeiterin**  
 University of Iceland, Institute of Earth Sciences, Reykjavík, Island  
 Fernerkundung subglazialer vulkanischer Wärmequellen

**06/2017 – 07/2017** **Junior Expertin für Luft- und Satellitenbildinterpretation**  
 GAF AG, München, Deutschland  
 Projekt „Jährliche landwirtschaftliche Subventionskontrolle“

**03/2017 – 05/2017** **Ehrenamtliche wissenschaftliche Mitarbeiterin**  
 University of Colima, Faculty of Sciences, Colima, Mexiko  
 Fernerkundung von aktiven Vulkanen in Mexiko

**05/2016 – 08/2016** **Wissenschaftliche Hilfskraft**  
 DLR, IMF, SAR Signalverarbeitung  
 Masterarbeit

**01/2015 – 03/2015** **Praktikantin**  
 DLR, DFD, Georisiken und zivile Sicherheit  
 Parameteranalysen zu polarimetrischen Radardaten

**11/2012 – 01/2015** **Assistenz**  
 Geographische Gesellschaft München, Deutschland

**02/2011 – 06/2011** **Praktikantin**  
 Instituto Costarricense de Electricidad (ICE), San José, Costa Rica  
 Tätigkeit im Bereich „Erneuerbare Energien“

## **Schulische und Akademische Ausbildung**

- 06/2018 – 06/2022**    **Promotion, Julius-Maximilians-Universität Würzburg  
(in Kooperation mit dem Deutschen Zentrum für Luft- und  
Raumfahrt)**  
Titel der Dissertation: „Remote Sensing of Supraglacial Lake  
Dynamics in Antarctica - Exploiting Methods from Artificial  
Intelligence for Derivation of Antarctic Supraglacial Lake Extents in  
Multi-Sensor Remote Sensing Data”
- 09/2015 – 11/2016**    **Environmental Mapping (M.Sc.), University College London**  
Titel der Masterarbeit: „Topographic change quantification and  
DEM uncertainty assessment using TanDEM-X and F-SAR DEM  
time series and quality maps: Application to the 2014-2015  
Bárðarbunga volcanic eruption, Iceland”
- 10/2011 – 03/2015**    **Geographie (B.Sc.), Ludwig-Maximilians-Universität München**  
Titel der Bachelorarbeit: „Volcanism as natural hazard in Iceland –  
local, regional and global consequences“
- 06/2009**                **Abitur am Lise-Meitner-Gymnasium Unterhaching**

## **Preise und Stipendien**

- 05/2022**                Stipendium der Helmholtz Information & Data Science Academy  
(HiDA) für einen dreimonatigen wissenschaftlichen Gastaufenthalt  
an der Universität in Tromsø, Norwegen
- 08/2017**                Stipendium des University of Iceland Research Fund für einen  
Forschungsaufenthalt in Reykjavík, Island
- 12/2016**                Reise-Stipendium für die GRSG 27th Annual Conference 2016 in  
London, Großbritannien

## **Sprachkenntnisse**

- Deutsch**                Muttersprache
- Englisch**                Fließend in Sprache und Schrift
- Französisch**            Gute Kenntnisse
- Spanisch**                Gute Kenntnisse

## **EDV Kenntnisse**

- Programmierung**    Python, Google Earth Engine JavaScript API, Bash-Scripting, IDL,  
MATLAB, C++
- GIS Anwendungen**    ArcGIS, QGIS, GDAL/OGR, SNAP, ENVI, ERDAS IMAGINE,  
PolSARpro, eCognition, SCENE, NEST
- Betriebssysteme**      Windows, Linux